Constraining Metamorphic and Tectonic Evolution in Convergent Terranes: How Trace Elements and Mineral Inclusions Shape Mechanical and Reconstructive Models

Kyle Thomas Ashley

Dissertation submitted to the faculty of the Virginia Polytechnic Institute and State University
in partial fulfillment of the requirements for the degree of

DOCTOR OF PHILOSOPHY
IN
GEOSCIENCES

§

Richard D. Law, Co-Chair
Robert J. Tracy, Co-Chair
Mark J. Caddick
Robert J. Bodnar
Jay B. Thomas
Andreas K. Kronenberg

§

March 26, 2015
Blacksburg, Virginia

Keywords: P-T-t-D evolution, quartz recrystallization, trace element distribution, elastic modeling, thermobarometry, growth-composition models, tectonic evolution

Constraining Metamorphic and Tectonic Evolution in Convergent Terranes: How Trace Elements and Mineral Inclusions Shape Mechanical and Reconstructive Models

Abstract

Conventional thermobarometry in metamorphic systems has been primarily limited to constraining peak temperature (or pressure) along a generalized *P-T* loop. This is largely attributed to the assumption that mineral assemblages and chemistries achieve a state closest to equilibrium with the maximum thermal (and therefore energetic) input at these peak conditions. However, this traditional approach is limited in providing much information about the evolution of a metamorphic terrane, which is modified by tectonic (kinematic) forces, fluid and component mobility, and heating duration.

The ubiquity of quartz in the continental crust has driven much interest in using the phase for thermobarometric purposes. In this dissertation, I discss the application of elastic theory in reconstructing conditions of inclusion encapsulation through inclusion pressure estimation with Raman spectroscopy. In some instances, overpressuring of quartz inclusions in garnet give evidence for high-pressure formation conditions. When analyses are collected from garnet core to rim, pressure paths along garnet growth can be inferred (if temperature can be reasonably estimated). In high-*T*, low-*P* terranes, quartz may become dilated if the inclusion adheres to the host. If a quartz inclusion is sufficiently stretched, transformation to a low-density polymorph may occur.

Trace element uptake, particularly Ti, have been characterized in quartz and understood to be the result of a temperature- (and to a lesser extent, pressure-) sensitive substitution for Si^{4+}. However, the application of the Ti-in-quartz thermobarometer in quartz mylonites has led to mixed results due to the low-Ti resetting that occurs with dynamic recrystallization. We applied defect energy simulations and took a global assessment of deformed quartz trace element chemistries to infer that sweeping grain boundaries provide short pathways that allows localized re-equilibration with a Ti-undersaturated medium, resulting in Ti removal from the quartz lattice. In addition, thermodynamic pseudosection modeling has provided a method to assess Ti activity as a dynamic parameter – one that evolves as the phase stability changes through prograde and retrograde metamorphic reactions. With this understanding, better growth-composition models can be derived to infer complex pressure-temperature-time-deformation (*P-T-t-D*) histories of metamorphic rocks.

These techniques and results are coupled with conventional thermobarometry techniques to provide a more comprehensive picture of the conditions experienced by a rock through the evolution, from burial to exhumation to the Earth's surface. The thermal evolution is used to provide conceptual thermal-kinematic models to explain tectonic evolution and heat advection in the continental lithosphere in ancient mountain belts.

Graciously dedicated to my future wife

Brittany Balhouse.

Acknowledgements

First and foremost, I must acknowledge the governing agency that made my tenure at Virginia Tech possible: ICTAS, the Institute for Critical Technology and Applied Sciences. It was an honor to receive the prestigious ICTAS Doctoral Scholar fellowship in support of my PhD research, and is the result of the forethought and hard work of my advisers Rick Law and Bob Tracy. This fellowship allowed me to greatly broaden my horizons over the past four years.

Most of the success of the diverse culmination of papers from my PhD work is attributed to my committee members and collaborators. I was fortunate to work with such a fantastic and encouraging group of people with a wide spectrum of expertise. They had invaluable insights that greatly improved these studies. This group of people includes Rick Law, Bob Tracy, Robert Bodnar, Mark Caddick, Jay Thomas, Andreas Kronenberg, Bill Carlson, Bob Darling, Matt Steele-MacInnis, Frank Spear, Laura Webb, and John Hughes. Whether enjoying a bev while sharing stories at the local pub, or having a passing conversation in the hallway, these people have shaped my interests the most during my vocation at Virginia Tech.

I am most thankful to the friends I have made and my ever-supporting family. In particular, some of the Structures Group bloaks have been a joy to be around and work with, including Don Stahr, Matt Francis, Ryan Thigpen, Kyle Overby, and Calvin Mako. In addition to friends, I met the love of my life, Brittany Balhouse, while at Virginia Tech. Last but not least, I am forever grateful to my parents, Wayne and Vickie Ashley. Your love and encouragement made this dream a reality. Thank you, for *absolutely everything*.

Attributions

Chapter 2 was published as: Ashley, K.T., Caddick, M.J., Steele-MacInnis, M., Bodnar, R.J., and Dragovic, B., 2014, Geothermobarometric history of subduction recorded by quartz inclusions in garnet, *Geochemistry, Geophysics, Geosystems*, **15***(2)*, 350-360. K.T. Ashley was responsible for project conception, elastic model refinement, sample analysis, data reduction and interpretations, figure development, and writing the manuscript. R.J. Bodnar (Virginia Tech, Blacksburg, VA) and M. Steele-MacInnis (ETH, Zurich, CH) helped in Raman spectra optimization, sample selection, geologic interpretations and manuscript revisions. M.J. Caddick (Virginia Tech, Blacksburg, VA) helped with interpretations and manuscript revision. B. Dragovic (Virginia Tech, Blacksburg, VA) provided the samples and aided with manuscript revisions.

Chapter 3 was published as: Ashley, K.T., Steele-MacInnis, M., and Caddick, M.J., 2014, *QuIB Calc*: A MATLAB® script for geobarometry based on Raman spectroscopy and elastic modeling of quartz inclusions in garnet, *Computers and Geosciences,* **66***,* 155-157. K.T. Ashley was responsible for script and GUI development, elastic model refinement, database construct, and writing the manuscript. M. Caddick (Virginia Tech, Blacksburg, VA) and M. Steele-MacInnis (ETH, Zurich, CH) suggested program modifications and aided in manuscript revisions.

Chapter 4 was submitted as: Ashley, K.T., Darling, R.S., Bodnar, R.J., and Law, R.D., *in review*, Significance of "stretched" mineral inclusions for reconstructing *P-T* exhumation history, *Contributions to Mineralogy and Petrology*. K.T. Ashley was responsible for analyzing samples with Raman spectroscopy, data reduction, applying elastic models, interpretations, figure development, and writing the manuscript. R.S. Darling (SUNY Cortland, Cortland, NY), R.J. Bodnar (Virginia Tech, Blacksburg, VA), and R.D. Law (Virginia Tech, Blacksburg, VA) provided critical input in modeling implications, promoted discussions on anisotropic elastic consequences and inclusion adhesion to the host, and aided in manuscript revisions. R. S. Darling provided Adirondack samples that analyzed in this study.

Chapter 5 was submitted as: Ashley, K.T., Law, R.D., Kronenberg, A.K., and Stahr, D.W., *in review*, Constraining water contents during near-peak metamorphism: Metamorphic water sequestration and modified rock mechanics, *Earth and Planetary Science Letters*. K.T. Ashley was responsible for developing/refining modeling approach, collecting bulk rock chemistries, pseudosection modeling, interpreting the data, writing the manuscript and generating the figures. R.D. Law (Virginia Tech, Blacksburg, VA), A.K. Kronenberg (Texas A&M, College Station, TX), and D.W. Stahr (Virginia Tech, Blacksburg, VA) provided critical input in modeling implications, promoted discussions on hydrolytic weakening, and edited the manuscript.

Chapter 6 was published as: Ashley, K.T., Carlson, W.D., Law, R.D., and Tracy, R.J., 2014, Ti resetting in quartz during dynamic recrystallization: Mechanisms and significance, *American Mineralogist*, **99**, 2025-2030. K.T. Ashley was responsible for X-ray diffraction measurements, Ti analyses, literature review and writing the manuscript. W.D. Carlson (UT Austin, Austin, TX) conducted simulations and with the other co-authors (R.D. Law and R.J. Tracy, Virginia Tech, Blacksburg, VA) gave input and insights into implications of Ti resetting in quartz during dynamic recrystallization.

Chapter 7 was published as: Ashley, K.T., and Law, R.D., 2015, Modeling prograde TiO_2 activity and its significance for Ti-in-quartz thermobarometry of pelitic metamorphic rocks, *Contributions to Mineralogy and Petrology,* **169**:23, 1-7. K.T. Ashley was responsible for the thermodynamic modeling and writing the manuscript. R.D. Law (Virginia Tech, Blacksburg, VA) provided geological implications and aided in manuscript revisions.

Chapter 8 was submitted as: Ashley, K.T., Law, R.D., Bodnar, R.J., and Eriksson, K.A., *in review*, Quartz inclusion in garnet: Time capsules of early mountain building, *Geological Society of America (Memoir)*. K.T. Ashley was responsible for growth-composition modeling, thermodynamic modeling, inclusion characterization with Raman spectroscopy, and writing the manuscript. R.D. Law, R.J. Bodnar, and K.A. Eriksson (Virginia Tech, Blacksburg, VA) provided expertise with respect to microstructural controls, fluid inclusion characterization, and diagenesis of muds. In addition, co-authors provided geologic interpretations and manuscript revisions.

Chapter 9 is in press as: Ashley, K.T., Thigpen, J.R., and Law, R.D., 2015, Prograde evolution of the Scottish Caledonides and tectonic implications, *Lithos,* doi: 10.1016/j.lithos.2015.03.011. K.T. Ashley was responsible for analyzing mineral chemistries, cathodoluminescence imaging, thermodynamic modeling, constraining prograde pressures and temperatures, modeling the duration of near-peak heating, and writing the manuscript. J.R. Thigpen (British Petroleum, Houston, TX) provided the tectonic models and wrote portions of the manuscript. R.D. Law (Virginia Tech, Blacksburg, VA) provided input and insights into implications of these results and aided in manuscript revisions.

Note: Reprint permission statements for all published work can be found in Appendix D. Full lisence agreements can be found within the supplementary document.

Contents

List of Tables

List of Figures

Chapter 2

Chapter 3

Chapter 4

Chapter 5

Chapter 6

Chapter 7

Chapter 8

Chapter 9

Appendix A

Appendix C

Summary of Notations

Thermodynamics and Crystal Chemistry

T	temperature
T_c	critical temperature in the Landau model
P	pressure
P_{th}	thermal pressure term used in modified Tait equation of state
R	gas constant (0.0083144 kJ K^{-1})
μ_i	chemical potential of component *i*
$\mu^\circ{}_i$	chemical potential of component *i at a reference standard state*
f_i	fugacity of component *i*
$f^\circ{}_i$	Fugacity of component *i* at a reference standard state
V	molar volume
S_0	adiabatic molar entropy
H	molar enthalpy
U	internal energy
$\bar{G}^\circ{}_i$	Gibbs free energy of component *i* at standard state
ΔG_{rxn}	Gibbs free energy of a reaction
θ	Einstein temperature
n_i	number of atoms in phase i
X_i^k	mole fraction of component i on site k in a phase
a_i	activity of component i in a solution
$[i]$	composition of trace element i (ppm)

Elastic Properties

α	thermal expansivity
κ	bulk modulus
κ'	first-order pressure derivative of bulk modulus
κ"	second-order pressure derivative of bulk modulus
dκ/dT	temperature derivative of bulk modulus
μ	shear modulus
γ	temperature integral of thermal expansivity
$\dot{\varepsilon}$	strain rate (sec^{-1})

Lattice Energetics and Structure

U	Buckingham potentials
θ	bond angle
θ_0	ideal bond angle
φ	Eulerian angle (fixed to 0° or 180° in X-ray diffraction measurements)

Additional Symbols

r_i	radius of phase i
x	inclusion size dependency term ($= r_{inclusion}/r_{host}$)
σT	temperature uncertainty
σP	pressure uncertainty (1σ = 68.3% confidence; 2σ = 95.4% confidence)
ν_i	Raman band at standard position i (cm^{-1})
$\Delta\nu_i$	Raman waveshift for i peak, relative to adiabatic standard position (cm^{-1})

Chapter 1

Introduction: Dissertation Organization

This dissertation covers a spectrum of topics from lattice energetics, elastic response, metamorphic evolution, deformation controls and consequences, thermodynamic applications, and tectonic reconstruction. While each chapter generally falls under the theme of understanding deformation and metamorphism as physiochemical drivers in the lithosphere, individual or groups of chapter(s) are stand alone with a more specific aim. Here, I briefly outline the reasons for the current organization.

Chapter 2 evaluates the physical response of included minerals to changing intensive variables and utilizes retained pressures to evaluate thermobarometric conditions during encapsulation. This seemed like a logical start, for the elastic properties of minerals characterize and predict the physical response of phases during progressive heating and burial. Chapter 3 stems from this work, providing a program on the MATLAB® platform to handle the iterative functions that go into these barometric calculations. Chapter 4 takes the modeling approach applied in Chapters 2 and 3 and investigates the presence of cristobalite inclusions in Adirondack garnets. Here, volumetric evolution of inclusions adhered to the container wall are dilated in response to the elastic properties of the host and inclusion

when exhumed from the pressure and temperature of formation. This work suggests these properties and dilation of inclusion minerals may promote phase transformations and lead to unexpected inclusion suites well removed from the pressures and temperatures of stability.

Chapter 5 combines mechanical and thermochemical considerations throughout rock deformation and metamorphism, making it a logical transition between earlier chapters (that apply elastic theory) and later chapters (that investigate mineral chemistries and thermodynamic modeling). This chapter takes a thermodynamic modeling approach to constrain peak metamorphic water content, activity and fugacity. The results are used to discuss the effects of reduced water fugacity (and activity) on rheologic properties of the continental crust, water sequestration, and potential implications on metamorphic (dis)equilibrium.

Chapter 6 simulates the defect energetics of substituting Ti for Si in the tetrahedral sites in quartz. In particular, the study was conducted to see if an appreciable amount of lattice strain results from the substitution, which may promote Ti expulsion during dynamic recrystallization (a strain-minimization process). High defect energies only emerge in super-saturated quartz (10s of weight percent TIO_2 – well above what is observed in nature) suggesting expulsion results from thermodynamic equilibration through sweeping (sub)grain boundaries, buffered by the Ti under-saturated intercrystalline medium. Chapter 7 provides a technique for modeling titania activity in *P-T* space, allowing for better temperature constraints and to limit activity estimates to observed minerals in thin section. Chapter 8 couples Ti distribution analysis of quartz inclusions in garnet with growth-composition modeling to infer conditions that would have led to quartz growth through diagenesis and early prograde metamorphism. Results are integrated with a fluid inclusion composition assessment in various microstructural settings to determine the evolution of fluid in the rock throughout the prograde and retrograde history. Chapter 9 applies conventional thermobarometry and pseudosection analysis

techniques to constrain pressure and temperature evolution across thrust sheets in the Moine Supergroup (northern Scotland). Results are used to develop thermal-kinematic models and describes the tectonic evolution during Scandian orogenesis. Ti in quartz is further applied here, where diffusion profiles in quartz inclusions in garnet are evaluated against with finite-difference diffusion models to constrain the duration of near-peak metamorphic heating.

Chapter 2

Geothermobarometric History of Subduction Recorded by Quartz Inclusions in Garnet

Kyle T. Ashley[1], Mark J. Caddick[1], Matthew Steele-MacInnis[1], Robert J. Bodnar[1], Besim Dragovic[1]

[1]*Department of Geosciences, Virginia Polytechnic Institute and State University, Blacksburg, VA 24061, USA*

Published January 2014 in *Geochemistry, Geophysics, Geosystems*.

Abstract

Burial histories of subduction zone rocks are often difficult to accurately constrain, owing to a lack of robust mineral geobarometers applicable to high pressure mineral assemblages. Knowledge of the depth-histories of subduction is, however, required for our understanding of global geochemical cycles, subduction-related seismicity, and the evolution of destructive tectonic boundaries.

The high spatial resolution of quartz inclusion geobarometry can be used to determine pressure evolution during metamorphic growth of individual garnet crystals. Quartz inclusions in garnet from Sifnos, Greece, preserve such a record of the pressure of garnet growth, allowing detailed reconstruction of the metamorphic evolution of these rocks. Pressure-dependent Raman spectra of quartz inclusions were combined with elastic modeling to infer the conditions at which they were trapped during garnet growth. All measured inclusions suggest that garnet growth occurred between 19 and 20.5 kbars, with little evidence for significant pressure variation during the garnet growth interval, which is interpreted to record ~ 100 °C of heating. Coupled with thermometry and geochronology, these results show that early, cold burial was followed by a phase of rapid heating, which immediately preceded exhumation. Garnet growth occurred primarily during this heating phase.

2.1 Introduction

Subduction zone metamorphism and devolatilization control many global geochemical cycles (e.g. Bebout, 2007; Sadofsky & Bebout, 2003) and may influence the generation of large-magnitude seismic events (e.g. Abers *et al.*, 2013; Hacker *et al.*, 2003b; Kerrick & Connolly, 2001). Much previous work has therefore focused on linking seismicity with mineral reactions, and pressure-temperature (*P*-*T*) paths experienced during subduction have been deduced based on the preserved mineral assemblages of exhumed rocks. Metamorphic temperatures are relatively straightforward to determine from mineral equilibria, whereas depths of mineral equilibration are less well known. Modeling of subduction velocities, mineral reaction rates, dehydration fluxes and exhumation mechanisms requires estimates of the pressures (depths) over which various mineral reactions occur. Furthermore, knowledge of the maximum depths reached by subducted rocks helps reveal the dynamic processes of exhumation.

Part of the difficulty in determining metamorphic depth from subducted rocks arises from the lack of common pressure-dependent mineral equilibria at depths below ~ 30–50 km, where plagioclase feldspar is absent. Ideally, new metamorphic geobarometers would be capable of yielding precise pressure estimates would require use of only commonly found minerals, and would not be susceptible

to significant resetting during exhumation. Here we demonstrate the utility of a barometer based on quartz, one of the most common minerals in Earth's crust.

The uncertainties concerning subduction zone pressures are exemplified by blueschists from the Greek Cycladic islands (Fig. 2.1). Previous work on the island of Sifnos (Fig. 2.2B) has identified evidence of high-pressure metamorphism (e.g. Forster & Lister, 2005; Matthews & Schliestedt, 1984), but estimates of the exact depths reached by the subducted rocks have varied considerably. The maximum

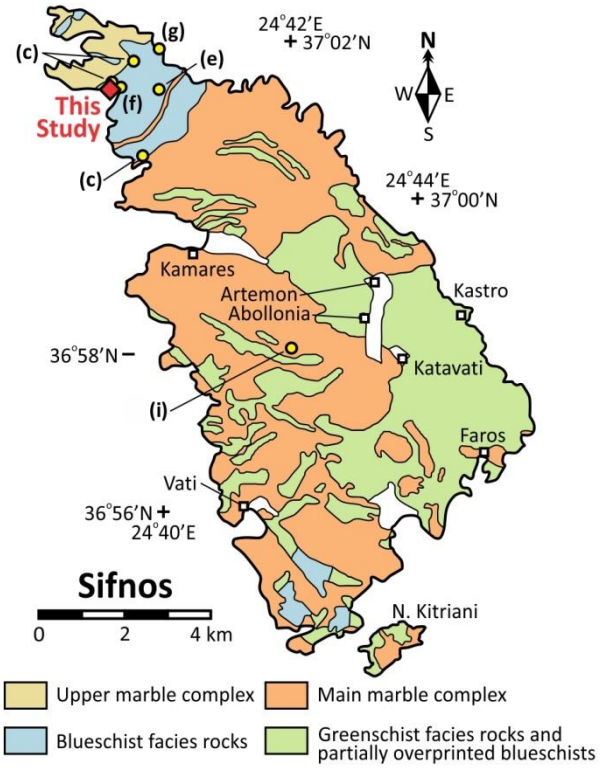

Figure 2.1. Generalized geologic map of Sifnos, Greece, emphasizing the spatial distribution of blueschist rocks. The sample discussed in this study is from the northern part of the island. Locations of samples discussed in previous studies are shown (letters refer to the studies cited in Fig. 2.2). Modified from Dragovic *et al.* (2012), Matthews & Schliestedt (1984), and Trotet *et al.* (2011).

depth reached by currently exposed rocks has been previously suggested to be from ~45 to 70 km (Fig. 2.2B), with more recent studies trending towards the greater depths within this range. It is unclear if these different pressures are real and reflect the juxtaposition of rocks that have been subducted to various depths (e.g. Avigad, 1993), or if the different pressures are an artifact related to the relative

imprecision of existing geobarometers and the prevalence of retrogressed lithologies on parts of the island.

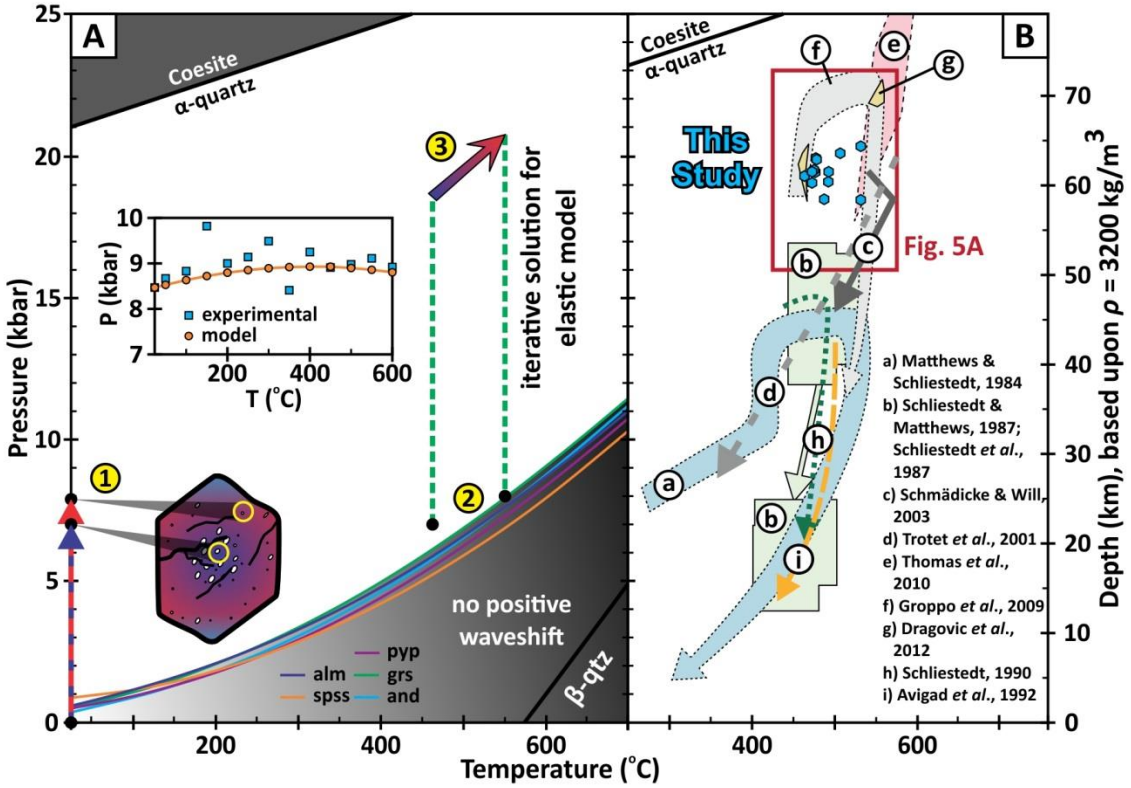

Figure 2.2. (**A**) Conceptual model outlining the steps for determining garnet growth pressure based on Raman analysis of quartz inclusions and elastic modeling. Garnet in thin section (at ambient *P* and *T*) contains sealed inclusions of quartz that record shifts in the position of the 464 cm^{-1} peak. In stage (**1**), measured peak shifts are used to determine current inclusion pressure at ambient *T* and atmospheric external *P*. In stage (**2**), temperatures of garnet growth during encapsulation are estimated by inclusion location, assuming constant growth rate over the inferred ~ 90 °C growth interval. The inset shows experimental (blue) and modeled (orange) pressure perturbations that result from heating the sample at surface pressures, and the small effects of temperature on the modeling results. Finally, in stage (**3**) an elastic model is iteratively applied to both garnet host and quartz inclusion to solve for the growth pressure. The limit of method applicability for α-quartz is shaded gray: the five colored lines represent the conditions from which there would be no resultant inclusion overpressuring and therefore no waveshift for a given garnet composition. (**B**) Resulting *P-T* points for various garnets analyzed in this study (blue hexagons). Previously constrained histories for Sifnos shown for comparison: a – Matthews & Schliestedt (1984); b – Schliestedt & Matthews (1987) and Schliestedt *et al.* (1987); c – Schmädicke & Will (2003); d – Trotet *et al.* (2001); e – Thomas *et al.* (2010); f – Groppo *et al.* (2009); g – Dragovic *et al.* (2012); h – Schliestedt (1990); i – Avigad *et al.* (1992).

2.2 Quartz as a Barometer

Like many blueschist terranes, high-pressure rocks from Sifnos contain abundant garnet crystals that grew during subduction (Dragovic *et al.*, 2012). The garnets contain a diverse suite of mineral inclusions that presumably nucleated and grew at the same time as (or before) the surrounding garnet host. Micron-scale inclusions of quartz are common in garnets porphyroblasts (e.g. Fig. 1.3, inset), and

thus determination of the pressure at which the quartz was included can be used to infer the growth conditions of host garnet.

The Raman peak positions of α-quartz are known to vary systematically with both *P* and *T* (e.g. Schmidt & Ziemann, 2000). Previous studies have demonstrated that the Raman characteristics of quartz can be used as a pressure monitor in experiments (e.g. Schmidt & Ziemann, 2000), and others have suggested that garnet may act as a sufficiently robust pressure vessel to preserve the internal pressure in natural mineral inclusions (Enami *et al.*, 2007). Inclusion barometry builds on the pioneering work of Rosenfeld, who speculated on the elastic effects of trapped mineral inclusions and their hosts (Rosenfeld & Chase, 1961), and first used piezobirefringence to directly estimate garnet growth pressures (Rosenfeld, 1969). Here, we show that (i) the pressure dependence of the v_{464} Raman peak position for quartz permits precise pressure determination in natural quartz inclusions from Sifnos, (ii) the pressure currently maintained within these grains is substantially less than the pressure at the time of trapping in garnet, and (iii) simple calculations based on elastic properties of garnet and quartz can account for this post-entrapment relaxation and recover the conditions of quartz inclusion which, as described above, corresponds to the conditions of garnet growth. Determining garnet growth conditions is of significant interest because garnet growth is associated with the generation of large amounts of metamorphic fluid (Baxter & Caddick, 2013; Hacker *et al.*, 2003a) and significant densification of the slab. Furthermore, garnet growth typically occurs progressively during burial, with late stage growth likely recording the maximum depths experienced in subduction zone rocks.

Our conceptual model can be summarized as follows: During garnet growth at high temperature and pressure, quartz (and other minerals) is commonly enclosed within the growing garnet crystal, with both host and inclusion experiencing identical pressure and temperature during growth and entrapment. External confining pressure and temperature decrease during exhumation, but pressure in the quartz inclusion is partially preserved and can be estimated based on *in-situ* Raman spectroscopic

analyses of the inclusions. Partial volumetric relaxation of the garnet during exhumation allows slight expansion of the quartz inclusion (therefore an isochoric trajectory is not followed), but this volume change can be quantified based on the elastic properties of inclusion and host. Thus, the true trapping pressure can be reconstructed based on the measured pressure at ambient conditions.

2.3 Geologic Setting, Sample Description and *P-T* History

Blueschists from the Cycladic Island of Sifnos, Greece, comprise part of a subduction-related accretionary complex (Avigad, 1993; Okrusch *et al.*, 1978) that is an excellent example of a high-*P* belt exhumed in a back-arc setting (Trotet *et al.*, 2001). Preservation of high-pressure lithologies has been attributed to the development of a series of detachment faults (Avigad, 1993; Lister, 1984; Ring *et al.*, 2011), which permitted rapid exhumation along a cool geotherm (Jolivet *et al.*, 1998). Previous estimates of peak metamorphic pressures from the northern Eclogite-Blueschist Unit (EBU; Fig. 2.1) range from ~ 15 kbar to ~ 23 kbar, with most recent studies yielding pressures at the upper end of this range (Fig. 2.2B). Peak *P* from the greenschist units has typically been harder to define (e.g. Matthews & Schliestedt, 1984; Schliestedt & Matthews, 1987; Schliestedt *et al.*, 1987). Peak temperatures were 450–550 ˚C (Fig. 2.2B), with previously determined temperature estimates for garnet growth of samples from the EBU used in this study to constrain quartz trapping temperatures in the elastic model. Garnet growth has been reported at ~ 46.5 Ma (Dragovic *et al.*, 2012), and recent $^{40}Ar/^{39}Ar$ apparent age spectra from white mica suggest retrogressive metamorphism as early as ~ 41 Ma (Forster & Lister, 2005). Dragovic *et al.* (2012) suggest that most garnet growth occurred over a ~ 2 kbar interval during heating from 460 °C to 550 °C. Miocene greenschist overprinting is extensive in central and southern Sifnos (Bröcker *et al.*, 2013; Ring *et al.*, 2011; Wijbrans *et al.*, 1990), while the sample studied here is typical of rocks from the EBU in recording the Eocene blueschist stage with only weak subsequent overprinting.

The metamorphic assemblage in the sample studied here includes garnet, glaucophane, epidote, paragonite, phengite, jadeitic-pyroxene, quartz, rutile and zircon ± hematite. Quartz is the dominant inclusion phase in garnet. Polished 30 µm thick sections were examined to identify quartz inclusions completely enclosed by garnet in three dimensions (Fig. 2.3 inset). This sample was selected for inclusion barometry because of its abundance of quartz inclusions without significant fracturing or alteration of the garnet. Sample 06MSF-6C from Dragovic *et al.* (2012) was collected < 2 km from this sample, whilst the samples described by Groppo *et al.* (2009) are from the same locality studied here. The apparent garnet growth temperature range inferred by both Groppo *et al.* (2009) and Dragovic *et al.* (2012) (Fig. 2.2B) and growth duration inferred by Dragovic *et al.* (2012) will therefore be adopted here for *P* fitting and geodynamic implications.

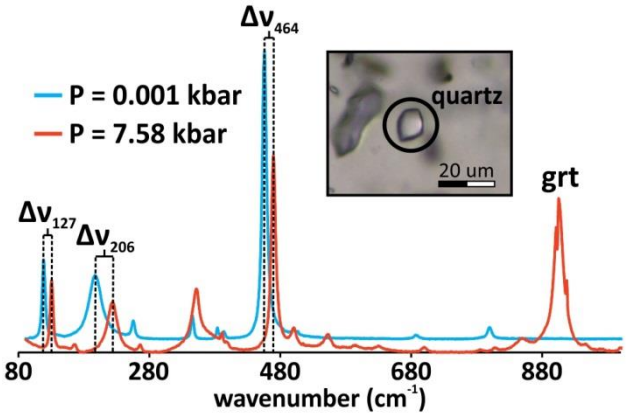

Figure 2.3. Example Raman spectra of quartz at room temperature and 1 bar (blue) and from an inclusion that is completely encapsulated (red; calculated *P* = 7.58 kbar at room temperature). Inset image shows a ~15 µm, completely encapsulated quartz inclusion in garnet (focused at the inclusion depth, not the sample surface).

2.4 Methods

2.4.1 Spectra Collection

Unpolarized Raman spectra were collected using the JY Horiba LabRam HR800 microprobe in the Department of Geosciences at Virginia Tech. We used a high-resolution 800 mm focal length spectrometer (1800 lines/mm grating) and a 514.57 nm (100 mW laser power at the source) argon laser, resulting in a spectral resolution of < 0.1 cm^{-1}. High spatial resolution (1 µm) is achieved using a confocal

microscope with a 400 µm hole and 150 µm slit with the 100x objective. A spectral range of *ca.* 74–633 cm^{-1} (centered on 360 cm^{-1}) was used to allow simultaneous collection of the three main peaks of quartz (*ca.* 464, 206 and 127 cm^{-1} at atmospheric pressure) and three Ar plasma lines (at 520.30, 266.29, and 116.04 cm^{-1}) used for calibration purposes over a 60s dwell time with three iterations. Analyses were collected throughout the thickness of the inclusion, with the center of the collected profile used (to ensure minimal mechanical interference from stress compaction at grain boundaries). Indeed, depth profile analyses of each crystal show larger waveshifts at the rims and 'plateaus' in crystal cores (*Appendix A*). Thus, pressures were mostly obtained from cores of large inclusions (5–15 µm) that were unzoned with respect to their Raman characteristics. Peak positions can typically be determined to ± 0.1 cm^{-1}, resulting in an inferred pressure precision of ± 0.12 kbar, considering regression fit uncertainties.

2.4.2 Element Mapping

Energy-dispersive X-ray spectroscopy (EDS) element maps were obtained using the Cameca SX-50 electron probe microanalyzer (EPMA) at Virginia Tech. Image maps were collected for Ca, Fe, Mg, Mn, Al, Si, Ti, and Cr at 15 kV accelerating potential with a 50 nA beam current. These element distribution maps were used to locate the growth centers of porphyroblasts and to determine when in the metamorphic history an individual quartz inclusion formed relative to garnet growth and the growth of other quartz inclusions (Fig. 2.4). Inclusion radial distances from the chemical cores were used to calculate volumetric position (assuming a spherical volume) within the garnets (i.e. considering volume growth, in three dimensions, rather than radial growth, in two dimensions).

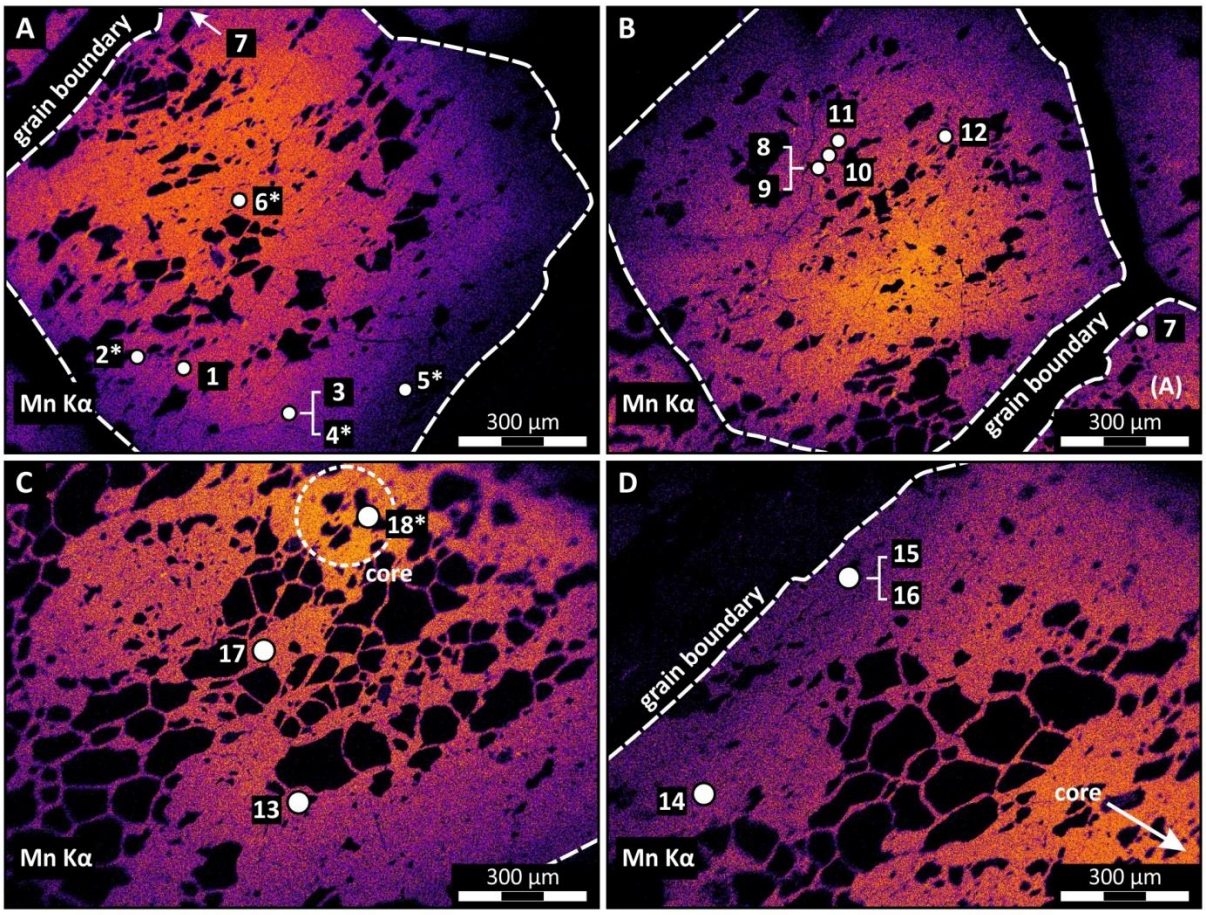

Figure 2.4. Mn Kα element EDS maps for garnets A (**A**), B (**B**), and C (**C**,**D**) (see Table 2.1). Mn is used as a proxy for locating garnet core (highest Mn is at the core). Inclusions locations discussed in this paper are shown. The "*" symbol indicates inclusions that do not meet the size requirements discussed in this manuscript.

2.4.3 Peak Refinements and Inclusion Pressure Calculation

Inclusions from core to rim of garnets (where available) were analyzed to constrain pressure evolution during garnet growth and to test the hypothesis that Sifnos garnet grew progressively during burial, i.e., as pressure increased. Currently preserved pressures were obtained based on shifts in the quartz v_{464} peak (Fig. 2.2A, step 1) and calculated through a 2nd-order polynomial regression (see *Appendix A*) based on the data of Schmidt & Ziemann (2000). The trapping temperature of each inclusion was estimated with respect to its position in the host crystal, assuming that garnet cores and rims grew at 460 and 550 ˚C, respectively (based on the results of Dragovic *et al.*, 2012), and that garnet growth was at a constant volumetric rate (e.g. Finlay & Kerr, 1987; Hoisch *et al.*, 2008). We emphasize

that although the temperatures used in our modeling to constrain trapping pressure are estimates based solely on their position relative to the host garnet core (with an assumed growth of 460 °C) and rim (550 °C), the pressures retrieved are relatively insensitive to uncertainties in these temperature estimates (± 0.35 kbar for a ± 25 ˚C uncertainty: Fig. 2.5B). This decoupling of uncertainty on temperature and pressure is confirmed by step-wise heating experiments on a carefully prepared garnet wafer with several quartz inclusions. In these, twenty-six analyses at 50 °C intervals show minimal heating-related pressure increase (blue squares, inset of Fig 2.1A), comparing well to results of the Zhang (1998) elastic model (orange lines and circles, inset of Fig 2.1A). The significance of this is that if an inclusion was trapped at higher temperatures than assumed, minimal pressure differences would result. Note that significant scatter exists in these heating data because a 600 lines/mm grating (rather than the 1800 lines/mm) was used to collect Raman spectra, resulting in poorer spectral resolution. Moreover, temperature fluctuations during heating and analysis reduced Raman peak intensity when collecting the Raman signal through the glass window on the heating stage, and uncertainties related to regression analysis in three dimensions (i.e. pressure-temperature-waveshift) also contribute to the scatter.

2.4.4 Formation Pressure Estimation and Elastic Model Selection

The original quartz trapping pressure was estimated from the inclusion pressure at room temperature based on Raman peak shift, using a simplified version of the Zhang (1998) elastic model:

$$P_{incl} = \frac{P_{ext}\left[\frac{1}{\kappa_{grt}} + \frac{3}{4\mu_{grt}}\right] + (1-x)\left(P_0\left[\frac{1}{\kappa_{qtz}} - \frac{1}{\kappa_{grt}}\right] + \gamma_{qtz} - \gamma_{grt}\right)}{\frac{1-x}{\kappa_{qtz}} + \frac{3}{4\mu_{grt}} + \frac{x}{\kappa_{grt}}} \qquad \text{(eq. 2.1)}$$

where P_{incl} is the inclusion pressure, P_{ext} is the external (atmospheric) pressure (1 bar), P_0 is the formation pressure, x is the inclusion size-dependent term, κ is the adiabatic bulk modulus, and μ_{grt} is

the adiabatic shear modulus of garnet. The dependence of κ and μ on temperature and pressure is weak (only 10% change from 0 to 40 kbar for pyrope), therefore using constant values for the adiabatic κ and μ is a good approximation and allows for the application of simple linear elasticity theory (Zhang, 1998). The required thermodynamic properties of quartz and garnet were obtained from the Holland & Powell (2011, and references therein) dataset. Here we assume that because the radius of the inclusion (r_{qtz}) is much less than the radius of the garnet host (r_{grt}), the ratio $r_{qtz}/r_{grt} \approx 0$, which removes the inclusion size-dependence term (x). The temperature dependence of the thermal expansion of the minerals is considered in this model by:

$$\gamma_{P=1\ bar} = \int_{T_0}^{T} \alpha_T \, dT \qquad \text{(eq. 2.2)}$$

where T is 298 K, T_0 is the formation temperature (in K), and α_T is the temperature dependence of thermal expansion expressions. For garnet, the thermal expansion fit parameters from Skinner (19660 are used. Due to the anomalous behavior of the elastic properties of quartz near the lambda (α-β) transition, a modification of the expression presented by Dorogokupets (1995) was implemented. We considered the pressure dependence of the position of the lambda transition for quartz, and used this in the thermal expansion equation (therefore, higher pressures have less effects resulting from this transition). This was done by replacing the critical temperature term (Dorogokupets, 1995, eq. 9) with the α–β transition curve equation from Mirwald & Massonne (1980). Increasing pressure causes the denominator in this expression to increase and accordingly reduces the anomalous effects of this transition. Application of this method is limited to P-T conditions that result in preserved inclusion pressures at the Earth's surface (i.e. $P_{incl} > 0$ bar). It is improbable that application can be extended to negative pressure systems since the vacuum created within the inclusion hole would result in the localized expansion of garnet (reducing the inclusion volume). This limit for quartz inclusions in different end-member compositions of garnet is shown as the shaded field in Fig. 2.2A. Therefore, quartz

inclusion Raman barometry is most sensitive and applicable to high-*P*, low-*T* systems when considering quartz inclusions in garnet.

The elastic model presented by Guiraud & Powell (2006) was also considered. The expression:

$$\frac{V_{grt}(P,T)}{V_{grt}(P_0,T_0)} = \frac{V_{qtz}(P_{incl},T)}{V_{qtz}(P_0,T_0)} - \frac{3}{4\mu_{grt}}(P_{incl} - P) \qquad \text{(eq. 2.3)}$$

takes into consideration the volume (*V*) changes that quartz experiences relative to a reference state (atmospheric conditions, for this study). We solve for the formation pressure by computing the volume of each phase along isothermal transects, until the difference between both sides of the equation is approximately zero. Because the elastic parameters are nested in these volume calculations, the computation of formation conditions is greatly simplified. The program Frendly (part of the Perple_X program package; Connolly, 2009) was used to calculate volumes along these transects with the Holland & Powell (2011) dataset.

At low temperatures (near room *T*), both the Zhang (1998) and Guiraud & Powell (2006) models predict similar formation pressures (Table 2.1). However, since the effects of the lambda transition are directly accounted for with our treatment of the Zhang (1998) model, this method was preferred for calculating trapping pressure, and presented results use this formulation. It is important to note, however, that because this technique is only applied to high-pressure rocks in this study (where the effects of the phase transition are minimal), results of these models only differ by ~1 kbar for entrapment pressure estimates. Different elastic calculation approaches may result in slightly different absolute formation pressures, however relative pressures calculated from core to rim of garnets would be unchanged.

The elastic properties appropriate for the measured composition of the host garnet near each inclusion were calculated by assuming ideal mixing between garnet end-members, using compositions

obtained from EPMA analysis. We estimate that the elastic model increases maximum pressure uncertainties to ~ ± 0.5 kbar, based on extrapolation of uncertainties in calculating inclusion pressures and the temperature dependence of the formation pressure calculation (see Fig. 2.5B for details).

Table 2.1 Raman data and calculated pressures

Incl. #	Grt #	Rad. %	Vol. %	$\Delta\nu_{464}$ (cm^{-1})	P_{incl} (kbar)	Temp. (°C)	$P_{G\&P}$ (kbar)	P_{Zhang} (kbar)
1	A	58.3	19.8	6.72	7.55	478	18.94	19.86
2*	A	75.3	42.7	7.61	8.58	498	21.30	22.18
3	A	67.0	30.0	6.00	6.72	487	17.36	18.46
4*	A	63.8	26.0	5.60	6.26	483	16.35	17.47
5*	A	81.8	54.8	5.82	6.51	509	17.13	18.44
6*	A	15.6	0.4	6.07	6.79	460	17.24	18.17
7	A	71.2	36.0	6.47	7.25	492	18.43	19.45
8	B	51.7	13.8	6.43	7.21	472	18.16	19.08
9	B	51.7	13.8	6.60	7.41	472	18.57	19.47
10	B	54.6	16.3	6.64	7.45	475	18.67	19.55
11	B	57.4	18.9	6.76	7.59	477	19.02	19.94
12	B	56.7	18.2	6.52	7.31	476	18.45	19.42
13	C	70.8	35.5	6.30	7.07	492	18.04	19.10
14	C	80.2	51.5	6.59	7.40	506	18.93	20.10
15	C	92.5	79.0	6.57	7.37	531	19.04	20.34
16	C	92.5	79.0	5.66	6.33	531	16.98	18.42
17	C	32.6	3.5	6.59	7.39	463	18.47	19.30
18*	C	19.0	0.7	7.51	8.46	461	20.68	21.30

Note: Temperatures are inferred based on inclusion positions within the host garnet, assuming constant volumetric growth rates between crystal core (at 460 °C) and rim (550 °C) [from Dragovic et al., 2012].
**Inclusion outside of 5–15 µm range and should not be considered.*
Rad. % – percent radial distance of inclusion from garnet core; Vol. % – percent volume distance of inclusion from garnet core; P_{incl} – inclusion pressure; P_{Zhang} – entrapment pressure, calculated with Zhang [1998] elastic model; $P_{G\&P}$ – entrapment pressure, calculated with Guiraud and Powell [2006] elastic model.

2.5 Results

Several Raman spectroscopic analyses were obtained from each of eighteen quartz inclusions hosted in three different garnet porphyroblasts in one sample. Inclusions near cracks or exposed to the thin section surface were avoided. Inclusions < 5 µm in diameter consistently yielded low-intensity spectra such that the peak positions could not be determined with sufficient precision. Moreover, such small inclusions are significantly affected by mechanical stress concentration phenomena produced at

the interface between the inclusion and host (De Wolf, 2003). Large inclusions (> 15 µm) have little surrounding garnet in a 30 µm thin section, allowing pathways for stress dissipation that reduces the

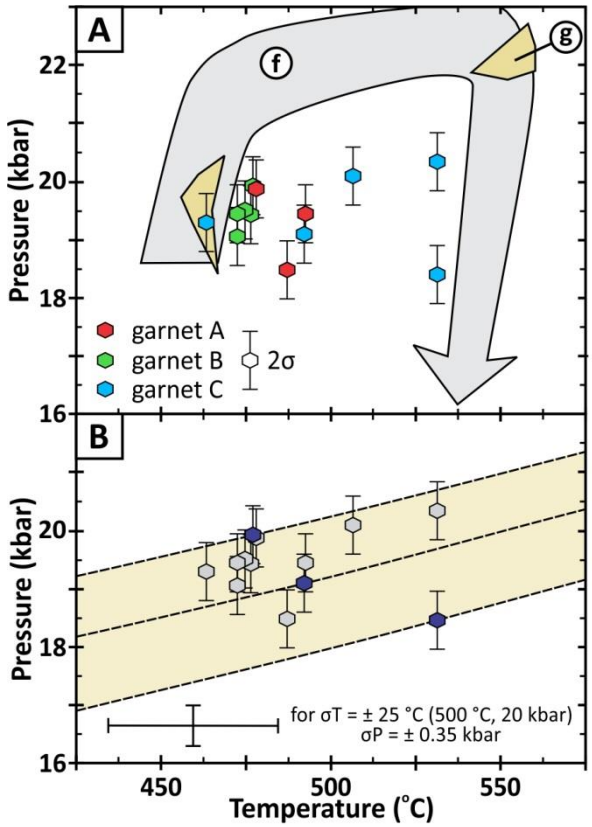

Figure 2.5. (**A**) Detail of resulting formation pressure calculated in this study. Each hexagon represents multiple analyses from a single inclusion, with color coding denoting the garnet host from which results were obtained. Inclusion locations within the host garnets are shown in Fig. 2.4. Pale gray arrow and yellow polygons are from Groppo *et al.* (2009) and Dragovic *et al.* (2012), respectively. (**B**) Contours of constant inclusion pressure are shown for three inclusions (purple filled) that span the pressure extents of the dataset. This illustrates how temperature uncertainty affects the calculated enclosure pressures, and the formation pressure uncertainty that would extrapolate from this. At 20 kbar and 500 °C, a σT of ±25 °C would result in a σP_0 of ±0.35 kbar. At higher pressures uncertainties decrease due to increased distance from the lambda transition in quartz (which is a significant contributing source for the positive slope and curvature of the contours above).

preserved inclusion pressure, even when cracks are absent and inclusions are not exposed at the surface. Thicker sections could be used to expand the inclusion sizes that could be analyzed, but resultant peak intensities would likely be reduced (producing larger uncertainties) due to the opacity of garnet. Therefore, results from inclusions < 5 µm and > 15 µm were not considered in the present study (Table 2.1 includes results from these rejected inclusions to demonstrate the effects of both under- and over-sized inclusions). A total of sixty-seven remaining analyses on thirteen completely encapsulated

inclusions from three garnets are included here (Fig. 2.4). Where possible, quartz inclusions from different locations within the garnet host (e.g. from the core and rim) were analyzed to decipher the burial history of garnet growth.

Measured Raman peak shifts in the quartz inclusions were consistently > 6 cm^{-1} (relative to the peak position at ~ 0.001 kbar; Table 2.1). A maximum measured peak shift of 6.57 cm^{-1} (inclusion pressure = 7.37 ± 0.28 kbar, 2σ) was obtained from a quartz inclusion located near the rim of a garnet crystal (inclusion 15, Table 2.1; Fig. 2.4). Elastic modeling suggests that this crystal was trapped at 20.3 kbar and 530 °C. The results of all analyzed inclusions suggest that garnet growth occurred from 19.1 (near the core) to a maximum of 20.3 kbar (assuming growth in the range 460–550 °C; Fig. 2.5A). Six inclusions near garnet cores (here correlated with trapping at ~ 475 °C) all return formation pressures of 19.5 ± 0.5 kbar, with no outliers (Fig. 2.5). The consistency of these results with respect to inclusion size and location within a single porphyroblast is remarkable and supports the inferred precision achievable via this technique. One inclusion near a garnet rim suggests a lower pressure (18.5 kbar) compared to other inclusions in this textural setting. The paucity of usable inclusions situated in the outermost garnet rims makes it difficult to assess definite trends in pressure evolution during this part of the growth history.

2.6 Implications for Sifnos Subduction

Previous pressure estimates for blueschist conditions on Sifnos have varied greatly, with only more recent studies (Dragovic *et al.*, 2012; Groppo *et al.*, 2009; Thomas *et al.*, 2010) suggesting peak pressures over 20 kbar (i.e. > 60 km depth). Our results are consistent with peak pressures of about 20 kbar. Available evidence from other similarly located rocks within the EBU on Sifnos implies that the majority of garnet growth took place over a short time interval (< 1 Myrs, Dragovic *et al.*, 2012), also

suggesting that these rocks quickly passed from a regime defining a moderate subduction geotherm to one of rapid heating. This may reflect the onset of slab-mantle coupling (Wada & Wang, 2009). Such heating pulses have previously been postulated for Cycladic rocks, with tectonic mode switches resulting in short-duration heating followed by decompression due to development of extensional shear zones (Forster & Lister, 2005; Lister *et al.*, 2001). The northern EBU on Sifnos consists of a variety of intensely deformed and metamorphosed lithologies, all tectonically juxtaposed (Avigad, 1993). Precise pressure estimates from several lithologies are now possible with further application of Raman quartz barometry and could help determine whether, indeed, structurally adjacent lithologies within the nappe experienced similar *P-T* histories during subduction and exhumation. Improved understanding of the temperature interval garnet grew under can have significant implications on the tectonic modes, such as: the need for orogenic surging followed by short duration of heating (Forster & Lister, 2005), relatively isothermal loading (Spear & Cheney, 2009), or isobaric growth during heating (Dragovic *et al.*, 2012).

2.7 Broader Conclusions – Precise Pressure Estimates for Deep Crustal Material

Quartz inclusions in garnet can record pressures of garnet growth, and our measurements track metamorphic evolution of a high-pressure sample from Sifnos. Accurate assessment of the conditions of metamorphism, and particularly the pressure ranges over which metamorphic reactions occur, are required for several reasons. In subducted terranes, such information may provide insight into rates of subduction (particularly at depth), rheology of the system, and maximum subduction depths – all of which are important parameters for understanding global tectonics. In addition, exhumation mechanics may result in the juxtaposition of rocks that reached significantly different depths, sampling a broad section of the subduction zone and reflecting widely different *P-T* histories. Understanding the extent of this juxtapositioning requires accurate assessment of depths of metamorphism; quartz inclusion

barometry may now allow us to infer metamorphic depths with unprecedented precision. Furthermore, the high spatial resolution permitted by this technique and the prevalence of quartz inclusions from core to rim throughout many garnet crystals can yield a remarkably detailed record of the evolution of pressure during metamorphism. Importantly, the quartz inclusion geobarometer does not require chemical equilibrium in the system; physical properties alone control the barometric record, and these properties are well known for both quartz and garnet. Moreover, retrogression does not overprint the original record as it does with most conventional thermobarometers. When coupled with geospeedometry techniques (e.g., Ti diffusion from host garnet into quartz inclusions; Spear *et al.*, 2012), this method could yield constraints on both the mechanisms and rates of exhumation in subduction settings.

With careful petrographic observation, microstructural setting and temperature estimation, the technique described here represents a powerful tool for deciphering the *P-T-D* metamorphic history and understanding the processes of subduction and exhumation. Recently quantified links between garnet growth in subduction zones and concomitant dehydration allow new insights into arc magma genesis and the return of volatiles to Earth's interior (Baxter & Caddick, 2013; Berger *et al.*, 2009; Dragovic *et al.*, 2012; Hacker, 2006), and quartz inclusion barometry can be applied to infer the pressures at which these processes occur. Furthermore, quartz inclusion barometry can permit better integration of geophysical observations of subduction zone seismicity with petrologic observations of metamorphic reaction, by helping to identify specific depths at which key densification and devolatilization reactions are prevalent and recorded by garnet growth.

Acknowledgements

We thank Rick Law and Nancy Ross for thoughtful discussions pertaining to this study. Review of this manuscript by Frank Spear is gratefully acknowledged, and Matt Kohn is thanked for significant

contributions that revealed crucial modeling considerations that were previously unclear to us. We are grateful for assistance with use of the Raman spectrometer at Virginia Tech by Charles Farley. This work is funded by a graduate research grant awarded by the Department of Geosciences, Virginia Tech.

References

Abers, G. A., Nakajima, J., Keken, P. E. v., Kita, S. & Hacker, B. R. (2013). Thermal-petrological controls on the location of earthquakes within subducting plates. *Earth and Planetary Science Letters* **369-370**, 178-187.

Avigad, D. (1993). Tectonic juxtaposition of blueschists and greenschists in Sifnos Island (Aegean Sea) - implications for the structure of the Cycladic blueschist belt. *Journal of Structural Geology* **15**, 1,459-451,469.

Avigad, D., Matthews, A., Evans, B. & Garfunkel, Z. (1992). Cooling during the exhumation of a blueschist terrane - Sifnos (Cyclades), Greece. *European Journal of Mineralogy* **4**, 619.

Baxter, E. F. & Caddick, M. J. (2013). Garnet growth as a proxy for progressive subduction zone dehydration. *Geology* **41**, 643-646.

Bebout, G. E. (2007). Metamorphic chemical geodynamics of subduction zones. *Earth and Planetary Science Letters* **260**, 373.

Berger, J., Caby, R., Liégeois, J.-P., Mercier, J.-C. C. & Demaiffe, D. (2009). Dehydration, melting and related garnet growth in the deep root of the Amalaoulaou Neoproterozoic magmatic arc (Gourma, NE Mali). *Geological Magazine* **146**, 173-186.

Bröcker, M., Baldwin, S. & Arkudas, R. (2013). The geological significance of $^{40}Ar/^{39}Ar$ and Rb-Sr white mica ages from Syros and Sifnos, Greece: A record of continous (re)crystallization during exhumation? *Journal of Metamorphic Geology* **31**, 629-646.

Connolly, J. A. D. (2009). The geodynamic equation of state: What and how. *Geochemistry Geophysics Geosystems* **10**, http://dx.doi.org/10.1029/2009GC002540.

De Wolf, I. (2003). Raman spectroscopy: About chips and stress. *Spectroscopy Europe* **15**, 6-13.

Dorogokupets, P. I. (1995). Equation of state for lambda transition in quartz. *Journal of Geophysical Research* **100**, 8,489-488,499.

Dragovic, B., Samanta, L. M., Baxter, E. F. & Selverstone, J. (2012). Using garnet to constrain the duration and rate of water-releasing metamorphic reactions during subduction: An example from Sifnos, Greece. *Chemical Geology* **314-317**, 9-22.

Enami, M., Nishiyama, T. & Mouri, T. (2007). Laser Raman microspectrometry of metamorphic quartz: A simple method for comparison of metamorphic pressures. *American Mineralogist* **92**, 1,303-301,315.

Finlay, C. A. & Kerr, A. (1987). Evidence for differences in growth rate among garnets in pelitic schists from northern Sutherland, Scotland. *Mineralogical Magazine* **51**, 569-576.

Forster, M. A. & Lister, G. S. (2005). Several distinct tectono-metamorphic slices in the Cycladic eclogite-blueschist belt, Greece. *Contributions to Mineralogy and Petrology* **150**, 523.

Groppo, C., Forster, M. A., Lister, G. S. & Compagnoni, R. (2009). Glaucophane schists and associated rocks from Sifnos (Cyclades, Greece): New constraints on the the P-T evolution from oxidized systems. *Lithos* **109**, 254.

Guiraud, M. & Powell, R. (2006). *P-V-T* relationships and mineral equilibria in inclusions in minerals. *Earth and Planetary Science Letters* **244**, 683-694.

Hacker, B. R. (2006). Pressures and temperatures of ultrahigh-pressure metamorphism: Implications for UHP tectonics and H_2O in subducting slabs. *International Geology Review* **48**, 1053-1066.

Hacker, B. R., Abers, G. A. & Peacock, S. M. (2003a). Subduction factory 1. Theoretical mineralogy, densities, seismic wave speeds, and H_2O contents. *Journal of Geophysical Research* **108**, 10-11.

Hacker, B. R., Peacock, S. M., Abers, G. A. & Holloway, S. D. (2003b). Subduction factory 2. Are intermediate-depth earthquakes in subducting slabs linked to metamorphic dehydration reactions? *Journal of Geophysical Research* **108**, 2030.

Hoisch, T. D., Wells, M. L. & Grove, M. (2008). Age trends in garnet-hosted monazite inclusions from upper amphibolite facies schists int eh northern Grouse Creek Mountains, Utah. *Geochimica et Cosmochimica Acta* **72**, 5505-5520.

Holland, T. & Powell, R. (2011). An improved and extended internally consistent thermodynamic dataset for phases of petrological interest, involving a new equation of state for solids. *Journal of Metamorphic Geology* **29**, 333-383.

Jolivet, L., Goffe, B., Bousquet, R., Oberhänsli, R. & Michard, A. (1998). Detachments in high-pressure mountain belts, Tethyan examples. *Earth and Planetary Science Letters* **160**, 31.

Kerrick, D. M. & Connolly, J. A. D. (2001). Metamorphic devolatilization of subducted oceanic metabasalts: Implications for seismicity, arc magmatism and volatile recycling. *Earth and Planetary Science Letters* **189**, 19-29.

Lister, G. S. (1984). Metamorphic core complexes of cordilleran type in the Cyclades, Aegean sea, Greece. *Geology* **12**, 221.

Lister, G. S., Forster, M. A. & Rawling, T. J. (2001). Episodicity during orogenesis. *Geological Society of London, Special Publications* **184**, 89-113.

Matthews, A. & Schliestedt, M. (1984). Evolution of the blueschist and greenschist facies rocks of Sifnos, Cyclades, Greece - A stable isotope study of subduction-related metamorphism. *Contributions to Mineralogy and Petrology* **88**, 150.

Mirwald, P. W. & Massonne, H. J. (1980). The low-high quartz and quartz-coesite transition to 40 kbar between 600^{o} and 1600^{o}C and some reconnaissance data on the effect of $NaAlO_2$ component on the low quartz-coesite transition. *Journal of Geophysical Research* **85**, 6983-6990.

Okrusch, M., Seidel, E. & Davis, E. (1978). The assemblage jadeite-quartz in the glaucophane rocks of Sifnos (Cyclades archipelago, Greece). *Neues Jahrbuch fur Mineralogie, Abhandlungen* **132**, 284-308.

Ring, U., Glodny, J., Will, T. M. & Thomson, S. (2011). Normal faulting on Sifnos and the South Cycladic Detachment System, Aegean Sea, Greece. *Journal of the Geological Society* **160**, 31.

Rosenfeld, J. L. (1969). Stress effects around quartz inclusions in almandine and the piezothermometry of coexisting aluminum silicates. *American Journal of Science* **267**, 317-351.

Rosenfeld, J. L. & Chase, A. B. (1961). Pressure and temperature of crystallization from elastic effects around solid inclusions in minerals? *American Journal of Science* **259**, 519-541.

Sadofsky, S. J. & Bebout, G. E. (2003). Record of forearc devolatilization in low-T, high-P/T metasedimentary suites: Significance for models of convergent margin chemical cycling. *Geochemistry Geophysics Geosystems* **4**, 9003.

Schliestedt, M. (1990). In: Carswell, D. A. (ed.) *Eclogite Facies Rocks*. New York: Chapman & Hall, 179.

Schliestedt, M., Altherr, R. & Matthews, A. (1987). Evolution of the Cycladic crystalline complex: Petrology, isotope geochemistry and geochronology. In: Helgeson, H. C. (ed.) *Chemical transport in metasomatic processes*.

Schliestedt, M. & Matthews, A. (1987). Transformation of blueschist to greenschist facies rocks as a consequence of fluid infiltration, Sifnos (Cyclades), Greece. *Contributions to Mineralogy and Petrology* **97**, 237-250.

Schmädicke, E. & Will, T. M. (2003). Pressure-temeprature evolution of blueschist facies rocks from Sifnos, Greece, and implications for the exhumation of high-pressure rocks in the Central Aegean. *Journal of Metamorphic Geology* **21**, 799-811.

Schmidt, C. & Ziemann, M. A. (2000). In-situ Raman spectroscopy of quartz: A pressure sensor for hydrothermal diamond-anvil cell experiments at elevated temperatures. *American Mineralogist* **85**, 1,725-721,734.

Skinner, B. J. (1966). Thermal expansion. In: Clark, S. P. J. (ed.) *Handbook of Physical Constants, Memoir 97*: Geological Society of America.

Spear, F. S., Ashley, K. T., Webb, L. E. & Thomas, J. B. (2012). Ti diffusion in quartz inclusions: Implications for metamorphic time scales. *Contributions to Mineralogy and Petrology* **164**, 977-986.

Spear, F. S. & Cheney, J. T. (2009). Petrologic evidence for episodic subduction. *Geological Society of America Abstracts with Programs* **41**, 357.

Thomas, J. B., Watson, E. B., Spear, F. S., Shemella, P. T., Nayak, S. K. & Lanzirotti, A. (2010). TitaniQ under pressure: The effect of pressure and temperature on the solubility of Ti in quartz. *Contributions to Mineralogy and Petrology* **160**, 743-759.

Trotet, F., Vidal, O. & Jolivet, L. (2001). Exhumation of Syros and Sifnos metamorphic rocks (Cyclades, Greece): New constraints on the P-T paths. *European Journal of Mineralogy* **13**, 901.

Wada, I. & Wang, K. (2009). Common depth of decoupling between the subducting slab and mantle wedge: Reconciling diversity and uniformity of subduction zones. *Geochemistry Geophysics Geosystems* **10**, 1-36.

Wijbrans, J. R., Schliestedt, M. & York, D. (1990). Single grain argon laser probe dating of phengites from the blueschist to greenschist transition on Sifnos (Cyclades, Greece). *Contributions to Mineralogy and Petrology* **104**, 582.

Zhang, Y. (1998). Mechanical and phase equilibria in inclusion-host systems. *Earth and Planetary Science Letters* **157**, 209-222.

Chapter 3

QuIB Calc: A MATLAB® Script for Geobarometry Based on Raman Spectroscopy and Elastic Modeling of Quartz Inclusions in Garnet

Kyle T. Ashley[1], Matthew Steele-MacInnis[1], Mark J. Caddick[1]

[1]*Department of Geosciences, Virginia Polytechnic Institute and State University, Blacksburg, VA 24061, USA*

Published February 2014 in *Computers and Geosciences*.

Graphical Abstract

Quartz inclusion thermobarometry utilizes the pressure- and temperature-sensitive Raman peak shifts of quartz inclusions in garnet to determine formation pressure and temperature (*PT*) conditions. The measured Raman shift indicates the pressure currently retained in the inclusions at ambient external conditions, such that entrapment *PT* conditions (i.e., *P* and *T* of garnet growth) can be determined by elastic modeling. Most generally, trapping *P* is obtained with this method, based on an independent estimate of *T*. Here we describe *QuIB Calc*, a MATLAB® program that iteratively solves for garnet growth conditions using the pressure retained in quartz inclusions (as revealed by Raman peak shifts). The program explicitly accounts for the anomalous effects of the quartz lambda transition on the thermal expansivity, and utilizes a mixing subroutine to account for the physical properties of garnet solid solutions. *QuIB Calc* thus facilitates sophisticated *PT* calculations using quartz inclusions, and is particularly effective for geobarometry in high pressure terranes.

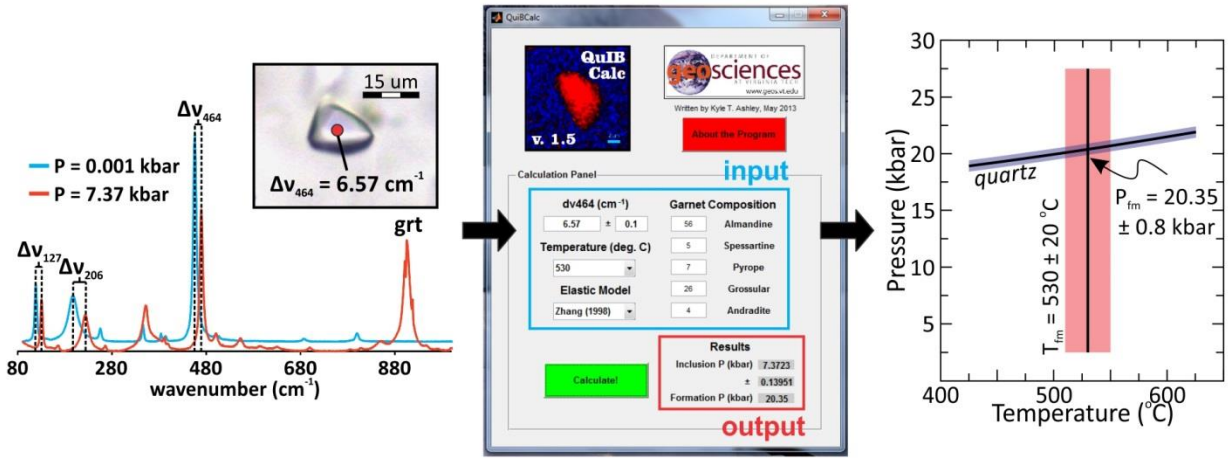

3.1 Introduction

Determining pressure-temperature (*P*-*T*) paths in metamorphic terranes is a key focus in metamorphic, tectonic, and structural geology. Accurate estimates of *P* and *T* are fundamental to understanding the development of subduction zones and orogenic belts, including metamorphic reactions, hydrous fluid and silicate melt production, and evolution of stress distribution in rocks (e.g. Bebout, 2007; Hacker *et al.*, 2003; Tichelaar & Ruff, 1993). Estimating metamorphic pressure is commonly less straightforward than determining temperature, and pressure estimates are particularly challenging for deep-crustal or subducted rocks in which plagioclase feldspar is absent (such that the pressure-dependent garnet-plagioclase equilibrium cannot be used as a barometer).

In an effort to overcome the challenges of high-pressure geobarometry, recent studies have emphasized the potential application of quartz inclusions in garnet (e.g. Enami *et al.*, 2007), based on the pioneering work of Rosenfeld (1969). Continued analytical and modeling developments have thus yielded improved resolution of pressure estimates for deeply subducted rocks by utilizing Raman spectroscopic analysis (Ashley *et al.*, 2014; Mouri & Enami, 2008). Specifically, the pressure-sensitive shifts of the ν_{464}, ν_{205} and ν_{128} peak positions for quartz (Schmidt & Ziemann, 2000) reveal the pressure retained in inclusions in garnet. An elastic model then solves for the trapping pressure during garnet growth, based on the physical properties of inclusion and host. The approach developed by Ashley *et al.* (2014) iteratively adjusts both quartz and garnet thermal expansivities and molar volumes as pressure is sequentially increased, solving for entrapment pressure (at known or assumed temperature). This approach uses an elastic model either from Guiraud and Powell (2006), Zhang (1998), or Van der Molen and Van Roermund (1986), and is based on the currently preserved pressure revealed by the measured shift of the ν_{464} Raman peak. Use of other quartz peaks for determining P_{inc} were not included in the code because the 464 cm^{-1} peak has the highest intensity and is the narrowest band, making peak fitting and determining absolute position the most accurate. In addition, there is spectral overlap between Raman peaks with garnet for the 206 cm^{-1} peak of quartz, which may incorporate additional uncertainty. Volume calculations include the elastic properties of quartz and five garnet compositional end-members in the Holland and Powell (2011) thermodynamic database. Molar volumes calculated at elevated *P* and *T* with these data generally yield < 0.1 % difference from available experimental results (e.g. Dorogokupets, 1995; Jorgensen, 1978; Raz *et al.*, 2002; Thiéblot *et al.*, 1998).

The need for an iterative solution sufficiently complicates use of this simple barometer that it requires either interfacing with existing programs to separately calculate the properties of quartz and garnet as functions of *P* and *T* (e.g. Perple_X's Frendly program; Connolly, 2009), or programming the appropriate data and equations of state for these calculations. To facilitate application of quartz

inclusion barometry, *QuIB Calc* was developed to robustly handle the elastic modeling within a user-friendly, graphical user interface (GUI) on the MATLAB® platform.

3.2 Database Construction

Lookup tables for the properties of quartz, almandine, pyrope, spessartine, grossular and andradite were constructed using the Holland and Powell (2011) dataset in the program Frendly (Connolly, 2009) in the range 1–30,000 bar and 300–800 ˚C (at 10 bar and 10 ˚C intervals). This approach was preferred over using data from various different databases to remain internally consistency. An additional profile was calculated for quartz at room temperature, because the volume of quartz at inclusion pressure is required for the elastic model. The data tables are included in the program download as tab-delimited text files that are read by *QuIB Calc*.

3.3 Computational Approach

Running *QuIB Calc* within MATLAB opens a pop-up window (Fig. 3.1) from which the user can input the following data for a given quartz inclusion: (i) measured waveshift of the Raman ν_{464} quartz peak; (ii) assumed metamorphic temperature corresponding with quartz inclusion entrapment; and (iii) approximate garnet composition near the inclusion position (in terms of the proportions of end-members). The measured waveshift of the quartz peak is initially used in a polynomial regression equation (Ashley *et al.*, 2014) to calculate the current inclusion pressure and uncertainty (at room temperature, with an adjustable spectral resolution).

The elastic modeling approaches used in this program may be selected via a drop-down menu. The Guiraud and Powell (2006) model requires knowledge of the volumes of quartz and garnet at room temperature and at formation conditions, and is rearranged into the following form:

$$\frac{V_{incl}(P_{incl}, 298)}{V_{incl}(P_0, T_0)} - \frac{V_h(1,298)}{V_h(P_0, T_0)} = \frac{3}{4\mu_{grt}}(P_{incl} - 1) \qquad \text{(eq. 3.1)}$$

where V_{incl} is the molar volume of the quartz inclusion (cm^3 mol^{-1}), V_h is the molar volume of the host garnet, P_0 and T_0 are pressure (bar) and temperature (K) of entrapment, respectively, P_{incl} is the current inclusion pressure (calculated by *QuIB Calc* from the waveshift), and μ_{grt} is the shear modulus of garnet (bar). *QuIB Calc* iteratively solves the left side of equation 1 by adjusting P_0 at an assumed value of T_0, until the difference between the left and right sides is minimized.

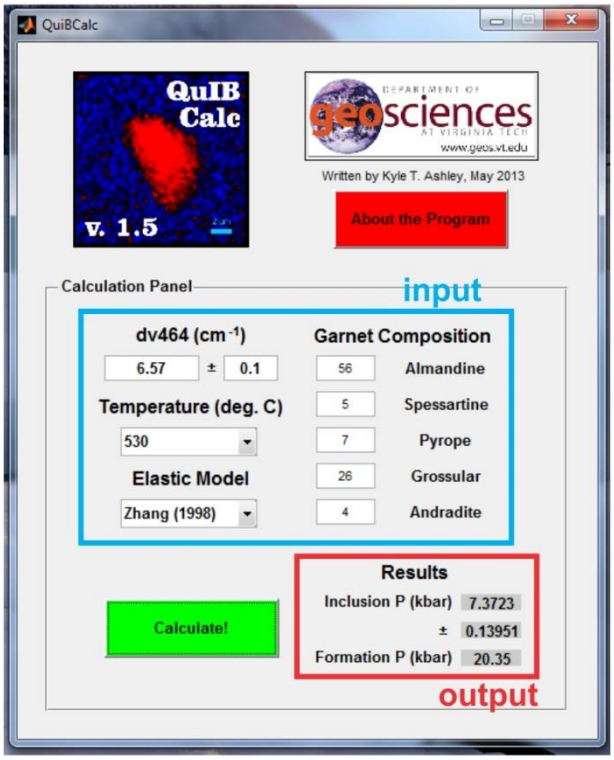

Figure 3.1. Screen capture of the QuIB Calc program window. Input and output clusters are highlighted, with an example calculation shown.

The Zhang (1998) model requires computation with the adiabatic bulk (κ) and shear (μ) moduli of quartz and garnet. Temperature dependence of the thermal expansivity (α_T) of both phases is considered by

$$\gamma = \int_{T_0}^{298\ K} \alpha_T \, dT \qquad \text{(eq. 3.2)}$$

where T_0 is the temperature of inclusion formation and α_T equations were taken from Skinner (1966, for garnet) and Dorogokupets (1995, for quartz). The elastic expression used is

$$P_{incl} = \frac{P_{ext}\left[\frac{1}{\kappa_{grt}} + \frac{3}{4\mu_{grt}}\right] + P_0\left[\frac{1}{\kappa_{qtz}} - \frac{1}{\kappa_{grt}}\right] + \gamma_{qtz} - \gamma_{grt}}{\frac{1}{\kappa_{qtz}} + \frac{3}{4\mu_{grt}}} \quad \text{(eq. 3.3)}$$

where P_{incl} is the inclusion pressure (bar), P_{ext} is 1 bar, and P_0 is the formation pressure. Much like the approach taken for the Guiraud and Powell (2006) model, an iterative solution is employed, where the calculated pressure is evaluated against the input pressure until the difference between the two is minimized. The computational approach taken with the Van der Molen and Van Roermund (1986) model is identical to this, with the expression:

$$P_{incl} = \left[\frac{\kappa_{qtz}}{\kappa_{grt}\left(3\kappa_{qtz} + 4\mu_{grt}\right)}\right]\left[P_{ext}\left(3\kappa_{grt} + 4\mu_{grt}\right) + P_0 4\mu_{grt}\left(\frac{\kappa_{grt}}{\kappa_{qtz}} - 1\right) - 4\mu_{grt}\kappa_{grt}\Delta T\Delta\alpha\right]$$

(eq. 3.4)

where ΔT is room minus formation temperature (in K) and $\Delta\alpha$ is α_{grt} minus α_{qtz} at temperature and pressure (to account for the lambda transition in quartz).

Natural garnets rarely have 'end-member' compositions. Therefore a mixing subroutine is included to approximate the elastic properties of natural garnet compositions. *QuIB Calc* employs a simple ideal mixing rule, such the end-member elastic properties are combined proportionally to their relative molar abundances. Compositional differences on the order of 5–10 mol% have little effect on pressure calculations, but assuming a pure end-member host (e.g. pure grossular) can lead to significant deviations in calculated pressures (>1 kbar) in some instances. Natural garnets do not exhibit ideal mixing between end-members (e.g., Bosenick *et al.*, 2001), but linear scaling of thermodynamic properties in garnet solid solution is a better approximation than assuming pure end-member values. The maximum difference from linearity between the pyrope-grossular solid solution is < 0.2 cm^3/mol

(Bosenick *et al.*, 2001) – much smaller than the deviation from assuming a pure endmember (*ca.* 1.2 cm^3/mol).

For example, a $\Delta\nu_{464}$ of 6.57 cm^{-1} and a *T* estimate of 530 °C, in a garnet host of 56% almandine + 7% pyrope + 26% grossular + 5% spessartine + 4% andradite yields an estimated trapping pressure of 20.35 kbar (Zhang, 1998, model; Fig. 3.1) or 19.06 kbar (Guiraud & Powell, 2006, model).

A subroutine is included in the program to verify if the apparent pressure at assumed temperature is within the stability field of α-quartz. The volumetric consequences of cooling an inclusion through the β–α transition are complex and depend on the pressure at which the transition occurs, so a dialog box warns the user if the calculated formation conditions are outside of the α-quartz stability field (beyond the applicability of this program). In addition, the quartz inclusion barometry technique appears to be best suited for high-*P*, low-*T* systems (little, if any, retained inclusion pressure is expected in high-*T* systems). Therefore extrapolation to the β-field is not warranted.

3.4 Conclusions

The MATLAB® program *QuIB Calc* calculates pressures of quartz inclusion entrapment in a garnet host, through iterative solution of elastic properties, based on the measured position of the ν_{464} Raman peak of quartz. It provides an easy-to-use interface that requires little prior knowledge of the MATLAB® language, facilitating straightforward and robust pressure calculations and obviating the need to separately compute elastic parameters or volumes using other programs. The program is available for download at *http://www.metamorphism.geos.vt.edu/Resources.html*.

Acknowledgements

We thank Robert Darling and an anonymous reviewer for their comments that improved the quality of the manuscript and improved efficiency and functionality of the code.

References

Ashley, K. T., Caddick, M. J., Steele-MacInnis, M., Bodnar, R. J. & Dragovic, B., 2014. Geothermobarometric history of subduction recorded by quartz inclusions in garnet. *Geochemistry Geophysics Geosystems*, **14**, doi: 10.1002/2013GC005106.

Bebout, G. E., 2007. Metamorphic chemical geodynamics of subduction zones. *Earth and Planetary Science Letters*, **260**, 373.

Bosenick, A., Dove, M. T., Heine, V. & Geiger, C. A., 2001. Scaling of thermodynamic mixing properties in garnet solid solutions. *Physics and Chemistry of Minerals*, **28**, 177-187.

Connolly, J. A. D., 2009. The geodynamic equation of state: What and how. *Geochemistry Geophysics Geosystems*, **10**(Q10014), http://dx.doi.org/10.1029/2009GC002540.

Dorogokupets, P. I., 1995. Equation of state for lambda transition in quartz. *Journal of Geophysical Research*, **100**(B5), 8,489-8,499.

Enami, M., Nishiyama, T. & Mouri, T., 2007. Laser Raman microspectrometry of metamorphic quartz: A simple method for comparison of metamorphic pressures. *American Mineralogist*, **92**, 1,303-1,315.

Guiraud, M. & Powell, R., 2006. *P-V-T* relationships and mineral equilibria in inclusions in minerals. *Earth and Planetary Science Letters*, **244**, 683-694.

Hacker, B. R., Peacock, S. M., Abers, G. A. & Holloway, S. D., 2003. Subduction factory 2. Are intermediate-depth earthquakes in subducting slabs linked to metamorphic dehydration reactions? *Journal of Geophysical Research*, **108**(B1), 11-1.

Holland, T. & Powell, R., 2011. An improved and extended internally consistent thermodynamic dataset for phases of petrological interest, involving a new equation of state for solids. *Journal of Metamorphic Geology*, **29**, 333-383.

Jorgensen, J. D., 1978. Compression mechanisms in α-quartz structures - SiO_2 and GeO_2. *Journal of Applied Physics*, **49**(11), 5,473-5,478.

Mouri, T. & Enami, M., 2008. Areal extent of eclogite facies metamorphism in the Sanbagawa belt, Japan: New evidence from a Raman microprobe study of quartz residual pressure. *Geology*, **36**(6), 503-506.

Raz, U., Girsperger, S. & Thompson, A. B., 2002. Thermal expansion, compressibility and volumetric changes of quartz obtained by single crystal dilatometry to 700 ^{o}C and 3.5 kilobars (0.35 GPa). *Schweizerische Mineralogische und Petrographische Mitteihurgen* **83**, 173-182.

Rosenfeld, J. L., 1969. Stress effects around quartz inclusions in almandine and the piezothermometry of coexisting aluminum silicates. *American Journal of Science*, **267**, 317-351.

Schmidt, C. & Ziemann, M. A., 2000. In-situ Raman spectroscopy of quartz: A pressure sensor for hydrothermal diamond-anvil cell experiments at elevated temperatures. *American Mineralogist*, **85**, 1,725-1,734.

Skinner, B. J., 1966. Thermal expansion. In: *Handbook of Physical Constants, Memoir 97* (ed Clark, S. P. J.), Geological Society of America.

Thiéblot, L., Roux, J. & Richet, P., 1998. High-temperature thermal expansion and decomposition of garnets. *European Journal of Mineralogy*, **10**, 7-15.

Tichelaar, B. W. & Ruff, L. J., 1993. Depth of seismic coupling along subduction zones. *Journal of Geophysical Research*, **98**(B2), 2017-2037.

Van der Molen, I. & Van Roermund, H. L. M., 1986. The pressure path of solid inclusions in minerals: The retention of coesite inclusions during uplift. *Lithos*, **19**(3-4), 317-324.

Zhang, Y., 1998. Mechanical and phase equilibria in inclusion-host systems. *Earth and Planetary Science Letters*, **157**, 209-222.

Chapter 4

Significance of "Stretched" Mineral Inclusions for Reconstructing *P-T* Exhumation History

Kyle T. Ashley[1], Robert S. Darling[2], Robert J. Bodnar[1], Richard D. Law[1]

[1]*Department of Geosciences, Virginia Polytechnic Institute and State University, Blacksburg, VA 24061, USA*

[2]*Department of Geology, State University of New York College at Cortland, P.O. Box 2000, Cortland, NY 13045, USA*

Submitted March 2014 in *Contributions to Mineralogy and Petrology*.

Abstract

Analysis of mineral inclusions in chemically and physically resistant hosts has proven to be valuable for reconstructing the *P-T* exhumation history of high-grade metamorphic rocks. The occurrence of cristobalite-bearing inclusions in garnets from Gore Mountain, New York, is unexpected because the peak metamorphic conditions reached are well removed (>600 °C too cold) from the stability field of this low-density silica polymorph that typically forms in high temperature volcanic environments. A previous study of samples from this area interpreted polymineralic inclusions consisting of cristobalite, albite and ilmenite as representing crystallized droplets of melt generated during a garnet-in reaction, followed by water loss from the inclusion to explain the reduction in inclusion pressure that drove the transformation of quartz to cristobalite. However, the recent discovery of monomineralic inclusions of cristobalite from the nearby Hooper Mine cannot be explained by this process. For these inclusions, we propose that the volume response to pressure and temperature changes during exhumation to the surface resulted in large tensile stresses within the silica phase that would be sufficient to cause transformation to the low density (low-pressure) form. Elastic modeling of other common inclusion-host systems suggests that the quartz-to-cristobalite example may not be a unique case. The aluminosilicate polymorph kyanite also has the capacity to retain tensile stresses if exhumed to the surface after being trapped as an inclusion in plagioclase at *P-T* conditions within the kyanite stability field, with the stresses developed during exhumation sufficient to produce a transformation to andalusite. These results highlight the elastic environment that may arise during exhumation, and provide a potential explanation of observed inclusions whose stability fields are well removed from *P-T* paths followed during exhumation.

4.1 Introduction

The presence of inclusions of one phase within a host mineral representing a different phase has been exploited to gain insight into the pressure-temperature-composition-time-deformation (*P-T-X-t-D*) evolution in studies of igneous and metamorphic systems (e.g. Chopin, 1984; St-Onge, 1987; Perrillat *et al.*, 2003; Hoisch *et al.*, 2008; Ashley *et al.*, 2014). For example, St-Onge (1987) analyzed biotite and plagioclase inclusions from core to rim in garnet to estimate pressure and temperature evolution with net transfer barometry and exchange thermometry, respectively. However, in rocks where petrologically important mineral assemblages (i.e. assemblages that constitute geobarometers of geothermometers) are not available or applicable, index minerals that provide more direct evidence for the formation conditions have been used, such as the presence of coesite inclusions in ultra-high-*P* garnet (e.g. Chopin, 1984; Smith, 1984) and cristobalite inclusions in granulite facies garnet (Darling *et al.*, 1997). Recent work has focused on applying Raman spectroscopic and X-ray diffraction techniques to analyze

inclusions that retain some record of the formation pressure as a consequence of the fact that the inclusion phase behaves elastically along the path from encapsulation through exhumation to the Earth's surface (e.g. Parkinson & Katayama, 1999; Enami *et al.*, 2007; Ashley *et al.*, 2014; Kouketsu *et al.*, 2014). These studies suggest that elastic differences between the host and inclusion mineral result in significant deviation from isochoric (constant volume) behavior, with substantial differences between externally applied and residual inclusion stresses, both in the compressive and tensile regimes. In many ways, this behavior is similar to that shown by fluid inclusions. At the *P-T* trapping conditions, the pressure in a fluid inclusion is equal to the confining pressure on the host phase. However, depending on the fluid composition and density, the pressure in the inclusion at room temperature may be much greater than the ambient pressure of ~0.1 MPa (Vityk *et al.*, 1994; 1995), or might be less than ambient pressure, resulting in a "stretched" fluid at negative pressures in the inclusion (Roedder, 1967; Alvarenga *et al.*, 1993; Krüger *et al.*, 2007; Fall *et al.*, 2009). The phrase "negative pressure" may be misleading, as it is not possible for absolute pressure to be negative. However, the term "negative pressure" is widely used among scientists studying water physics, vascular plants, and fluid inclusions (see Caupin & Strook, 2013 and references therein) and pressure values less than zero are commonly reported. In physics, the Casimir pressure (Casimir, 1948) defines the force per area between two closely spaced parallel plates, and the Casimir pressure is negative because the force between the plates is attractive. In the fluid inclusion literature (Roedder, 1967; Krüger *et al.*, 2007) "negative" pressures are purely the result of an arithmetic extrapolation of an isochore to some temperature on a P-T diagram plotted on a linear scale such that the pressure at that temperature is <0. When considering solid inclusions as in the present study, resultant inclusion stresses generated as *P-T* conditions change should be considered; the sign is indicative of the vector direction of the applied stress, where positive and negative values indicate compressive and tensile stresses, respectively. Thus, our use of the term "negative pressure" simply refers to a phase under tension.

Rocks exhumed from high-pressures are particularly susceptible to metamorphic overprinting during exhumation to the Earth's surface, precluding the use of mineral assemblages to infer the earlier *P-T* history (e.g. Matthews and Schliestedt, 1984; Grevel *et al.*, 2009). Inclusions preserve a record of the depths reached during processes such as subduction and may reveal rheological characteristics of the mantle. For example, the recent discovery of inclusions of ringwoodite, a high-*P* olivine polymorph with the capacity to incorporate water, in diamond has been interpreted to indicate that diamonds form in the mantle at least as deep as the lower transition zone (where ringwoodite is a stable phase) and that large quantities of water may be present in the mantle transition zone (Pearson *et al.*, 2014). These findings are largely dependent on the reliability of indicator minerals as direct evidence for pressures (and therefore depths, if a pressure-depth model is assumed) of formation. Because perfect pressure vessels (i.e. a completely incompressible host mineral) do not exist in nature, some volumetric relaxation occurs in the inclusion during exhumation, which may lead to the formation of polymorphs. Examples include partial conversion (i.e. the entire product is not transformed to reactant) of coesite to α-quartz (Gillet *et al.*, 1984) and partial conversion of ringwoodite to wadsleyite and olivine (Pearson *et al.*, 2014).

4.2 Sample Selection

We considered two case studies of inclusions from granulite-facies rocks of the Adirondack Mountains, NY. The first sample was collected near the town of Port Leyden, New York (western Adirondack Highlands; Fig. 4.1). Quartz inclusions were trapped in peritectic garnets at temperatures <800 °C and pressures of ~0.6 GPa (Florence *et al.*, 1995; Darling, 2013; Fig. 4.2a,b). The second case study is of cristobalite inclusions in garnet from the former Hooper Mine in the central Adirondacks, ~100 km east of where the Port Leyden sample was collected (Fig. 4.1; Fig. 4.2c-f). Petrologic analysis of rocks surrounding the Hooper Mine by Spear and Markussen (1997) constrained peak metamorphism at

~850 °C and 0.65–0.8 GPa, with garnet growth occurring along the early cooling path. At these conditions, β-quartz is the stable silica polymorph that should be trapped as inclusions in garnet (Fig. 4.3). Owing to slow cooling rates inferred for the Adirondacks Highlands, temperatures remained above 600 °C for 50–100 million years (e.g. Mezger *et al.*, 1991; Bonamici *et al.*, 2011, and references therein). If *P-T* conditions during metamorphism at the Hooper Mine were based on cristobalite inclusions in garnet, one would interpret the garnets to have formed at T>1470°C and P<~0.5 GPa, resulting in an error in inferred formation conditions of ~0.7 GPa and >600 °C and well outside the stability field of the host garnet. These two samples were selected for comparison in this study because, despite similar formation conditions, silica is present in two different forms – as quartz to the west and as cristobalite to the east. Therefore, the Port Leyden sample may provide valuable insights into potential drivers for cristobalite transformation that occurred in the Hooper Mine sample.

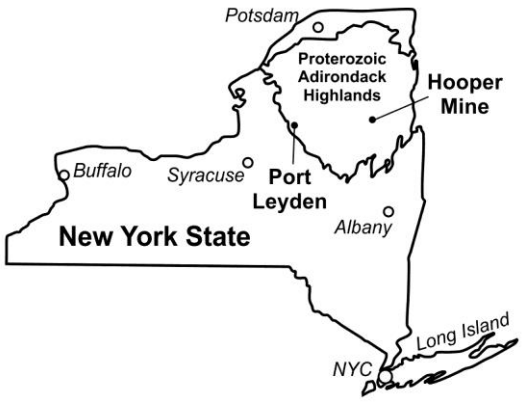

Figure 4.1. Generalized map of the state of New York outlining the Adirondack Highlands and locations of Hooper Mine and Port Leyden samples (modified from Darling, 2013).

4.3 *P-T* Stability Limits of Silica (SiO_2) Phases

The majority of crystalline silica (SiO_2) in the Earth's crust is in the form of α-quartz (Heaney, 1994), but other low-density polymorphs are common in specific geologic environments. For example, β-tridymite and/or β-cristobalite often crystallize during cooling of volcanic rocks (e.g. Horwell *et al.*, 2013) and have been documented from shallow contact metamorphic environments (Heaney, 1994).

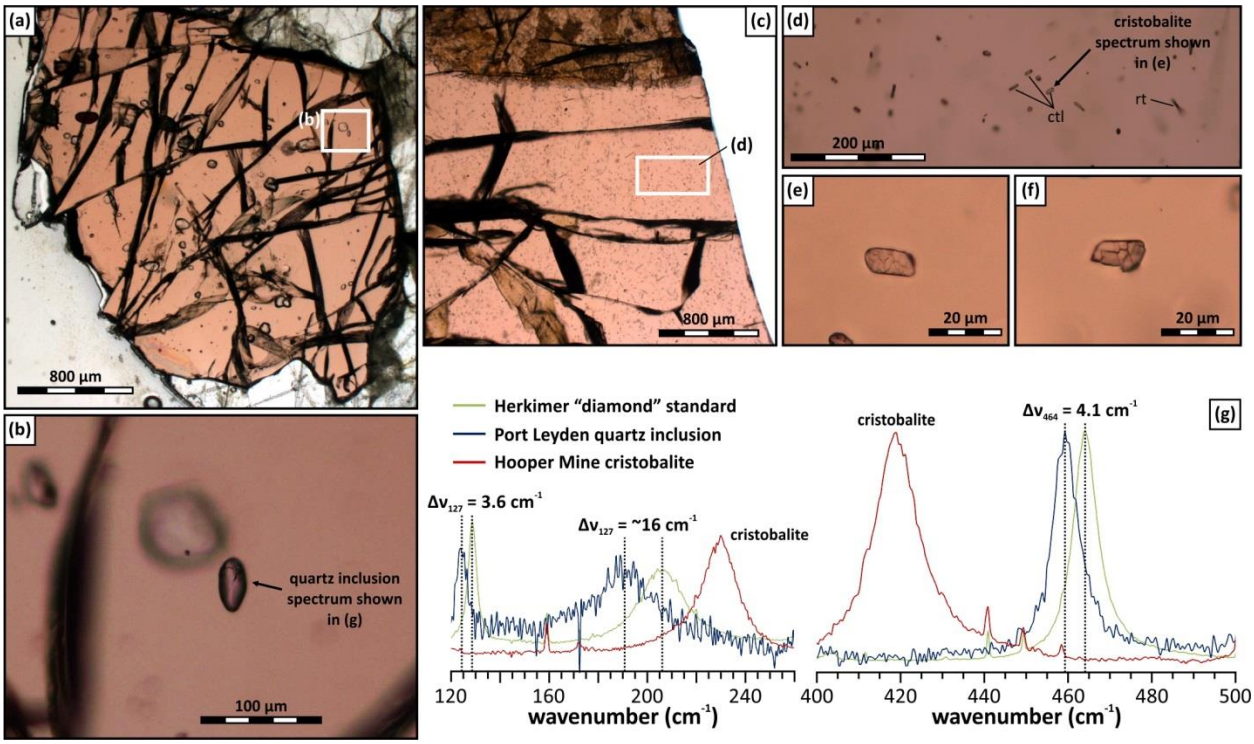

Figure 4.2. Photomicrographs and Raman spectra of inclusions of inclusions in Adirondack garnets. (a) Garnets from Fort Leyden contain isolated quartz inclusions (b) that show negative Raman waveshifts from adiabatic standard measurements (e). (f-j) Cristobalite inclusions in garnet from the former Hooper Mine. Cristobalite inclusions exhibit fractures that result from the volume change during transformation from β- to α-cristobalite upon cooling. (g) Raman spectra of quartz inclusions from Fort Leyden show encapsulated quartz inclusions that are currently dilated, with negative waveshifts of the ν_{464} line in quartz of ~-4.1 cm^{-1}. Raman spectra of the cristobalite inclusions from the Hooper mine are distinct form the quartz spectrum.

These phases also form during the devitrification of silicate glasses (Abeele *et al.*, 1981; Rivera *et al.*, 1987), and form as low-temperature precipitates (Klasik, 1975). Stable cristobalite and tridymite may form during contact metamorphism and in tectonically active zones, however, they readily convert to α-quartz with decreasing temperature (e.g. Moehlman, 1935; Van Valkenburg Jr. & Buie, 1945; Green & Fitz III, 1993). While there is a general consensus concerning the *P-T* range over which tridymite is stable, there is debate concerning whether tridymite will form at all in the absence of a catalyst (e.g. Fenner, 1913; Flörke, 1955; Eitel, 1957; Hill & Roy, 1958; Sato, 1963). It is generally accepted that tridymite is stable at the pressure and temperature conditions illustrated in Figure 4.3. Trace impurities (particularly Na-silicate, even in amounts of ~ 0.2% Na_2O; Cole, 1934) greatly reduce the temperatures required for conversion of quartz to these low-density polymorphs. In addition, cristobalite readily forms

from quartz before tridymite due to the greater energy requirements to break Si-O bonds and restructure the crystal of tridymite relative to cristobalite (Cole, 1934).

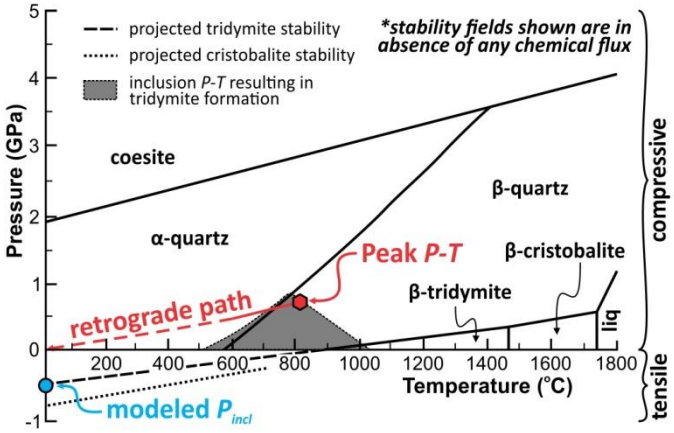

Figure 4.3. Silica polymorph stability in pressure-temperature projection (after Klein & Hurlbut, 1993; Shen *et al.*, 1993). The tridymite and cristobalite transition lines are linearly extrapolated to room temperature (into the tensile stress field). The shaded field represents the elastically modeled minimum conditions needed to generate sufficient stretching to stabilize a low-density polymorph. The peak metamorphic conditions for the Gore Mountain granulites (hexagon; Spear & Markussen, 1997) coincide with conditions required for tridymite to be stable at room temperature (resultant P_{incl} calculated to be *ca.* -0.5 GPa).

4.4 The Cristobalite Dilemma in High Pressure Rocks

Darling *et al.* (1997) described metastable α-cristobalite inclusions in garnet from a granulite facies metabasite from the Barton Mine on Gore Mountain, in the Adirondack Mountains, New York. Its presence was confirmed through electron microprobe analyses, Raman spectroscopy, hysteresis measurements (identifying the transformation to β-cristobalite), and petrographic observations (e.g. isotropic nature of β-cristobalite). Inclusions are polymineralic with albite and ilmenite and are widely disseminated in garnet. Darling *et al.* (1997) interpreted these inclusions to be the result of a garnet-in reaction that produced (and included inside the growing garnets) hydrous Na-Al-silicate melt, followed by dehydration by diffusion of the aqueous component out of the inclusions and into the surrounding host. This process was interpreted to provide adequate pressure decrease to drive cristobalite crystallization. The crystallization could have been further aided by the fluid and albite components of the inclusion, which would provide the Na-silicate component that promotes low temperature conversion of a higher density silica polymorph to cristobalite. However, about 5 km northwest of the

Barton Mine (Gore Mountain), the former Hooper Mine contains porphyroblastic garnets with cristobalite-only inclusions (reported here for the first time; Fig. 4.2c-f). No other phases were identified during Raman spectroscopic analysis of the inclusions. These inclusions are problematic to interpret as a result of fluid loss because of their unlikely origin as pure silica melt. Therefore, another retrograde process must be involved. We propose that the cristobalite inclusions in garnet at the Hooper Mine were initially encapsulated as inclusions of quartz that subsequently experienced transformation during exhumation. Herein, we investigate the elastic evolution of a quartz inclusion in garnet to determine if the physical properties of the host and inclusion phases are sufficient to account for the transformation of quartz to cristobalite during exhumation.

4.5 Analytical and Computational Methods

4.5.1 Raman Spectroscopy of Inclusions

Unpolarized spectra of quartz inclusions in samples from the western Adirondacks were collected on a JY Horiba LabRam HR800 Raman microprobe. A high-resolution 800 mm focal length spectrometer (1800 lines/mm grating) and a 514.57 nm (100 mW source laser power) argon laser were used in the analysis. High spatial (~1 µm) resolution was achieved using a confocal microscope with a 100x objective (NA = 0.90). The confocal aperture was set at 400 µm and a 150 µm slit width was used. A spectral range of *ca.* 73.8–633.1 cm^{-1} (centered on 360 cm^{-1}) was used to allow simultaneous collection of the three main peaks of quartz (ca. 464, 206 and 127 cm^{-1} at ambient conditions) over a 60 second dwell time with three iterations, with a spectral resolution after fitting of <0.1 cm^{-1}. Three Ar plasma lines (at 520.30, 266.29, and 116.04 cm^{-1}) were collected simultaneously during each inclusion analysis for calibration purposes and to correct for environmental and electronic drift. The Raman shift of the 464 cm^{-1} quartz band was converted to inclusion pressure using the calibration of Ashley *et al.* (2014), derived from the Schmidt and Ziemann (2000) dataset.

The ν_{464} band for quartz was used for pressure determination instead of the ν_{206} band because ν_{206} is weaker and asymmetric (especially at higher temperatures), making the determination of peak position less precise. In addition, there is an interaction "cross term" effect between temperature and pressure (Schmidt & Ziemann, 2000), such that it is impossible to decipher the pressure and temperature by studying coupled $\nu_{464\text{-}206}$ waveshifts (e.g. Enami *et al.*, 2007) without additional information. Enami *et al.* (2007) reported exceptional reproducibility of the ν_{464} and ν_{127} bands when oriented standards are analyzed at ambient conditions (consistently within ±0.04 cm^{-1}). However, measurements of the ν_{206} band by Enami *et al.* (2007) show considerably more scatter (> ±0.3 cm^{-1}). When peak separation (e.g. ω_1 representing the distance between the ca. 464 and 206 cm^{-1} peaks) is used, the large uncertainties on the ν_{206} peak position are propagated through the calculation, resulting in greater overall uncertainty in the estimated inclusion pressures. The main benefit of the approach by Enami *et al.* (2007) is that absolute peak positions are not needed (only the relative peak positions). However, improved uncertainties may be achieved by making a linear correction for drift using precisely located bounding argon plasma lines (e.g. Schmidt & Ziemann, 2000; Ashley *et al.*, 2014). In addition, the use of only the ν_{464} band was preferred here because there is no interference from the host garnet, as is observed for the ν_{206} band which shows interference from low-intensity garnet bands at *ca.* 205–220 cm^{-1} (Enami, 2012). The lower-frequency Raman bands for quartz contain additional Si-O torsional vibrations (Kingma & Hemley, 1994), which adds additional complications when coupling peak shifts for inclusion pressure calculation.

4.5.2 Elastic Modeling Approach

The internal pressures retained by inclusions after exhumation were calculated using the thermoelastic model of Guiraud and Powell (2006). This computational approach requires volume

estimation at encapsulation and surface conditions. For this, the program Perple_X (Connolly, 2009) was implemented, utilizing the Holland and Powell (2011) thermodynamic database and following the volume calculation approach of Holland and Powell (2011) through a modified Tait equation of state. Interpretation of quartz data required application of landau theory to account for anomalous heat capacities that result from order-disorder effects when passing through the α-β quartz transition. Therefore, the pressure-sensitive approach taken by Holland and Powell (1998, and references therein) was implemented. This approach was applied for volume calculation owing to its ability to replicate experimental data up to high pressures (Holland & Powell, 2011) and the availability of an internally consistent database that allowed various inclusion-host systems to be tested across a range of *P-T* data. Shear moduli for almandine garnet (92.1 GPa), anorthite plagioclase (~39.5 GPa), and diamond (538.0 GPa) were taken from Wang and Ji (2001), Brown et al. (*in revision*), and McSkimin and Andreatch (1972), respectively.

First, the volumes of the inclusion and host were calculated at the pressure and temperature of interest (~850 °C, ~0.7 GPa for the Hooper Mine sample; Spear & Markussen, 1997). Host volume at adiabatic pressure and temperature was subsequently calculated, with an isothermal volume-pressure profile calculated for the inclusions from -1.0–+1.0 GPa (in 0.001 GPa increments) at room temperature. We iterate the thermoelastic model of Guiraud and Powell (2006) with the inclusion pressure and resultant inclusion volume data until a solution is found (the difference between the host and inclusion side equals zero). This computational approach results in isomeke (lines of constant inclusion pressure; Angel *et al.*, 2014) projections in *P-T* space that are identical to those produced by Kohn (2014).

4.6 Inclusion Adhesion to the Host Wall and Resultant Inclusion Dilation

4.6.1 Tensile Stresses Acting on Quartz Inclusions

It has been widely documented that fluids can exist in a metastable stretched state by adhering to the walls of the containing host mineral (e.g. Roedder, 1967; Alvarenga *et al.*, 1993; Krüger *et al.*, 2007; Fall *et al.*, 2009). Recent studies have shown that solid mineral inclusions may also exist in a stretched state under tension (e.g. Sato *et al.*, 2009; Nishiyama & Aikawa, 2011; Kouketsu *et al.*, 2014), and preservation of this stretched state is contingent upon the ability of the host to maintain large pressure differentials. While there are considerable data to support the fact that mineral inclusions can exist in a stretched state, the mechanism(s) that may lead to this condition are poorly understood. One possibility is that adhesion of a mineral inclusion to the surrounding host is favored because it minimizes surface energies (e.g. DeVore, 1956; Barrow & Bowden, 1987). The development of interatomic Coulombic interactions resulting from unsatisfied (dangling) bonds at the inclusion-host interface is an epitaxial mechanism that might reduce surface energies, with oriented attachment maximizing bonding affinities and further stabilizing the interface (Kretz, 1966; Zhang & Banfield, 2014). The resultant energy barrier that develops acts as a sub-microscopic scaffold to support connectivity, and would accommodate the acquired tensile stresses in the inclusion. However, the forces at work at this boundary are unknown, and the specific bonding mechanism that locks quartz to the surrounding garnet is not required to interpret our results. The important consideration is that bonding (or adhesion) of some type does occur, because we observe *in-situ* dilated quartz. In the garnets from Port Leyden, the peak position of inclusion quartz is shifted by -4.1 cm^{-1} from the position expected at ambient conditions (0.1 MPa; Fig. 4.2g) – this is equivalent to an inclusion pressure of -0.44 GPa. The 464 cm^{-1} Raman line represents O motion in symmetric Si-O-Si stretching-bending modes (Kingma & Hemley, 1994), and thus dilation of the crystal lattice would be required to produce a negative Raman waveshift. If quartz had

detached from the garnet wall at any time during exhumation, the 464 cm^{-1} line would not be shifted and a void space would be generated in the inclusion (which has not been observed).

4.6.2 Cristobalite Transformation

The evolution in inclusion pressure of the sample from the Hooper Mine along several potential retrograde *P-T* paths (Fig. 4.4a) was calculated using the elastic modeling approach discussed above. The model assumed that a pure β-quartz inclusion was trapped in almandine garnet, at peak *P-T* conditions (~850 °C, ~0.7 GPa; Spear & Markussen, 1997).

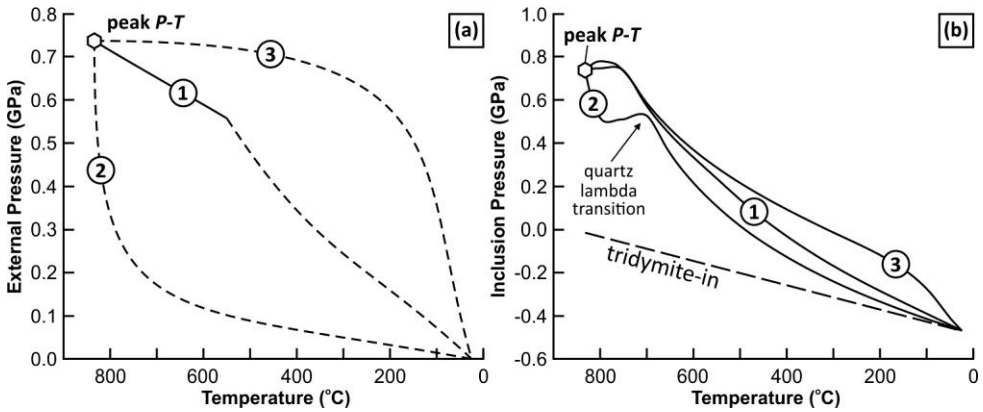

Figure 4.4. (a) Various pressure-temperature paths used for modeling inclusion pressure evolution. Path 1 is from Spear and Markussen (1997); Path 2 exhibits isothermal decompression prior to cooling; Path 3 represents isobaric cooling before decompression. (b) Inclusion pressure-temperature paths resulting from designated paths shown in (a). Regardless of the path followed, the exhumed rock will always return inclusion pressures of -0.47 GPa, which is just within the projected tridymite stability field.

Three retrograde paths were examined to test if different exhumation paths result in inclusion pressures that overstep any of the cristobalite or tridymite stability fields during cooling. The first path considered (1) is based on petrologic evidence presented by Spear and Markussen (1997). The second path assumes nearly isothermal decompression followed by cooling from low pressures, while path three follows an isobaric cooling trend before decompression (Fig. 4.4a). The model results suggest that despite large differences between the externally applied lithostatic pressure and the pressure on the encapsulated inclusion (0.47 GPa), the inclusion does not enter into the extrapolated tridymite field until

the rock is nearly at the surface (Fig. 4.4b). It should be noted that larger tensile stresses are expected if encapsulation occurred post-peak conditions but prior to passing into the α-quartz stability field; if the quartz was included at 700 °C and 0.68 GPa, the pressure differential would be -0.55 GPa. The conclusion that quartz converts to cristobalite late in the cooling history is important because cristobalite formation is metastable in this scenario and would readily transform to tridymite over geologically short time scales (Cole, 1934). As previously mentioned, the rocks in this area of the Adirondacks remained hot for an extended period of time. Therefore, transformation must have occurred while temperatures were sufficiently low, where kinetics would inhibit conversion of cristobalite to tridymite (possibly at T < 350–400 °C; Mosenfelder & Bohlen, 1997; Perrillat *et al.*, 2003; Kohn, 2014). In addition, transformation must have occurred at temperatures greater than 270 °C because the inclusions formed as high cristobalite and underwent volume reduction cracking upon cooling (Darling *et al.*, 1997). As discussed earlier, the conditions required for the α-quartz to cristobalite or α-quartz to tridymite transformations are very sensitive to even small amounts of impurities, and it is therefore likely that the conversion may have required smaller tensile stresses to proceed than are estimated here. Cristobalite also readily forms before tridymite due to the energy required to break bonds as tridymite converts from the trigonal crystal system (Cole, 1934).

The initial transformation of quartz into cristobalite provides a nucleus for continued crystal growth and accelerates further conversion (Cole, 1934). Transformation is initiated on the outside of the inclusion, and continues inward until the entire crystal has been transformed. This is important when considering the stress that can be accommodated while maintaining adhesion to the container wall, as conversion would reduce tensile stress at the boundary (the quartz-to-cristobalite reaction results in a molar volume increase) and the surface accommodating the tensile stress would migrate inward toward the inclusion core until complete conversion is reached. Owing to the volume increase occurring during this reaction, residual tensile stresses would not be expected following the conversion to cristobalite.

4.6.3 Consideration of Anisotropic Deviatoric Stresses

Briggs and Ramdas (1977) determined energy shifts for the Raman ν_{464} band along different crystallographic directions (parallel to <a> and parallel to <c>) in response to uniaxial compression. For a uniaxial compressive force of 1.0 GPa, a maximum frequency shift difference of 1.7 cm^{-1} is observed (Fig. 4.5). This elastic anisotropy is expected to generate deviatoric stress and deform the crystal lattice as the stress increases. Angel *et al.* (2014) estimate 20–40% deviatoric stress may be generated relative to an applied hydrostatic stress. For inclusions that retain large pressure differentials compared with the externally applied pressure, this may result in errors when applying linear elasticity theory and when collecting "bulk" stress measurements (e.g. through Raman spectroscopy). X-ray diffraction provides the advantage of providing *in-situ* anisotropic stress information. Angel *et al.* (2014) found that errors resulting from this simplification are relatively small; for a quartz inclusion trapped in garnet at 0.7 GPa and 380 °C, the error in the calculated inclusion pressure (0.45 GPa) is only 0.01 GPa. Because our results are of a similar magnitude (albeit in the tensile regime), we expect similar (negligible) errors for the deviatoric stress resulting from the anisotropic nature of quartz.

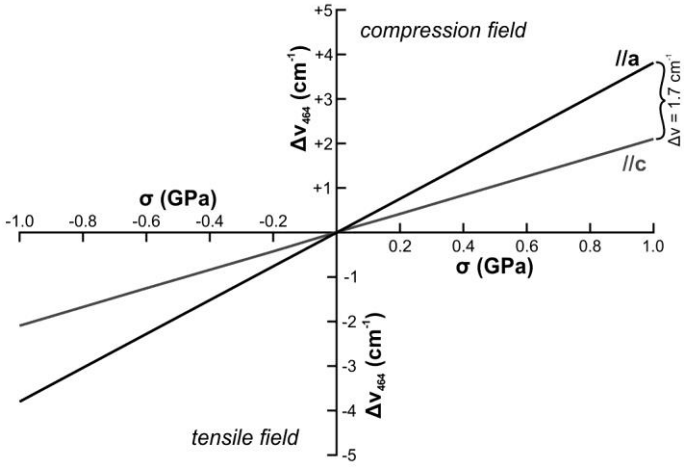

Figure 4.5. Uniaxial compression and resultant frequency shift of the 464 cm^{-1} line for quartz (modified from Briggs & Ramdas, 1977). The anisotropic behavior of quartz is expected to cause variations in ν_{464} of up to 1.7 cm^{-1}, depending on crystallographic direction.

4.6.4 Application to Other Inclusion-Host Systems

Other inclusion mineral-host systems that may experience similar transformations due to the retained inclusion stresses were also examined using the methods described above. Inclusion minerals considered are calcite/aragonite, K-feldspar, graphite, Al-silicates (kyanite, sillimanite, andalusite), and olivine polymorphs in garnet, plagioclase and diamond hosts. The results revealed two types of inclusion mineral behavior. The first involves minerals that preserve pressure during decompression, and retain some level of positive residual pressure in the inclusion *within the elastic window* (i.e. temperatures lower than the onset of crystal plasticity). This group includes graphite, sillimanite, andalusite, calcite/aragonite, and the olivine polymorphs. With the exception of graphite, for which the slope of the isomeke projected in *P-T* space is independent of temperature (Kohn, 2014), each phase has the potential to generate tensile stresses at sufficiently high temperatures. We tested scenarios in which ringwoodite or coesite might be produced if an inclusion of olivine or quartz, respectively, were over-pressured during exhumation. However, because perfect pressure vessels do not exist in nature (the bulk modulus would approach infinity, making it completely incompressible), partial relaxation of the inclusion occurs and, although significant pressures are retained, they are insufficient to cause formation of a polymorph stable at pressures greater than the trapping pressure.

The second group of minerals includes those that have the potential to develop large tensile stresses within their stability fields when completely encapsulated inclusions are exhumed to the surface. In addition to quartz, results indicate that kyanite included in plagioclase is the only phase that would show this behavior, generating <-0.3 GPa pressure if included near the aluminosilicate triple-point (536 °C, 0.43 GPa; Fig. 4.6). These residual stresses would be sufficiently large to result in the transformation of kyanite to andalusite when projected into the tensile regime. Therefore, to the best of our knowledge, quartz and kyanite are the only common mineral inclusions capable of undergoing transformation due to large tensile stresses resulting from elastic evolution during the retrograde path.

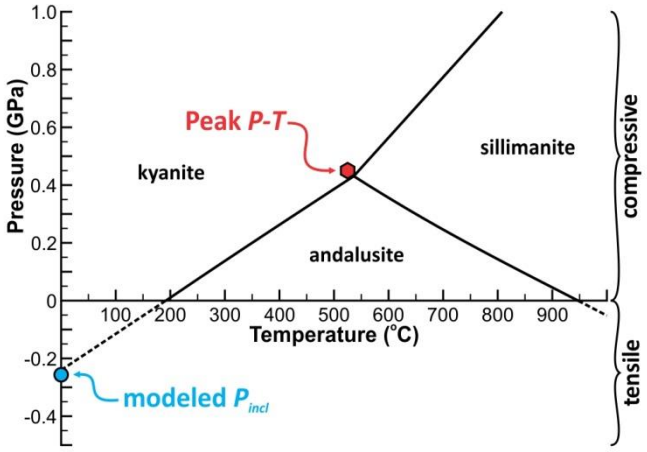

Figure 4.6. *P-T* stability of Al_2SiO_5 phases, with calculated inclusion pressure that results when kyanite is included in anorthite plagioclase near the triple point. Stability field was calculated from the thermodynamic data of Holland and Powell (2011).

4.7 Implications for Interpreting the Origin of Mineral Inclusions

In this study, we show that quartz inclusions in garnet can be under significant tensile stress and that the stress may be sufficiently large to cause transformation to cristobalite, as in the case ofinclusions in Hooper Mine garnet. This scenario documents the important effect that elastic properties of the host and inclusion system have on the phases preserved as mineral inclusions that are observed at the Earth's surface. These results document the ability of host phases to retain inclusions in a metastable stretched state, as recently recognized in other studies (e.g. Kouketsu *et al.*, 2014). This work also suggests that inclusions have the ability to bind to the host wall and to preserve large tensile stresses at the micro-scale. In addition, and perhaps more importantly, this stretched state could result in a metastable polymorph transformation, provided that tensile stresses are sufficiently large. Although our results suggest that this phenomenon may be limited to only a few common mineral systems (SiO_2 and Al_2SiO_5 polymorphs in garnet and plagioclase, respectively), it nevertheless reflects the importance of physioelastic properties of the host-inclusion system on mineral assemblages generated during exhumation.

Acknowledgements

We thank Matthew Steele-MacInnis for thoughtful discussions on several aspects of this study. Review of earlier drafts of this manuscript by Frank Spear, John Wheeler, and Evangelos Moulas greatly improved the quality of this work.

References

Abeele, W.V., Wheeler, M.L. & Burton, B.W. (1981). Geohydrology of Bandelier Tuff. *Los Alamos National Laboratory Report* LA-8962.

Alvarenga, A.D., Grimsditch, M., & Bodnar, R.J. (1993). Elastic properties of water under negative pressures. Journal of Chemical Physics **98**, 8392-8396.

Angel, R.J., Mazzucchelli, M.L., Alvaro, M., Nimis, P. & Nestola, F. (2014). Geobarometry from host-inclusion systems: The role of elastic relaxation. *American Mineralogist* **99**, 2146-2149.

Ashley, K.T., Caddick, M.J., Steele-MacInnis, M., Bodnar, R.J. & Dragovic, B. (2014). Geothermobarometric history of subduction recorded by quartz inclusions in garnet. *Geochemistry Geophysics Geosystems* **15**, 350-360.

Barrow, N.J. & Bowden, J.W. (1987). A comparison of models for describing the adsorption of anions on a variable charge mineral surface. *Journal of Colloid and Interface Science* **119**, 236-250.

Bonamici, C.E., Kozdon, R., Ushikubo, T. & Valley, J.W. (2011). High-resolution *P-T-t* paths from $\delta^{18}O$ zoning in titanite: A snapshot of late-orogenic collapse in the Grenville of New York. *Geology* **39**, 959-962.

Briggs, R.J. & Ramdas, A.K. (1977). Piezospectroscopy of the Raman spectrum of α-quartz. *Physical Review B* **16**, 3815-3826.

Brown, J.M., Angel, R.J. & Ross, N. (*in revision*). Elasticity of plagioclase feldspars.

Casimir, H.B.G. (1948). Proceedings of the Koninklijke Nederlandse Akademie van Wetenschappen. **B51**, 793.

Caupin, F. & Stroock, A.D. (2013). The stability limit and other open questions on water at negative pressure. *Liquid Polymorphism: Advances in Chemical Physics* **152**, 51-80.

Chopin, C. (1984). Coesite and pure pyrope in high-grade blueschists of the Western Alps: A first record and some consequences. *Contributions to Mineralogy and Petrology* **86**, 107-118.

Cole, S.S. (1934). The conversion of quartz into cristobalite below 1000 °C, and some properties of the cristobalite formed, *American Ceramic Society (Refractories Division)*, Cincinnati, Ohio.

Connolly, J.A.D. (2009). The geodynamic equation of state: What and how. *Geochemistry Geophysics Geosystems* **10**, 1-19.

Darling, R.S. (2013). Zircon-bearing, crystallized melt inclusions in peritectic garnet from the western Adirondack Mountains, New York State, USA. *Geofluids* **13**, 453-459.

Darling, R.S., Chou, I.M. & Bodnar, R.J. (1997). An occurrence of metastable cristobalite in high-pressure garnet granulite. *Science* **276**, 91-93.

DeVore, G.W. (1956). Surface chemistry as a chemical control on mineral association. *Geology* **64**, 31-55.

Eitel, W. (1957). Structural anomalies in tridymite and cristobalite. *American Ceramic Society Bulletin* **57**, 142-148.

Enami, M. (2012). Influence of garnet hosts on the Raman spectra of quartz inclusions. *Journal of Mineralogical and Petrological Sciences* **107**, 173-180.

Enami, M., Nishiyama, T. & Mouri, T. (2007). Laser Raman microspectrometry of metamorphic quartz: A simple method for comparison of metamorphic pressures. *American Mineralogist* **92**, 1,303-301,315.

Fall, A., Rimstidt, J. D. & Bodnar, R. J. (2009). The effect of fluid inclusion size on determination of homogenization temperature and density of liquid-rich aqueous inclusions. *American Mineralogist* **94**, 1569-1579.

Fenner, C. N. (1913). The stability relations of the silica minerals. *American Journal of Science* **36**, 331-384.

Florence, F. P., Darling, R. S. & Orrell, S. E. (1995). Moderate pressure metamorphism and anatexis due to anorthosite intrusion, western Adirondack Highlands, New York. *Contributions to Mineralogy and Petrology* **121**, 424-436.

Flörke, O. W. (1955). Strukturanomalien bei Tridymit und Cristobalit. *Berichte der Deutschen Keramischen Gesellschaft* **32**, 369-381.

Gillet, P., Ingrin, J. & Chopin, C. (1984). Coesite in subducted continental crust: *P-T* history deduced from an elastic model. *Earth and Planetary Science Letters* **70**, 426-436.

Green, J. C. & Fitz III, T. J. (1993). Extensive felsic lavas and rheoignimbrites in the Keweenawan Midcontinent Rift plateau volcanics, Minnesota: Petrographic and field recognition. *Journal of Volcanology and Geothermal Research* **54**, 177-196.

Grevel, C., Schreyer, W., Grevel, K.-D., Schertl, H.-P. & Willner, A. P. (2009). REE distribution, mobilization and fractionation in the coesite-bearing 'pyrope quartzite' and related rocks of the Dora-Maira Massif, Western Alps. *European Journal of Mineralogy* **21**, 1213-1224.

Guiraud, M. & Powell, R. (2006). *P-V-T* relationships and mineral equilibria in inclusions in minerals. *Earth and Planetary Science Letters* **244**, 683-694.

Heaney, P. J. (1994). Structure and chemistry of the low-pressure silica polymorphs. In: Heaney, P. J., Prewitt, C. T. & Gibbs, G. V. (eds.) *Silica: Physical Behavior, Geochemistry, and Materials Applications*. Washington, D.C.: Mineralogical Society of America, 1-40.

Hill, V. G. & Roy, R. (1958). Silica structure studies. VI. On tridymite. *Transactions of the Brittish Ceramic Society* **57**, 496-510.

Hoisch, T. D., Wells, M. L. & Grove, M. (2008). Age trends in garnet-hosted monazite inclusions from upper amphibolite facies schists in the northern Grouse Creek Mountains, Utah. *Geochimica et Cosmochimica Acta* **72**, 5505-5520.

Holland, T. & Powell, R. (2011). An improved and extended internally consistent thermodynamic dataset for phases of petrological interest, involving a new equation of state for solids. *Journal of Metamorphic Geology* **29**, 333-383.

Holland, T. J. B. & Powell, R. (1998). An internally consistent thermodynamic data set for phases of petrological interest. *Journal of Metamorphic Geology* **16**, 309-343.

Horwell, C. J., WIlliamson, B. J., Llewellin, E. W., Damby, D. E. & Le Blond, J. S. (2013). The nature and formation of cristobalite at the Soufrière Hills volcano, Montserrat: Implications for the petrology and stability of silicic lava domes. *Bulletin of Volcanology* **75**, 19.

Kingma, K. J. & Hemley, R. J. (1994). Raman spectroscopic study of microcrystalline silica. *American Mineralogist* **79**, 269-273.

Klasik, J. A. (1975). High cristobalite and high tridymite in a Middle Eocene deep-sea chert. *Science* **189**, 631-632.

Klein, C. & Hurlbut, C. S. J. (1993). *Manual of Mineralogy, 21st edn.* New York: John Wiley.

Kohn, M. J. (2014). "Geoba-Raman-try": Calibration of spectroscopic barometers and thermometers for mineral inclusions. *Earth and Planetary Science Letters* **388**, 187-196.

Kouketsu, Y., Nishiyama, T., Ikeda, T. & Enami, M. (2014). Evaluation of residual pressure in an inclusion-host system using negative frequency shift of quartz Raman spectra. *American Mineralogist* **99**, 433-442.

Kretz, R. (1966). Interpretation of the shape of mineral grains in metamorphic rocks. *Journal of Petrology* **7**, 68-94.

Krüger, Y., Stoller, P., Rička, J. & Frenz, M. (2007). Femtosecond lasers in fluid inclusion analysis: Overcoming metastable phase states. *European Journal of Mineralogy* **19**, 693-706.

Matthews, A. & Schliestedt, M. (1984). Evolution of the blueschist and greenschist facies rocks of Sifnos, Cyclades, Greece - A stable isotope study of subduction-related metamorphism. *Contributions to Mineralogy and Petrology* **88**, 150.

McSkimin, H. J. & Andreatch, P. (1972). Elastic moduli of diamond as a function of pressure and temperature. *Journal of Applied Physics* **43**, 2944-2948.

Mezger, K., Rawnsley, C. M., Bohlen, S. R. & Hanson, G. N. (1991). U-Pb garnet, titanite, monazite , and rutile ages: Implications for the duration of high-grade metamorphism and cooling histories, Adirondack Mountains, New York. *Journal of Geology* **99**, 415-428.

Moehlman, R. S. (1935). Quartz paramorphs after tridymite and cristobalite. *American Mineralogist* **20**, 808-810.

Mosenfelder, J. L. & Bohlen, S. R. (1997). Kinetics of the coesite to quartz transformation. *Earth and Planetary Science Letters* **153**, 133-147.

Nishiyama, T. & Aikawa, K. (2011). Implication of the residual pressure recorded in quartz inclusions in garnet from high *T* metamorphic terranes. *Japan Geoscience Union Meeting Abstract*, SMP046-005.

Parkinson, C. D. & Katayama, I. (1999). Present-day ultrahigh-pressure conditions of coesite inclusion in zircon and garnet: Evidence from laser Raman microspectroscopy. *Geology* **27**, 979-982.

Pearson, D. G., Brenker, F. E., Nestola, F., McNeill, J., Nasdala, L., Hutchison, M. T., Matveev, S., Mather, K., Silversmit, G., Schmidt, S., Vekemans, B. & Vincze, L. (2014). Hydrous mantle transition zone indicated by ringwoodite included within diamond. *Nature* **507**, 221-224.

Perrillat, J. P., Daniel, I., Lardeaux, J. M. & Cardon, H. (2003). Kinetics of the coesite-quartz transition: Application to the exhumation of ultrahigh-pressure rocks. *Journal of Petrology* **44**, 773-788.

Rivera, E., Celaya, L. E. & Rincón, J. M. (1987). Microstructural characterization of an opal glass in the Na_2O-CdO-SiO_2 system. *Materials Letters* **5**, 185-188.

Roedder, E. (1967). Metastable superheated ice in liquid-water inclusions under high negative pressure. *Science* **155**, 1413-1417.

Sato, K., Santosh, M. & Tsunogae, T. (2009). A petrologic and laser Raman spectroscopic study of sapphirine–spinel–quartz–Mg-staurolite inclusions in garnet from Kumiloothu, southern India: Implications for extreme metamorphism in a collisional orogen. *Journal of Geodynamics* **47**, 107-118.

Sato, M. (1963). X-ray study of tridymite (1): On tridymite M and tridymite S. *Mineralogical Journal (Japan)* **4**, 115-130.

Schmidt, C. & Ziemann, M. A. (2000). In-situ Raman spectroscopy of quartz: A pressure sensor for hydrothermal diamond-anvil cell experiments at elevated temperatures. *American Mineralogist* **85**, 1,725-721,734.

Shen, A. H., Bassett, W. A. & Chou, I. M. (1993). The α-β transition at high temperatures and pressures in a diamond-anvil cell by laser interferometry. *American Mineralogist* **78**, 694-698.

Smith, D. C. (1984). Coesite in clinopyroxene in the Caledonides and its implications for geodynamics. *Nature* **310**, 641-644.

Spear, F. S. & Markussen, J. C. (1997). Mineral zoning, *P-T-X-M* phase relations, and metamorphic evolution of some Adirondack Granulites, New York. *Journal of Petrology* **38**, 757-783.

St-Onge, M. R. (1987). Zones poikiloblasic garnets: *P-T* paths and syn-metamorphic uplift through 30 km of structural depth, Wopmay Orogen, Canada. *Journal of Petrology* **28**, 1-21.

Van Valkenburg Jr., A. & Buie, B. F. (1945). Octahedral cristobalite with quartz paramorphs from Ellora Caves, Hyderabad State, India. *American Mineralogist* **30**, 526-535.

Vityk, M. O. & Bodnar, R. J. (1995). Do fluid inclusions in high-grade metamorphic terranes preserve peak metamorphic density during retrograde decompression? *American Mineralogist* **80**, 641-644.

Vityk, M. O., Bodnar, R. J. & Dudok, I. V. (1995). Natural and synthetic re-equilibration textures of fluid inclusions in garnet (Marmarosh Diamonds): Evidence for refilling under conditions of compressive loading. *European Journal of Mineralogy* **7**, 1071-1087.

Vityk, M. O., Bodnar, R. J. & Schmidt, C. (1994). Fluid inclusions as tectonothermobarometers: Relation between *P-T* history and re-equilibration morphology during crustal thickening. *Geology* **22**, 731-734.

Wang, Z. & Ji, S. (2001). Elasticity of six polycrystalline silicate garnets at pressure up to 3.0 GPa. *American Mineralogist* **86**, 1209-1218.

Zhang, H. & Banfield, J. F. (2014). Interatomic Coulombic interactions as the driving force for oriented attachment. *CrystEngComm* **16**, 1568-1578.

Chapter 5

Constraining Water Contents During Near-Peak Metamorphism: Metamorphic Water Sequestration and Modified Rock Mechanics

Kyle T. Ashley[1], Richard D. Law[1], Donald W. Stahr III[1]

[1]*Department of Geosciences, Virginia Polytechnic Institute and State University, Blacksburg, VA 24061, USA*

Submitted March 2014 to *Earth and Planetary Science Letters*.

Abstract

The presence of water, and its mobility and concentration in the continental crust, are important to overcoming kinetic barriers of metamorphic reactions and to deformation mechanisms that affect crustal rheology. Traditionally, sub-solidus Barrovian sequence rocks are assumed to be saturated with water. However, deviation from a saturated state can result in large deviations in the thermodynamic conditions that govern the kinetics of reactions and mechanical behavior of a rock. In this paper, we implement temperature-composition (*T-X*) thermodynamic models across a range of water concentrations to further constrain the water activity and fugacity of two samples from the western Himalay (Sutlej Valley, NW India) that exemplify mechanical effects of under-saturation. From these models, modal phase abundances are determined and compared to measured proportions. Minimized differences between theoretical and actual abundances are taken to replicate water concentrations at near-peak metamorphism (if pressure and temperature can be reasonably constrained). For these predicted water contents, system H_2O chemical potentials are calculated. Water activities are predicted when the system H_2O chemical potential is taken relative to a saturated system at pressure and temperature (i.e. a standard state). A structurally higher sample in the Sutlej Valley is found to have been under-saturated with respect to water, and as a result is buffered by a reduced water activity (~0.6). This reduced activity calls for a ~40% reduction in water fugacity. A consequence of large decreases in water fugacity is a reduction of hydrolytic weakening of quartz in the rock, resulting in a rock that would be mechanically harder and strain less over a given geologic time interval than a system that is saturated with water. In addition, the importance of water on modifying solidus temperatures, and aiding in overcoming kinetic barriers, suggests under-saturated rocks may have difficulties in achieving metamorphic equilibrium if time scales are sufficiently short.

5.1 Introduction

Fluids play a fundamental role in the lithosphere, often regulating thermodynamic and rheologic modifications (Yardley, 2009). Water weakening or softening alters the strength of rocks (Griggs, 1967) and may support the activation of slip systems in silicates (Tullis *et al.*, 1973; Blacic, 1975; Law, 2014). The presence of a fluid medium facilitates diffusion and aids minerals in overcoming kinetic reaction barriers (Yardley & Bodnar, 2014). At shallow depths in the crust, fluids concentrate precious metals and form ore deposits. Metamorphic dehydration reactions may release water in deep subduction channels, which lowers the melting temperature of the overriding mantle rocks and reduces the coefficient of friction along the channel, resulting in earthquake nucleation at intermediate depths (Dragovic *et al.*, 2012, and references therein). Despite the importance of water in altering crustal properties, retrieving the concentrations of water at peak metamorphic temperatures is challenging. Because the moderately-

deep continental crust cannot be sampled *in-situ*, we rely on rocks exhumed from these depths to infer conditions at peak metamorphism or during burial. Given the susceptibility of rocks to undergo retrograde modification of their mineral assemblages and chemistries, this near-peak information may be obscured. Rehydration is common during exhumation and is evident by chloritized phylosilicates and the re-emergence of low-*T* phases (such as epidote). In this regard, taking the bulk water content of a rock collected at Earth's surface may be misleading and overestimate concentrations at peak metamorphism.

Here we present a computational approach to determining near-peak metamorphic water contents, activities and resultant fugacity. While determining water concentrations at peak metamorphism is not a new consideration (e.g., Lamb & Valley, 1988; Tenczer *et al.*, 2006; Dragovic *et al.*, 2012), our approach is not limited to recognizing specific reactions and utilizes comprehensive, internally-consistent thermochemical databases. Our modeling considers a closed system (with respect to all components, including H_2O). This allows for assessment of the partitioning of H_2O between minerals and the availability of H_2O as a free phase for any metamorphic composition and assemblage (if the bulk rock chemistry and peak paragenesis can be reasonably constrained or identified). Measured mineral abundances are compared to modeled abundances, determined at independently constrained pressures and temperatures of interest, to refine the amount of water that was present at peak temperatures. Flow laws for quartz (and other silicates) are thought to depend on water fugacity (Kohlstedt *et al.*, 1995; Hirth *et al.*, 2001). Our results are used to calculate water fugacity of the rock at these conditions, with a discussion on the implications of water under-saturated rocks for rheologic parameters and chemical disequilibrium.

5.2 Geologic Framework and Sample Characterization

This study utilizes two rock samples (S-09-66 and S-09-93B) from the eastern part of the Sutlej Valley located in the western Himalaya (Himachal Pradesh administrative district of NW India; Fig. 5.1). Both samples represent different near-peak water conditions and emphasize the benefit of our modeling approach. The samples are part of a 10 km thick sequence of Greater Himalayan Series gneisses, bounded below and to the west by the Main Central Thrust (MCT) and above and to the east by the Sangla Detachment (SD), the local equivalent to the South Tibetan Detachment System. Migmatite-grade metamorphic conditions were reached at higher structural levels on this section, with peak metamorphism occurring at ~40–22 Ma (Caddick, 2004; Vannay *et al.*, 2004). These samples were collected and described by Law *et al.* (2013) and Stahr (2013) and we use the thermal data inferred by these authors.

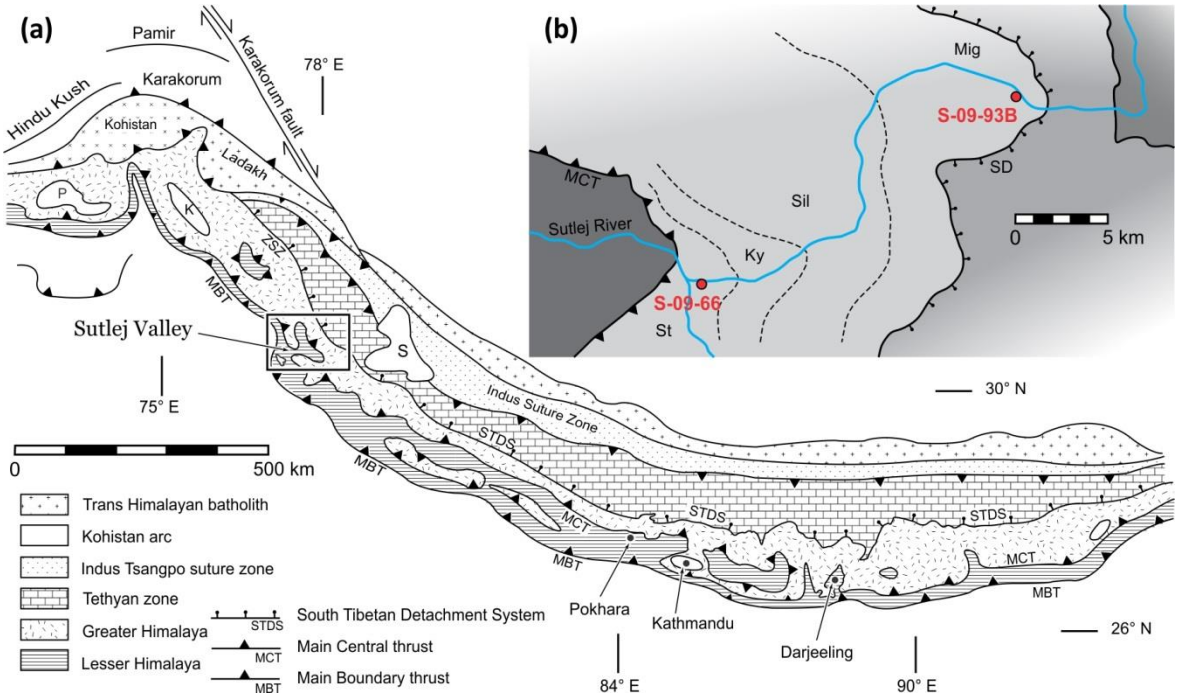

Figure 5.1. (a) Generalized geology map of the Himalaya, modified from Law *et al.* (2013) – adapted after Burchfiel *et al.* (1992), Searle *et al.* (2003), Célérier *et al.* (2009), Larson *et al.* (2010), and Long *et al.* (2011). (b) Inset map of eastern Sutlej Valley showing sample locations and metamorphic zones; modified after Vannay & Grasemann (1998), Vannay *et al.* (1999), and Stahr (2013). Structural contacts: MBT – Main Boundary thrust; MCT – Main Central thrust; STDS – South Tibetan Detachment System; SD – Sangla Detachment; ZSZ – Zandkar shear zone. Metamorphic zones: St – staurolite; Ky – kyanite; Sil – sillimanite; Mig – migmatite (partial melt).

Sample S-09-66 is a garnet schist located ~350 m above the inferred position of the MCT and contains the assemblage staurolite, garnet, biotite, white mica, quartz, ilmenite, and tourmaline (± epidote and apatite). Peak pressures of ~7.5 kbar and temperatures of ~600 °C were inferred by Law *et al.* (2013); prograde decompressional heating was determined by Stahr (2013), with ~6.5 kbar pressure at peak *T*. Sample S-09-93B is a kyanite-garnet granulite situated ~10.7 km above the inferred position of the Main Central Thrust (<400 m below the mapped position of the Sangla Detachment). The rock contains the assemblage kyanite, garnet, biotite, white mica, quartz, plagioclase, K-feldspar, ilmenite, tourmaline, and graphite (± apatite; Fig. 5.2). Peak metamorphic pressures are estimated to be ~9 kbar (Law *et al.*, 2013), with decompressional heating to peak metamorphic *T* at 700 °C (Law *et al.*, 2013; Stahr, 2013). Pressures at peak *T* must have remained above 7.8 kbar due to the transformation of kyanite to sillimanite at temperatures below this (Holdaway, 1971). No fluid inclusions are observed in either sample; rather mica inclusions are abundant and disseminated throughout the matrix quartz.

5.3 Methods and Modeling Approach

5.3.1 Analytical Methods

Representative samples of whole rock were powdered using an aluminum ball mill and fluxed with $Li_2B_4O_7$ into homogeneous glass disks. Disks were analyzed for major oxide and trace elements with the PANalytical 2404 X-ray fluorescence (XRF) vacuum spectrometer at Franklin and Marshall College (Table 5.1). Ferric iron and volatile/combustible amounts were estimated through titration and loss on ignition (LOI), respectively. Modal abundances of minerals in each sample were estimated through point counting (Stahr, 2013, unpublished PhD thesis) or through X-ray powder diffraction (XRPD). Diffraction measurements were made using a MiniFlex II Rigaku powder X-ray diffractometer at the University of Vermont. Spectra are produced using a Cu filament with a 30 kV accelerating potential and a 15 μA current. Scan speeds of $0.2°\cdot min^{-1}$ were made in 0.02° increments across a scan range of 10–100°.

Measurements were conducted on back-packed slides with powders resulting from the milling process described above. Refinement of modal proportions is made through a Rietveld method, which has been determined to be accurate within ±3 wt % at a 95% confidence level when measuring clay minerals (Hillier, 2000). Proportions are normalized to only the peak metamorphic mineral assemblage, with removal of retrograde minerals from calculated totals (e.g., chlorite and epidote).

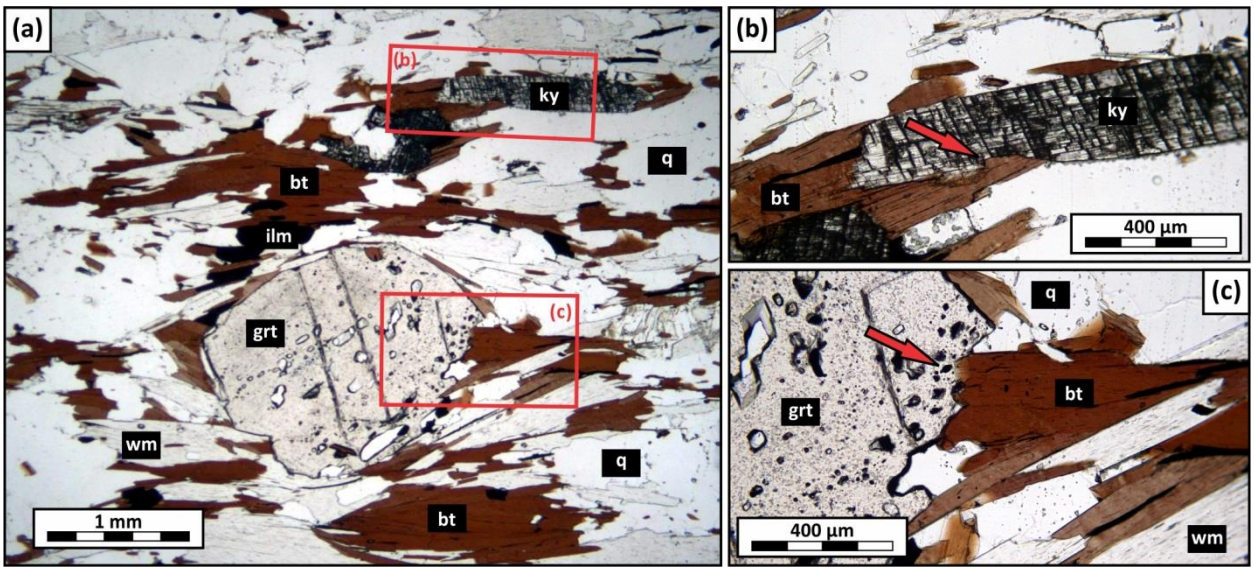

Figure 5.2. Trasmitted, plane-polarized light photomicrographs for sample S-09-93B. (a) A peak metamorphic paragenesis of garnet, biotite, kyanite, white mica, quartz, feldspar, and ilmenite is observed. Biotite intergrowth with (b) kyanite and (c) garnet (arrows) provides petrographic evidence for these phases growing synchronously during peak metamorphism. The presence of kyanite places restrictions on minimum pressures (>7.8 kbar) reached during peak heating due to the close proximity to sillimanite transformation at these high temperatures (700 °C).

Table 5.1. X-ray fluorescence bulk rock data (wt. %)

Sample	SiO_2	TiO_2	Al_2O_3	FeO_{tot}	MnO	MgO	CaO	Na_2O	K_2O	P_2O_5	LOI	Total
S-09-66	55.66	0.81	25.03	8.01	0.10	2.22	0.45	0.58	6.08	0.18	3.77	100.07
S-09-93B	72.52	0.69	14.20	5.06	0.10	1.95	0.37	0.47	4.01	0.09	2.05	100.09

FeO_{tot}: total Fe represented in the divalent state (Fe^{2+} = Fe^{3+} x 0.8996); LOI: lost on ignition

5.3.2 Thermodynamic Modeling

Gridded minimization thermodynamic calculations were made using the program Perple_X (Connolly, 2009) for the system MnO-Na_2O-CaO-K_2O-FeO-MgO-Al_2O_3-SiO_2-H_2O-TiO_2 (MnNCKFMASHT), with the 2004 update of the Holland and Powell (1998) thermochemical database. Activity models implemented in all calculations are those used by Ashley *et al.* (2015) with the addition of the silica melt

model of White *et al.* (2001), including the White *et al.* (2007) modification of the faL and foL olivine melt end-members (an enthalpy adjustment to more closely reflect total Fe and Mg in silicate melt). Quartz, kyanite, sillimanite, rutile and titanite were treated as pure phases, with a chemically unmixed H_2O fluid phase considered. The effect of a CO_2 component to the fluid phase has been ignored because only minor displacement of phase boundaries in *P-T* space occurs with this incorporation (Connolly & Cesare, 1993; Pattison, 2006). Modeling results may vary depending on the solution models implemented by the user, however, they should be consistent between computational programs (e.g., Thermocalc; Powell *et al.*, 1998) as long as solution models and thermodynamic data remain the same.

For assumed peak-metamorphic pressures, temperature-composition (*T-X*) sections were calculated. The modeled temperature range extends to ±50 °C from the estimated peak metamorphic temperature. The compositional range extends from no water present to a maximum possible concentration determined through loss on ignition measurements. This is a valid maximum consideration because maximum dehydration is expected at peak temperatures, with only rehydration likely during retrogression (i.e., near-peak water concentrations higher than the measured LOI measurements is unlikely). In addition, the measured LOI represents total combustible amounts by weight; organic material and other volatiles would add towards this total, further suggesting that the maximum near-peak H_2O amounts were below the measured LOI.

Modal proportions of phases are calculated at the estimated peak *T* for varying X_{H_2O} with Perple_X. Residuals determined by subtracting measured from computed phase proportions are used to assess the deviation of the model from true mineral abundances. Minimum residuals are interpreted to be indicative of water concentrations at near-peak metamorphism, which is used to determined water activity and fugacity.

Chemical potentials of the H_2O component (μ_{H_2O}) were calculated using Perple_X across the composition profile at the estimated peak metamorphic temperature. Water activities (a_{H_2O}) are calculated following the computational approach employed by Ashley and Law (2015), which is outlined here. The computed μ_{H_2O} is evaluated against an idealized reference state at known pressure and temperature ($\mu^\circ_{H_2O}$). This idealized standard state chemical potential was determined by saturating the bulk rock chemistry with water until a free fluid phase was present in all modeled assemblage fields across the temperature range of interest. The water activity is calculated using the expression

$$a_{H_2O} = exp\left[\frac{\mu_{H_2O} - \mu^\circ_{H_2O}}{RT}\right] \quad \text{(eq. 5.1)}$$

where R is the gas constant (8.31446 J K^{-1} mol^{-1}) and T is temperature (K). If the rock is saturated with respect to water, to the extent where a free fluid phase is produced, then $\mu^\circ_{H_2O} = \mu_{H_2O}$ and $a_{H_2O} = 1.0$. If water is restricted to crystallographic sites in minerals, $a_{H_2O} < 1.0$ (decreasing to zero if the rock is completely dry).

Similarly, an effective water fugacity may be calculated when evaluating μ_{H_2O} against $\mu^\circ_{H_2O}$, in terms of the H_2O fugacity in a water-saturated system ($f^\circ_{H_2O}$) through the expression

$$f_{H_2O} = f^\circ_{H_2O} \cdot exp\left[\frac{\mu_{H_2O} - \mu^\circ_{H_2O}}{RT}\right]. \quad \text{(eq. 5.2)}$$

This expression can be simplified to the effective fugacity given as the product of $f^\circ_{H_2O}$ and the calculated H_2O activity. Standard state fugacities are calculated using the analytical solution by Sterner and Pitzer (1994):

$$lnf_{H_2O} = \left[ln\rho + \frac{A^{res}}{RT} + \frac{P}{\rho RT}\right] + ln(RT) - 1 \quad \text{(eq. 5.3)}$$

where A^{res} is the residual (non-ideal) Helmholtz energy and ρ is the molar density (calculated using the equation of state of water by Pitzer & Sterner, 1994).

5.4 Results

5.4.1 Modeled Phase Stability and Modal Proportions

Temperature-composition modeling of sample S-09-66 shows the destabilization of white mica at low water conditions ($X_{H_2O} < 0.2$; Fig. 5.3a). Increasing water content stabilizes a single paragenesis for the majority of the modeled *T-X* space, including K-feldspar, plagioclase, white mica, ilmenite, garnet, biotite, kyanite and quartz. Over a short compositional window ($X_{H_2O} = 0.75 - 0.80$), staurolite begins to stabilize while kyanite and the feldspars are consumed; white mica is produced at the expense of K-feldspar and kyanite through the reaction 2 kyanite + 2 K-feldspar + H_2O = 2 muscovite + 2 quartz (Fig. 5.3c). White mica continues to be produced until the availability of kyanite and feldspar is exhausted. At higher water contents, a saturation limit is reached where no more white mica can accommodate water uptake and a free fluid phase is generated (at higher temperatures, with chlorite stability at T < 590 °C). The abundance of water and Al_2O_3 promotes staurolite stability, with Fe obtained from minor biotite, garnet and ilmenite resorption (Fig. 5.3c). At higher temperatures (>645 °C), the transformation from kyanite to sillimanite occurs. In sample S-09-66, the presence of staurolite and the absence of kyanite and chlorite restricts the peak metamorphic paragenesis to temperatures >590 °C and $X_{H_2O} > 0.76$ (2.87 wt. % H_2O); thus, application of the model to the observed phases suggests that the system was saturated with respect to water (a free fluid phase is modeled).

Similar stability fields and reactions are observed for the modeled *T-X* section for S-09-93B. However some minor deviations should be noted, including: (i) rutile is stabilized at lower water contents (due to the high pressure); (ii) kyanite reacts to sillimanite at T > 715 °C; (iii) stuarolite is not

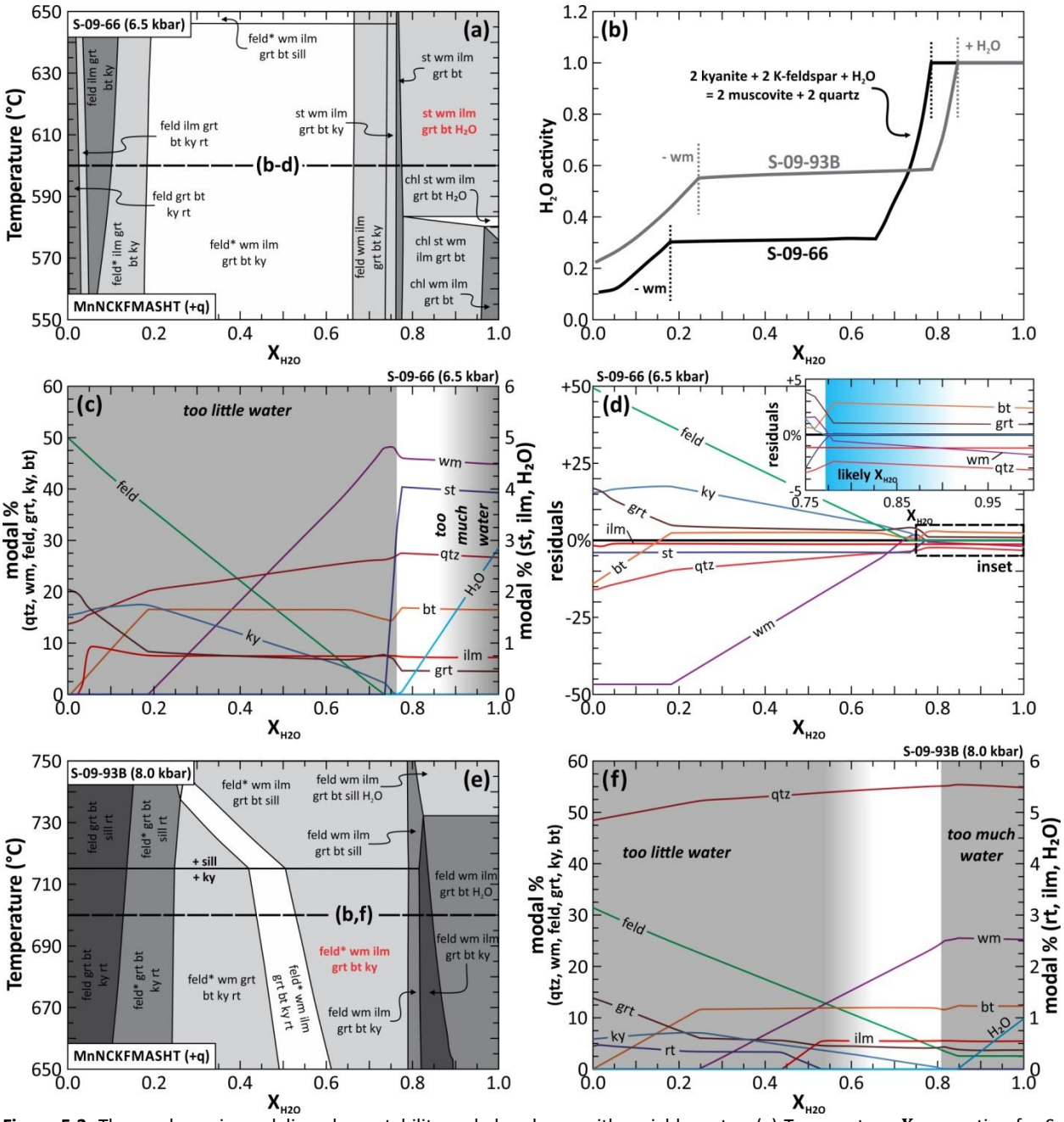

Figure 5.3. Thermodynamic modeling phase stability and abundance with variable water. (a) Temperature-X_{H_2O} section for S-09-66 in the system MnNCKFMASHT (6.5 kbar). The field labeled in red contains the assemblage observed in the rock. Isothermal profile used for panels (b)-(d) is shown. (b) Water activity profiles are determined for peak metamorphic temperatures for samples S-09-66 and -93B. If the rocks are water under-saturated (where H_2O is bound in the micas), a_{H_2O} is <1.0. (c) Mode percent of phases with increasing water content and (d) calculated residuals (predicted minus measured abundances) are used in further refining peak metamorphic water content. For S-09-66, X_{H_2O}= 0.78–0.9 (2.94–3.39 wt. % H_2O). (e) *T-X* stability section for S-09-93B with (f) calculated mode percent of phases for 700 °C and increasing water content. X_{H_2O}= 0.6–0.8 (1.23–1.66 wt. % H_2O) for this sample. Asterisks on feldspars denote fields where two feldspars are stable (K-feldspar and plagioclase).

stable at these higher temperatures and pressures; and (iv) a free H_2O phase is predicted at $X_{H_2O} > 0.85$ (~1.76 wt. % H_2O; Fig. 5.3e). The same muscovite producing reaction described above is also observed (Fig. 5.3f). Unlike sample S-09-66, this rock contains feldspar (plagioclase and K-feldspar) and kyanite, which restricts the maximum near-peak water contents to $X_{H_2O} < 0.79$ (only K-feldspar is stable at water concentrations greater than this). Peak temperature and water content can be further constrained by the absence of rutile in the rock ($X_{H_2O} \gtrsim 0.55$; Fig. 5.3f). The stability of kyanite and not sillimanite is useful for this sample because the estimated peak metamorphic temperature (700 °C) is close to the Al_2SiO_5 univariant curve, requiring pressures greater than ~7.8 kbar for kyanite to be stable (further restricting minimum pressures at peak temperature). With these considerations, the peak metamorphic water content of sample S-09-93B must have been 1.14–1.64 wt. % H_2O – about half that estimated for sample S-09-66.

While the stable metamorphic paragenesis of each sample greatly restricts the near-peak water concentrations, further refinements can be made by considering the modal proportion of phases that are modeled (Fig. 5.3c,e), relative to the proportions observed in the rock. In Figure 5.3d, we show the residuals that result from differences between modeled and observed mineral proportions in sample S-09-66 (see Fig. 5.4 for measured mineral abundances). At low water concentrations, the modal proportion of undifferentiated feldspar (the sum of K-feldspar and plagioclase) is greatly overestimated in the model (up to +50%). At higher water contents, the residuals are very small (within ±2.5%; Fig. 5.3d inset), suggesting $X_{H_2O} > 0.775$. After water forms a free fluid phase, no appreciable difference in phase proportions results (the addition of more water just adds to the total H_2O abundance in the matrix). For sample S-09-93B, this approach indicates that significant changes in the modal % of muscovite, feldspar and kyanite occur over a relatively small X_{H_2O} window; feldspar decreases from 10.7 to 4.0 modal % and muscovite increases from 15.3 to 24.0 modal % along the X_{H_2O} increase from 0.6 to 0.8 (Fig. 5.3f). The small proportions of feldspar (plagioclase and K-feldspar) and kyanite (~6 and ~2

modal % respectively), and high amounts of white mica (>20 modal %) suggest that near peak water concentrations reached $X_{H_2O} = 0.70 - 0.79$ (1.45–1.64 wt. % H_2O; Fig. 5.3f).

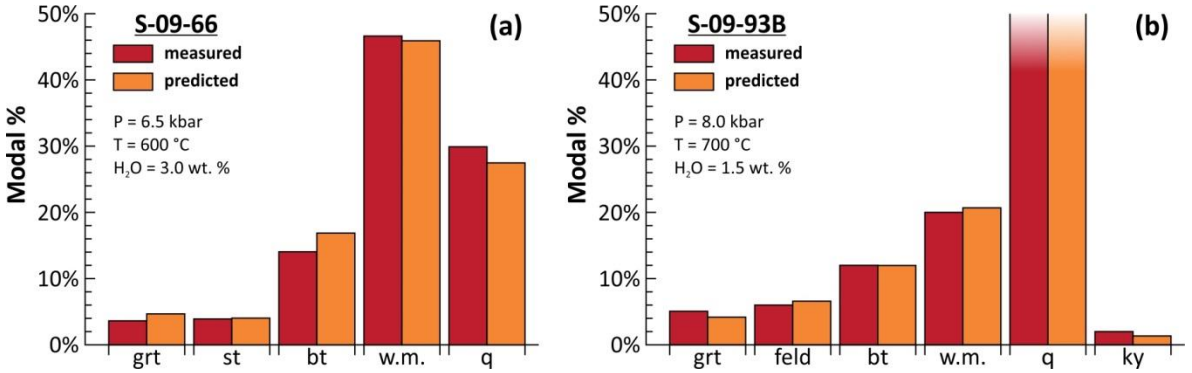

Figure 5.4. Measured and predicted modal abundance of phases for samples (a) S-09-66 and (b) S-09-93B for the given temperature, pressure and water concentration at peak metamorphism (water concentration is constrained in this study). Accessory phases (e.g., ilmenite) are not shown due to their low abundance in the rocks. Feldspar is undifferentiated, and includes the sum of plagioclase and K-feldspar.

5.4.2 Calculated Water Activities

From the modeled *T-X* sections in Fig. 5.3, H_2O chemical potentials were calculated along isothermal profiles with increasing water contents. For these profiles, peak temperature estimates reported by Law *et al.* (2013) were used. Chemical potentials at $X_{H_2O} = 1.0$ for both samples were considered as the standard state value because the assemblages modeled at these concentrations all contained water as a free fluid phase (suggesting the system is saturated with respect to H_2O). Both samples resulted in similar $a_{H_2O} - X_{H_2O}$ trends (Fig. 5.3b). For assemblages that do not exhibit white mica stability, biotite is the dominant phase for water sequestration in crystallographic sites, resulting in very low activity values (a_{H_2O} decreasing towards zero as the bulk rock tends towards completely dry). Once muscovite is stabilized, water activities reach a plateau (at 0.3 and ~0.6 for samples S-09-66 and S-09-93B, respectively); at these conditions, white mica provides a stable buffer regardless of the amount of water available at a fixed pressure and temperature. Once plagioclase is consumed, and K-feldspar and kyanite approach total consumption, a large increase in water activity occurs over a small range of water concentrations (Fig. 5.3b). Once saturation is reached, peak a_{H_2O} of 1.0 are sustained. For the

mole fractions of water constrained for samples S-09-66 and S-09-93B, a_{H_2O} is calculated to have been 1.0 and 0.58, respectively. Sample S-09-93B illustrates that even a small amount of under-saturation may lead to significantly reduced water activities. These results are consistent with petrographic observations that quartz in these samples does not contain any observed fluid inclusions; rather, white mica inclusions are widely disseminated in matrix quartz. This is a function of water being largely sequestered in crystallographic sites of white mica, rather than its presence as an extensive free fluid phase in the matrix. Although a free water phase is predicted for S-09-66, the amount of water expected is small (<<1 wt. %), and the high abundance of white mica leads to its incorporation in muscovite as opposed to matrix fluids.

5.5 Discussion

5.5.1 Water Constraints from Minimized Residuals

In the above sections, we showed how considering modal proportions of phases in the rock can be used to further refine estimates on near-peak water contents. This approach wasn't very informative for sample S-09-66 because the peak paragenesis suggests the rock was saturated with respect to water (therefore the H_2O activity was 1.0) and further refinements with these large water contents would not change the buffering of water in the system. This approach proved more useful for sample S-09-93B, nearly halving the mole fraction range in water that was constrained when assuming the stable assemblage alone. However, with kyanite and the two feldspars stabilized at lower water concentrations (for which water is constrained to crystallographic sites in the micas), there is a large range of water concentrations that buffers a constant water activity (Fig. 5.3b). In this case, further refining the near-peak water doesn't greatly impact the effective concentration of H_2O or the buffering of water by white mica in the rock. Therefore the amount of insight gained from making these additional measurements and calculations will vary greatly between rocks of different composition and pressures and

temperatures reached. High-temperature/low-water rocks with few metamorphic minerals (or a variety of minerals that contain some speciation of water in crystallographic sites) are expected to produce optimal results through this refinement.

5.5.2 Reduced Water Fugacity

From the water contents constrained above, equation 5.2 is implemented to determine effective water fugacities. For sample S-09-66, where $a_{H_2O} = 1.0$, f_{H_2O} is equal to the standard state (466 MPa at 600 °C and 6.5 kbar). However, the reduced water activity for sample S-09-93B results in a 42% decrease in f_{H_2O} from the reference state – down from 877 MPa to 509 MPa (Fig. 5.5).

In some instances across the modeled *T-X* sections, a relatively small decrease in water content results in a large decrease in water fugacity. For sample S-09-93B, the difference between X_{H_2O} of 0.9 and 0.8 (0.21 wt. %) results in a f_{H_2O} reduction of 322.8 MPa (at 700 °C) – a 37% decrease. However, for the stability field constrained for this rock, an identical decrease in water content at the same temperature results in only a 2 MPa reduction in f_{H_2O} (-0.23%). This is due to the large decrease in a_{H_2O} when the system becomes under-saturated with respect to water and white mica buffers this component. Therefore, depending on the conditions during metamorphism, some rocks may be susceptible to a large water fugacity decrease with minor dehydration, while others may sustain a "fixed" fugacity for a large range in water concentrations. For the samples presented in this study, the amount of error introduced from uncertainties in water concentrations is vanishingly small. Rather, temperature uncertainties may introduce the majority of error in these calculations. This is less important for sample S-09-66, where the system is saturated with respect to water; however a departure from saturation occurs if actual temperatures were <580 °C and a minor decrease in fugacity is expected (albeit small, as chlorite stability buffers a high a_{H_2O} for the system). A temperature

uncertainty of ±25 °C for S-09-93B would have a more significant impact on calculated f_{H_2O}, with a 52.4% reduction calculated for minimum temperatures and a 30.7% decrease expected at higher temperatures. However, chlorite is not observed in sample S-09-66, and sample S-09-93B is restricted to peak temperatures of 715 °C due to the transformation to sillimanite above this temperature; thus, the range in potential water fugacities must be less than that assumed for temperature uncertainties of ±25 °C. Regardless, the important finding is that sample S-09-93B is under-saturated with respect to water at near-peak metamorphism, and a consequence of these dry conditions is a rock with a greatly reduced water fugacity relative to an assumed standard state.

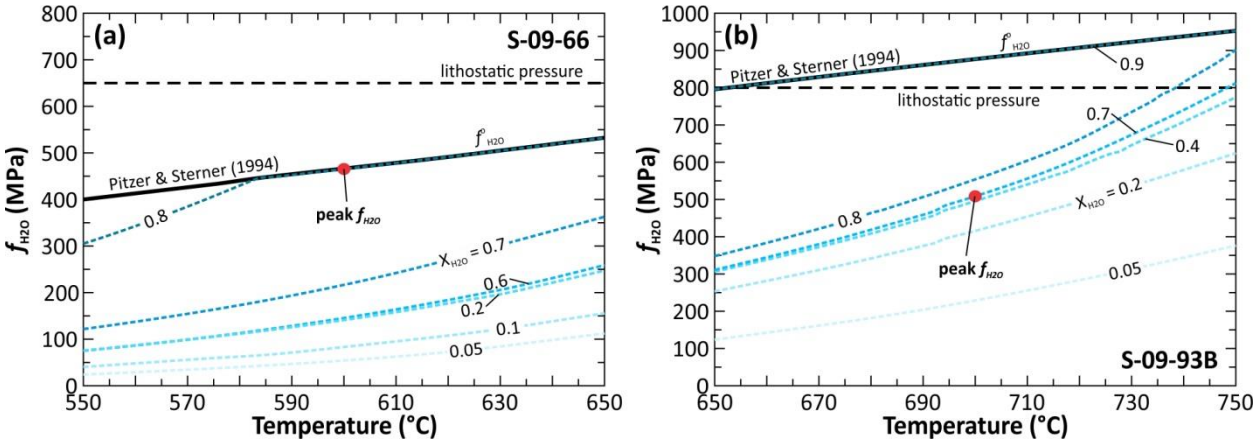

Figure 5.5. Calculated water fugacity for different water concentrations for samples (a) S-09-66 and (b) S-09-93B. In some instances, small decreases in water content for the rock can under-saturate the sample with respect to water and significantly decrease the calculated water fugacity. For example, a ~50% decrease in $\boldsymbol{f_{H_2O}}$ is expected with a reduction in $\boldsymbol{X_{H_2O}}$ from 0.8 to 0.7 for sample S-09-66. In other instances, only relatively minor changes are observed in calculated fugacity with large water decreases (e.g., 0.6 to 0.2 for sample S-09-66), resulting from white mica stabilizing the water activity for a majority of water under-saturated conditions.

5.5.3 Impact of Low Water on Achieving Metamorphic Equilibrium

A well-known consequence of saturating a rock with water is the change in the projected solidus temperature. Webb *et al.* (2015) discuss the importance of subsolidus water loss during rock compaction on the melting temperature of felsic rocks. The solidus temperature for their sample VM94G decreases over 200 °C with increasing water content, until a critical point is reached where the rock is saturated, and an independent H_2O component in projected for the modeled assemblages (see

their Fig. 2c). However, even solid-state metamorphic equilibrium is impeded by low water conditions. In the overstepping of a metamorphic reaction, kinetic barriers must be overcome. Temperature is an important parameter, with increases driving the metamorphic reaction toward equilibrium. However, the presence of a fluid medium also facilitates diffusion and reaction kinetics (Jamtveit & Austrheim, 2010; Yardley & Bodnar, 2014). For metamorphic petrologic studies investigating equilibrium field assemblages for thermobarometry constraints, it is typically assumed that metamorphic reaction rates are sufficiently fast to achieve equilibrium. In the classical model of Barrovian metamorphism, where burial and conductive heating occurs over millions of years with fluids present, this assumption is probably valid. Under-saturation in sub-solidus rocks would, however, slow kinetic progress and diffusion required for metamorphic reactions to achieve equilibrium. Recent studies of Barrovian terranes suggest that metamorphic heating occurs under much shorter time scales than previously considered. In central-eastern Vermont, for example, Spear *et al.* (2012) and Spear (2014) conclude near-peak heating occurred in a few hundred thousand years, two orders of magnitude different from rates assumed in continental collision models of England and Thompson (1984), and well below the achievable resolution of isotopic dating techniques. Therefore, it is worth considering whether diffusion and reaction kinetics are sufficient to allow peak metamorphic equilibrium to be achieved. In the absence of fluids, rapid changes in temperature may lead to a "moving target" equilibrium, and metamorphic systems may need to be analyzed as disequilibrium systems governed by kinetics.

5.5.4 Rheologic Considerations

The computational approach we present here provides a way to determine near-peak metamorphic water content and values of f_{H_2O} for fluid water-absent and fluid-present conditions. In some instances, the bulk rock may be under-saturated with respect to water – either because it is

inherently dry or through the sequestration of water in hydrous phylosilicates. In instances where peak metamorphism is inferred to be synchronous with deformation (as is the case in eastern Sutlej; Law *et al.*, 2004), effects of thermodynamic conditions on flow laws can be made. Quartz flow laws are widely applied to estimate average strain rates in quartz mylonites and to determine the amount of strain acquired for a given deformation event (if duration of deformation can be reasonably constrained). Here we consider the effect of a reduced H_2O fugacity on the calculated strain rate with the parameterization by Hirth *et al.* (2001). Strain rates ($\dot{\varepsilon}$) are calculated through the expression $\dot{\varepsilon}\ (s^{-1}) = A f_{H_2O}^{m} \sigma^{n} exp(-Q/RT)$, where *A* is the material constant (log(*A*) = $10^{-11.2}$ $MPa^{-n}{\cdot}s^{-1}$), m and n are experimentally and naturally derived best fit parameters (m = 1 and n = 4), σ is differential stress (MPa), and Q is activation energy (135 $KJ{\cdot}mol^{-1}$). A 25 °$C{\cdot}km^{-1}$ geotherm is considered, with lithostatic pressure calculated assuming an average continental crust density of ~2.7 $g{\cdot}cm^{-3}$ (~26.5 $MPa{\cdot}km^{-1}$). Pressures and temperatures determined through a depth profile are used to calculate water fugacity (using eq. 5.3). Figure 5.6a illustrates the decrease in calculated strain rate that results from a reduction in water fugacity from a standard state by 50% and 75%. As previously shown (Fig. 5.5a), a sharp decrease in f_{H_2O} (~50%) may occur with a minor decrease in bulk water content (with a X_{H_2O} decrease from 0.8 to 0.7), resulting from the instability of muscovite in preference for kyanite and K-feldspar stability and the sequestration of water in phylosilicate crystallographic sites. A reduction in strain rate reflects an increase in effective viscosity of the rock (or deformation rate at a fixed differential stress) under dry conditions. For the applied differential stresses considered (150 and 15 MPa), the strain rates predicted for lower f_{H_2O} are about half an order of magnitude lower. For a rock subjected to differential stresses of 15 MPa at 600 °C, the calculated strain rate would shift from $1x10^{-12}$ to $5x10^{-13}$ s^{-1} when assuming water-saturated conditions versus a fugacity reduced by 50%. Similar results are obtained for higher differential stresses (~100 MPa) and lower temperatures (400 °C), with a decrease in strain rate from $1x10^{-11}$ to $5x10^{-12}$ s^{-1}. Clearly, the effects of differential stress and temperature on strain rate are

large, and these parameters must be determined to evaluate differences in strain rate due to water saturated and under-saturated conditions. Figure 5.6b shows that these effects may be most significant at lower temperatures (and higher differential stresses), where the lines of constant inferred average strain rate are spaced further apart with the same variations in standard state water fugacity.

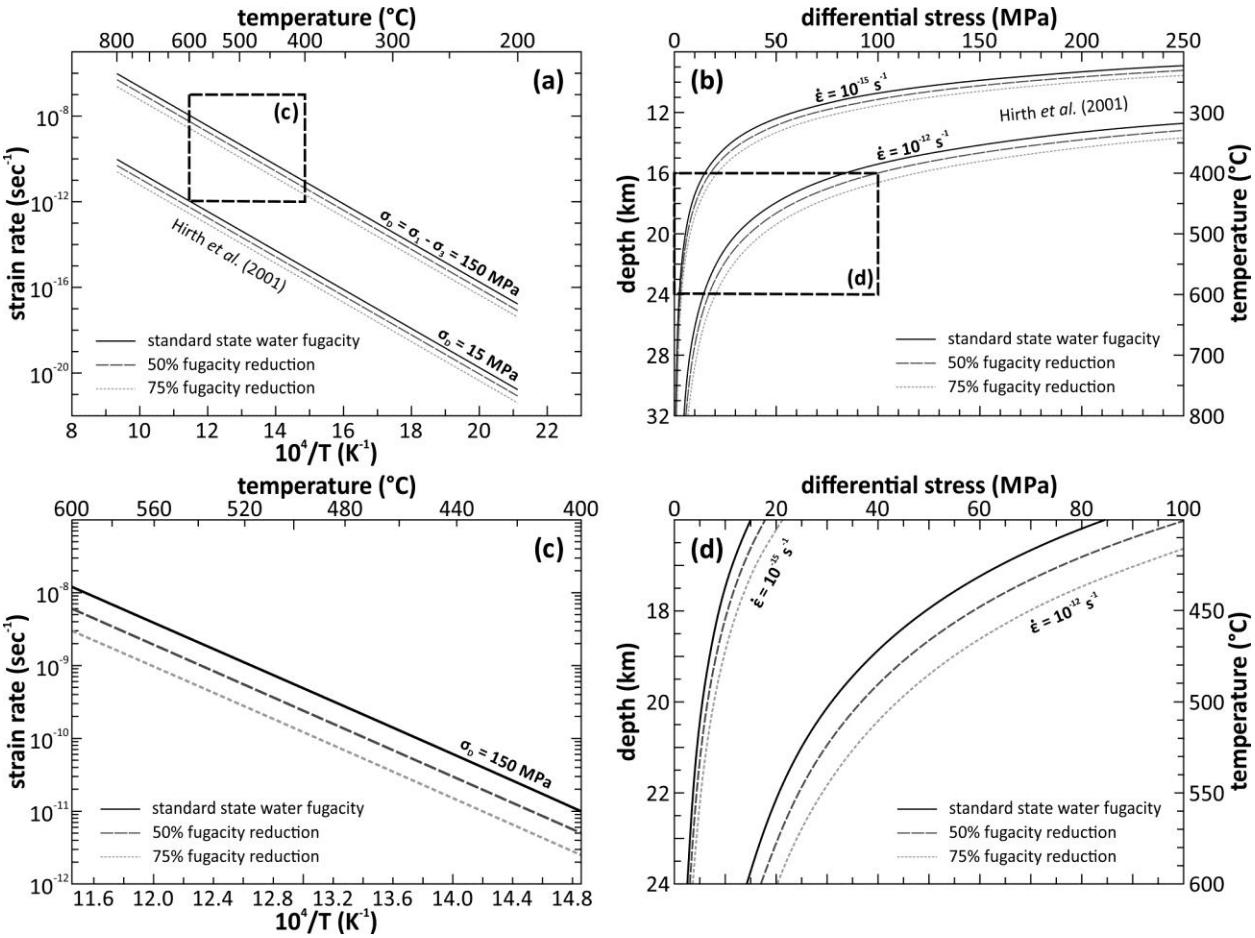

Figure 5.6. Calculated effects of water fugacity reduction on strain rate calculation using the flow law of Hirth *et al.* (2001). (a) For a given differential stress, similar strain rate perturbations are expected for reduced f_{H_2O}; a 75% reduction results in an order of magnitude decrease in strain rate for a differential stress of 150 MPa. (b) These effects are expected to be more significant at low temperatures and high differential stresses. (c) and (d) show detailed projections from (a) and (b), respectively, for the 400–600 °C temperature window.

Water saturation is ubiquitously considered in the literature when applying quartz flow laws to sub-solidus rocks. With no consideration for the effects of water under-saturation on the calculated fugacity (either because the rocks are inherently dry or through the sequestration of water in crystallographic sites), an order of magnitude or greater of error may emerge. The model provided here

can be used to evaluate f_{H_2O} under widely varying conditions and can eliminate this potential source of error.

5.5.5 Limitations and Assumptions

Constraining peak water contents of rocks that are more siliceous or have bulk compositions that give rise to a small number of metamorphic minerals can be difficult. This is largely due to the lack of phases whose measured and calculated mineral proportions can be compared and the large resultant modeled metamorphic stability fields. Therefore this technique is optimal for rocks such as the aluminous granulites in eastern Sutlej (where six or more phases aid in these refinements), as opposed to constraints that can be applied to siliceous psammitic rocks. This limits direct application to quartzites or other single-phase rocks, for which structural, crystal fabric, and paleostress data can be obtained without complicating effects of secondary phases on grain boundary textures. While direct comparisons cannot be made between siliceous and aluminous samples, trends in water activity (and therefore water fugacity) across structural transects may provide insight into water distribution across a particular structural interval. This may have important structural/tectonic implications if a particular section of a transect is determined to be saturated or under-saturated relative to water, when combined with inferences that can be drawn for surrounding rocks. If little water is present and a white mica is stable at peak metamorphism, then water may be sequestered into a crystalline structure rather than being available as an intergranular medium in the matrix. Alternatively, if H_2O is present as a supercritical fluid at high temperatures, its mobility through rocks may be that of a gas while it dissolves minerals like a liquid. Above this critical point, a free fluid phase would easily infiltrate surrounding rocks, therefore nearby rocks would share fluid characteristics of the rocks being studied. This could have substantial implications for the strength of the rock and the ability to chemically re-equilibrate (under short

geologic time scales). In addition, interpretations of the trend of water activity across a structural transect may provide insight into whether the bounding faults serve as a conduit to aid in fluid mobility and transport.

Another assumption made when using pseudosection modeling to constrain peak water contents is the sophistication of the implemented solution models in replicating the water budget in nature. Some models consider an idealized solution, where a fixed amount of water is accommodated in the phase. Other phases that incorporate "trace" amounts of water in nature (e.g., quartz) are not accounted for in the models. Even a few hundred ppm H_2O in quartz would account for a non-negligible amount of water within the rock if quartz is abundant. If phases are accommodating more water than the solution models allow, further under-saturation is expected.

5.6 Additional Comments and Considerations

Care must be taken when estimating peak-metamorphic water content through the method described above and applying these H_2O activities to project new stability fields across the entirety of *P-T* space for thermobarometry applications. Water may not remain in the system, or may be reintroduced to the system, throughout the *P-T-t* evolution of a rock, making it a dynamic parameter rather than a static value. Authors who wish to determine *P-T* evolution through a fixed (albeit, reduced) H_2O activity approach are likely to misrepresent some portion of the modeled pseudosection.

More insight may be gained by utilizing the retrograde overprinting in metamorphic rocks to assess fluid flux within the rock. Chloritization of biotite is indicative of rehydration of the rock at cooler temperatures. With this introduction of new fluid during cooling, the rock will tend towards a water-saturated state; chemistries of chlorite (and epidote) may then be applied with water-saturated pseudosections to infer *P-T* conditions (and therefore depths) for the time of infiltration. If faults

associated with exhumation and retrograde reactions serve as fluid conduits and introduce fluid back into the rock, then *P-T* data gained by analysis of any late-stage rehydration may help to constrain the depths of faulting.

Acknowledgements

We thank Stan Mertzman and John Hughes for help with sample preparation and analytical work. This work is supported by the National Science Foundation under grant Nos. EAR-1220345 (awarded to R.D. Law) and EAR-1220138 (awarded to A. K. Kronenberg).

References

Ashley, K. T. & Law, R. D. (2015). Modeling prograde TiO_2 activity and its significance for Ti-in-quartz thermobarometry of pelitic metamorphic rocks. *Contributions to Mineralogy and Petrology* **169**, 1-7.

Ashley, K. T., Thigpen, J. R. & Law, R. D. (2015). Prograde evolution of the Scottish Caledonides and tectonic implications. *Lithos*, http://dx.doi.org/10.10116/j.lithos.12015.10103.10011.

Blacic, J. D. (1975). Plastic deformation mechanisms in quartz: The effect of water. *Tectonophysics* **27**, 271-294.

Burchfiel, B. C., Zhiliang, C., Hodges, K. V., Yuping, L., Royden, L., Changrong, D. & Jiene, X. (1992). The South Tibetan Detachment System, Himalayan Orogen: Extension contemporaneous with and parallel to shortening in a collisional mountain belt. *Geological Society of America Special Paper* **269**, 41.

Caddick, M. J. (2004). Tectono-Metamorphic Evolution of the Central and Western Himalaya. Cambridge University, UK, PhD thesis.

Célérier, J., Harrison, T. M., Webb, A. A. G. & Yin, A. (2009). The Kumaun and Garwhal Lesser Himalaya, India: Part 1. Structure and stratigraphy. *Geological Society of America Bulletin* **121**, 1262-1280.

Connolly, J. A. D. (2009). The geodynamic equation of state: What and how. *Geochemistry Geophysics Geosystems* **10**, 1-19.

Connolly, J. A. D. & Cesare, B. (1993). C-O-H-S fluid composition and oxygen fugacity in graphitic metapelites. *Journal of Metamorphic Geology* **11**, 379-388.

Dragovic, B., Samanta, L. M., Baxter, E. F. & Selverstone, J. (2012). Using garnet to constrain the duration and rate of water-releasing metamorphic reactions during subduction: An example from Sifnos, Greece. *Chemical Geology* **314-317**, 9-22.

England, P. & Thompson, A. B. (1984). Pressure-temperature-time paths of regional metamorphism, Part I: Heat transfer during the evolution of regions of thickened continental crust. *Journal of Petrology* **25**, 894-928.

Griggs, D. T. (1967). Hydrolytic weakening of quartz and other silicates. *Geophysical Journal International* **14**, 19-31.

Hillier, S. (2000). Accurate quantitative analysis of clay and other minerals in sandstones by XRD: Comparison of a Rietveld and a reference intensity ratio (RIR) method and the importance of sample preparation. *Clay Minerals* **35**, 291-302.

Hirth, G., Teyssier, C. & Dunlap, W. J. (2001). An evaluation of quartzite flow laws based on comparisons between experimentally and naturally deformed rocks. *International Journal of Earth Science* **90**, 77-87.

Holdaway, M. J. (1971). Stability of andalusite and the aluminum silicate phase diagram. *American Journal of Science* **271**, 97-131.

Holland, T. J. B. & Powell, R. (1998). An internally consistent thermodynamic data set for phases of petrological interest. *Journal of Metamorphic Geology* **16**, 309-343.

Jamtveit, B. & Austrheim, H. (2010). Metamorphism: The role of fluids. *Elements* **6**, 153-158.

Kohlstedt, D. L., Evans, B. & Mackwell, S. J. (1995). Strength of the lithosphere: Constraints imposed by laboratory experiments. *Journal of Geophysical Research* **100**, 17,587-517,602.

Lamb, W. M. & Valley, J. W. (1988). Granulite facies amphibole and biotite equilibria, and calculated peak-metamorphic water activities. *Contributions to Mineralogy and Petrology* **100**, 349-360.

Larson, K. P., Godin, L. & Price, R. A. (2010). Relationship between displacement and distortion in orogens: Linking the Himalayan foreland and hinterland in Central Nepal. *Geological Society of America Bulletin* **122**, 1116-1134.

Law, R. D. (2014). Deformation thermometry based on quartz c-axis fabrics and recrystallization microstructures: A review. *Journal of Structural Geology* **66**, 129-161.

Law, R. D., Searle, M. P. & Simpson, R. L. (2004). Strain, deformation temperatures and vorticity of flow at the top of the Greater Himalayan Slab, Everest Massif, Tibet. *Journal of the GEological Society, London* **161**, 305-320.

Law, R. D., Stahr, D., Francsis, M. K., Ashley, K. T., Grasemann, B. & Ahmad, T. (2013). Deformation temperatures and flow vorticities near the base of the Greater Himalayan Series, Sutlej Valley and Shimla Klippe, NW India. *Journal of Structural Geology* **54**, 21-53.

Long, S., McQuarrie, N., Tobgay, T. & Hawthorne, J. (2011). Quantifying internal strain and deformation temperature in the eastern Himalaya, Bhutan: Implications for the evolution of strain in thrust sheets. *Journal of Structural Geology* **33**, 579-608.

Pattison, D. R. M. (2006). The fate of graphite in prograde metamorphism of pelites: An example from the Ballachulish aureole, Scotland. *Lithos* **88**, 85-99.

Pitzer, K. S. & Sterner, S. M. (1994). Equations of state valid continuously from zero to extreme pressures for H_2O and CO_2. *Journal of Chemical Physics* **101**, 3111-3116.

Powell, R., Holland, T. J. B. & Worley, B. A. (1998). Calculating phase diagrams involving solid solutions via non-linear equations, with examples using THERMOCALC. *Journal of Metamorphic Geology* **16**, 577-588.

Searle, M. P., Simpson, R. L., Law, R. D., Parrish, R. R. & Waters, D. J. (2003). The structural geometry, metamorphic and magmatic evolution of the Everest massif, High Himalaya of Nepal - South Tibet. *Journal of the Geological Society of London* **160**, 345-366.

Spear, F. S. (2014). The duration of near-peak metamorphism from diffusion modelling of garnet zoning. *Journal of Metamorphic Geology* **32**, 903-914.

Spear, F. S., Ashley, K. T., Webb, L. E. & Thomas, J. B. (2012). Ti diffusion in quartz inclusions: Implications for metamorphic time scales. *Contributions to Mineralogy and Petrology* **164**, 977-986.

Stahr, D. W. (2013). Kinematic evolution, metamorphism, and exhumation of the Greater Himalayan Series, Sutlej River and Zanskar regions of NW India. *Department of Geosciences*: Virginia Tech, 125.

Sterner, S. M. & Pitzer, K. S. (1994). An equation of state for carbon dioxide valid from zero to extreme pressures. *Contributions to Mineralogy and Petrology* **117**, 362-374.

Tenczer, V., Powell, R. & Stüwe, K. (2006). Evolution of H_2O content in a polymetamorphic terrane: The Plattengneiss Shear Zone (Koralpe, Austria). *Journal of Metamorphic Geology* **24**, 281-295.

Tullis, J., Christie, J. M. & Griggs, D. T. (1973). Microstructures and preferred orientations in experimentally deformed quartzites. *Geological Society of America Bulletin* **84**, 297-314.

Vannay, J.-C. & Grasemann, B. (1998). Inverted metamorphism in the High Himalay of Himachal Pradesh NW India: Phase equilibria versus thermobarometry. *Schweizerische Mineralogische und Petrographische Mitteihurgen* **78**, 107-132.

Vannay, J.-C., Grasemann, B., Rahn, M., Frank, W., Carter, A., Baudraz, V. & Cosca, M. (2004). Miocene to Holocene exhumation of metamorphic crustal wedges in the NW Himalaya: Evidence for tectonic extrusion coupled to fluvial erosion. *Tectonics* **23**, TC1014.

Vannay, J.-C., Sharp, Z. D. & Grasemann, B. (1999). Himalayan inverted metamorphism constrained by oxygen isotope thermometry. *Contributions to Mineralogy and Petrology* **137**, 90-101.

Webb, G., Powell, R. & McLaren, S. (2015). Phase equilibria constraints on the melt fertility of crustal rocks: The effect of subsolidus water loss. *Journal of Metamorphic Geology* **33**, 147-165.

White, R. W., Powell, R. & Holland, T. J. B. (2001). Calculation of partial melting equilibria in the system Na_2O-CaO-K_2O-FeO-MgO-Al_2O_3-SiO_2-H_2O (NCKFMASH). *Journal of Metamorphic Geology* **19**, 139-153.

White, R. W., Powell, R. & Holland, T. J. B. (2007). Progress relating to calculation of partial melting equilibria for metapelites. *Journal of Metamorphic Geology* **25**, 511-527.

Yardley, B. W. (2009). The role of water in the evolution of the continental crust. *Journal of the Geological Society* **166**, 585-600.

Yardley, B. W. & Bodnar, R. J. (2014). Fluids in the Continental Crust. *Geochemical Perspectives* **3**, 127.

Chapter 6

Ti Resetting in Quartz during Dynamic Recrystallization: Mechanisms and Significance

Kyle T. Ashley[1], William D. Carlson[2], Richard D. Law[1], Robert J. Tracy[1]

[1]*Department of Geosciences, Virginia Polytechnic Institute and State University, Blacksburg, VA 24061, USA*

[2]*Department of Geological Sciences, University of Texas at Austin, Austin, TX 78712, USA*

Published October 2014 in *American Mineralogist*.

Abstract

The ubiquity of quartz in continental crust, and the involvement of SiO_2 in multiple metamorphic processes such as reactions, fluid flux, and solution-transfer processes, makes quartz an obvious choice for reconstructing prograde metamorphic conditions in a variety of rock types. Recent studies have shown the usefulness of analyzing Ti distribution in quartz to constrain pressure - temperature - (relative) time - deformation (*P-T-t-D*) in metamorphosed tectonites. New high-precision single crystal X-ray diffraction volume constraints on Ti-doped and chemically pure quartz provide further evidence for substitution of Ti^{4+} for Si^{4+} in the tetrahedral site in quartz, with resultant lattice strain on the structure.

Recent applications of the Ti-in-quartz thermobarometer to dynamically recrystallized quartz have identified recrystallized subgrains that contain lower Ti concentrations ([Ti]) than their host porphyroclasts. In addition, [Ti] are lower than expected for the temperatures of recrystallization. Atomistic simulations that estimate energetic perturbations resulting from Ti incorporation into the quartz lattice indicate that significant increases in strain energy occur only at very high [Ti]; the strain-energy increase is negligible for [Ti] typical of quartz grown under mid-crustal conditions. This suggests that lattice strain rarely provides an appreciable driving force for Ti loss from quartz; instead, it appears that subgrain boundaries and dislocation arrays migrating through recrystallizing quartz crystals can promote localized re-equilibration, thermodynamically regulated by the composition of the intergranular medium (typically undersaturated in Ti). It therefore appears that analyses from dynamically recrystallized quartz cannot be meaningfully interpreted until methods are developed that can account quantitatively for the reduction of Ti resulting from crystal plastic flow.

6.1 Introduction

Thermobarometry is of key importance in metamorphic and structural petrology for reconstructing the pressure-temperature-deformation (*P-T-D*) histories of metamorphic tectonites and the geologic evolution of orogenic terranes. Peak metamorphism is often considered because equilibration is most prominent at peak temperature and speaks most directly to the depth the rocks reached and the mechanisms for burial and exhumation. Tectonic models are derived from *P-T* profiles with respect to structural transects to explain the evolution of the tectonic environment. The Ti-in-quartz ("TitaniQ") thermobarometer has been applied to a wide variety of rocks in various tectonic environments since its initial calibration by Wark & Watson (2006). Applied to pelitic schists metamorphosed at mid-crustal depths, the TitaniQ thermobarometer has been shown to be an effective monitor of Si-flux resulting from: (i) metamorphic reactions, (ii) strain-induced solution transfer, and (iii) Si-charged fluid influx (Ashley *et al.*, 2013). The commonality among these three re-equilibration scenarios is that they are all the result of quartz growth events. In no cases studied by Ashley *et al.*

(2013) were peak-*T* conditions preserved. This is because of the low diffusivity of Ti in quartz under typical Barrovian metamorphic conditions and the inability of Ti in the quartz lattice to re-equilibrate at tectonically significant time scales under the *PT* conditions studied. Recent attempts have been aimed at interpreting results from deformed quartzites. However, dynamically recrystallized quartz has concentrations of Ti ([Ti]) much lower than expected for the temperatures required to activate dislocation slip systems for the inferred recrystallization regimes (e.g., Grujic *et al.*, 2011; Ashley *et al.*, 2013; Nachlas *et al.*, 2013). In this article, we discuss: (i) potential mechanisms to drive quartz re-equilibration with respect to Ti (growth *vs.* recrystallization); (ii) crystallographic and energetic consequences resulting from Ti substitution for Si, including atomistic simulation to evaluate interactions among Ti defects; and (iii) the effect of dynamic recrystallization on Ti solubility in quartz. Insights gained from application of the TitaniQ thermobarometer to quartz mylonites by various research groups are discussed to help guide future applications of the TitaniQ thermobarometer in geologically appropriate scenarios.

6.2 Titanium Incorporation in Quartz

6.2.1 Crystallographic incorporation

The incorporation of Ti^{4+} into quartz has previously been attributed to isomorphic and isoelectronic substitution for the Si^{4+} ion, with significant temperature and, to a lesser extent, pressure, influences (e.g., Müller *et al.*, 2003). Numerous experiments, including X-ray absorption near-edge structure (XANES) and density functional theory (DFT) calculations, support the tetrahedral incorporation of Ti^{4+}, with no evidence for octahedral coordination (Thomas *et al.*, 2010, and references therein). The stereochemistry of Si^{4+} in the tetrahedral sites is controlled by ~50/50 ionic-covalent bonding with oxygen (determined through electronegativity, electron-density calculations, and valence-

bond structuring; Pauling, 1980), forming four molecular hybrid orbitals (sp^3) that are arranged in a regular tetrahedral form to minimize electron repulsion. Ionic modeling of the substitution alone cannot explain this exchange, because Ti^{4+} ions may not be of appropriate size. However, a bonding-orbital (covalent) model could explain this substitution because the electronic configurations of Ti^{4+} (with zero *3d* electrons) would result in no crystal field stabilization energy resulting between the transition metal and the ligands (Burns, 1970), and would minimize lattice energies, except for strain energy, with this coordination. Ti may also be present in quartz as nano-inclusions or mineral precipitates; in that case, however, six-fold coordination is expected, as in rutile and brookite. It is important to determine unequivocally the dominant incorporation mechanisms of Ti in quartz because the most appropriate functional form of the thermodynamic equations used to describe the temperature dependence is different for different mechanisms: precipitate-based incorporation is better described by an Arrhenian temperature-dependence equation (with a diffusion coefficient), rather than the configurational entropy mixing term used for substitution in the lattice. For example, in the case of non-lattice structural substitution, pressure and temperature would strongly affect precipitate densities and could yield the [Ti] correlation previously described in the literature (e.g. Wark & Watson, 2006; Thomas *et al.*, 2010).

6.2.2 Volume XRD measurements

The hydrothermal experimentation technique used to grow quartz at *P* and *T* conditions of interest in Thomas *et al.* (2010) relies on quenching the sample to preserve Ti atoms in their incorporated crystallographic sites. Absolute X-ray diffraction (XRD) volumetric measurements are warranted here for samples prepared in this manner, because elastic properties are not quenchable and regress to ambient values after the experiment is finished (Raz *et al.*, 2002). Ti present as rutile nanoinclusions or precipitates would be expected to induce some degree of lattice strain, but should not

expand the lattice volume. Any observable volume increase may be an indication that Ti substitutes for Si in the tetrahedral site.

Single-crystal X-ray diffraction measurements were conducted on a customized Huber four-circle goniometer diffractometer fitted with an unfiltered Mo sealed-tube X-ray source (without a monochromator). Measurements are made with a fixed-φ mode and driven 0.001° per motor step for ω and χ. For a complete description of the experimental set-up and instrumentation conditions used, see Angel *et al.* (1997).

The diffractometer was driven by the program SINGLE (Angel *et al.*, 2000), which uses vector-least-squares refinement of unit-cell parameters and 8-position peak-centering algorithms (described by Angel *et al.*, 1997) to produce extremely high-precision measurements. Lattice refinements on a synthetic high-Ti sample from Thomas *et al.* (2010) (QTip-38, *ca.* 380 ppm Ti) and on a chemically pure crystal were completed to determine if volume perturbation with Ti substitution exists. Both crystals were untwinned and nearly spherical. The resultant refined lattice volumes are 113.0180(40) $Å^3$ and 113.1342(236) $Å^3$ for the chemically-pure standard and Ti-doped crystal, respectively; this difference is statistically significant at the 95% confidence level.

6.3 Mechanisms for Ti redistribution

Due to multiple re-equilibrating drivers active during dynamic recrystallization of quartz (e.g., chemical thermodynamics, strain-minimizing dislocation creep systems, etc.), understanding the dominant factor controlling Ti redistribution is important for thermobarometric calibrations. Here we examine two mechanisms for loss of Ti from the quartz lattice during recrystallization, which differ importantly in terms of the principal driving force for Ti loss.

6.3.1 Mechanism 1: Strain-driven relocation of Ti

Substitution of Ti into a Si site in quartz will induce strain on the structure; the strain energy increases non-linearly with Ti concentration, because Ti atoms in close proximity yield greater total strain than Ti atoms far from one another. Such structural strain is thus an energetic driver for Ti atoms in quartz to migrate to positions with maximum separation. If an appropriate path for fast diffusion is made available (e.g., as a grain boundary sweeps through the crystal), then movement of Ti ions completely out of the quartz grain and into the intergranular medium or a subgrain boundary is expected to decrease the energy of the quartz structure. However, for this mechanism to be a primary driver for Ti redistribution in quartz undergoing crystal plastic flow, the energy perturbation resulting from the removal must be appreciable at [Ti] observed in natural settings. That is, if removing a Ti atom from a quartz crystal results in a negligible decrease in strain energy, this mechanism may be insufficient to drive Ti mobility.

6.3.2 Mechanism 2: Localized thermodynamic control from intergranular medium

An alternative mechanism for Ti loss during deformation is local re-equilibration within a microenvironment where the intergranular medium constitutes the subgrain boundary. Fluids present in this region would control the effective concentration of TiO_2, where the TiO_2 activity is most likely below unity (i.e., not rutile-saturated). In this scenario, chemical-potential differences would be the dominant driving force for Ti loss from quartz and would result in [Ti] much lower than expected when assuming an activity close to 1 (typically valid for metapelites; Ghent & Stout, 1984).

6.4 Atomistic Simulation of Interactions among Ti Defects

Atomistic simulation provides a means of estimating the magnitude of the increases in strain energy due to interactions of Ti defects at varying levels of concentration. Such calculations help to discriminate between the two mechanisms described above, by identifying concentration levels below which the defects are sufficiently far apart that further reduction in concentration has only a negligible effect on the lattice energy.

These simulations use interatomic potentials based on an ionic model with formal integral charges. Short-range interactions for Si^{4+}–O^{2-}, Ti^{4+}–O^{2-}, and O^{2-}–O^{2-} are described by two-body Buckingham potentials, for which the potential (U) for ions separated by distance r is given by $U(r) = A \cdot \exp(-r/\rho) - (C/r^6)$. O-Si-O bending terms have the form $U(\theta) = \frac{1}{2} K_B (\theta - \theta_0)^2$. Oxygen-ion polarizability (shell model of Dick & Overhauser, 1958) is included via a core-shell interaction potential at separation r of the form $U(r) = \frac{1}{2} k r^2$. We note that although the potential set used by Lewis & Catlow (1986) included polarizability for Ti, the effect is negligibly small and is therefore omitted in this work. Cation-cation interactions beyond electrostatics are neglected. Values for potential parameters and their sources are given in Table 6.1. This potential set was shown by Sanders *et al.* (1984) to successfully reproduce the known properties of SiO_2 polymorphs, including α-quartz as modeled here.

All simulations were performed using GULP, the General Utility Lattice Program (Gale, 1997; Gale & Rohl, 2003). Calculations were done in the static limit (T = 0 K, P = 0 GPa). Defect energies in this limit approximate corresponding defect enthalpies at elevated temperatures to within a few percent (Taylor *et al.*, 1997), and defect free energies in silicates (garnet) have been shown to change very little across a wide range of geologic temperatures and pressures (Carlson *et al.*, 2014). Lattice energies were computed for supercells containing a single Ti atom in place of Si, relaxing the structure to its minimum energy state. Sizes of supercells were progressively increased to evaluate the energy variance with decreasing [Ti], and increasing Ti-Ti distance (Table 6.2). The energy due to defect interactions drops off

sharply with increased Ti-Ti spacing (Fig. 6.1), and is negligible at separation distances > ~30 Å, which corresponds to < 1000 ppm Ti. To validate this result, the energy of a single isolated defect (Ti in limit of infinite dilution) was evaluated using the embedded-cluster method and the two-region Mott-Littleton approach (Mott & Littleton, 1938), with region sizes progressively enlarged until energy convergence was achieved (region 1 radius = 18 Å (3397 atoms); region 2 radius = 24 Å (4688 atoms)). The energy calculated in this way for an isolated defect is indistinguishable from the defect energy for a 9x9x9 supercell, confirming the inference that interactions between Ti defects are energetically negligible once [Ti] drops below ~1000 ppm.

Table 6.1. Parameters for interatomic potentials

Interaction	A (kJ·mol^{-1})	ρ (Å)	C (kJ·mol^{-1}·Å^{-6})	Source
$Si^{4+} – O^{2-}$	123878	0.3205	1028	1
$Ti^{4+} – O^{2-}$	84637	0.3810	868	2
$O^{2-} – O^{2-}$	2196384	0.1490	2690	1
Interaction	**Shell charge (|e|)**		k (kJ·mol^{-1}·Å^{-2})	**Source**
O^{2-} (core-shell)	-2.86902		7229	3, 1
Interaction	**K_B (kJ·mol^{-1}·rad^{-2})**		**θ_0 (°)**	**Source**
$O^{2-} – Si^{4+} – O^{2-}$	2.097		109.47	1

Notes: All short-range interactions for O^{2-} act on the shell of the ion. The cut-off distance for the Si^{4+}–O^{2-} and Ti^{4+}–O^{2-} Buckingham potentials was 12 Å.
Sources: 1 - Sanders et al. (1984); 2 - Lewis and Catlow (1986); 3 - Purton et al. (1996).

Table 6.2. Lattice energies (per 2 oxygens) of α-quartz supercells with single Ti substitution

Supercell dim.	No. of unit cells	Supercell comp. Ti	Si	O	[Ti] (ppm)	[Ti] (wt. %)	Min. Ti-Ti dist. (Å)	Lattice Energy (kJ·mol^{-1})
1x1x1	1	1	2	6	239290	23.93	4.835	-11903.74
2x2x2	8	1	23	48	32744	3.27	9.669	-12352.89
3x3x3	27	1	80	162	9795	0.98	14.504	-12399.40
4x4x4	64	1	191	384	4142	0.41	19.339	-12410.74
5x5x5	125	1	374	750	2123	0.21	24.174	-12414.77
6x6x6	216	1	647	1296	1229	0.12	29.008	-12416.56
7x7x7	343	1	1028	2058	774	0.08	33.843	-12417.47
8x8x8	512	1	1535	3072	519	0.05	38.678	-12417.98
9x9x9	729	1	2186	4374	364	0.04	43.512	-12418.28

Abbreviations: dim. – dimensions; no. – number; comp. – composition; min. – minimum; dist. – distance.

6.5 Discussion

Titanium distribution in quartz can be qualitatively evaluated using cathodoluminescence (CL) imaging through blue filtration, due to the proportionality of Ti concentration to the resultant CL

emission (Wark & Spear, 2005; Rusk *et al.*, 2006; Rusk *et al.*, 2008; Spear & Wark, 2009). Zoning patterns in individual grains can be interpreted with respect to pressure-temperature-growth histories (Spear & Wark, 2009; Ashley *et al.*, 2013), whereas distribution analysis of a population of grains can be interpreted in the context of deformation histories.

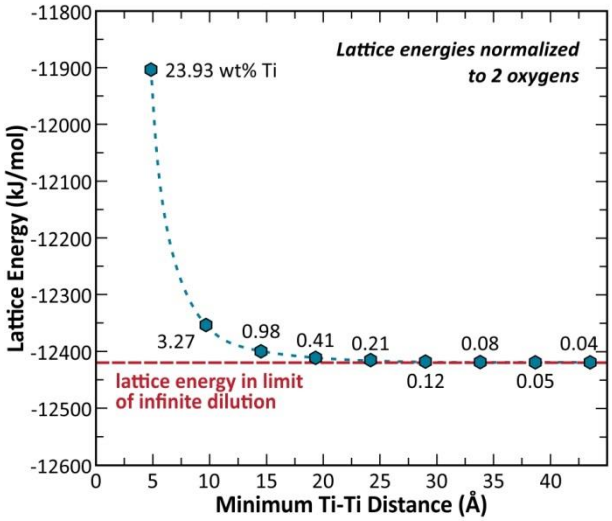

Figure 6.1. Calculated lattice energy for supercells of varying dimension, each containing a single Ti cation substituting for Si. Small supercells contain high [Ti] and yield elevated lattice energies due to interactions among closely spaced defects; however, at lower concentrations, with Ti cations separated by > ~30 Å or more, this energy perturbation is negligible.

Here we will evaluate the results from a compilation of various studies in which Ti-in-quartz thermometry was applied to dynamically recrystallized quartz in shear zones to obtain temperatures of deformation. Our intent is to make a global evaluation of mechanisms driving Ti re-equilibration, rather than focusing on results from one field site.

6.5.1 Experimentally deformed Ti-doped quartz aggregates

Investigating the effects that crystal plastic flow has on Ti redistribution is difficult due to the large number of variables that may perturb the system. For a quartz mylonite, for example, water weakening, strain rate, grain size, temperature, and other factors all influence crystal mechanics. From a thermodynamic perspective, starting aggregate heterogeneity, TiO_2 activity, diffusion, and the presence

of fluids on defects and grain boundaries further complicate this assessment. Many of these variables are difficult to constrain accurately in natural settings, and cross-term effects may obscure some intrinsic trends. Nachlas *et al.* (2013) conducted dynamic deformation experiments at constant *P* and *T* in a shear-assembly apparatus for various strain rates. They developed an innovative doping technique to prepare homogenized quartz aggregates of known starting [Ti]. These experiments evaluated the influence of constrainable variables (starting [Ti], strain rate, water content, duration, etc.) on grain size, resultant recrystallized grain [Ti], and subgrain heterogeneity. Newly formed recrystallized grains typically have [Ti] much lower than expected when using the Thomas *et al.* (2010) calibration for the experimental conditions. More importantly, Nachlas *et al.* (2013) recognized the impact of duration of dynamic recrystallization for resultant trace element composition, and acknowledged the significance of kinetics and diffusion on Ti redistribution.

6.5.2 [Ti] in recrystallized quartz subgrains in natural systems

Recent applications of the TitaniQ thermobarometer have pursued the effects of crystal plastic flow on Ti resetting. The findings from Ashley *et al.* (2013), Grujic *et al.* (2011) and Kidder *et al.* (2013) are discussed to provide a natural context for interpreting the data presented in this study. In each investigation, recrystallized subgrains contained [Ti] lower than that of their host porphyroclastic cores (Fig. 6.2).

The study by Ashley *et al.* (2013) emphasized the utility of the TitaniQ thermobarometer in constraining *P-T-D* histories and monitoring Si-flux in metapelitic tectonites. The results presented in that study are in good agreement with previous petrologic estimates on the same rocks. The abundant biotite present in their samples acts as a weak interconnected phase that accommodates strain in the rock, with dynamically recrystallized quartz being largely absent as a result. Two generations of quartz

veining were observed in the Ashley *et al.* (2013) investigation: undeformed retrograde veins, and pre- or syn-kinematic veins that are extensively recrystallized by subgrain rotation recrystallization. Ti-in-quartz thermometry on recrystallized grains results in temperature estimates lower than expected from the inferred recrystallization mechanisms. This is an interesting observation, considering that undeformed quartz in these rocks yields expected temperatures, suggesting that dynamic recrystallization had a significant impact on the resultant [Ti] present in grains. Ashley et al. did not interpret the analytical results from these deformed quartz veins due to this discrepancy.

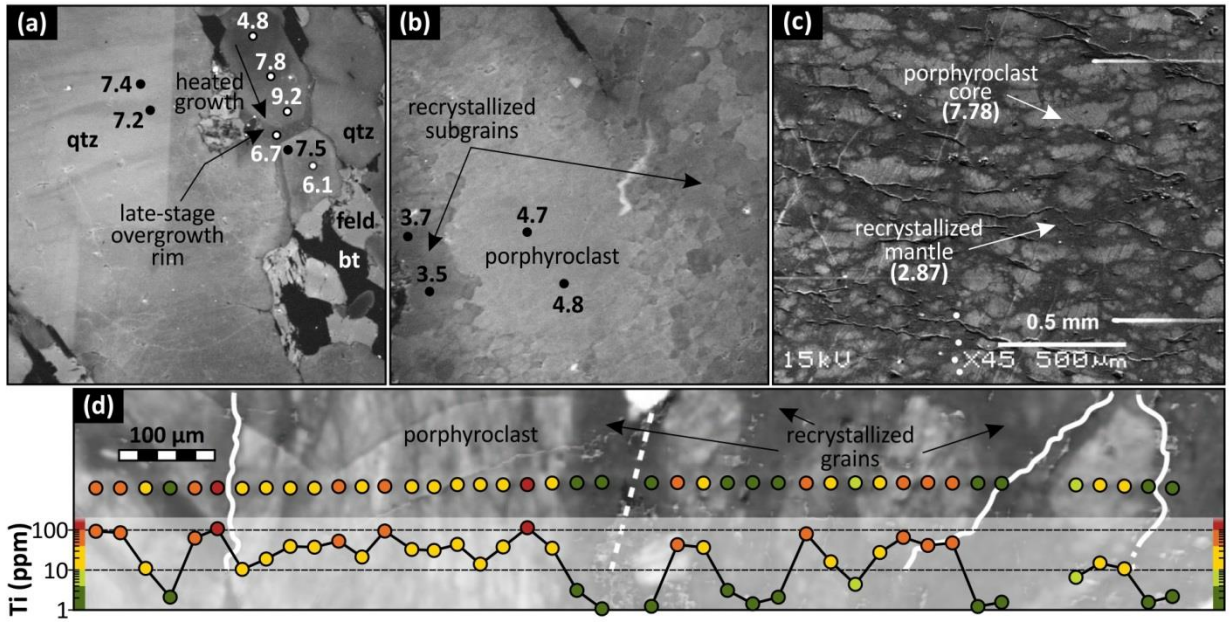

Figure 6.2. CL imaging for Ti distribution analysis in quartz mylonites from: (a,b) Ashley *et al.* (2013); (c) Grujic *et al.* (2011); (d) Kidder *et al.* (2013). (a) Ti equilibration during quartz growth events has aided in reconstructing prograde and early retrograde *P-T-D* histories in quartz tectonites (Ashley *et al.*, 2013). However, in dynamically recrystallized quartz, subgrains typically contain lower [Ti] than relict porphyroclastic cores (appearing darker in CL images; b-d). These Ti-deficient grains result in temperature estimates much lower than those produced by other thermobarometric techniques.

The Tonale mylonites studied by Grujic *et al.* (2011) have been extensively investigated and this locality is often used as a natural laboratory for petrologic and fabric studies. Despite a well-constrained *P-T* framework, many of the recrystallized quartz grains contain [Ti] much lower than expected from syn-deformation metamorphic mineral assemblages when using the Thomas *et al.* (2010) calibration. Decreasing the TiO_2 activity to *ca.* 0.2 results in temperature estimates that agree reasonably well with

previous petrologic studies, but in the subgrain-rotation recrystallization regime, calculated temperatures are still much lower than indicated by metamorphic mineral assemblages. Although Grujic *et al.* acknowledge that it is unclear why the TiO_2 activities in quartz mylonites would be so low, they attribute this discrepancy to: (i) recrystallization influencing the activity (or resulting in an apparent activity) and, (ii) the importance of a Ti-phase that may be recrystallizing or participating in a metamorphic reaction that is synchronous with quartz recrystallization (an observation also discussed by Thomas, 2013). Considering the effects of recrystallization on the apparent TiO_2 activity explains why adjusting the activity may work for some regimes (e.g., dynamic recrystallization) but does not extrapolate into other regimes (e.g., subgrain rotation recrystallization). This is to be expected because different recrystallization regimes may have different mechanisms operating to minimize intracrystalline strain. For example, subgrain rotation recrystallization may have dominant rhomb and prismatic slip to homogenize dislocation densities (Blacic, 1975), whereas grain boundary bulging recrystallization may be dominated by basal slip (Hirth & Tullis, 1992).

Kidder *et al.* (2013) suggested two important factors should be considered when analyzing [Ti] in recrystallized quartz: (i) the duration of deformation may have a significant impact on Ti resetting due to diffusional limits (also acknowledged by Nachlas *et al.*, 2013, in the experimental deformation studies discussed above); and (ii) the importance of deviation of fluid pressure from lithostatic pressure. The equivalence of fluid and lithostatic pressure is often assumed, and in many systems may be appropriate (e.g., magmas, mid-to-deep crustal metamorphism, very dry rocks). However, in systems where the fluid pressure deviates greatly from lithostatic pressure (e.g., shallow quartz veins), this difference could have a significant impact on the solubility of Ti in quartz and may result in erroneous estimated temperatures.

6.5.3 Lattice energetics with Ti substitution

The XRD measurements conducted in this study reflect structural adjustments that result from substituting Ti for Si on tetrahedral sites. The observed (mean) volume difference can be attributed to differences in [Ti] because all other conditions (e.g., analytical conditions, crystal morphology, absence of twins) are identical. A larger unit cell volume is measured for the Ti-doped quartz, suggesting that substituting the larger Ti cation for Si results in an expanded lattice. The larger uncertainty for the measured volume of the Ti-doped crystal is likewise attributed to lattice strain resulting from the substitution of Ti for Si.

Our atomistic simulations illustrate the energy consequences of substituting Ti in quartz for a range of concentrations. Quartz grown under typical Barrovian metamorphic conditions contains [Ti] in the 10s of ppm or less. At these concentrations, there would be a negligible increase in lattice energy relative to a pristine crystal (Fig. 6.1). This suggests that the amount of lattice strain resulting from typical levels of Ti substitution is not sufficient to drive significant Ti redistribution. Therefore, localized thermodynamic factors must provide the dominant driving force for removing Ti from quartz.

Diffusion rates for Ti in quartz at temperatures < 600 °C are sluggish (Cherniak *et al.*, 2007), and the duration of deformation in tectonic systems may be too short to expect complete equilibration of the recrystallized subgrains. For example, deformation is believed to have occurred in < 1 Myr for the Tonale mylonites (Grujic *et al.*, 2011). At the temperatures reported for subgrain rotation recrystallization in that study, the maximum distance of diffusion is < 10 µm. The process of sweeping grain boundaries and dislocations through the crystals during dynamic recrystallization provides short pathways for Ti diffusion. This intergranular medium would regulate the thermodynamics of this re-equilibration, and any fluids present would likely be far removed from TiO_2 saturation. Unlike new quartz growth, for which activity is driven by a larger effective ("bulk rock") composition (controlled by

local mineral content in a microstructural domain), the effective composition regulating Ti partitioning during dynamic recrystallization is of a much smaller volume (<10 radial microns). Therefore thermodynamically controlled re-equilibration would result in the removal of Ti from the lattice, aided by the short diffusive pathways when migrating dislocations and subgrain boundaries are present.

6.6 Implications

Proper recognition of the mechanisms for Ti re-equilibration in quartz is essential to minimize the potential for erroneous temperature or pressure estimates. We question the interpretation of measurements from extensively recrystallized quartz by means of calibrations that were derived from growth experiments (e.g., Thomas *et al.*, 2010; Huang & Audétat, 2012). Previous studies acknowledged the importance of starting heterogeneity in the deforming quartz aggregate and duration of deformation on equilibrating subgrains. This study adds to these observations by noting the importance of sweeping grain boundaries and defects through the crystals to establish TiO_2-undersaturated thermodynamic "microenvironments" that drive diffusion of Ti out of the crystal structure. Although the strain-energy increase produced by the substitution of Ti for Si on tetrahedral sites in quartz is likely to be energetically unimportant in typical Barrovian-sequence rocks, high-Ti quartz in other systems may have a significant energy driver for redistributing Ti. Future work should focus on a calibration that takes into consideration the dynamic recrystallization regime, duration of deformation, and greatly reduced TiO_2 activities. This would serve as a more appropriate expression to infer temperatures of deformation.

Considering the current state of the Ti-in-quartz thermobarometer, the following protocols are recommended to ensure appropriate usage:

1. CL imaging of quartz should always be conducted to prevent erroneous interpretations that may arise from assuming homogenized Ti distributions that are not actually present.

2. In instances where there is evidence for quartz growth (e.g., via quartz-producing metamorphic reactions, strain-induced solution transfer, Si-influx), the Thomas *et al.* (2010) calibration should be used. This may only be warranted in systems where pore fluid pressure is equal to the lithostatic pressure (e.g., application to mid-crustal rocks); in other circumstances, the Huang & Audétat (2012) calibration may be preferred.
3. Interpreting Ti-in-quartz data from dynamically recrystallized quartz should be done with caution or avoided until a calibration is developed that considers the mechanisms driving re-equilibration on these localized scales, along with the duration of recrystallization. It is likely that [Ti] in recrystallized quartz will yield spuriously low temperatures if the Thomas *et al.* (2010) calibration is used, and applying calibrations that result in higher *T* estimates for these conditions (e.g., Huang & Audétat, 2012) may also be erroneous.
4. When estimating temperatures from vein quartz, TiO_2 activity should be carefully considered, in recognition that veins free of Ti-saturated phases are common, and within such veins, restricted equilibration with the surrounding host rock may preclude rutile saturation.

Acknowledgements

We are very grateful for the assistance of John Hughes, Elinor Spencer, Jing Zhao and Nancy Ross in the collection of X-ray diffraction analyses. We thank John Hughes for his review of this manuscript and Oliver Tschauner for editorial handling. This paper is based on work supported by the National Science Foundation under grant No. EAR-1220345 (awarded to R.D. Law) and by a Grant-In-Aid of Research from Sigma Xi, The Scientific Research Society (awarded to K.T. Ashley). The Texas Advanced Computing Center (TACC) at the University of Texas at Austin provided high-performance computing resources used for atomistic simulation.

References

Angel, R. J., Allan, D. R., Miletich, R. & Finger, L. W. (1997). The use of quartz as an internal pressure standard in high-pressure crystallography. *Journal of Applied Crystallography* **30**, 461-466.

Angel, R. J., Downs, R. & Finger, L. W. (2000). High-temperature-high-pressure diffractometry. In: Hazen, R. M. & Downs, R. (eds.) *High-Temperature and High-Pressure Crystal Chemistry*. Washington, DC: Reviews in Mineralogy and Geochemistry, 559-596.

Ashley, K. T., Webb, L. E., Spear, F. S. & Thomas, J. B. (2013). *P-T-D* histories from quartz: A case study of the application of the TitaniQ thermobarometer to progressive fabric development in metapelites. *Geochemistry Geophysics Geosystems* **14**, 3821-3843.

Blacic, J. D. (1975). Plastic deformation mechanisms in quartz: The effect of water. *Tectonophysics* **27**, 271-294.

Burns, R. G. (1970). *Mineralogical Applications of Crystal Field Theory*. Great Britain: Cambridge University Press.

Carlson, W. D., Gale, J. D. & Wright, K. (2014). Incorporation of REEs in aluminosilicate garnet: Energetics from atomistic simulation. *American Mineralogist* **99**, 1022-1034.

Cherniak, D. J., Watson, E. B. & Wark, D. A. (2007). Ti diffusion in quartz. *Chemical Geology* **236**, 65-74.

Dick, B. G., Jr. & Overhauser, A. W. (1958). Theory of the dielectric constants of alkali halide crystals. *Physical Review* **112**, 90-103.

Gale, J. D. (1997). GULP: A computer program for the symmetry-adapted simulations of solids. *Faraday Transactions* **93**, 629-637.

Gale, J. D. & Rohl, A. L. (2003). The General Utility Lattice Program (GULP). *Molecular Simulation* **29**, 291-341.

Ghent, E. D. & Stout, M. Z. (1984). TiO_2 activity in metamorphosed pelitic and basic rocks: principles and applications to metamorphism in southeastern Canadian Cordillera. *Contributions to Mineralogy and Petrology* **86**, 248-255.

Grujic, D., Stipp, M. & Wooden, J. L. (2011). Thermometry of quartz mylonites: Importance of dynamic recrystallization of Ti-in-quartz reequilibration. *Geochemistry Geophysics Geosystems* **12**, 1-19.

Hirth, G. & Tullis, J. (1992). Dislocation creep regimes in quartz aggregates. *Journal of Structural Geology* **14**, 145-159.

Huang, R. & Audétat, A. (2012). The titanium-in-quartz (TitaniQ) thermobarometer: A critical examination and re-calibration. *Geochimica et Cosmochimica Acta* **DOI: 10.1016/j.gca.2012.01.009**, 31.

Kidder, S., Avouac, J.-P. & Chan, Y.-C. (2013). Application of titanium-in-quartz thermobarometry to greenschist facies veins and recrystallized quartzites in the Hsüehshan range, Taiwan. *Solid Earth* **4**, 1-21.

Lewis, G. V. & Catlow, C. R. A. (1986). Defect studies of doped and undoped Barium Titanate using computer simulation techniques. *Journal of Physics and Chemistry of Solids* **47**, 89-97.

Mott, N. F. & Littleton, M. J. (1938). Conduction in polar crystals. I. Electrolytic conduction in solid salts. *Transactions of the Faraday Society* **34**, 485-499.

Müller, A., Wiedenbeck, M., Van Den Kerkhof, A. M., Kronz, A. & Simon, K. (2003). Trace elements in quartz - a combined electron microprobe, secondary ion mass spectrometry, laser-ablation ICP-MS, and cathodoluminescence study. *European Journal of Mineralogy* **15**, 747-763.

Nachlas, W. O., Hirth, G., Teyssier, C., Whitney, D. L. & Zimmermann, M. (2013). Synthesis and deformation of a Ti doped quartz aggregate. *EGU General Assembly*, EGU2013-9892.

Pauling, L. (1980). The nature of silicon-oxygen bonds. *American Mineralogist* **65**, 321-323.

Purton, J. A., Allan, N. L., Blundy, J. & Wasserman, E. A. (1996). Isovalent trace element partitioning between minerals and melts — a computer simulation model. *Geochimica et Cosmochimica Acta* **60**, 4977-4987.

Raz, U., Girsperger, S. & Thompson, A. B. (2002). Thermal expansion, compressibility and volumetric changes of quartz obtained by single crystal dilatometry to 700 ^{o}C and 3.5 kilobars (0.35 GPa). *Schweizerische Mineralogische und Petrographische Mitteihurgen* **83**, 173-182.

Rusk, B. G., Lowers, H. A. & Reed, M. H. (2008). Trace elements in hydrothermal quartz: Relationships to cathodoluminescent textures and insights into vein formation. *Geology* **36**, 547-550.

Rusk, B. G., Reed, M. H., Dilles, J. H. & Kent, A. J. R. (2006). Intensity of quartz cathodoluminescence and trace-element content in quartz from the porphyry copper deposit at Butte, Montana. *American Mineralogist* **91**, 1,300-301,312.

Sanders, M. J., Leslie, M. & Catlow, C. R. A. (1984). Interatomic potentials for SiO_2. *Journal of the Chemical Society, Chemical Communications*, 1271-1273.

Spear, F. S. & Wark, D. A. (2009). Cathodoluminescence imaging and titanium thermometry in metamorphic quartz. *Journal of Metamorphic Geology* **27**, 187-205.

Taylor, M. B., Barrera, G. D., Allan, N. L., Barron, T. H. K. & Mackrodt, W. C. (1997). Free energy of formation of defects in polar solids. *Faraday Discussions* **106**, 377-387.

Thomas, J. B. (2013). Experimental calibration of a Ti-in-quartz thermobarometer: An overview for applications to mylonites. *EGU General Assembly Conference Abstracts*, 8555.

Thomas, J. B., Watson, E. B., Spear, F. S., Shemella, P. T., Nayak, S. K. & Lanzirotti, A. (2010). TitaniQ under pressure: The effect of pressure and temperature on the solubility of Ti in quartz. *Contributions to Mineralogy and Petrology* **160**, 743-759.

Wark, D. A. & Spear, F. S. (2005). Titanium in quartz: Cathodoluminescence and thermometry. *Geochimica et Cosmochimica Acta Supplement* **69**, A592.

Wark, D. A. & Watson, E. B. (2006). TitaniQ: A titanium-in-quartz geothermometer. *Contributions to Mineralogy and Petrology* **152**, 743-754.

Chapter 7

Modeling Prograde TiO_2 Activity and its Significance for Ti-in-quartz Thermobarometry of Pelitic Metamorphic Rocks

Kyle T. Ashley[1], Richard D. Law[1]

[1]*Department of Geosciences, Virginia Polytechnic Institute and State University, Blacksburg, VA 24061, USA*

Published February 2015 in *Contributions to Mineralogy and Petrology*.

Abstract

Since its calibration, the Ti-in-quartz thermobarometer has been applied to a wide variety of geologic scenarios. The abundance of quartz in the continental crust and the involvement of silica in metamorphic reactions, deformation, and fluid-flux processes make it a particularly powerful tool for constraining the pressure and temperature evolution of rocks, which is essential for developing tectonic models. Being able to quantitatively determine the solubility of Ti in quartz, however, is dependent upon being able to determine the activity of TiO_2 in the rock during quartz growth or re-equilibration.

Here we calculate TiO_2 chemical potentials of the system relative to that of rutile (as a standard state), projected in *P-T* space for an average sub-aluminous pelite composition. Titania activities are calculated from these dependent potentials, with resultant activities used to correct for Ti isopleth projection in the Thomas *et al.* (2010) solubility equation. The modeling results are in good agreement with previous studies that suggests ilmenite-bearing assemblages buffer high TiO_2 activities, and titanite-bearing assemblages have much lower activities (≥0.5). At elevated temperatures, however, significant deviation from an assumed average pelite activity of 1.0 occurs, where the projected Ti concentration in quartz is up to 400% different when assuming a dynamic system activity. This is due, in part, to the sequestering of Ti in biotite during heating and the destabilization of Ti-oxides at higher temperatures. With quartz-producing reactions, deformation-driven solution-transfer processes, and other Si-mobilization events occur during the prograde and retrograde history of metapelites, and assuming TiO_2 activities associated with the peak metamorphic paragenesis may be misleading and result in significant errors in *P-T* calculations.

7.1 Introduction

The solubility of TiO_2 in quartz is strongly temperature and (to a lesser extent) pressure dependent, thereby providing a potentially powerful thermobarometer. This thermobarometer is increasingly informative due to the ubiquity of quartz in continental crust and the involvement of silica in metamorphic reactions, solution-transfer processes, and Si-charged fluid flux. Quantifying the amount of Ti likely to be incorporated into the quartz lattice is dependent upon several variables, including thermodynamic controls (enthalpy, entropy and volume), temperature (*T*), pressure (*P*), and the activity of TiO_2 (a_{TiO_2}). Growth experiments at elevated *P* and *T* constrain the thermodynamics of the exchange of Ti for Si in the tetrahedral site in quartz (Wark & Watson 2006; Thomas *et al.*, 2010; Huang & Audétat, 2012). The lesser dependence of pressure on the system allows for adequate temperature estimation even if pressure can only be approximately constrained. Solubility of Ti in quartz is dependent on a_{TiO_2}, which is typically assumed to be fixed when quartz is grown or recrystallized in the presence of Ti-

bearing phases. Titania activity may be calculated in systems where TiO_2 is not an essential stoichiometric component. It is important to accurately constrain this activity, because errors in calculated temperatures may arise if deviation from the true activity is large.

Ghent & Stout (1984) defined potential equilibria assemblages where titania activity could be reasonably constrained, with results suggesting activities of ~1 and ≥0.8 for metapelites and amphibolite-facies felsic gneisses, respectively. In rutile-absent samples, the Gibbs free energy of the reaction *$2FeTiO_3 = TiO_2 + Fe_2TiO_4$* has been used to calculate the effective (bulk) a_{TiO_2} (Wark *et al.*, 2007; Ashley *et al.*, 2013), where $FeTiO_3$ is ilmenite and Fe_2TiO_4 is ulvöspinel (TiO_2 is dissolved in phases). The Gibbs energy of formation (ΔG°_{fmn}) from the Holland & Powell (1998) database can be used to calculate the Gibbs energy for the above reaction. A Van't Hoff (or Vukancic-Vukovic equation) chemical thermodynamic reaction isotherm can be used in conjunction with the equilibrium constant that relates ΔG_{rxn} to the chemical equilibrium constant (K_{eq}), where $\Delta G_{rxn} = -RTln(K_{eq})$. Incorporating the end-member activities of the products and reactants gives

$$\Delta G_{rxn} = -RTln\left[\frac{a_{TiO_2}.a_{Fe_2TiO_4}}{\left(a_{FeTiO_3}\right)^2}\right].$$

Assuming ideality, where component activity is equivalent to the mole fraction of the Ti end-members, the equation can be re-arranged to calculate titania activity:

$$a_{TiO_2} = \frac{\exp\left(\frac{-\Delta G_{rxn}}{RT}\right) \cdot Y^2}{X}$$

where *X* and *Y* are the activities of ulvöspinel and ilmenite, respectively. Despite the utility of implementing these reactions for activity calculation in the absence of rutile, several problems may prevent the successful application of this potential thermometer. For example, ilmenite may form hematite lamellae and re-equilibrate (Harlov, 2000; McEnroe *et al.*, 2002). Also, there is very little ulvöspinel component in most metamorphic magnetites, and small analytical errors are likely to

extrapolate to large errors in a_{TiO_2}, restricting this application to magmatic rocks (F. Spear, personal communications).

In this paper we implement pseudosection modeling to calculate system a_{TiO_2} across the modeled *P-T* space. This approach bypasses the need for considering various Ti-reactions and allows for the calculation of titania activity in the absence of rutile, ilmenite and titanite. With the output activity maps, corrected Ti-isopleth projections into *P-T* space can be computed. The benefit to this approach is that quartz-producing metamorphic reactions can be better interpreted with respect to modeled a_{TiO_2}, giving pressure or temperature estimates with less uncertainty than would be expected if it is assumed that TiO_2 activity is constant throughout the prograde evolution.

7.2 Modeling approach and considerations

Thermodynamic modeling was conducted for the system MnO-Na_2O-CaO-K_2O-FeO-MgO-Al_2O_3-SiO_2-H_2O-TiO_2 (MnNCKFMASHT) through gridded minimization calculations using the program Perple_X (Connolly, 2009) with the 2004 update of the Holland & Powell (1998) thermochemical database. Perple_X predicts the most stable configuration of phases through a Gibbs free energy minimization approach (Connolly & Kerrick, 1987). Results from these calculations should be identical to results acquired in other programs (e.g. THERMOCALC; Powell *et al.*, 1998) as long as the thermodynamic data and solution models are the same. Solution models used are as follows: 1) Staurolite, garnet, chlorite, chloritoid, and hydrous cordierite formulation after Holland & Powell (1998), extended for Mn solid solution after Mahar *et al.* (1997). 2) Ideal mixing for ilmenite-geikielite-pyrophanite; ternary feldspar from Fuhrman & Lindsley (1988); white mica (Coggon & Holland, 2002; Auzanneau *et al.*, 2010), not allowing for tschermaks or Ti substitutions in the Ca- and Na-subsystems; Ti-Fe^{3+}-biotite (Tajčmanová *et al.*, 2009), extended to Mn solution after Tinkham *et al.* (2001). 3) Amphibole model after Dale *et al.* (2005); 4) compound formation for orthopyroxene after Powell & Holland (1999), with Holland & Powell

(2011) modified site populations. 5) Clinopyroxene based on the Holland & Powell (1996) non-ideal quasi-ordered omphacite, modified for non-ideal Ca-tschermaks after Zeh *et al.* (2005). 6) Silicate melt modeling after White *et al.* (2001), with the White *et al.* (2007) modification of the faL (fayalite in melt) and foL (forsterite in melt) olivine melt end-members (an enthalpy adjustment to more closely reflect total Fe+Mg in silicate melt). It is safe to assume that the ilmenite-geikielite-pyrophanite solid solution is an ideal solution for two reasons. First, the majority of metamorphic ilmenites are restricted close to the ideal $FeTiO_3$ composition, with very high (>0.9) ilmenite activities in sub-aluminous metapelites (e.g. Ashley *et al.*, 2013) and metabasites (e.g. Ghent & Stout, 1984). In addition, only small deviations from ideality are detectable in such ilmenite-pyrophanite solution (O'Neill *et al.*, 1989), and the exchange would not alter the stoichiometry with respect to TiO_2. Quartz, rutile and titanite were considered as pure phases. Fluid was considered in excess and treated as pure H_2O.

Mineral abbreviations follow Whitney & Evans (2010) with the exception of "wm" for white mica. Calculations were based on the Mahar *et al.* (1997) modified average sub-aluminous pelite composition of Shaw (1956), including MnO with a reduced CaO content (Table 7.1). Additionally, modeling of an average greywacke composition (after Brownlow, 1996, and references therein) was conducted to observe the effects of a lower clay component in the protolith rock (for meta-psammitic and semi-pelitic rocks). The composition used did not include a MnO component, therefore a minor amount (0.05 mole %) was included to better reflect concentrations observed in nature.

Table 7.1. Bulk rock chemical data for average rock type compositions (in molar %)

Rock-type	SiO_2	TiO_2	Al_2O_3	FeO_{tot}	MnO	MgO	CaO	Na_2O	K_2O	Ref.
Pelite	71.13	0.67	11.61	5.78	0.10	4.65	1.39	1.99	2.68	1,2
Greywacke*	75.71	0.21	9.42	2.79	0.05	3.18	2.63	4.14	1.88	3

**A minor MnO component was added because no data was reported for this component*
References: 1 – Shaw (1956); 2 – Mahar et al. (1997); 3 – Brownlow (1996, and references therein)

For the modeled *P-T* window, chemical potentials of the TiO_2 component (μ_{TiO_2}) were calculated with Perple_X (being the result of the computed molar Gibbs free energy). Modeling was

performed on the complex (and realistic) MnNCKFMASHT system to take into account the effects of solid solution. Initial calculations were isobaric along a heating profile (Figs. 7.1 and 7.2). Titania activity may be calculated when evaluating μ_{TiO_2} against an idealized standard state chemical potential ($\mu^\circ_{TiO_2}$).

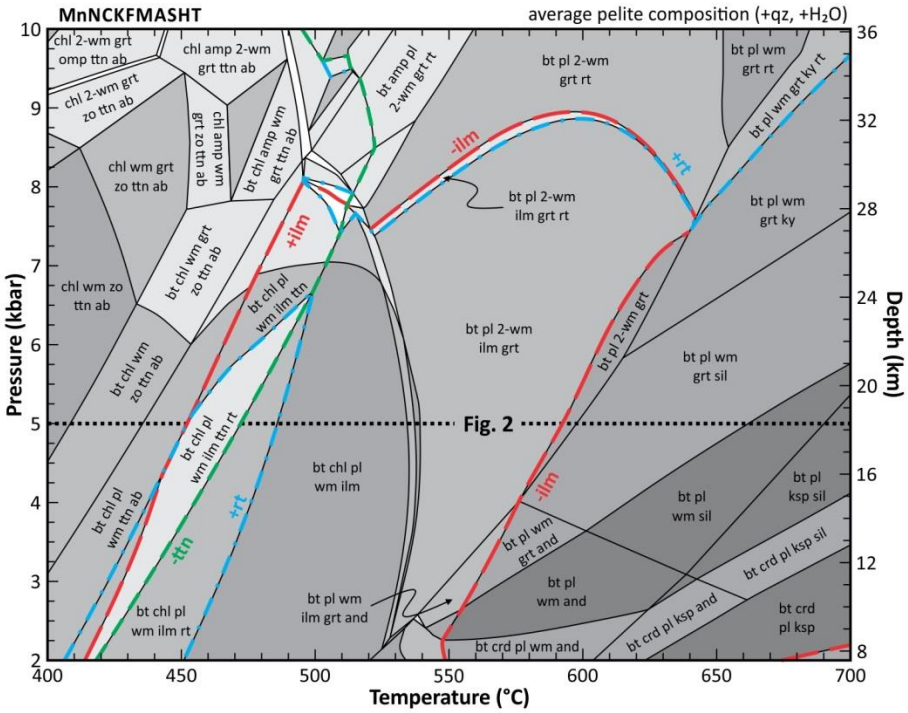

Figure 7.1. Modeled mineral stability for an average pelitic rock in the system Mn-Na_2O-CaO-K_2O-FeO-MgO-Al_2O_3-SiO_2-H_2O. Bold lines denote stability limits of the Ti-oxide phases. The position of the isobaric profile shown in Fig. 7.2 is indicated by the dotted line. Quartz and water is considered in excess. Darker shaded fields denote higher variance. Mineral abbreviations from Whitney & Evans (2010).

These standard state values were calculated for the *P-T* conditions of interest by saturating the modeled system in TiO_2 (thus stabilizing rutile in every mineral assemblage stability field), and calculating the dependent potential of rutile at each *P* and *T*. This is completed using the modeled entropy (S) and enthalpy (H) of rutile to determine the molar Gibbs free energy of pure TiO_2 at the *T* and *P* of interest – which is equal to the chemical potential of rutile at these conditions (Spear, 1993). This is expressed by

$$\mu^\circ_{TiO_2} = \bar{G}^\circ_{TiO_2} = U + PV - TS = H - TS \qquad \textit{(eq. 7.1)}$$

where *U* is the internal energy and *V* is volume. Component activity can then be calculated by the expression

$$a_{TiO_2} = exp\left[\frac{\mu_{TiO_2} - \mu^{\circ}{}_{TiO_2}}{RT}\right] \qquad \textit{(eq. 7.2)}$$

where *R* is the gas constant (8.31446 J K^{-1} mol^{-1}) and *T* is temperature (in K). If pure rutile is present as a phase in the bulk rock, $\mu^{\circ}{}_{TiO_2} = \mu_{TiO_2}$ and $a_{TiO_2} = 1.0$.

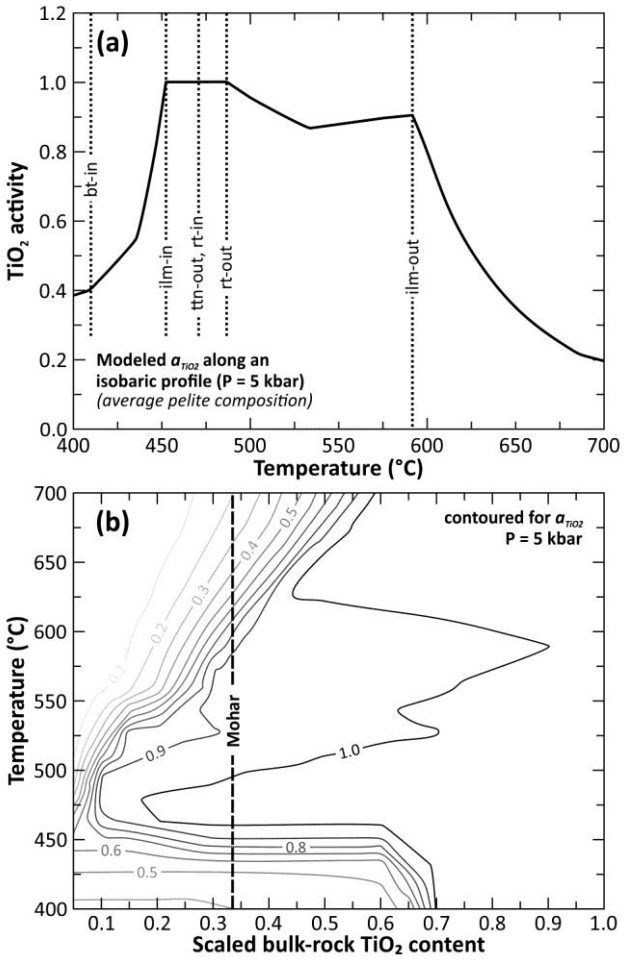

Figure 7.2. (a) Calculated TiO_2 activity for an isobaric (5 kbar) profile of increasing temperature for an average pelite composition. This modeling suggests that TiO_2 activity is quite dynamic, and rapidly decreases outside the ilmanite stability field. (b) The effects of varying bulk-rock TiO_2 on corresponding component activity. The *x*-axis represents TiO_2 variation (in molecular proportions) between 0.1% (at *x* = 0.05) and 2.0% (at *x* = 1.0). The bold line indicates the average pelite composition shown in (a).

Corrections to the fixed a_{TiO_2} projection of Ti isopleths (e.g. Fig. 7.3a; Thomas *et al.*, 2010) can be completed through any of the Ti-in-quartz solubility equations. Here, we use the equation by Thomas *et al.* (2010) and calculate expected Ti concentrations ([Ti]) in quartz with the expression

$$RT\ ln\ X_{TiO_2}^{quartz} = -60952 + 1.520 \cdot T(K) - 1741 \cdot P(kbar) + RT\ ln\ a_{TiO_2}. \qquad \textit{(eq. 7.3)}$$

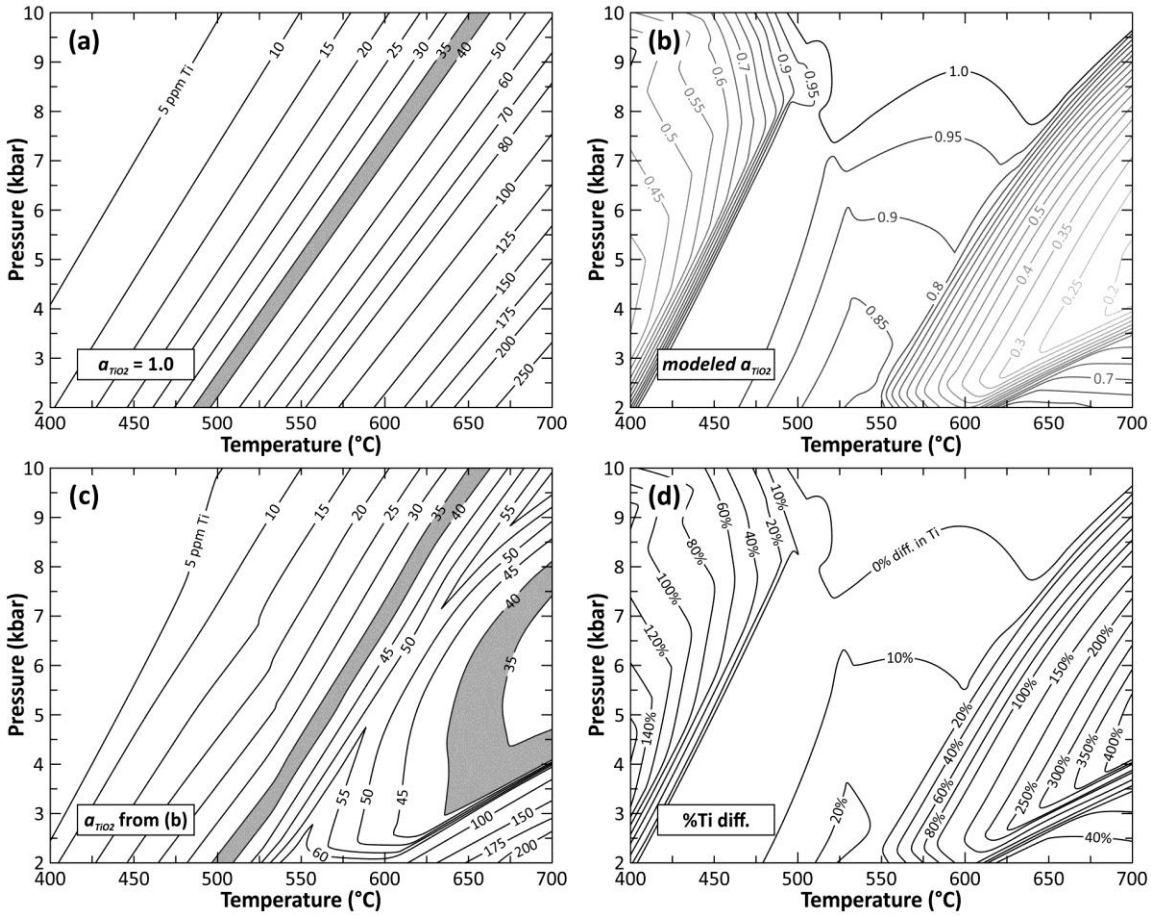

Figure 7.3. (a) *P-T* projected Ti isopleths assuming a fixed titania activity of 1.0 (from Thomas *et al.*, 2010). (b) Modeled $\boldsymbol{a_{TiO_2}}$ for average pelitic bulk composition from Mahar *et al.* (1997). (c) Corrected Ti isopleth projection, based on the activity map calculated in (b). (d) Percent difference between [Ti] in quartz assuming a fixed activity of 1.0 and the $\boldsymbol{a_{TiO_2}}$ modeled shown in (b). Temperature greater than 600 °C and less than 450 °C have significant variance in [Ti], up to 400% at 700 °C (4 kbar).

7.3 Results

Pseudosection modeling of the average pelite composition shows the stabilization of ilmenite and rutile at the expense of titanite at ~450 °C, with rutile being largely restricted to high-*P* space (>8 kbar) and ilmenite stable at pressures below this (Fig. 7.1). Ilmenite break-down occurs starting at 550 °C, extending to higher temperatures for higher pressures. This is consistent with what is observed in rocks from eastern Vermont (Ashley *et al.*, 2013) and northern Scotland (Thigpen *et al.*, 2013), where garnet porphyroblasts contain an abundance of ilmenite inclusions that the matrix is largely devoid of. With garnet growth initiated at < 550 °C in both these studies, heating to peak temperatures would

result in ilmenite breakdown and explain the ilmenite distribution observed in these rocks. Outside the ilmenite window, mica (particularly biotite) is the major reservoir for Ti budgeting, with biotite sequestering more Ti at higher temperatures (e.g. Henry *et al.*, 2005; Chambers & Kohn, 2012).

Chemical potential of TiO_2 was modeled at 5 kbar between 400 and 700 °C (Fig. 7.2a). Calculated a_{TiO_2} across this profile shows that high activities are coincident with the presence of ilmenite (>0.85) and rutile (1.0). When buffered by the presence of titanite, the modeled activity is found to be variable; between 0.4 and 1.0 within a 50 °C window. At temperatures above the stability field of ilmenite (>480 °C), a_{TiO_2} rapidly decreases down to 0.2 at 700 °C. In Figure 7.2b the effect of varying bulk rock TiO_2 in the modeled activity profiles is considered, from 0.1–2.0 mole % (*x*-axis = 0.05–1.0). Results of this variation modeling suggest rocks that are depleted in TiO_2 relative to the average pelite considered here (labeled "Mahar" in Fig. 7.2b) produce a significant reduction in a_{TiO_2} in the modeled *P-T* space; minor increases in TiO_2 saturate the rock with this component and increase the activity across the temperature profile.

Pressure has a significant effect on resultant a_{TiO_2}, due to the stabilization of rutile at higher *P* (Fig. 7.3b), and results in larger temperature windows where titania activity is ~1.0. For example, at 9 kbar titania activities are greater than 0.9 between 490 and 690 °C; at 4 kbar this temperature range is limited to 435–510 °C, with activities down to 0.2 at 700 °C. The implications of this variable activity become evident when Ti-isopleths are projected in *P-T* space (Fig. 7.3c) and compared to isopleths calculated assuming a constant activity of 1.0 for pelites (Fig. 7.3a). At temperatures above 600 °C, Ti concentrations in quartz decrease with increasing temperature, which is counter-intuitive to the substitution. When considering [Ti] of 35–40 ppm with a constant a_{TiO_2} of 1.0, the calculated temperature is 575 °C (at 6 kbar). When using the variable-activity corrected isopleths, two solutions are possible for this concentration and pressure: at 580 °C and 650–675 °C. At lower pressures, this offset would be even greater. The relative discrepancy between assuming a fixed versus variable titania

activities can be considered by taking the percent difference between projected isopleth concentration in *P-T* space (Fig. 7.3d). In the titanite stability field, differences up to 100% are observed. Even greater offsets occur at high temperatures and moderate pressures (up to 400%). If bulk rock compositions are semi-pelitic or psammitic, Ti solubility in quartz is buffered with very low titania activities (Fig. 7.4), and only a very small window (425–475 °C, below 3 kbar) results in activities above 0.9.

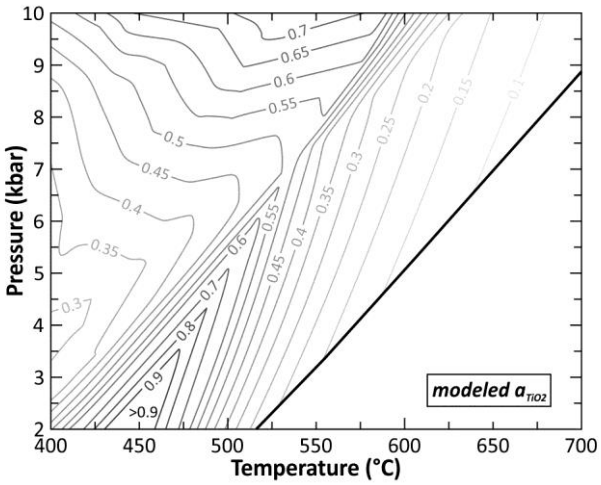

Figure 7.4. Calculated titania activities in *P-T* space for a metamorphosed greywacke. The field to the right of the bold line only has biotite, feldspar and quartz stable, and no activities could be calculated.

7.4 Discussion

The modeling presented here suggests a_{TiO_2} has a dynamic variability in *P-T* space for average pelite compositions. If quartz is produced within the ilmenite and rutile stability fields, it would equilibrate with high a_{TiO_2}. If growth occurs in the presence of titanite, the activity is typically 0.5 or above. These results are consistent with previous studies that calculate component activities based on appropriate reactions (Ghent & Stout, 1984; Wark *et al.*, 2007; Chambers & Kohn, 2012). Chambers & Kohn (2012) calculated titania activities using Ti in biotite, muscovite, and amphibole; however these calculations result in considerable scatter and sometimes produce values above 1.0, which suggests super-saturation and is thermodynamically impermissible. Their study does recognize that GRIPS (garnet-rutile-ilmenite-plagioclase-quartz equilibrium) based estimation of TiO_2 activity in ilmenite-

bearing rocks is consistently nearly rutile saturated; results that are replicated here. It is important to note that thermodynamic calculations are sensitive to the solution models and thermodynamic datasets chosen and may vary if other models are implemented.

In this study, the Ti-in-quartz solubility equation by Thomas *et al.* (2010) was preferred for several reasons. First, Ti analyses by Ashley *et al.* (2013) in eastern Vermont indicate temperatures consistent with temperatures of quartz-producing metamorphic reactions when this calibration is considered. Use of the Huang & Audétat (2012) calibration results in temperatures >100 °C higher than expected for these rocks, based on the peak metamorphic paragenesis and exchange thermobarometry results. In addition, the Huang & Audétat (2012) experiments produced quartz with highly variable Ti concentrations. A recent study (Thomas *et al.*, 2015) conducted static recrystallization reversal experiments that confirm the ability of quartz to re-equilibrate at various pressures and temperatures, despite its original starting composition, that is identical to concentrations predicted by the Thomas *et al.* (2010) solubility equation. A more critical evaluation of the various solubility equations is made by Thomas *et al.* (2015).

The susceptibility of quartz to participate in metamorphic reactions and the mobility of silica in deformation processes during the prograde evolution of a rock may result in zoned quartz (such as reported by Ashley *et al.*, 2013) that has radically different observed a_{TiO_2} during different re-equilibration events. Owing to the slow diffusivity of TiO_2, post growth modifications through volume diffusion due to perturbations in pressure and temperature are minimal unless temperatures are high (e.g. >700 °C) and/or metamorphic heating occurring over sufficiently long time scales (Spear *et al.*, 2012; Ashley *et al.*, 2013). Therefore this evolutionary record is expected to be preserved, unless re-equilibrated through dynamic recrystallization (see discussion by Ashley *et al.*, 2014 on the effects of dynamic recrystallization on Ti resetting). The modeled Ti isopleth projections presented here show the effects of such variability on Ti solubility in quartz. Therefore, assuming fixed activities of ~1.0 for pelites

could result in large temperature errors, unless re-equilibration occurred in the presence of ilmenite or rutile. Rocks metamorphosed via contact metamorphism are expected to be most impacted by these solubility consequences. The approach we present here provides a simple method for observing the evolution of this component activity and allows for better constraints when interpreting prograde quartz growth.

Acknowledgements

We thank reviewer Bruce Watson and handling editor Chris Ballhaus for their constructive comments that greatly improved the clarity and discussion of this paper. We thank Frank Spear for insightful discussions pertaining to thermodynamic components of this work. This work is supported by the National Science Foundation under grant No. EAR-1220345 (awarded to R.D. Law).

References

Ashley, K. T., Carlson, W. D., Law, R. D. & Tracy, R. J. (2014). Ti resetting in quartz during dynamic recrystallization: Mechanisms and significance. *American Mineralogist* **99**, 2025-2030.

Ashley, K. T., Webb, L. E., Spear, F. S. & Thomas, J. B. (2013). *P-T-D* histories from quartz: A case study of the application of the TitaniQ thermobarometer to progressive fabric development in metapelites. *Geochemistry Geophysics Geosystems* **14**, 3821-3843.

Auzanneau, E., Schmidt, M. W., Vielzeuf, D. & Connolly, J. A. D. (2010). Titanium in phengite: A geobarometer for high temperature eclogites. *Contributions to Mineralogy and Petrology* **159**, 1-24.

Brownlow, A. H. (1996). *Geochemistry*. Uper Saddle River, NJ: Prentice Hall.

Chambers, J. A. & Kohn, M. J. (2012). Titanium in muscovite, biotite, and hornblende: Modeling, thermometry, and rutile activities of metapelites and amphibolites. *American Mineralogist* **97**, 543-555.

Coggon, R. & Holland, T. (2002). Mixing properties of phengitic micas and revised garnet-phengite thermobarometers. *Journal of Metamorphic Geology* **20**, 683-696.

Connolly, J. A. D. (2009). The geodynamic equation of state: What and how. *Geochemistry Geophysics Geosystems* **10**, 1-19.

Connolly, J. A. D. & Kerrick, D. M. (1987). An algorithm and computer program for calculating composition phase diagrams. *Calphad* **11**, 1-55.

Dale, J., Powell, R., White, R. W., Elmer, F. L. & Holland, T. J. B. (2005). A thermodynamic model for Ca-Na clinoamphiboles in Na_2O-CaO-FeO-MgO-Al_2O_3-SiO_2-H_2O-O. *Journal of Metamorphic Geology* **23**, 771-791.

Fuhrman, M. L. & Lindsley, D. H. (1988). Ternary-feldspar modeling and thermometry. *American Mineralogist* **73**, 201-215.

Ghent, E. D. & Stout, M. Z. (1984). TiO_2 activity in metamorphosed pelitic and basic rocks: principles and applications to metamorphism in southeastern Canadian Cordillera. *Contributions to Mineralogy and Petrology* **86**, 248-255.

Harlov, D. E. (2000). Titaniferous magnetite-ilmenite thermometry and titaniferous magnetite-ilmenite-orthopyroxene-quartz oxygen barometry in granulite facies gneisses, Bamble Sector, SE Norway: Implications for the role of high-grade CO_2-rich fluids during granulite genesis. *Contributions to Mineralogy and Petrology* **139**, 180-197.

Henry, D. J., Guidotti, C. V. & Thomson, J. A. (2005). The Ti-saturation surface for low-to-medium pressure metapelitic biotites: Implications for geothermometry and Ti-substitution mechanisms. *American Mineralogist* **90**, 316-328.

Holland, T. & Powell, R. (2011). An improved and extended internally consistent thermodynamic dataset for phases of petrological interest, involving a new equation of state for solids. *Journal of Metamorphic Geology* **29**, 333-383.

Holland, T. J. B. & Powell, R. (1996). Thermodynamics of order-disorder in minerals: II. Symmetric formalism applied to solid solutions. *American Mineralogist* **81**, 1425-1437.

Holland, T. J. B. & Powell, R. (1998). An internally consistent thermodynamic data set for phases of petrological interest. *Journal of Metamorphic Geology* **16**, 309-343.

Huang, R. & Audétat, A. (2012). The titanium-in-quartz (TitaniQ) thermobarometer: A critical examination and re-calibration. *Geochimica et Cosmochimica Acta* **DOI: 10.1016/j.gca.2012.01.009**, 31.

Mahar, E., Powell, R., Holland, T. J. B. & Howell, N. (1997). The effect of Mn on mineral stability in metapelites. *Journal of Metamorphic Geology* **15**, 223-238.

McEnroe, S. A., Harrison, R. J., Robinson, P. & Langenhorst, F. (2002). Nanoscale haematite-ilmenite lamellae in massive ilmenite rock: An example of 'lamellar magnetism' with implications for planetary magnetic anomalies. *Geophysical Journal International* **151**, 890-912.

O'Neill, H. S. C., Pownceby, M. I. & Wall, V. J. (1989). Activity-composition relations in $FeTiO_3$-$MnTiO_3$ ilmenite solid solutions from EMF measurements at 1050-1300 K. *Contributions to Mineralogy and Petrology* **103**, 216-222.

Powell, R. & Holland, T. J. B. (1999). Relating formulations of the thermodynamics of mineral solid solutions: Activity modeling of pyroxenes, amphiboles, and micas. *American Mineralogist* **84**, 1-14.

Powell, R., Holland, T. J. B. & Worley, B. A. (1998). Calculating phase diagrams involving solid solutions via non-linear equations, with examples using THERMOCALC. *Journal of Metamorphic Geology* **16**, 577-588.

Shaw, D. M. (1956). Geochemistry of pelitic rocks. Part III: Major elements and general chemistry. *Geological Society of America Bulletin* **67**, 919-934.

Spear, F. S. (1993). *Metamorphic Phase Equilibria and Pressure-Temperature-Time Paths*. Washington D.C.: Mineralogical Society of America.

Spear, F. S., Ashley, K. T., Webb, L. E. & Thomas, J. B. (2012). Ti diffusion in quartz inclusions: Implications for metamorphic time scales. *Contributions to Mineralogy and Petrology* **164**, 977-986.

Tajčmanová, L., Connolly, J. A. D. & Cesare, B. (2009). A thermodynamic model for titanium and ferric iron solution in biotite. *Journal of Metamorphic Geology* **27**, 153-165.

Thigpen, J. R., Law, R. D., Loehn, C. L., Strachan, R. A., Tracy, R. J., Lloyd, G. E., Roth, B. L. & Brown, S. J. (2013). Thermal structure and tectonic evolution of the Scandian orogenic wedge, Scottish

Caledonides: Integrating geothermometry, deformation temperatures, and kinematic-thermal modeling. *Journal of Metamorphic Geology* **31**, 813-842.

Thomas, J. B., Watson, B. E., Spear, F. S. & Wark, D. A. (2015). TitaniQ recrystallized: Experimental confirmation of a Ti-in-quartz calibration. *Contributions to Mineralogy and Petrology* **169**, 1-16.

Thomas, J. B., Watson, E. B., Spear, F. S., Shemella, P. T., Nayak, S. K. & Lanzirotti, A. (2010). TitaniQ under pressure: The effect of pressure and temperature on the solubility of Ti in quartz. *Contributions to Mineralogy and Petrology* **160**, 743-759.

Tinkham, D. K., Zuluaga, C. A. & Stowell, H. H. (2001). Metapelite phase equilibria modeling in MnNCKFMASH: The effect of variable Al_2O_3 and MgO/(MgO+FeO) on mineral stability. *Mineralogical Society of America: Geological Materials Research* **3**, 1-43.

Wark, D. A., Hildreth, W., Spear, F. S., Cherniak, D. J. & Watson, E. B. (2007). Pre-eruption recharge of the Bishop magma system. *Geology* **35**, 235-238.

Wark, D. A. & Watson, E. B. (2006). TitaniQ: A titanium-in-quartz geothermometer. *Contributions to Mineralogy and Petrology* **152**, 743-754.

White, R. W., Powell, R. & Holland, T. J. B. (2001). Calculation of partial melting equilibria in the system Na_2O-CaO-K_2O-FeO-MgO-Al_2O_3-SiO_2-H_2O (NCKFMASH). *Journal of Metamorphic Geology* **19**, 139-153.

White, R. W., Powell, R. & Holland, T. J. B. (2007). Progress relating to calculation of partial melting equilibria for metapelites. *Journal of Metamorphic Geology* **25**, 511-527.

Whitney, D. L. & Evans, B. W. (2010). Abbreviations for names of rock-forming minerals. *American Mineralogist* **95**, 185-187.

Zeh, A., Klemd, R. & Barton, J. M. (2005). Petrological evolution in the roof of the high-grade metamorphic Central Zone of the Limpopo Belt, South Africa. *Geological Magazine* **142**, 229-240.

Chapter 8

Quartz Inclusions in Garnet: Time Capsules of Early Mountain Building

Kyle T. Ashley[1], Richard D. Law[1], Robert J. Bodnar[1], Kenneth A. Eriksson[1]

[1]*Department of Geosciences, Virginia Polytechnic Institute and State University, Blacksburg, VA 24061, USA*

Submitted January 2015 in *Geological Society of America (Memoir)*.

Abstract

The prograde history of a rock holds important information concerning the processes occurring during early stages of convergence associated with mountain building. However, much of this information is lost due to overprinting at near-peak conditions or through retrograde modification during exhumation. Fortunately, inclusions encapsulated in rigid porphyroblasts may preserve a record of conditions experienced early in the rock's history.

In recent years it has been well documented that titanium substitution in quartz has a strong temperature and pressure dependence and may therefore provide a useful thermobarometer. Quartz inclusions in garnet porphyroblasts from the Strafford Dome, eastern Vermont, have homogeneous Ti concentrations ([Ti]) that differ from matrix quartz – this matrix quartz retains a history of Si-liberating metamorphic reactions and Si-bearing fluid influx. We apply growth-composition models to evaluate potential processes associated with Ti partitioning in quartz, before encapsulation in garnet, including a model for constant rate of quartz volume increase (growth) due to mineral dissolution-transfer processes and growth as a result of Si-producing diagenetic and metamorphic reactions. Because these processes typically occur at low temperatures, quartz with exceedingly low [Ti] (<<1 ppm) would be formed and cannot account for the homogeneous Ti distribution at concentrations between 2.5 and 5 ppm observed in our Strafford Dome sample. Therefore, early prograde dynamic recrystallization must have occurred to re-equilibrate and homogenize Ti distribution in the quartz that later became encapsulated in garnet.

Fluid inclusions and mineral inclusions within quartz inclusions in garnet were also evaluated to constrain the burial path of our sample. Despite the absence of carbonaceous material in the matrix, quartz inclusions contain abundant high-density CO_2 and graphite inclusions. Isolated graphite inclusions yield temperatures of 408 °C using the Raman spectroscopy of carbonaceous material (RSCM) thermometer. Healed fractures in inclusion quartz are evident by linear trails of fluid and mineral inclusions. Graphite inclusions within healed fractures indicate formation temperatures of 488 °C. Matrix quartz contains fewer inclusions, and only CO_2 fluid inclusions were observed. An H_2O component was not observed in the measured fluid inclusions, which may indicate that any water in the fluid was sequestered in hydrous silicate minerals during the early prograde metamorphism or that the H_2O component reacted with the surrounding quartz host and formed a hydrous-silicate film (e.g., opal). Titanite (sphene) inclusions are preserved as isolated grains in quartz inclusions and are absent from matrix quartz as a result of destabilization at temperatures greater than ~475 °C (along the modeled steady state geotherm). An interesting consequence of being shielded in quartz inclusions in garnet is the preservation of titanite at conditions far removed (by ~75 °C) from its modeled stability field (peak temperature = 550 °C).

The findings of this study exemplify the utility of garnet hosts to preserve inclusion minerals from chemical modification and recrystallization during later events. As such, they provide a window into the early orogenic stages and provide insights concerning the mechanisms controlling equilibration of quartz. Our results add to the metamorphic framework for the Strafford Dome established by previous studies of rocks from eastern Vermont by providing previously unavailable details of their early prograde conditions.

8.1 Introduction

Our understanding of the pressure-temperature (*P-T*) evolution of rocks in ancient mountain belts is typically limited to the late prograde or peak metamorphism stages. This is in part due to continuous chemical and mineralogical equilibration as rocks are exposed to higher temperatures during the prograde stage. For instance, pressures and temperatures are typically constrained through the exchange of divalent cations in metapelitic assemblages above greenschist facies. With slower kinetics and lower diffusivities as temperature decreases during retrogression, modification of this chemical signature may be limited, allowing us insight into the near-peak metamorphic conditions. Retrograde overprinting may preserve a new metamorphic paragenesis, providing evidence for the exhumation path. In addition, thermochronology allows one to infer the rate of cooling that occurred. However, for early prograde metamorphism, our knowledge is limited due to the frequent participation of earlier-formed minerals in metamorphic reactions, chemical modification at elevated temperatures, and the susceptibility of minerals to recrystallization (which may modify mineral chemistries). As a result of these processes, the early prograde conditions associated with metamorphism and mountain building are poorly understood.

Recent work suggests that our best opportunity for accessing the early history of a metamorphic rock may be through study of inclusion minerals in rigid, poikiloblastic metamorphic hosts. Garnet represents such a suitable host due to: (i) its resistance to deformation, (ii) (relatively) high temperature for the onset of plasticity, (iii) its largely chemically inert character with respect to quartz, and (iv) garnet tends to passively overgrow and encapsulate (include) a variety of minerals during its formation. The inclusion of a mineral grain in garnet shields the grain from interaction with the bulk rock and later fluids, preserving the pre-encapsulation composition in some cases (particularly in unfractured garnets where there are no pathways to allow chemical connectivity with the matrix). Although some exceptions exist (e.g., ilmenite inclusions in garnet continue to exchange Mn and Fe at higher temperatures), high

field-strength elements (e.g., Ti, Al, V) in silicate minerals are less likely to be modified by diffusion, especially in the absence of fluids. Assessing trace element distributions in quartz, therefore, may provide information about processes that occurred prior to encapsulation. One such example is incorporation of Ti in quartz, and the partitioning of Ti between other phases and quartz can be the result of several processes including:

(i) Continuous growth due to solution transfer processes, which would provide a continuous record for early prograde evolution.

(ii) Growth associated with quartz-producing diagenetic and metamorphic reactions

(iii) Compositions retained from a sedimentary source in the case of detrital garnet grains. This would be beneficial in sedimentary provenance sourcing and provide insight into the ancient terranes that have been eroded away.

(iv) Growth associated with discrete Si-influx events, which may be linked to tectonic processes (e.g., thrust faults acting as a conduit for fluid infiltration).

(v) Extensive recrystallization (dynamic or static) that resets [Ti] in quartz prior to inclusion in garnet.

(vi) Early brittle-fracture features resulting from faulting, with linear bands and brecciated textures present in inclusions correlating with healing of these fractures.

Here, we present quartz growth models for Ti partitioning during diagenetic/metamorphic evolution, and characterize the processes associated with Ti distribution within quartz inclusions. Model results are evaluated with respect to sample 09SD08A from the Strafford Dome, eastern Vermont that was described and characterized by Ashley *et al.* (2013). This sample was selected because the pressure-temperature (*P*-*T*) history of the area is well constrained by previous studies (Menard & Spear, 1994), including the linkage of heating profiles to quartz-producing metamorphic reactions (Ashley *et al.*, 2013) and near-peak geospeedometry results on 09SD08A from diffusion studies in quartz (Spear *et al.*, 2012)

and garnet (Spear, 2014). Also, the sample shows similarities in quartz inclusion Ti chemistry and duration of metamorphism to Barrovian rocks from the Moine thrust sheet in northern Scotland (Ashley *et al.*, *in review*), suggesting the possibility that results obtained here may be applicable in other similar environments. In addition to the growth models, fluid inclusions in quartz are evaluated to infer fluid controls on the localized environment at the time of quartz formation prior to inclusion in garnet. Graphite inclusions in quartz in different microstructural settings are analyzed to infer temperatures of deformation evolution through Raman spectroscopy of carbonaceous material (RSCM) thermometry. Rutile needles are used to make qualitative inferences about original protolith quartz trace element composition and to identify a potential sedimentary provenance. Implications for these findings are then discussed to further enhance our understanding of early prograde evolution in convergent orogens and to elucidate the importance of mineral shielding to inhibit reequilibration

8.2 Sample Characterization

Sample 09SD08A is a semi-pelitic garnet schist from the Devonian Gile Mountain Formation in east-central Vermont. This is a flysch deposit with interleaving pelitic and psammitic layers, with minor calcareous units (Doll, 1944; Fisher & Karabinos, 1980). The rock reached staurolite-kyanite grade and contains the assemblage garnet + quartz + biotite + muscovite + plagioclase + accessories. Inter-kinematic garnets (i.e., grown between deformation events; see Passchier & Trouw, 2005, for details of terminology) contain linear trails of inclusion quartz oriented at an oblique angle to the matrix foliation (φ up to 35°; Fig. 8.1a,b). The matrix contains a spaced foliation defined by compositional layering and mica preferred orientation (Ashley *et al.*, 2013). The shape-preferred orientation of quartz is aligned parallel to the dominant matrix foliation (S_2). Strain shadows on the fringes of garnet porphyroblasts

consist of quartz, feldspar and mica. Late-stage, coarse-grained quartz veining is concordant with the S_2 foliation.

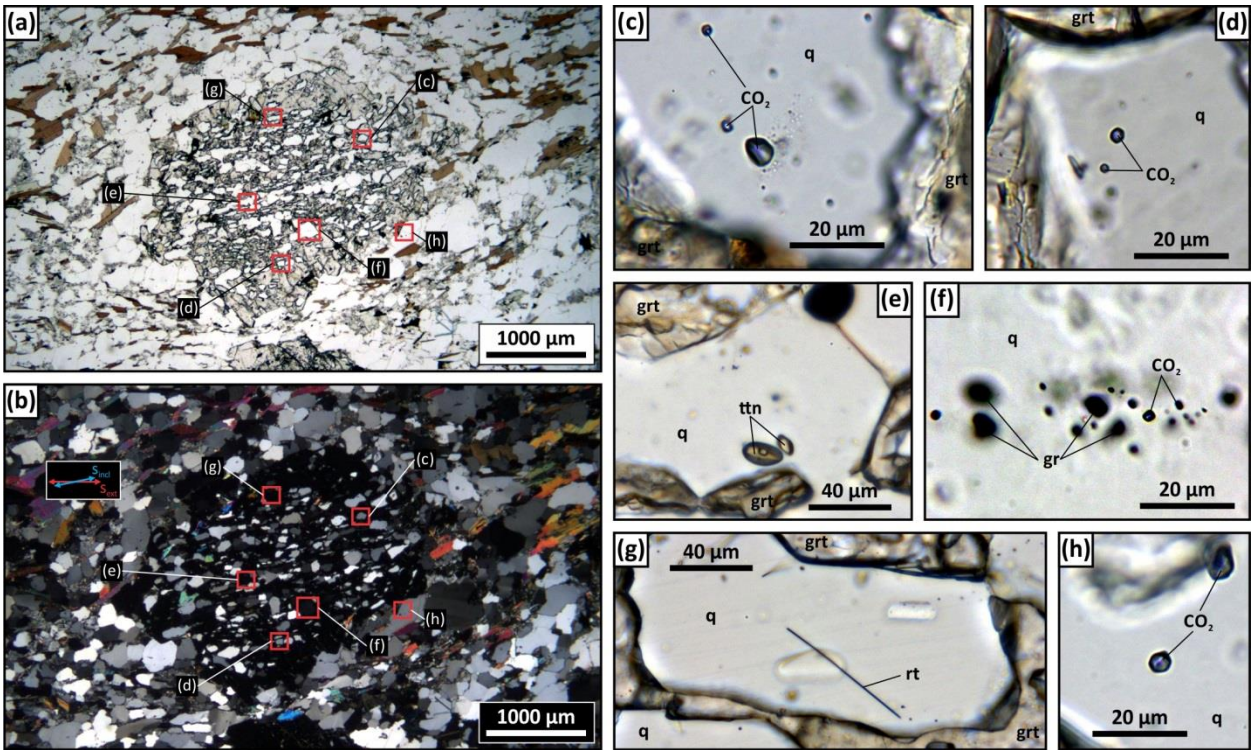

Figure 8.1. Photomicrographs of sample 09SD08A. (a) Transmitted and (b) cross-polarized images of a garnet porphyroblast with linear inclusion trails oriented at slight obliquity to the matrix foliation. Locations of (c)-(h) are shown. Quartz inclusions in garnet contain: (c,d) isolated inclusions of high-density liquid CO_2, (e) titanite, (f) healed fractures consisting of graphite and CO_2 inclusions, and (g) rutile needles. In comparison, matrix quartz (h) contains sparse isolated inclusions of CO_2.

Quartz and ilmenite inclusions are abundant in garnet. Quartz inclusions contain randomly oriented rutile needles (Fig. 8.1g), whereas matrix quartz contains none. Cathodoluminescence (CL) imaging and high-resolution trace element analysis of inclusion quartz by Ashley *et al.* (2013) revealed homogeneous compositions of 2.5–5 ppm Ti. CL intensity is proportional to [Ti], therefore intensity distribution is used to characterize Ti distribution (Spear & Wark, 2009). Linear bands of higher Ti cross-cut inclusions (Fig. 8.2a,d), with a diffusive gain of Ti around grain boundaries as a result of post-encapsulation heating (Spear & Wark, 2009; Spear *et al.*, 2012). Spear *et al.* (2012) utilized these diffusion profiles to constrain the duration of near-peak metamorphism at ~1.6 Myrs (time interval from encapsulation, to peak temperature, and cooling to 460 °C). In comparison, matrix quartz contains more

complex zoning patterns, with an increase in Ti toward the rim attributed to growth through Si-producing metamorphic reactions, with sharp, low-Ti overgrowths resulting from Si-influx during retrogression (Ashley *et al.*, 2013).

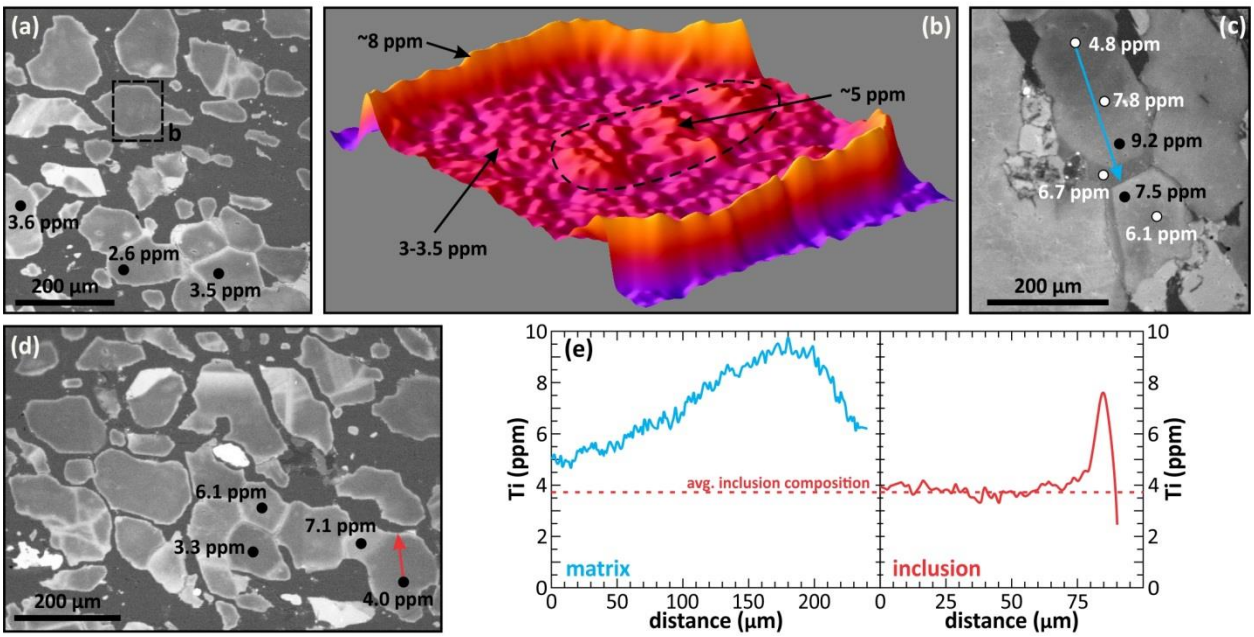

Figure 8.2. Trace element distribution characterized by CL imaging in inclusion and matrix quartz. (a,d) Inclusions have homogeneous low-Ti cores with thin higher-Ti rims that developed through diffusion of Ti from the garnet host. (b) 3D surface Ti map of the outlined area in (a). Patches of higher-Ti cores are preserved and may be remnants of undeformed porphyroclasts. (c) Matrix quartz contain complex zoning patterns, where grains with gradients of increasing Ti have low-Ti rim overgrowths that form annealed boundaries with neighboring grains. (e) Quartz composition profiles across matrix grains (blue) and inclusions (red) in garnet. Profiles are created by calibrating the CL intensities to the local Ti measurements. Matrix and inclusion traverses are from transects shown in (c) and (d), respectively. Data and images from Ashley (2011) and Ashley *et al.* (2013).

8.3 Analytical Methods

8.3.1 Thermodynamic modeling

Thermodynamic calculations were made using a gridded minimization approach in the program Perple_X (Connolly, 2009) in the system MnO-Na_2O-CaO-K_2O-FeO-MgO-Al_2O_3-SiO_2-H_2O-TiO_2 (MnNCKFMASHT). The 2004 update of the Holland & Powell (1998) thermochemical database was implemented to model equilibrium phase stability across a *P-T* window from 100–650 °C and 0.5–10 kbar (Fig. 8.3). Solution models considered are summarized in Table 8.1. Quartz, rutile and titanite were

regarded as pure phases, with a pure H_2O fluid phase assumed to be in excess. Mineral abbreviations follow Whitney & Evans (2010) with the exception of "wm" for white mica.

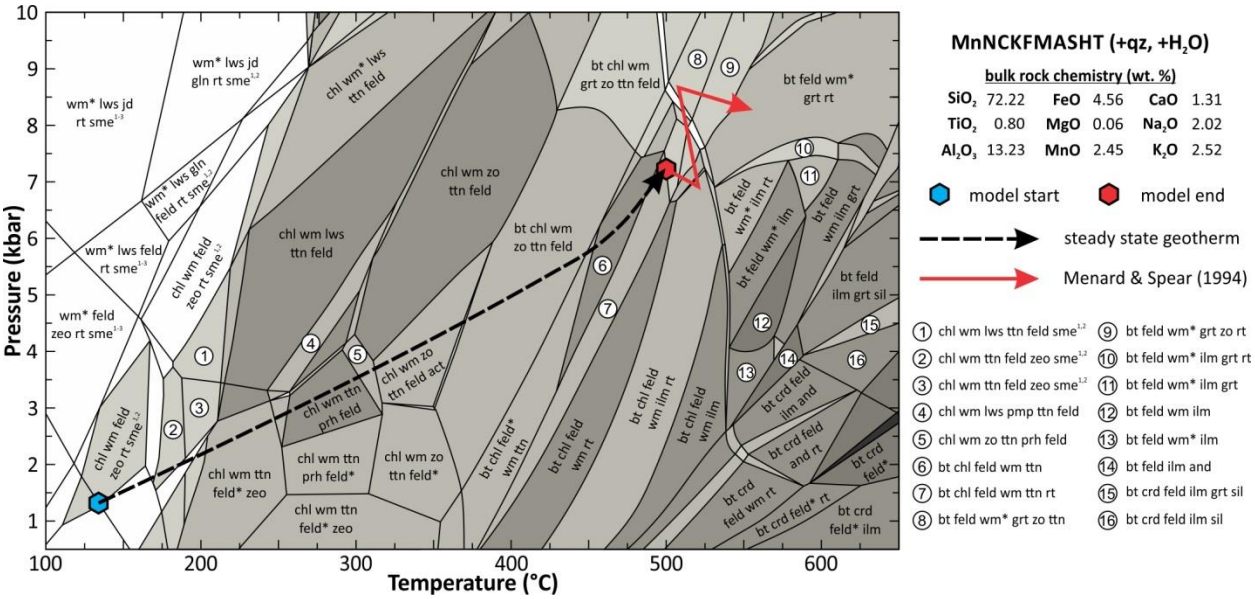

Figure 8.3. Thermodynamic phase-stability model in the system MnO-Na_2O-CaO-K_2O-FeO-MgO-Al_2O_3-SiO_2-H_2O-TiO_2 (MnNCKFMASHT) for a representative bulk rock composition of (in wt. % oxide): 72.22% SiO_2, 0.80% TiO_2, 13.23% Al_2O_3, 4.562% FeO. 0.06% MnO, 2.45% MgO, 1.31% CaO, 2.02% Na_2O, and 2.52% K_2O, with water considered in excess. Dashed line represents the steady state geotherm *P-T* profile used in this study.

Table 8.1. Solution models considered in thermodynamic calculations

Mineral(s)	Reference	Notes
staurolite, garnet, chlorite, chloritoid, and hydrous cordierite	Holland and Powell (1998)	Extended for Mn solid solution after Mahar et al. (1997)
ilmenite-geikielite-pyrophanite	Holland and Powell (2011)	Ideal mixing
feldspar (ternary)	Fuhrman and Lindsley (1988)	
white mica	Coggon and Holland (2002); Auzanneau et al. (2010);	Does not allow for tschermaks or Ti substitutions in the Ca- and Na-subsystems
Ti-Fe^{3+} biotite	Tajčmanová et al. (2009)	Extended to Mn solution after Tinkham et al. (2001)
amphibole	Dale et al. (2005)	
orthopyroxene	Powell and Holland (1999)	Modified site populations of Holland and Powell (2011)
clinopyroxene	Holland and Powell (1996)	Non-ideal quasi-ordered omphacite, modified for non-ideal Ca-tschermaks after Zeh et al. (2005)
silicate melt	White et al. (2001)	Including White et al. (2007) modification of the faL and foL olivine melt end-members (an enthalpy adjustment to more closely reflect total Fe+Mg in silicate melt)

Notes: quartz, rutile and titanite treated as pure, with unmixed H_2O fluid phase considered in excess.

A dynamic titania activity (a_{TiO_2}) is considered for the modeled *P-T* window, following the protocol of Ashley & Law (2015), which is summarized here. The chemical potential of TiO_2 is calculated from the thermodynamic output of the models. Additional calculations are made after saturating the bulk chemistry in TiO_2, which results in the stabilization of rutile across the entirety of the modeled *P-T*

space. Chemical potentials for this system represent an idealized standard state, which can be used relative to the measured system TiO_2 chemical potential to determine the affinity towards rutile (i.e., a_{TiO_2}). For pelite compositions, the modeling indicates that although large portions of *P-T* space have titania activities ~1.0, some portions are substantially lower than this, resulting in large errors when projecting Ti isopleths relative to an assumed fixed activity (Ashley and Law, *in review*). Ti concentrations in quartz were calculated at different pressures and temperatures using the solubility equation of Thomas *et al.* (2010). This calibration was preferred over others (e.g., Wark & Watson, 2006; Huang & Audétat, 2012) because: (i) the equation includes a pressure-dependent solubility term and, (ii) previous work correlates Ti concentrations in metapelitic rocks to quartz growth during silica-producing metamorphic reactions (Ashley *et al.*, 2013), with the Thomas *et al.* (2010) solution providing the best fit to previous pressure and temperature estimates on the rocks. However, it should be noted that these calibrations cannot be applied to dynamically recrystallized quartz, because dislocation arrays and subgrain boundaries sweeping through recrystallizing quartz crystals may result in local re-equilibration with an intergranular medium rather than with the bulk rock (Ashley *et al.*, 2014b).

8.3.2 Growth-composition modeling

Chemical zoning in quartz formed during prograde metamorphism is investigated through implementation of growth-composition models. The analytical solutions are well suited for evaluating the effects of various processes on the partitioning behavior of Ti into quartz prior to encapsulation in garnet. For all calculations, quartz growth is considered to follow a steady state geotherm (one-layer model) derived from Fourier's Law (Spear, 1993) with average bulk constants for a standard pelitic crust (thermal conductivity, k = 2.25 W m^{-1} K^{-1}; heat production from radioactive decay, A = 0.75 µW m^{-3}; heat flow, Q* = 30 mW m^{-2}; crust thickness, D = 35 km; Figs. 8.3 and 8.4). We recognize that assuming a

steady state burial path is an over-simplification of the process; however, it is considered here for two reasons: (i) the relative burial trend (i.e., the *P-T* trajectory) is more important than the exact path

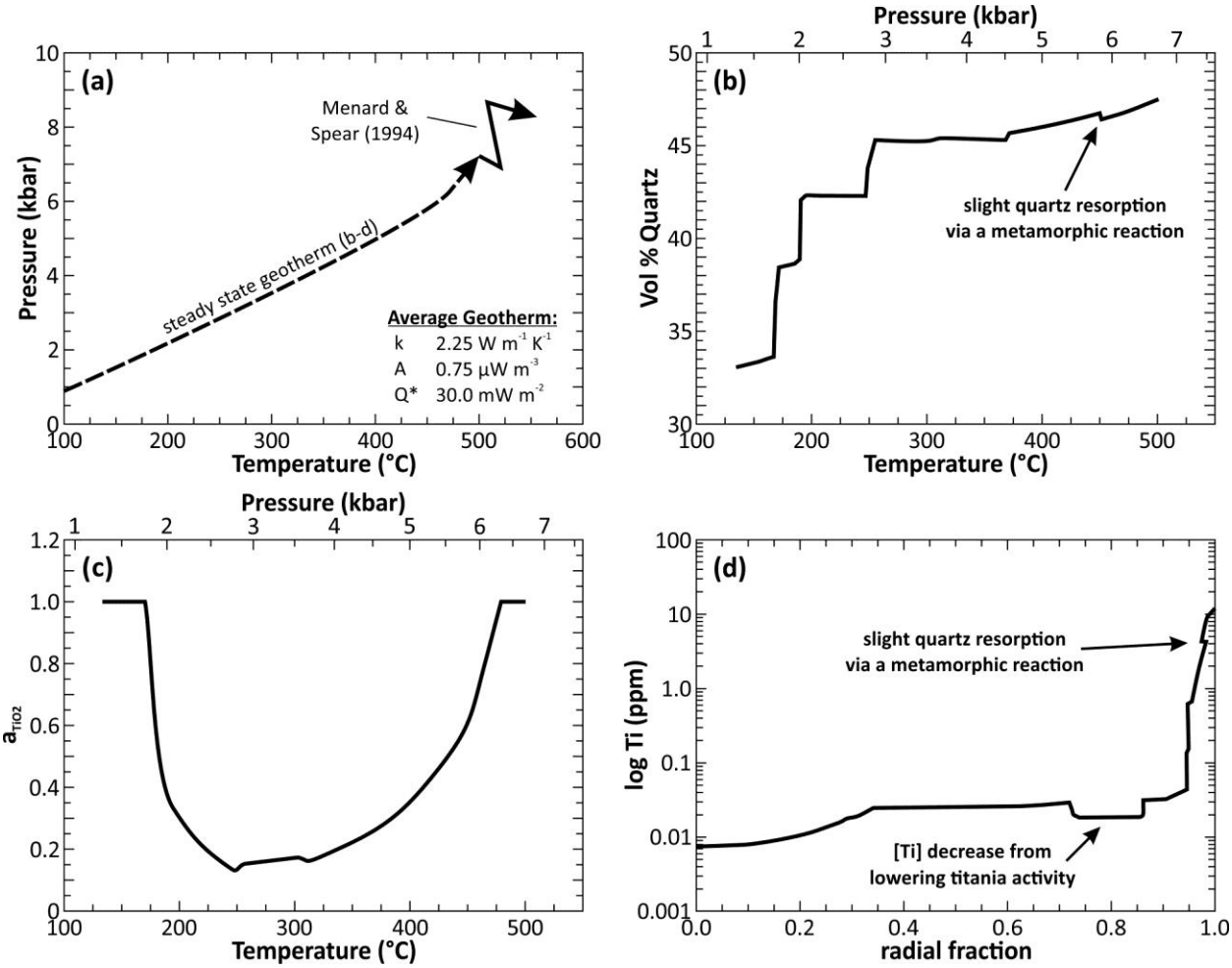

Figure 8.4. Thermodynamic modeling results for quartz production and titania activity that are used in growth-composition models (Fig. 8.5). (a) Projection of an average steady state geotherm in *P-T* space. Garnet growth path from Menard & Spear (1994) shown for reference. (b) Volume percent quartz in bulk rock along the steady state geotherm shown in (a) is output from thermodynamic calculations. A drastic increase in quartz is observed at temperatures < 300 °C and is attributed to Si release during diagenetic reactions (such as a smectite to illite transformation). Only minor amounts of silica are liberated due to metamorphic reactions (> 300 °C). (c) Calculated titania activity along the profile shown in (a). At low temperatures, ilmenite and rutile are not stable, resulting in low titania activities. Stabilization of sphene, and later ilmenite, produces an increased a_{TiO_2} at temperatures > ~400 °C. (d) Simulated Ti concentrations in quartz as a function of radial fraction (core = 0, rim = 1), using the silica liberation results in (b) and the dynamic titania activity modeled in (c). This modeling suggests ~95% of the radial profile observed would contain Ti concentrations < 100 ppb, with a sharp increase in Ti at the rim. The profile presented in (d) is used for the quadrant projection shown in Fig. 8.5c.

taken; i.e., a higher geothermal gradient should produce a compositional growth zoning similar to that determined in this study (albeit shifted towards higher Ti concentrations); and (ii) a perturbed system will evolve towards a steady state providing time scales are sufficiently long. In addition, it is important

to mention that all scenarios investigated here follow ideal end-member solutions, whereas in nature processes would be coupled and more complex than described here. The starting model temperature is 134 °C and the maximum temperature is that at which garnet growth starts (500 °C; Menard & Spear, 1994; Ashley *et al.*, 2013). Illustrative representations of these simulation results are presented as quadrant cross-sections of spherical grains, where volume growth is transformed to radial growth to more meaningfully reflect the crystal cross-section (analogous to that imaged in a thin section cut through a quartz crystal; Fig. 8.5).

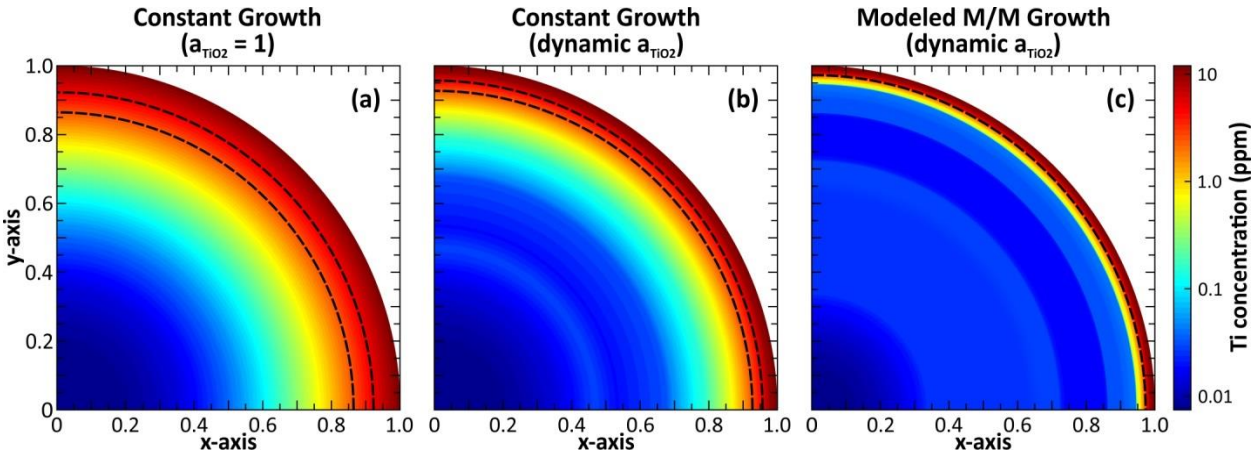

Figure 8.5. Growth-composition models for Ti in quartz along the steady state geotherm shown in Fig. 8.4a. (a,b) Constant volume growth with a fixed titania activity of 1.0 (a) and dynamic activity (b) considered. (c) Growth attributed to Si-producing diagenetic and metamorphic reactions (with dynamic activity applied). Ti concentrations are shown on a log-scale to emphasize zoning patterns across a large compositional range. Dashed lines boarder zones equivalent to Ti concentrations observed in inclusions in sample 09SD08A (2.5–5 ppm Ti).

The first situation investigated involves a constant volume rate of quartz growth, with a fixed titania activity of 1.0 (Fig. 8.5a). This model is equivalent to solution-transfer processes leading to a constant rate of precipitation of silica on quartz grain boundaries during burial. Scenario two (Fig. 8.5b) also assumes a constant volume rate of quartz growth, however titania activity is considered to be dynamic and changes according to the stable Ti-buffering phase (Fig. 8.3). For the third model (Fig. 8.5c), quartz growth occurs during silica-liberating diagenetic and metamorphic reactions. To determine the volume percent of quartz precipitation along the profile established in Fig. 8.4, the *werami* subsidiary

program to the Perple_X package is implemented. Modeling results are evaluated against inclusion and matrix quartz chemistries observed in sample 09SD08A to infer equilibration conditions.

8.3.3 Raman spectroscopic characterization of fluid inclusions

Unpolarized Raman spectra were collected using the JY Horiba LabRam HR (800 mm) microprobe at Virginia Tech, with a 600 lines/mm grating. Excitation was by a green 514.57 nm (100 mW) solid-state argon laser focused through a 100x objective, with collection by an electronically cooled open electrode CCD. Spectra ranges of ~370–2125 cm^{-1} (centered on 1300 cm^{-1}) and ~2500–2900 cm^{-1} (centered on 3225 cm^{-1}) were measured over 3 accumulations at 10–30 s. Times were adjusted to maximize peak intensities while avoiding detector saturation. The presence of CO_2 in fluid inclusions was evident by the Fermi diad at 1285 cm^{-1} and 1388 cm^{-1}, with H_2O identification through the broad band from ~3100–3700 cm^{-1}. Fluid inclusions from multiple locations within sample 09SD08A were analyzed. Isolated fluid inclusions and inclusions along linear trails of healed fractures in quartz inclusions in garnet were analyzed for composition and mineral content. These results are compared to fluid inclusions in matrix quartz to better constrain evolution of fluids during progressive metamorphism and to assess the ability of garnet to shield fluid and mineral inclusions contained in inclusion quartz from chemical re-equilibration.

8.3.4 Raman spectroscopy of carbonaceous material thermometry

Graphite commonly forms in metasedimentary rocks during diagenesis and metamorphism of organic material. During the conversion from amorphous carbonaceous material to well crystallized graphite with increasing metamorphic grade the Raman spectrum changes systematically (Beyssac *et al.*,

2002). Beyssac *et al.* (2002) derived a linear expression to correlate the degree of graphitization to temperature. A peak area ratio (R2) is used, where R2 = D1/(G+D1+D2) (where D1, G and D2 represent the areas under the D1, G and D2 peaks, respectively) and T (°C) = -455·R2+641. D1–D3 are defect bands at 1350cm^{-1}, 1620 cm^{-1} and 1500 cm^{-1}, respectively, and G is a graphite band at 1580 cm^{-1}. D2 and D3 form shoulders on the G band, with D3 neglected because it is difficult to resolve as a result of the relatively low-intensity and broadness, and overlap with the G band. A peak intensity ratio (R1) equals D1/G. Estimated uncertainty in temperature with the peak area technique is ±50 °C (Beyssac *et al.*, 2002; Rahl *et al.*, 2005). Completely encapsulated graphite inclusions in quartz were analyzed in this study to avoid complications associated with measuring graphite exposed to the thin section surface, where a vectorized high stress induced through mechanical polishing may cause surface flaking and deflection of crystal orientation.

Analytical conditions that were used for fluid inclusion characterization were also used for graphite analyses. A six-degree polynomial baseline correction is implemented, with peak fitting through a Gaussian function. Graphite was analyzed from two microstructural settings in quartz inclusions in garnet: as isolated inclusions within the quartz crystals and from linear inclusion trails along healed fractures in quartz. Analysis of these two populations was conducted to correlate temperatures with quartz growth/recrystallization and fracture healing, respectively.

8.4 Results

8.4.1 Phase stability, quartz growth and titania activities

At the start of the modeled profile, 19.1 modal % stilbite (zeolite) and 6.5 modal % stilpnomelane (smectite) are stable, in addition to 7.1% chlorite (Fig. 8.6a). By ~190 °C, all stilbite and

stipnomelane transforms to laumontite and illite (white mica). Further heating produces prehnite (epidote; ~250 °C), with zoisite and minor amounts of actinolite stable above ~305 °C; increases in modal abundances of chlorite, albite and quartz balance the reactions during progressive heating through the anchizone and into the epizone. A significant amount of quartz growth is expected during these reactions (>15%; Figs. 8.3 and 8.4b). Minor (< 1 volume %) quartz resorption is observed at ~450 °C associated with An-rich plagioclase above the peristerite gap (Fig. 8.4b).

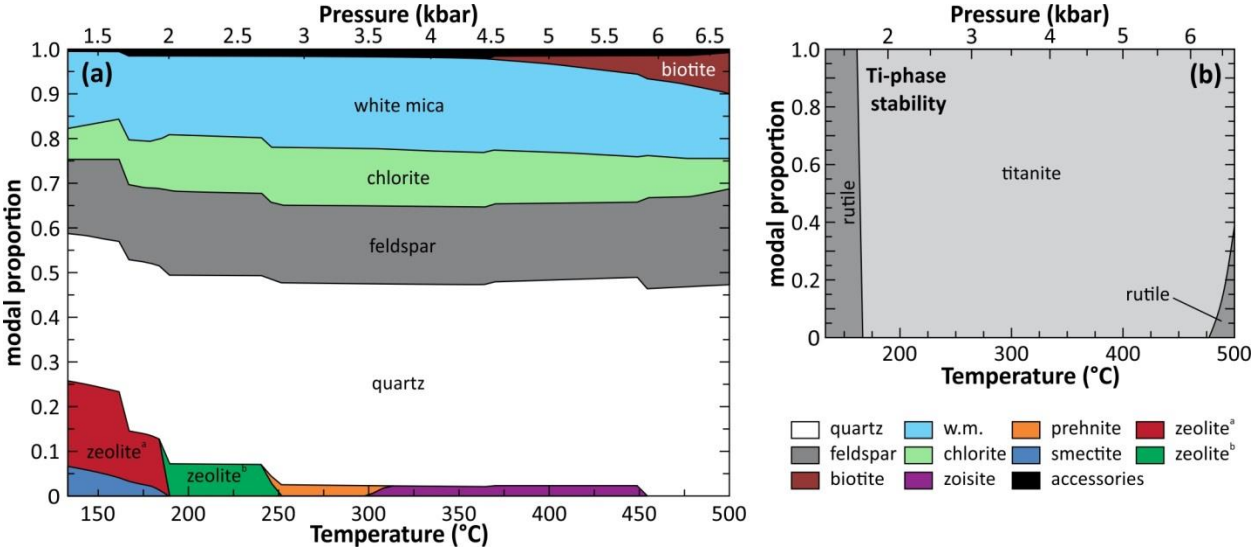

Figure 8.6. Modeled phase abundance (in modal proportion) along the steady state geotherm profile shown in Figs. 8.3 and 8.4. (a) At lower temperatures, smectite and zeolite clay minerals are stable. Prograde heating results in the release of silica during clay transformation to white mica (w.m.), producing an increase in the overall abundance of quartz. Accessory minerals include rutile, ilmenite, titanite and actinolite. Zeolite[a] and zeolite[b] refers to stilbite and laumonite varieties, respectively. (b) Model proportion of Ti-bearing accessory phases. Fields where rutile (or ilmenite) is stable would facilitate Ti solubility in quartz with a titania activity of ~1.0.

Biotite growth initiates at ~370 °C (4.5 kbar), with garnet-in reactions occurring at ~500 °C (6.8 kbar; Fig. 8.3). Garnet growth results in rapid consumption of chlorite, which by ~530 °C reacts out and results in silica release that is interpreted by Ashley *et al.* (2013) to lead to precipitation of matrix quartz during heating.

Rutile is stable at low temperatures (< 200 °C); however it occurs in very low abundance (< 0.5 modal %) and is likely the result of diagenetic growth through dissolution of Ti-rich detrital minerals such as rutile or titanite (e.g., Valentine & Commeau, 1990). This results in titania activities of 1.0 at low

temperatures (Fig. 8.4c). At higher temperatures (> 200 °C) titanite is present which results in a reduction of a_{TiO_2}, until rutile stabilizes near 500 °C (Fig. 8.6b).

8.4.2 Chemical zoning during quartz growth

The first two growth-composition simulations assumed a constant volume rate of quartz growth through processes such as solution transfer. Both simulations predict increasing Ti from quartz core to rim, corresponding to increasing solubility of Ti in quartz during heating, with peak concentrations of ~10 ppm Ti immediately preceding inclusion of the quartz into the garnet host (Fig. 8.5a,b). The consideration of dynamic titania activity results in a reduction in Ti associated with the absence of ilmenite or rutile stability, where there is a decrease in titania activity (Fig. 8.4c). These effects are most notable at radial fractions 0.5–0.7 in Fig. 8.5b, with continued growth along the heating path resulting in lower Ti concentrations due to the reduced TiO_2 activity. In addition, [Ti] > 1.0 ppm is restricted to the radial fractions > 0.85 (Fig. 8.5b), compared to < 0.8 required for the model, assuming a_{TiO_2}= 1.0 (Fig. 8.5a).

The third growth model considers silica production through diagenetic and metamorphic reactions and shows a significantly different zonation pattern. The majority of growth occurs at T < 300 °C and the resultant quartz contains very low concentrations of Ti (~95 radial % of quartz contains <50 ppb Ti; Figs. 8.4d and 8.5c). Late stage quartz growth through Si-liberating metamorphic reactions precipitates rims with higher [Ti], up to ~10 ppm – similar to the constant growth models. The same Ti depletion zone resulting from reduced titania activity observed in Fig. 8.5b is seen in Figs. 8.4d and 8.5c; however, it is offset towards the rim due to variable volume growth rates during burial.

Portions of the modeled quartz within the compositional range measured in sample 09SD08A (2.5–5 ppm Ti) are illustrated by dashed lines in Fig. 8.5. In each scenario, this zone is small – about 12% of the radial fraction for constant growth at a_{TiO_2}= 1.0, decreasing to < 2% of the radial fraction when growth through reactions is considered.

8.4.3 Fluid inclusion characterization

Twelve fluid and six mineral inclusions from quartz inclusions in garnet and from matrix quartz were analyzed to understand the mineral and fluid distribution in these microstructural domains. Quartz inclusions in garnet contain isolated inclusions of high-density (liquid) CO_2, graphite, rutile and titanite (Fig. 8.7b). CO_2 inclusions typically have an equant or negative crystal shape and only rarely contain two phases (liquid and vapor) at room temperature. This indicates that the density of the CO_2 in the inclusion is greater than the density of liquid CO_2 in equilibrium with vapor at room temperature, or >0.75 g cm^{-3}. Analysis of the fluids shows sharp, high-intensity bands, which is characteristic of liquid CO_2. Likewise, healed fractures in quartz inclusions in garnet contain high-density CO_2 and graphite inclusions (Fig. 8.7c). Inclusions are less abundant in matrix quartz, and where analyzed, only consist of liquid CO_2 (Fig. 8.7d). H_2O was not detected in any of the inclusions analyzed, as evidenced by the absence of the broad H_2O band at ~3100–3700 cm^{-1} (Fig. 8.7). We note, however, that Lamadrid *et al.* (2014) documented that small amounts of H_2O may be present but not detected during analysis of CO_2-rich inclusions at room temperature, but may be revealed during analysis at higher temperature. All inclusions observed were small (a few µm in diameter); however the largest documented (~8 µm) fluid inclusions are present as isolated inclusions in quartz inclusions in garnet.

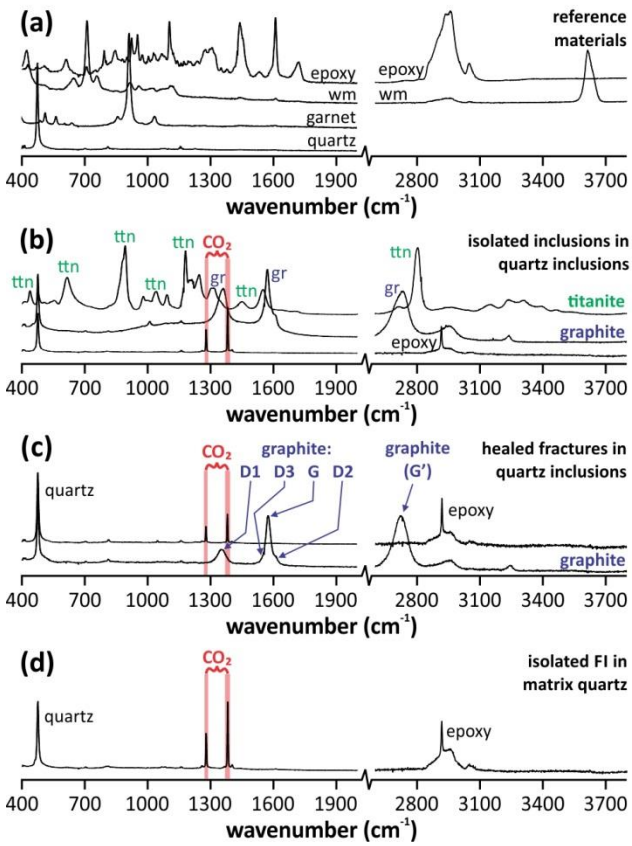

Figure 8.7. Raw (unmodified) Raman spectra of mineral and fluid inclusions in sample 09SD08A. (a) Reference spectra of quartz, garnet, white mica, and epoxy. Most measurements include epoxy lines due to analyzing in transparent phases with 30 µm thin sections; epoxy lines are a typical artifact associated with using thin sections cemented to glass plates. (b) Measurements of isolated fluid and mineral inclusions within quartz inclusions in garnet. Inclusions typically consist of high density liquid CO_2 inclusions, with minor amounts of graphite and titanite inclusions observed. (c) Graphite and high density liquid CO_2 inclusions analyzed in healed linear fractures from quartz inclusions in garnet. (d) Fluid inclusions in matrix quartz are less common than observed in quartz inclusions within garnet. Composition of the fluid is only liquid CO_2, with no H_2O peaks present. Graphite and titanite were not observed as inclusion phases in matrix quartz.

8.4.4 Temperature constraints from Raman spectroscopy

Analyses of isolated graphite inclusions in quartz result in smaller G/D1 peak intensity ratios and more pronounced D2 shoulders on the graphite band than observed for graphite inclusions along healed fractures in quartz. This trend is generally indicative of lower temperatures and less well-crystallized graphite (Kouketsu *et al.*, 2014; their Fig. 2). Peak positions, intensities, widths and areas obtained from Raman analysis are listed in Table 8.2 (Fig. 8.8). The resultant peak intensity ratios (R1) for the graphite are 0.69 and 0.36 and the peak area ratios (R2) are 0.52 and 0.35 for the isolated inclusions and

inclusions along healed fractures, respectively. This equates to temperatures of 408 ± 50 °C for isolated inclusions and 488 ± 50 °C for inclusions along healed fractures.

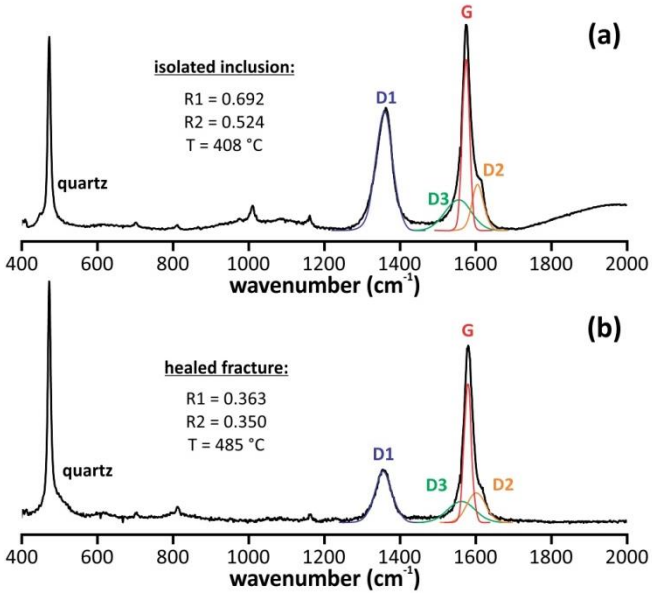

Figure 8.8. Raman spectroscopy analyses on completely encapsulated graphite inclusions in quartz grains that in turn are preserved as inclusions in garnet. Graphite is analyzed as isolated inclusions within the quartz crystals (a) and along healed fractures (b). Location and peak-fitting results of the defect bands (D1–D3) and graphite band (G) are shown, with calculated peak area ratios and resultant RSCM temperatures. Spectra have undergone background correction.

Table 8.2. Raman spectroscopy peak fitting results on graphite inclusions

Loc.	band type	position (cm^{-1})	intensity (a.u.)	FWHM (cm^{-1})	peak area	Results	
isolated	D1	1359.9	13827.1	55.11	473755	**R1 =**	**0.688**
	G	1578.9	20089.9	23.95	306903	**R2 =**	**0.524**
	D2	1611.0	5263.8	36.54	123159	**T (°C) =**	**408**
	D3	1558.2	3512.1	87.67	195932		
healed fracture	D1	1358.1	1362.3	56.41	47772	**R1 =**	**0.363**
	G	1584.2	3757.2	24.09	57768	**R2 =**	**0.343**
	D2	1605.4	870.6	60.55	33729	**T (°C) =**	**488**
	D3	1562.9	486.9	89.15	27637		

Loc. – microstructural location; FWHM – full width half maxima; a.u. – arbitrary units

8.5 Discussion

8.5.1 Evaluating the validity of models for predicting quartz production through diagenesis

One of the growth models considered here examines quartz precipitated as a result of Si-liberating diagenetic and metamorphic reactions (Fig. 8.5c). Considering the volume of quartz produced

through these processes, diagenesis is more important than metamorphism because significant silica production occurs during the early prograde history. van de Kamp (2008) estimated the amount of silica released through the transformation of smectite to illite to muscovite, assuming conservation of alumina. This work is based on the fact that smectite clays alter to less siliceous illite (and at higher temperatures, muscovite) during burial and heating (e.g., Hower *et al.*, 1976; Lynch *et al.*, 1997). Nearly 95% of the transformation from smectite to illite occurs at ≤ 200 °C, with an equivalent amount of illite being converted to muscovite by 300 °C (Merriman & Frey, 1999). The findings of van de Kamp (2008) suggests the alteration of sedimentary muds to shales releases ~14–20 wt. % SiO_2 during heating from surface temperatures to 200 °C, with an additional 18–28 wt. % silica evolved by 500 °C. Our simulations suggest that >12 volume % (~16.5 wt. %) of quartz is produced during heating from 134 °C to 300 °C (Fig. 8.4b), with little additional silica produced through metamorphic reactions at higher temperatures (until the ~3 volume % chlorite-out, silica-producing reaction at ~525 °C discussed by Ashley et al., 2013, is reached). Thus, these results are similar to estimates of the amount of silica produced during the smectite to muscovite transformation in the same temperature window (~15 wt. %; van de Kamp, 2008, their Fig. 1). Likewise, zeolite-group minerals are expected to liberate significant amounts of silica during diagenesis. Heulandite group zeolites are high in silica, containing Si/Al ratios of 4.74–5.19 (Tsolis-Katagas & Katagas, 1990), which is greater than that observed for smectite (Si/Al ratios of ~3; van de Kamp, 2008). The higher silica release predicted in our thermodynamic models relative to a pure smectite evolution by van de Kamp (2008) is likely due to the stability of stilbite (zeolite) at low temperatures, which contains 27 cations per formula unit (cpfu) of Si, decreasing to 4 cpfu Si in the transformation to laumonite (zeolite) at ~190 °C. The actual amount of silica produced is thus sensitive to the starting mineral assemblage, which can be reasonably constrained through pseudosection modeling of the representative bulk rock composition. The large amount of silica produced predicted by the thermodynamic models is consistent with the findings by van de Kamp (2008) and suggests that the

majority of quartz growth should occur at low temperatures (< 300 °C). This is consistent with observations of natural samples. These calculations assume silica remains in the system (closed-system) and is not liberated from the rock, which forms the basis of the isochemical thermodynamic models. Leached silica from shales (i.e., removed from the rock) would inhibit continued quartz growth, in which other growth processes would have to be active.

8.5.2 Early prograde growth processes

Neither of the numerical growth models considered in this paper produce Ti-zoning characteristics similar to those observed in quartz inclusions in garnet grains from sample 09SD08A. Whereas the analyzed profiles have homogeneous Ti concentrations (± a few ppm Ti), growth through solution transfer and diagenetic/metamorphic reactions would result in strongly zoned crystals that span over three orders of magnitude in Ti concentration (Fig. 8.9). Ti variations of this magnitude would be easily resolved, owing to the sensitivity of CL imaging, and therefore solution-transfer and reaction-producing events cannot be the primary mechanism responsible for the observed Ti distribution in quartz. Rather, the homogenized, low-Ti characteristics of the inclusion quartz are identical to quartz that has been dynamically recrystallized through subgrain rotation (Grujic *et al.*, 2011; Ashley *et al.*, 2013; Kidder *et al.*, 2013). These recent studies have shown that regardless of the original (undeformed) quartz porphyroclast composition, newly recrystallized grains have [Ti] <10 ppm. This appears to be a commonly observed consequence of dynamic recrystallization through subgrain rotation, and speaks to the efficiency of this mechanism in liberating Ti from the quartz lattice (Ashley et al., 2014b). In addition, remnants of porphyroclasts are observed as partially recrystallized subgrains that contain higher [Ti] than the newly formed subgrains (Grujic *et al.*, 2011; Ashley *et al.*, 2013). We interpret the patches of

higher Ti concentration in the inclusion quartz (Fig. 8.2a,d) as being an artifact of this heterogeneous and incomplete recrystallization process.

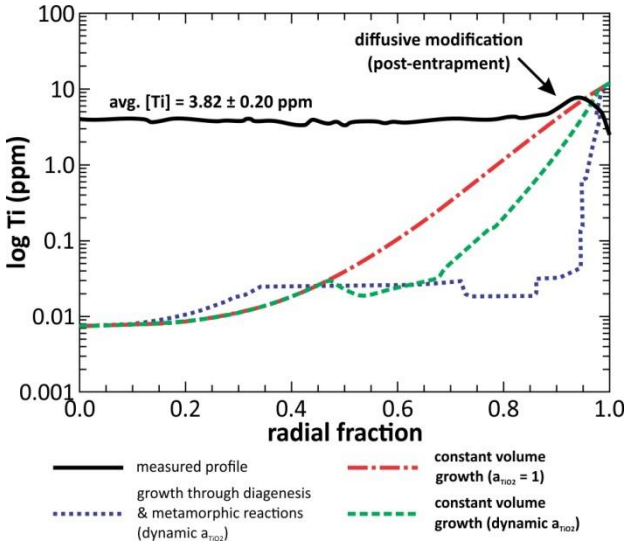

Figure 8.9. Comparison of Ti distribution from growth-composition models (Fig. 8.5) and measured Ti profiles in inclusion quartz (sample 09SD08A; Ti analyses from Ashley *et al.*, 2013). Measured profile is from arrowed traverse shown in Fig. 8.2d. Except for the rim composition, all models predict much lower Ti concentrations than observed.

The presence of triple-junctions between inclusion quartz grains (Fig. 8.2a,d) also supports the interpretation that re-equilibration of Ti in quartz inclusions represents a pre-encapsulated recrystallization event. Static recrystallization may be attributed to the period of heating after dynamic recrystallization re-equilibrates quartz chemistries. Temperatures and/or duration of heating that occurred before encapsulation of quartz in garnet must have been sufficient to promote development of quartz grain boundary migration from an irregular to an optimal low-energy configuration, as indicated by observed triple-junctions between inclusion boundaries. Fracturing and healing of fractures must have occurred post-recrystallization but prior to encapsulation because: (i) healed fractures cross-cut quartz grain boundaries and regions of quartz with reset Ti chemistries and, (ii) encapsulation would inhibit fracture healing due to the isolation from fluids present in the matrix. Brittle fracturing that post-dates recrystallization at higher temperatures could be the result of a localized rapid increase in strain rate, shifting the rock from the plastic to the brittle regime (Knipe, 1989, 1990). However, such

interpretations applied to our sample are speculative and cannot be confirmed due to the limitations on the data that may be retrieved from inclusion quartz (e.g., grain size analysis for paleo-stress and strain rate estimation).

8.5.3 Fluid evolution during progressive metamorphism, with implications on thermodynamic modeling

The widespread presence of high-density, liquid CO_2 fluid inclusions with no observed H_2O is significant for several reasons. First, these fluid inclusions occur in quartz that grew throughout the prograde history (both inclusion and matrix quartz). Carbonaceous material is not present in the matrix, suggesting that the fluid component of the rock contained, to some extent, CO_2 *throughout the duration of the prograde history*, resulting from the maturation of biogenic carbon (Huff & Nabelek, 2007). The presence of CO_2-rich fluid inclusions in quartz inclusions that formed during the prograde history has important implications concerning the origin of CO_2-rich fluid inclusions in medium to high-grade metamorphic rocks. Often the isochores for the fluid inclusions do not project through the peak metamorphic conditions. This, in turn, has led some workers to suggest that the fluid inclusions have re-equilibrated volumetrically along the retrograde path (Sterner & Bodnar, 1989; Vityk *et al.*, 2000), or that the fluid inclusions originally contained an H_2O-CO_2 mixed fluid and later experienced post-entrapment loss of H_2O (Hollister, 1990; Bakker & Jansen, 1991), whereas still other workers have suggested that the CO_2-rich fluid inclusions were trapped late in the metamorphic history during retrogression (Lamb *et al.*, 1987; Lamb, 1990). The presence of CO_2-rich fluid inclusions in quartz inclusions that formed and were encapsulated in garnet along the prograde path suggests that at least in some cases CO_2-rich fluids were present during prograde and/or peak metamorphism.

Thermodynamic models are commonly applied in metamorphic petrology to constrain stability fields of mineral assemblages, which can be used to infer *P-T* conditions experienced by the rock. These

models require knowledge of the fluid composition throughout the metamorphic history. When carbonaceous material is not observed in the matrix, a pure H_2O fluid phase is typically assumed. The presence of CO_2 could have an impact on the predicted mineral stability fields, typically resulting in extension of these fields to higher temperatures (e.g., Will *et al.*, 1990; Evans *et al.*, 2010). This translation of phase boundaries is most notable with the minor addition of CO_2 to the fluid at lower temperatures (e.g., 400 °C), because a_{CO_2} increases asymmetrically and rapidly at $X_{CO_2} < 0.2$ in the CO_2–H_2O system (Sterner & Pitzer, 1994; Holland & Powell, 2003). In this scenario, temperature reported for metamorphic reactions may be underestimated. The scarcity of CO_2 fluid inclusions in matrix quartz relative to inclusion quartz may suggest a significant degassing of fluids from the rock during progressive burial, as suggested by Yardley & Bodnar (2014). This is expected, as metamorphic decarbonation would continue to higher temperatures as more carbon is lost from the system. The removal of CO_2 may minimize the impact CO_2 has on modeled phase stability, leaving peak *P-T* estimation through this method the most reliable part of the entire metamorphic history.

The presence of titanite inclusions is significant for two reasons. First, if the temperatures retrieved from isolated graphite inclusions are valid, the isolated titanite crystals would have formed within their respective stability window (albeit at the upper-temperature limit) before rutile and ilmenite stabilize at higher temperatures (>410 °C; Fig. 8.6). This correlation between observed and predicted assemblages increases our level of confidence in the ability of the applied thermodynamic models to simulate processes occurring in nature. As mentioned previously, addition of CO_2 to these models would result in the extension of mineral stabilities to higher temperatures. This also confirms that titania activities would have been < 1.0 during the time of quartz re-equilibraiton prior to inclusion in garnet. The presence of titanite inclusions, despite the transformation to rutile at temperatures much lower than the peak temperature (550 °C) suggests that inclusion of minerals inside rigid hosts may greatly extend the stability range of the trapped phases to greater temperatures. This may be a function

of not having the appropriate components necessary to form the new phase (unlikely, as rutile would only require TiO_2), or due to the pressurization that occurs when minerals are fully encapsulated in rigid hosts (e.g., Rosenfeld & Chase, 1961; Enami *et al.*, 2007; Ashley *et al.*, 2014a). Quartz would not necessarily serve as a "rigid" host for titanite; however the surrounding garnet would expand less during a heating profile than would the quartz inclusion (quartz has a larger thermal expansivity, especially when approaching the lambda transition to β-quartz), allowing the quartz inclusion to become pressurized. This pressurization would be transferred to the titanite inclusion, providing a localized inclusion pressure environment that would be greater than the externally applied lithostatic pressure and would extend titanite stability to higher temperature.

8.5.4 Assumptions about provenance through a back calculation approach

The involvement of quartz in metamorphic reactions, solution transfer processes and dynamic recrystallization makes this mineral exceedingly susceptible to overprinting of early prograde conditions. This is unfortunate as detrital quartz grains could potentially give insight into the bedrock source from which they were eroded. However, quartz inclusions in garnet, as we show here, potentially provide a record for early prograde conditions in the bedrock source that otherwise would have been overprinted had the quartz grains not been encapsulated by garnet. Furthermore, the presence of rutile needles in the quartz inclusions may allow some basic, first-order assumptions about the provenance of the original sedimentary quartz.

Rutile needles in quartz are typically interpreted to have formed by exsolution of Ti from the quartz lattice (Cherniak *et al.*, 2007). The presence of the needles in inclusion quartz but not in matrix quartz suggests that rutile is inherited from the pre-sedimentary source or is a byproduct of exsolution via early prograde processes. Rutile needles in quartz are most often found in high temperature

metamorphic, volcanic, and hydrothermal quartz, which is logical considering the amount of Ti required before rutile nucleation and growth would occur (at least 100s of ppm Ti). Growth of the needles is the result of diffusion from Ti in quartz and often results in Ti depletion halos around the rutile needles (e.g., Cherniak *et al.*, 2007; Ague & Eckert, 2012).

However, in our sample 09SD08A, no depletion halos are observed; rather, localized Ti enrichment is observed in the surrounding quartz. This is attributed to diffusion into the quartz post-needle formation, during metamorphic heating and cooling of this rock (Spear & Wark, 2009; Spear *et al.*, 2012). As previously shown, Ti concentrations in quartz inclusions in garnet are very consistent – typically between 2.5 and 5 ppm. If the needles formed via exsolution through diffusion, a more heterogeneous chemistry would be expected in the quartz inclusions (especially considering the short duration of near peak heating in this field area; Spear *et al.*, 2012; Spear, 2014). In fact, at distances well removed from the rutile needles (100s of μm), one would expect to find Ti concentrations representing the original Ti concentrations prior to needle formation. The original concentrations would have to be sufficiently large to provide enough Ti to exsolve the needles observed, but no such concentrations have been recorded for sample 09SD08A. The mechanism we propose for rutile needle formation in this sample is the early prograde dynamic recrystallization of high-Ti (protolith) quartz, a process that is effective at liberating Ti from quartz (Ashley *et al.*, 2014b). Sweeping grain boundaries and intragranular fluids would provide pathways to transport Ti throughout the crystal, for standard volume diffusion at these low temperatures (<500 °C) would be too sluggish to localize the Ti (Ti will diffuse 0.79 μm in 1 Myr at 500 °C). This process would produce homogeneous quartz with localized domains of high Ti that could later exsolve to form rutile needles.

Regardless of the needle-forming mechanism, assumptions concerning the original quartz composition (and qualitative or semi-quantitative insights into the composition of the quartz in the

sedimentary protolith) can be made through back calculations. Such calculations are rudimentary, but such thought experiments may provide insights into the chemistry and formation conditions of pre-modified quartz, helping to further constrain interpretations related to sedimentary provenance.

8.5.4.1 *Reconstructing quartz chemistries to aggregates of various grain sizes*

In sample 09SD08A, rutile needles are widely spaced and typically measure <1.25 µm in diameter with variable lengths. Lengths of needles are difficult to estimate because they are commonly oriented oblique to the thin section plane, thus their measured length is shorter than their real length. Needles nearly parallel to the plane of the thin section are ~35 µm in length (longer for needles of smaller diameter, and shorter for needles of greater diameter). Using these dimensions, and treating the needles as cylinders, we can calculate the volume of rutile present in these inclusions, and then, using the density (4.23 $g \cdot cm^{-3}$) and molar mass (79.87 $g \cdot mol^{-1}$) of pure rutile, the number of moles of TiO_2 contained in the needles can be calculated.

However, there are several limitations to this method. Firstly, we do not know the original grain size of the pre-recrystallized quartz, because dynamic recrystallization is a grain-size reducing mechanism. Also, static recrystallization (annealing) is indicated within these inclusions by triple junctions in quartz (Fig. 8.2a,d). Lastly, we cannot accurately assess the extent of post deformation solution-transfer processes in quartz. With these limitations in mind, we calculated the relationship between quartz grain size and expected Ti concentration prior to needle formation (Fig. 8.10). In these calculations, quartz is treated as spherical grains, with a density of 2.65 $g \cdot cm^{-3}$ and a molar mass of 60.08 $g \cdot mol^{-1}$. For reference, a range of current inclusion grain sizes was included in Fig. 8.10. Because the inclusions are highly elongated, they are treated as ellipses (oblate spheroids), where the long and short axes are measured to calculate volume, and grain sizes are derived from a sphere of the same volume.

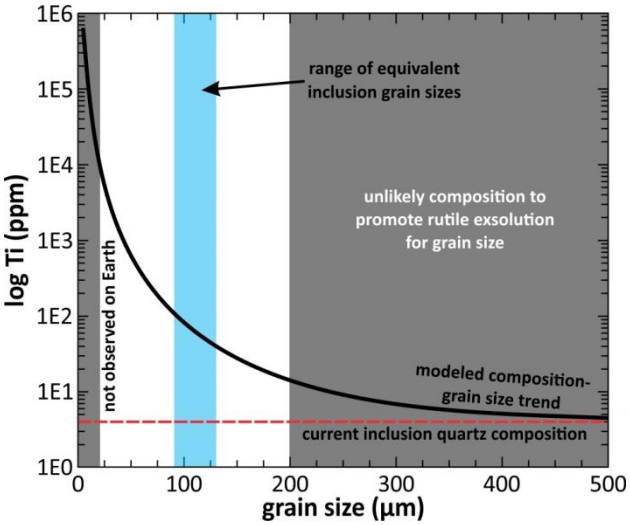

Figure 8.10. Correlation between Ti concentrations in quartz and starting average grain size for quartz aggregates, determined through back calculating the number of moles of TiO_2 present within rutile needles. Shaded fields are unlikely starting compositions (for details see discussion). The range of equivalent grain sizes observed as quartz inclusions in garnets are shown for reference.

With these calculations, we found that an exponential decrease in Ti concentration is required with an increase in starting quartz grain size (Fig. 8.10). Average aggregate grain sizes <40 µm in diameter are expected to contain Ti concentrations >1 wt. %. For average grain sizes >230 µm, concentrations are expected to be below 10 ppm Ti. Therefore, the majority of average dynamically recrystallized quartz grain sizes observed in nature (<200 µm; Stipp *et al.*, 2010) would be expected to have Ti concentrations ranging from 10's of wt. % to ~15 ppm.

The range of possible grain sizes (and thus original compositions) can be further refined by identifying scenarios not typically observed. For example, exceedingly small quartz crystals (<20 µm) would be expected to have over 10,000 ppm (10 wt. %) Ti. To the best of our knowledge, quartz of this composition has never been reported, and even if quartz did exist with this composition, the defect energies associated with this much substitution of the larger Ti^{4+} cation would be expected to expel the Ti, returning the lattice configuration to a lower energy state (Ashley *et al.*, 2014b). Likewise, large grain sizes (>225 µm) are expected to have concentrations <10 ppm. While such low concentrations are observed in nature, the amount of diffusive transport required is significant and unlikely over the near-

peak heating time scales inferred for these rocks. Only a small range in quartz grain sizes contains Ti concentrations similar to those observed in metapelites up to granulite facies (<50 ppm for T <700 °C; Fig. 3 from Ashley & Law, 2015). Therefore, the most likely scenario for original quartz composition is high Ti, such as observed in high temperature metamorphism (>700 °C), igneous rocks, and pegmatitic quartz. The latter can be reasonably excluded because pegmatite quartz typically forms large crystals (mm to cm scale, depending on the size of pockets in the pegmatite body), whereas the maximum grain size for these concentrations would be ~120 μm. At smaller grain sizes, Ti transport through defects and sweeping grain boundaries is possible. Note that if the volume of the rutile needles is an underestimate, the data shown in Fig. 8.10 would translate towards higher Ti concentrations. This suggests that quartz in these rocks is derived from high-*T* metamorphic or igneous rocks, and through dynamic recrystallization of this Ti-saturated quartz, Ti is liberated and rutile needles are able to form.

As noted above, this approach involves several assumptions and simplifications. In addition to the issues described above, the non-spherical shape of quartz grains would have an effect on the simulations when determining volume of quartz. Also, we assume the original quartz crystal is homogeneous with respect to Ti distribution. Lastly, we treated the rutile needles as isolated grains in an infinite medium of chemically homogeneous quartz (3.82 ppm used, as per the profile shown in Fig. 8.9, and a median value for the range of compositions analyzed). It would be very difficult to assess the original distribution of rutile needles, and few are ever observed in proximity to one another. However, with all of these considerations taken into account, Fig. 8.10 can be used as a *qualitative/semi-quantitative* guide to the original composition of the quartz crystals.

8.5.5 New perspectives on metamorphic evolution

Results of this study allows us to infer a more detailed metamorphic history of sample 09SD08A than was previously possible. Here, we combine these results with previous findings to provide a chronology of events and processes that occurred throughout the *P-T* evolution of the sample (see Fig. 8.11 for a graphical summary of this evolution).

High-Ti quartz formed in a high grade metamorphic or igneous source and was subsequently eroded and transported to form a flysch deposit in the foreland basin of the developing orogen (Doll, 1944; Fisher & Karabinos, 1980). During early stages of burial, clay minerals were transformed into micas through the anchi- and epizones, releasing silica in the process. At ~410 °C, Ti in the original quartz re-equilibrated to very low concentrations (2.5–5 ppm) during subgrain rotation recrystallization of quartz. During recrystallization, isolated inclusions of CO_2, graphite and titanite were encapsulated in the quartz. Grain boundaries were progressively annealed into low-energy configurations during heating, promoting triple-junction "foam" textures between neighboring quartz grains. Brittle fracturing followed, potentially associated with a localized and instantaneous increase in strain rate. Healing of fractures in the quartz occurred at ~490 °C, trapping inclusions of graphite and CO_2. During these early stages, water was largely sequestered into hydrous silicate phases.

Fracture healing was immediately followed by the overstepping of the garnet isograd, with garnet growth encapsulating quartz grains that had a preferred alignment along an S_1 slaty cleavage. Once included, Ti began to diffuse from garnet into the grain boundaries of inclusion quartz. Garnet shielded and disconnected inclusion quartz from chemical communication with the matrix and prevented further recrystallization. Nappe emplacement followed garnet growth, resulting in an isothermal pressure increase of ~2 kbar (Menard & Spear, 1994). Garnets were rotated during development of the S_2 schistosity.

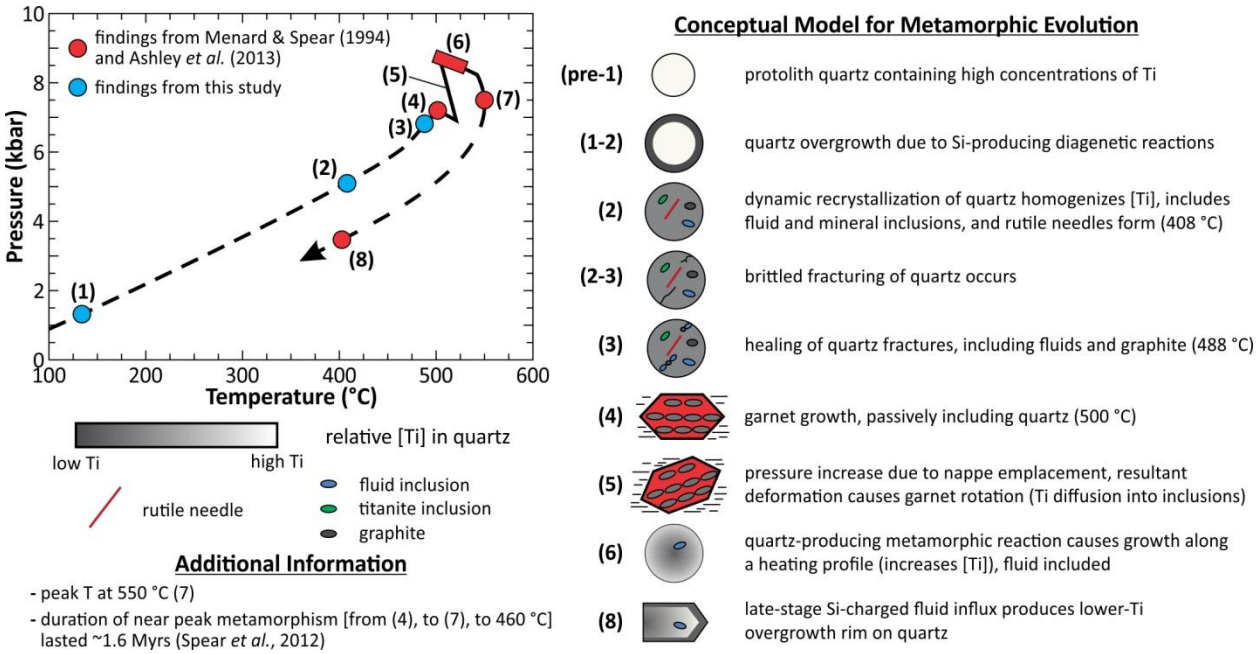

Figure 8.11. Conceptual model for the metamorphic evolution of sample 09SD08A, including findings from Menard & Spear (1994), Spear *et al.* (2012), Ashley *et al.* (2013) and this study.

Immediately following nappe emplacement, the chlorite-out reaction was overstepped and matrix quartz was overgrown with released silica, incorporating higher concentrations of Ti during continued heating (Ashley *et al.*, 2013). Matrix quartz contains few CO_2 inclusions, probably because of removal of carbon from the rock through metamorphic decarbonation processes. Peak temperatures of ~550 °C were reached (Menard & Spear, 1994) before rapid cooling to 460 °C occurred. Rapid cooling is required to impede further diffusion of Ti from the surrounding garnet host into the inclusion quartz. These diffusive profiles are short (<6 µm) and call for near-peak metamorphism to occur in a short amount of geologic time (~1.6 Myr), suggesting pulsed-style metamorphism (Spear *et al.*, 2012). At cooler temperatures (<450 °C), late-stage Si-charged fluid influx occurred resulting in rim overgrowths in matrix quartz of lower Ti concentrations (Ashley *et al.*, 2013).

8.6 Conclusions

This study presents growth-composition models for evaluating mechanisms of Ti equilibration in quartz during early prograde metamorphic evolution. These models show that subsequent recrystallization resets any prior chemistry, and suggest that rocks where garnet growth occurs at lower temperatures would be more informative for probing earlier into the prograde history. This would be particularly so for high-Mn rocks, in which earlier garnet growth may be promoted. The evaluation of fluid and mineral inclusions provides insight into temperatures of deformation processes and the evolution and composition of the fluid component of the rock. Investigations in metamorphic petrology are continuing migrate away from the classical limitations of inferring generic loops to peak pressures and temperatures. Here, we show the potential to deconvolve unprecedented complex histories with respect to pressure, temperature, metamorphic timing and duration, deformation, fluid flux and reactions. With the investigation of quartz inclusions in garnet, we are able to infer environmental controls from the early stages of orogenesis, the signatures of which are typically overprinted and lost during progressive heating and deformation.

Acknowledgements

We thank Brian Romans for thoughtful discussions and direction during the early stages of this work. We are grateful for assistance with use of the Raman spectrometer at Virginia Tech for fluid inclusion characterization by Charles Farley. This work is supported by the National Science Foundation under grant No. EAR-1220345 (awarded to R.D. Law).

References

Ague, J. J. & Eckert, J. O. J. (2012). Precipitation of rutile and ilmenite needles in garnet: Implications for extreme metamorphic conditions in the Acadian Orogen, U.S.A. *American Mineralogist* **97**, 840-855.

Ashley, K. T. (2011). TitaniQ thermobarometry of fabric development in the Strafford Dome, Vermont: Linking microstructures to orogenic processes. *Department of Geology*. Burlington: University of Vermont, 270.

Ashley, K. T., Caddick, M. J., Steele-MacInnis, M., Bodnar, R. J. & Dragovic, B. (2014a). Geothermobarometric history of subduction recorded by quartz inclusions in garnet. *Geochemistry Geophysics Geosystems* **15**, 350-360.

Ashley, K. T., Carlson, W. D., Law, R. D. & Tracy, R. J. (2014b). Ti resetting in quartz during dynamic recrystallization: Mechanisms and significance. *American Mineralogist* **99**, 2025-2030.

Ashley, K. T. & Law, R. D. (2015). Modeling prograde TiO_2 activity and its significance for Ti-in-quartz thermobarometry of pelitic metamorphic rocks. *Contributions to Mineralogy and Petrology* **169**:23, 1-7.

Ashley, K. T., Thigpen, J. R. & Law, R. D. (*in review*). Prograde evolution of the Scottish Caledonides and tectonic implications. *Lithos*.

Ashley, K. T., Webb, L. E., Spear, F. S. & Thomas, J. B. (2013). *P-T-D* histories from quartz: A case study of the application of the TitaniQ thermobarometer to progressive fabric development in metapelites. *Geochemistry Geophysics Geosystems* **14**, 3821-3843.

Auzanneau, E., Schmidt, M. W., Vielzeuf, D. & Connolly, J. A. D. (2010). Titanium in phengite: A geobarometer for high temperature eclogites. *Contributions to Mineralogy and Petrology* **159**, 1-24.

Bakker, R. J. & Jansen, J. B. H. (1991). Experimental post-entrapment water loss from synthetic CO_2-H_2O inclusions in natural quartz. *Geochimica et Cosmochimica Acta* **55**, 2215-2230.

Beyssac, O., Goffé, B., Chopin, C. & Rouzaud, J. N. (2002). Raman spectra of carbonaceous material in metasediments: A new geothermometer. *Journal of Metamorphic Geology* **20**, 859-871.

Cherniak, D. J., Watson, E. B. & Wark, D. A. (2007). Ti diffusion in quartz. *Chemical Geology* **236**, 65-74.

Coggon, R. & Holland, T. (2002). Mixing properties of phengitic micas and revised garnet-phengite thermobarometers. *Journal of Metamorphic Geology* **20**, 683-696.

Connolly, J. A. D. (2009). The geodynamic equation of state: What and how. *Geochemistry Geophysics Geosystems* **10**, 1-19.

Dale, J., Powell, R., White, R. W., Elmer, F. L. & Holland, T. J. B. (2005). A thermodynamic model for Ca-Na clinoamphiboles in Na_2O-CaO-FeO-MgO-Al_2O_3-SiO_2-H_2O-O. *Journal of Metamorphic Geology* **23**, 771-791.

Doll, C. G. (1944). A preliminary report on the geology of the Strafford Quadrangle, Vermont. *Vermont Geological Survey*, 14-28.

Enami, M., Nishiyama, T. & Mouri, T. (2007). Laser Raman microspectrometry of metamorphic quartz: A simple method for comparison of metamorphic pressures. *American Mineralogist* **92**, 1,303-301,315.

Evans, K. A., Powell, R. & Holland, T. J. B. (2010). Internally consistent data for sulphur-bearing phases and application to the construction of pseudosections for mafic greenschists facies rocks in Na_2O-CaO-K_2O-FeO-MgO-Al_2O_3-SiO_2-CO_2-O-S-H_2O. *Journal of Metamorphic Geology* **28**, 667-687.

Fisher, G. W. & Karabinos, P. (1980). Stratigraphic sequence of the Gile Mountain and Waits River Formations near Royalton, Vermont. *Geological Society of America Bulletin* **91**.

Fuhrman, M. L. & Lindsley, D. H. (1988). Ternary-feldspar modeling and thermometry. *American Mineralogist* **73**, 201-215.

Grujic, D., Stipp, M. & Wooden, J. L. (2011). Thermometry of quartz mylonites: Importance of dynamic recrystallization of Ti-in-quartz reequilibration. *Geochemistry Geophysics Geosystems* **12**, 1-19.

Holland, T. & Powell, R. (2003). Activity-composition relations for phases in petrological calculations: An asymmetric multicomponent formulation. *Contributions to Mineralogy and Petrology* **145**, 492-501.

Holland, T. & Powell, R. (2011). An improved and extended internally consistent thermodynamic dataset for phases of petrological interest, involving a new equation of state for solids. *Journal of Metamorphic Geology* **29**, 333-383.

Holland, T. J. B. & Powell, R. (1996). Thermodynamics of order-disorder in minerals: II. Symmetric formalism applied to solid solutions. *American Mineralogist* **81**, 1425-1437.

Holland, T. J. B. & Powell, R. (1998). An internally consistent thermodynamic data set for phases of petrological interest. *Journal of Metamorphic Geology* **16**, 309-343.

Hollister, L. S. (1990). Enrichment of CO_2 in fluid inclusions in quartz by removal of H_2O during crystal-plastic deformation. *Journal of Structural Geology* **12**, 895-901.

Hower, J., Eslinger, E., Hower, M. E. & Perry, E. A. (1976). Mechanism of burial metamorphism of argillaceous sediment: 1. Mineralogical and chemical evidence. *Geological Society of America Bulletin* **87**, 725-737.

Huang, R. & Audétat, A. (2012). The titanium-in-quartz (TitaniQ) thermobarometer: A critical examination and re-calibration. *Geochimica et Cosmochimica Acta* **DOI: 10.1016/j.gca.2012.01.009**, 31.

Huff, T. A. & Nabelek, P. I. (2007). Production of carbonic fluids during metamorphism of graphitic pelites in a collisional orogen - An assessment from fluid inclusions. *Geochimica et Cosmochimica Acta* **71**, 4997-5015.

Kidder, S., Avouac, J.-P. & Chan, Y.-C. (2013). Application of titanium-in-quartz thermobarometry to greenschist facies veins and recrystallized quartzites in the Hsüehshan range, Taiwan. *Solid Earth* **4**, 1-21.

Knipe, R. J. (1989). Deformation mechanisms - recognition from natural tectonites. *Journal of Structural Geology* **11**, 127-146.

Knipe, R. J. (1990). Microstructural analysis and tectonic evolution in thrust systems: Examples from the Assynt region of the Moine Thrust Zone, Scotland. In: Barber, D. J. & Meredith, P. G. (eds.) *Deformation Processes in Minerals, Ceramics and Rocks*, Mineralogical Society of Great Britain and Ireland, Unwin Hyman, London, 228-261.

Kouketsu, Y., Mizukami, T., Mori, H., Endo, S., Aoya, M., Hara, H., Nakamura, D. & Wallis, S. R. (2014). A new approach to develop the Raman carbonaceous material geothermometer for low-grade metamorphism using peak width. *Island Arc* **23**, 33-50.

Lamadrid, H. M., Lamb, W. M., Santosh, M. & Bodnar, R. J. (2014). Raman spectroscopic characterization of H_2O in CO_2-rich fluid inclusions in granulite facies metamorphic rocks. *Gondwana Research* **26**, 301-310.

Lamb, W. M. (1990). Fluid inclusions in granulites: Peak vs. retrograde formation. In: Vielzeuf, D. & Vidal, P. (eds.) *Granulites and Crustal Evolution*, 419-433.

Lamb, W. M., Valley, J. W. & Brown, P. E. (1987). Post-metamorphic CO_2-rich fluid inclusions in granulites. *Contributions to Mineralogy and Petrology* **96**, 485-495.

Lynch, F. L., Mack, L. E. & Land, L. S. (1997). Burial diagenesis of illite/smectite in shales and the origins of authigenic quartz and secondary porosity in sandstones. *Geochimica et Cosmochimica Acta* **61**, 1995-2006.

Mahar, E., Powell, R., Holland, T. J. B. & Howell, N. (1997). The effect of Mn on mineral stability in metapelites. *Journal of Metamorphic Geology* **15**, 223-238.

Menard, T. & Spear, F. S. (1994). Metamorphic *P-T* paths from calcic pelitic schists from the Strafford Dome, Vermont, USA. *Journal of Metamorphic Geology* **12**, 811-826.

Merriman, R. J. & Frey, M. (1999). Patterns of very low-grade metamorphism in metapelitic rocks. In: Frey, M. & Robinson, D. (eds.) *Low-Grade Metamorphism*, Blackwell Science Ltd., Oxford, UK, 313.

Passchier, C. W. & Trouw, R. A. J. (2005). *Microtectonics*. Berlin: Springer, Federal Republic of Germany (DEU).

Powell, R. & Holland, T. J. B. (1999). Relating formulations of the thermodynamics of mineral solid solutions: Activity modeling of pyroxenes, amphiboles, and micas. *American Mineralogist* **84**, 1-14.

Rahl, J. M., Anderson, K. M., Brandon, M. T. & Fassoulas, C. (2005). Raman spectroscopic carbonaceous material thermometry of low-grade metamorphic rocks: Calibration and application to tectonic exhumation in Crete, Greece. *Earth and Planetary Science Letters* **240**, 339-354.

Rosenfeld, J. L. & Chase, A. B. (1961). Pressure and temperature of crystallization from elastic effects around solid inclusions in minerals? *American Journal of Science* **259**, 519-541.

Spear, F. S. (1993). *Metamorphic Phase Equilibria and Pressure-Temperature-Time Paths*. Washington D.C.: Mineralogical Society of America.

Spear, F. S. (2014). The duration of near-peak metamorphism from diffusion modelling of garnet zoning. *Journal of Metamorphic Geology* **DOI: 10.1111/jmg.12099**.

Spear, F. S., Ashley, K. T., Webb, L. E. & Thomas, J. B. (2012). Ti diffusion in quartz inclusions: Implications for metamorphic time scales. *Contributions to Mineralogy and Petrology* **164**, 977-986.

Spear, F. S. & Wark, D. A. (2009). Cathodoluminescence imaging and titanium thermometry in metamorphic quartz. *Journal of Metamorphic Geology* **27**, 187-205.

Sterner, S. M. & Bodnar, R. J. (1989). Synthetic fluid inclusions - VII. Re-equilibration of fluid inclusions in quartz during laboratory-simulated metamorphic burial and uplift. *Journal of Metamorphic Geology* **7**, 243-260.

Sterner, S. M. & Pitzer, K. S. (1994). An equation of state for carbon dioxide valid from zero to extreme pressures. *Contributions to Mineralogy and Petrology* **117**, 362-374.

Stipp, M., Tullis, J., Scherwath, M. & Behrmann, J. H. (2010). A new perspective on paleopiezometry: Dynamically recrystallized grain size distributions indicate mechanism changes. *Geology* **38**, 759-762.

Tajčmanová, L., Connolly, J. A. D. & Cesare, B. (2009). A thermodynamic model for titanium and ferric iron solution in biotite. *Journal of Metamorphic Geology* **27**, 153-165.

Thomas, J. B., Watson, E. B., Spear, F. S., Shemella, P. T., Nayak, S. K. & Lanzirotti, A. (2010). TitaniQ under pressure: The effect of pressure and temperature on the solubility of Ti in quartz. *Contributions to Mineralogy and Petrology* **160**, 743-759.

Tinkham, D. K., Zuluaga, C. A. & Stowell, H. H. (2001). Metapelite phase equilibria modeling in MnNCKFMASH: The effect of variable Al_2O_3 and MgO/(MgO+FeO) on mineral stability. *Mineralogical Society of America: Geological Materials Research* **3**, 1-43.

Tsolis-Katagas, P. & Katagas, C. (1990). Zeolitic diagenesis of Oligocene pyroclastic rocks of the Metaxades area, Thrace, Greece. *Mineralogical Magazine* **54**, 95-103.

Valentine, P. C. & Commeau, J. A. (1990). Fine-grained rutile in the Gulf of Maine - diagenetic origin, source rocks, and sedimentary environement of deposition. *Economic Geology* **85**, 862-876.

van de Kamp, P. C. (2008). Smectite-illite-muscovite transformations, quartz dissolution, and silica release in shales. *Clays and Clay Minerals* **56**, 66-81.

Vityk, M. O., Bodnar, R. J. & Doukhan, J. C. (2000). Synthetic fluid inclusions: XV. TEM investigation of plastic flow associated with re-equilibration of synthetic fluid inclusions in natural quartz. *Contributions to Mineralogy and Petrology* **139**, 285-297.

Wark, D. A. & Watson, E. B. (2006). TitaniQ: A titanium-in-quartz geothermometer. *Contributions to Mineralogy and Petrology* **152**, 743-754.

White, R. W., Powell, R. & Holland, T. J. B. (2001). Calculation of partial melting equilibria in the system Na_2O-CaO-K_2O-FeO-MgO-Al_2O_3-SiO_2-H_2O (NCKFMASH). *Journal of Metamorphic Geology* **19**, 139-153.

White, R. W., Powell, R. & Holland, T. J. B. (2007). Progress relating to calculation of partial melting equilibria for metapelites. *Journal of Metamorphic Geology* **25**, 511-527.

Whitney, D. L. & Evans, B. W. (2010). Abbreviations for names of rock-forming minerals. *American Mineralogist* **95**, 185-187.

Will, T. M., Powell, R. & Holland, T. J. B. (1990). A calculated petrogenetic grid for ultramafic rocks in the system CaO-FeO-MgO-Al_2O_3-SiO_2-CO_2-H_2O. *Contributions to Mineralogy and Petrology* **105**, 347-358.

Yardley, B. W. & Bodnar, R. J. (2014). Fluids in the Continental Crust. *Geochemical Perspectives* **3**, 127.

Zeh, A., Klemd, R. & Barton, J. M. (2005). Petrological evolution in the roof of the high-grade metamorphic Central Zone of the Limpopo Belt, South Africa. *Geological Magazine* **142**, 229-240.

Chapter 9

Prograde Evolution of the Scottish Caledonides and Tectonic Implications

Kyle T. Ashley[1], J. Ryan Thigpen[1], Richard D. Law[1]

[1]*Department of Geosciences, Virginia Polytechnic Institute and State University, Blacksburg, VA 24061, USA*

Published March 2015 in *Lithos*.

Abstract

Recent thermometric analyses of samples collected in thrust-parallel structural transects across the Scandian (435–415 Ma) orogenic wedge in northwest Scotland provide a comprehensive characterization of the synorogenic retro-wedge thermal architecture. However, the paucity of petrologically-important metamorphic mineral phases (e.g. staurolite, Al-silicates) has limited investigation of pressure-temperature (*P-T*) histories, which hinders our ability to examine the nature of orogen-scale kinematic and thermal coupling. New data collected along a foreland-to-hinterland transect from the Moine to the Naver thrust sheets provides additional constraints for characterizing the prograde metamorphic evolution. In addition, we characterized Ti diffusion profiles in quartz inclusions in garnet to constrain duration of metamorphic heating. These results are used to develop coupled kinematic-thermal models of Scandian orogenic evolution.

Early garnet core growth conditions are constrained by isopleth intersections, with peak *P-T* estimates determined by conventional exchange and net transfer thermobarometry and thermodynamic calculations. Most samples follow normal prograde heating and burial profiles, with peak conditions of 450 °C and 5.0 kbar in the immediate hanging wall to the Moine thrust, increasing in temperature and pressure to 733 °C and 9.5 kbar in the immediate hanging wall to the Naver thrust. These normal prograde pressure trajectories are interpreted to reflect burial of incipient thrust sheets beneath the overriding wedge at the leading edge of the orogen. Prograde heating coeval with burial is interpreted to result from surface-directed isotherm perturbation due to thrust-related advection in the overriding wedge. One exception to this is a sample from the top of the Moine thrust sheet, where prograde heating occurs during decompression (540 °C and 8.1 kbar to 590 °C and 7.0 kbar). In this case, the short lag times between motion on the Moine and Ben Hope thrusts may have limited advectionary heating until after exhumation associated with motion on the underlying Moine thrust was underway. Ti diffusion profiles in quartz inclusions in garnet suggest the near-peak thermal evolution of these rocks occurred over very short time scales (<200,000 years). While most of the garnets are inferred to be Scandian in age, we document evidence for pre-Scandian garnet cores in structurally higher (more hinterland positioned) samples that must have grown under higher temperatures. In the hanging wall of the Moine thrust, high grossular garnets with estimated formation conditions >9 kbar are probably of detrital origin.

9.1 Introduction

Most orogenic wedges can be subdivided into three basic components: (i) a high-grade (upper amphibolite, rarely granulite) central hinterland that is often migmatitic and intruded by anatectic melts; (ii) a medium-grade (greenschist to upper amphibolite facies) exterior hinterland juxtaposed structurally beneath and above the high-grade hinterland and separated from the latter by major ductile shear zones; and (iii) an anchizone foreland fold-thrust belt at the leading edges of the pro- and retro- sides of the wedge. The boundaries that separate these zones commonly accommodate substantial thrust-, and in some cases, normal-sense displacement of 10's to 100's of km. Often, displacement along these

structures is so great that it leads to juxtaposition of rocks that do not share a common bedrock source or finite deformation history. Motion on these structures may drive advection (and thus control the redistribution of heat-producing material) and may act in conjunction with climate to focus erosion and exhumation which, in turn, can substantially influence the thermal structure of the orogen. Huerta *et al.* (1998) suggested that the gross thermal structure of orogenic belts largely depends on the redistribution of asthenospheric heat and crustal (radiogenic) heat-producing material through advective processes of subduction, accretion, and erosion. This thermal structure in turn controls rheology and the associated deformation mechanism response, which determines the nature and distribution of strain localization. Thus, characterizing the kinematic evolution of these structures is critical to understanding the thermal evolution of orogenic wedges.

The kinematic evolution of exterior (foreland) fold-thrust belts, including the displacement magnitude of large structures within them, can be analyzed using area and line-length restoration techniques tied to detailed geologic mapping, but these methods are less useful for kinematic analysis of the more hinterland thrust sheets. Over the last 20 years, a number of two-dimensional analytical (e.g. Royden, 1993) and numerical (e.g. Willett *et al.*, 1993; Beaumont *et al.*, 2004) studies have addressed the more complex evolution of orogenic wedges. However, because the wedge is generally treated as a deformation continuum in these models, fault architecture and strain localization cannot readily be considered. In these systems, the orogenic wedge must be treated as a thermal continuum, but the presence of faults and shear zones with significant displacement magnitudes (>100 km) indicate that, even at the scale of the entire orogen, the wedge should not be treated as a kinematic continuum. Consequently, the kinematic evolution of these ductile thrust sheets (and in some cases normal detachments) in the orogenic hinterland must be characterized, as motion on these structures can fundamentally affect orogenic style.

Although ductile thrust sheets in the orogenic hinterland cannot be reconstructed using standard kinematic analysis techniques, it is possible to evaluate first-order crustal-scale kinematic scenarios by using detailed *P-T* trajectories. Here, we utilize thermodynamic modeling, phase compositions, and microstructures to produce detailed *P-T* histories of four samples collected across major ductile thrust sheets of the Scandian (mid-Silurian) orogenic retro-wedge in northern Scotland (Figs. 9.1 and 9.2). From foreland to hinterland these include: the base (sample MT-07-05) and top (MT-09-09) of the Moine thrust sheet, middle of the Ben Hope thrust sheet (MT-09-12), and the base of the Naver thrust sheet (MT-09-96). In addition, Ti diffusion profiles preserved by quartz inclusions in garnet are used to constrain the duration of heating within the Moine thrust sheet. These petrologic results provide critical constraints for tectonic models of Scandian orogenesis in NW Scotland.

9.2 Tectonic Setting

The Northern Highland Terrane of Scotland was affected by two Caledonian orogenic events associated with closure of the Lower Paleozoic Iapetus Ocean (Strachan *et al.*, 2002, 2010 and references therein). The Grampian event at 475-460 Ma resulted from collision of the Laurentian margin and an oceanic arc (Dewey & Shackleton, 1984). The Scandian event at 435-415 Ma resulted from collision of Baltica with this segment of the Laurentian margin (Coward, 1990; Dallmeyer et al., 2001; Dewey & Strachan, 2003; Kinny *et al.*, 2003) and was associated with formation of the major ductile thrusts of the Caledonian wedge (Moine, Ben Hope, Naver, Sgurr Beag and Skinsdale, in ascending structural order).

The Scandian orogenic wedge in northern Scotland is composed of anchizone grade foreland thrusts (lower Moine thrust zone; MTZ), a foreland-to-hinterland transition zone (upper MTZ), and four major ductile thrust sheets (Moine, Ben Hope, Naver, Skinsdale in ascending structural order) that are

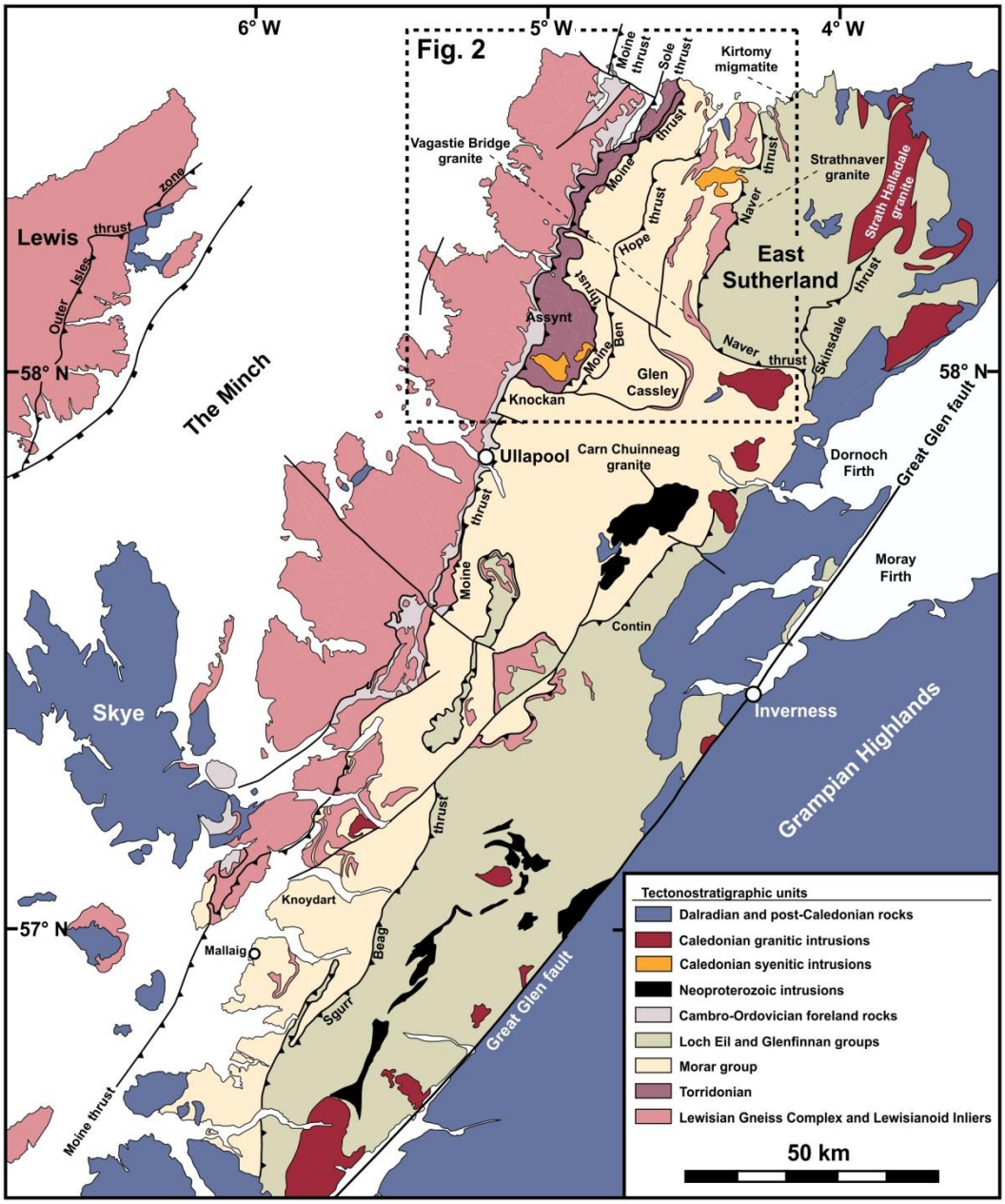

Figure 9.1. Map of major lithotectonic units in northern Scotland. Location of main study area presented in Fig. 9.2 is indicated by box outline. Modified from Thigpen *et al.* (2013) and references therein.

variably deformed, metamorphosed and internally imbricated by subordinate ductile thrusts (Figs. 9.1 and 9.2; Holdsworth *et al.*, 2001; Strachan *et al.*, 2002). The Naver and Skinsdale thrust sheets represent the migmatitic central hinterland of the orogen, while the Ben Hope and Moine thrust sheets comprise the medium-grade exterior hinterland. The Moine thrust zone (MTZ), which represents the foreland-to-hinterland transition zone of the Scandian wedge, accommodated shortening via dominantly brittle

structures (Sole thrust and imbricate zones) developed at lower (foreland-positioned) structural levels and by ductile thrust displacement and pervasive deformation at now higher (hinterland-positioned) structural levels (see reviews by Strachan *et al.*, 2002; Butler, 2010).

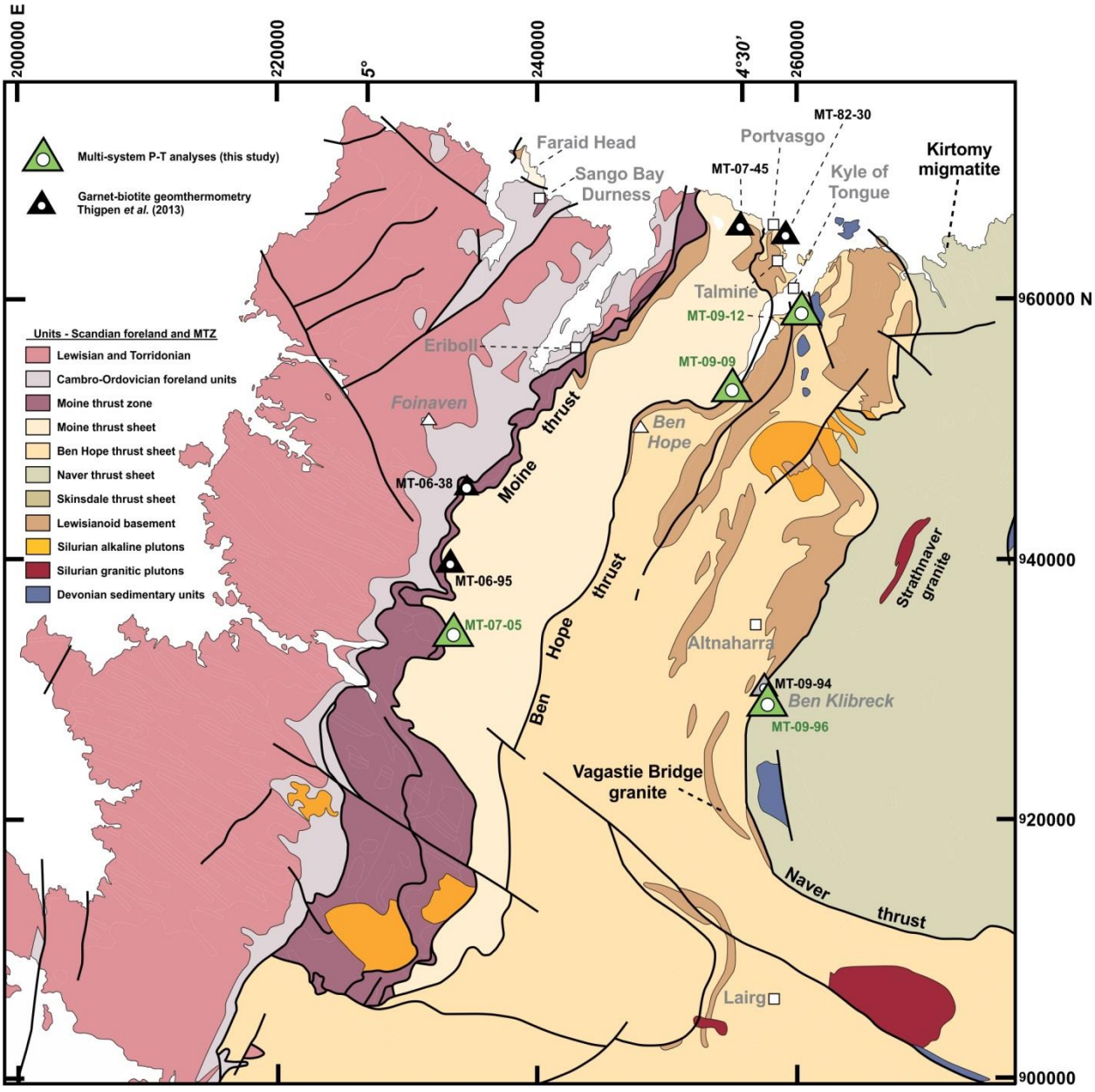

Figure 9.2. Detailed geologic map of study area showing locations of samples analyzed in this study and nearby samples also referred to in text. Modified from Thigpen *et al.* (2013) and references therein.

Traditionally, the Barrovian metamorphic mineral assemblage in Moine Supergroup rocks of the Northern Highlands Terrane was either attributed to Knoydartian (Neoproterozoic; Barr *et al.*, 1986) and

Grampian (475-460 Ma; Kelley & Powell, 1985; Powell & Phillips, 1985; Harris, 1995; Rogers *et al.*, 2001) orogenesis or to Scandian thrust-related isotherm telescoping and retrogression of one of these earlier metamorphic events (see Barr *et al.*, 1986, for a historical perspective). However, extensive evidence for high temperature ductile deformation associated with Scandian (435-420 Ma) thrusting (Freeman *et al.*, 1998; Dallmeyer *et al.*, 2001; Kinny *et al.*, 2003; Thigpen *et al.*, 2010a, 2010b, 2013) has revealed an enigma concerning the nature of metamorphism coeval with Scandian deformation. It is now known from dating of structurally-constrained metagranites in the Moine Supergroup rocks that the dominant 'D_2' structures formed during the Silurian-age Scandian phase of the Caledonian orogeny (Kinny *et al.*, 2003; Alsop *et al.*, 2010). Also, abundant thermochronologic data indicates cooling from temperatures >550 °C during or immediately after Scandian orogenesis (Dallmeyer *et al.*, 2001). By using deformation temperatures estimated from quartz c-axis fabric opening angles on orogen-perpendicular sampling transects, Thigpen *et al.* (2013) suggested that the thermal sequence across the Scandian orogenic wedge was mostly intact and likely resulted from thrust stacking during that event. Other evidence for this included: (i) undisputed Scandian age deformation temperatures that are equivalent to calculated metamorphic temperatures from similar structural levels, (ii) mineral textural and chemical relationships suggesting prograde Scandian growth, (iii) a progressive increase in deformation temperatures towards structurally higher (hinterland) positions in the Scandian orogenic wedge, and (iv) a lack of major thermal break across the Moine and Ben Hope thrust sheets (as would be expected with thrust telescoping of an earlier thermal sequence).

9.2.1 Moine and Ben Hope Thrust Sheets

The Moine thrust sheet, which in the study area (Figs. 9.1 and 9.2) is bound to west by the Moine thrust and to the east by the Ben Hope thrust, is mainly composed of Moine Supergroup (Morar Group) psammite, semipelite, and pelite, with inliers of Lewisianoid basement gneiss (Holdsworth *et al.*,

2001). The Ben Hope thrust lies structurally above and to the east of the Moine thrust sheet and extends from the north Sutherland coast to southern Assynt (Figs. 9.1 and 9.2; Holdsworth *et al.*, 2001; Leslie *et al.*, 2010). From the north coast to Ben Hope, it can be easily recognized by the juxtaposition of Lewisianoid basement inliers and amphibolite-facies rocks, thrust to the west over Moine Supergroup psammites within a retrograde mylonite zone of variable thickness (Holdsworth, 1987, 1989; Holdsworth & Grant, 1990; Burns, 1994; Holdsworth *et al.*, 2001). Further south, Leslie *et al.* (2010) proposed that the Ben Hope thrust turns west to join the Moine thrust along the southeastern-most part of the Assynt recess (Fig. 9.1; see also British Geological Survey, 2012). D_2 deformation, which is interpreted to have occurred coeval with Scandian thrusting (Alsop *et al.*, 2010), resulted in development of tight to isoclinal F_2 folds, a pervasive subhorizontal foliation (S_2), and a pronounced mineral stretching lineation interpreted to lie sub-parallel to the direction of Scandian thrust transport (see reviews by Strachan *et al.*, 2002; Law & Johnson, 2010; Strachan *et al.*, 2010).

9.2.2 Naver Thrust Sheets

Structurally higher and to the east, the Naver thrust emplaces mostly migmatitic Moine gneiss above unmigmatized Moine and Lewisianoid rocks of the Ben Hope thrust sheet (British Geological Survey, 1996, 1997, 2004). Zircon U-Pb dating of migmatites (467 ± 10 Ma and 461 ± 13 Ma; Kinny *et al.*, 1999) and anatectic (Strathnaver, Fig. 9.2) granites (464 ± 26 Ma; Kinny *et al.*, 2003) at the base of the Naver thrust sheet demonstrates the occurrence of a mid-Ordovician (Grampian) tectono-thermal event that clearly pre-dates Scandian orogenesis. Granulite facies assemblages in mafic rocks of the Naver thrust sheet yield *P-T* estimates of 11–12 kbars at 650–700 °C, interpreted to represent Grampian metamorphic conditions (Friend *et al.*, 2000). The high-*P* assemblage is constrained by the age of migmatization (467 ± 10 Ma; Kinny *et al.*, 1999). Later microstructural decompression effects are

recorded in plagioclase moats developed between garnet and matrix mineral phases and yield *P-T* conditions of ~650 °C at ~10 kbars and ~600 °C at 7–8 kbars (Friend *et al.*, 2000).

In the Naver thrust sheet (Fig. 9.1) and its immediate footwall, fibrolite is observed in pelites and calcic plagioclase (An>75) and calcic pyroxene in calc-silicates (Soper & Brown, 1971). In the immediate vicinity of the Naver thrust, both the footwall and hanging wall were penetratively deformed during Scandian thrusting, yet these minerals are not retrogressed (Kinny *et al.*, 2003). Johnson and Strachan (2006) suggested that middle to upper amphibolite facies metamorphism in the Naver thrust sheet may have been coeval with Scandian age thrusting, an interpretation that is consistent with a number of observations, including: (i) a U-Pb monazite age of 431 ± 10 Ma (2σ) from the Kirtomy migmatite (Figs. 9.1 and 9.2; Kinny *et al.*, 1999), (ii) synkinematic *P-T* conditions of ~645 °C and ~5 kbars from fibrolite-bearing pelite above the Naver thrust (Barr *et al.*, 1986), and (iii) U-Pb titanite cooling ages of 416 ± 3 Ma and 413 ± 3 Ma from synkinematic metagranites (Kinny *et al.*, 2003).

9.2.3 Constraints on the Timing of Thrusting

The timing of thrusting in the Scandian wedge is constrained by relationships between thrusts and intrusions. To the NE of the Assynt district in the Moine thrust sheet near Loch Merkland (NC 3881 2926), a U-Pb age of 415 ± 6 Ma was obtained for a syn-D_2 (Scandian) metagranite (Alsop *et al.*, 2010). Other granite sheets that were emplaced and deformed during Scandian thrusting yield zircon U-Pb ages of 428 ± 8 Ma (Vagastie Bridge granite, upper Ben Hope thrust sheet; Figs. 9.1 and 9.2), and 429 ± 11 Ma (Strathnaver granite, lower Naver thrust sheet; Figs. 9.1 and 9.2)(Kinny *et al.*, 2003). At the top of the Scandian wedge along the Skinsdale thrust, the Strath Halladale granite (Fig. 9.1) is pervasively deformed and yields a U-Pb monazite (thrusting) age of 426 ± 2 Ma (Kocks *et al.*, 2006).

During and immediately following Scandian thrusting, a progressive exhumation history is recorded in mineral cooling ages (Fig. 9.2) as reported by Dallmeyer *et al.* (2001; $^{40}Ar/^{39}Ar$ cooling) and Kinny *et al.* (2003; U-Pb titanite cooling). In the Ben Hope thrust sheet, $^{40}Ar/^{39}Ar$ hornblende (closure T between 578 and 490 °C, for cooling rates of 500 to 5 °C Ma^{-1} and grain radii of 80 µm; Harrison, 1981) and muscovite (closure T ~350 °C for a cooling rate of 0.74 °C Ma^{-1} and modeled cylinder radius of 150 µm; Hames & Bowring, 1994) analyses yield virtually indistinguishable ages of 421–412 Ma and 423–416, respectively, suggesting rapid cooling. In the Naver thrust sheet, along the leading edge of the Naver thrust, $^{40}Ar/^{39}Ar$ muscovite (423–417 Ma) and hornblende (421–414 Ma) ages are likewise indistinguishable. At structurally higher positions, near the top of the Naver thrust sheet, $^{40}Ar/^{39}Ar$ hornblende ages (412–404 Ma) record a slightly younger cooling history. Titanite cooling ages of samples collected from the top of the Ben Hope thrust sheet (413 ± 3 Ma) and in the immediate hanging wall of the Naver thrust (416 ± 3 Ma) record a similar cooling history as the $^{40}Ar/^{39}Ar$ methods. Cherniak (1993) estimated titanite Pb closure temperatures to be ~600 and ~240 °C (100 µm radius and 10 °C Ma^{-1} cooling) for crystalline and metamict titanite, respectively; closure temperatures for similar grain sizes (<300 µm) and cooling rates (10–100 °C Ma^{-1}) were determined to be higher (700–800 °C) by Spencer *et al.* (2013).

9.3 Analytical Methods

We sampled pelite horizons from three thrust sheets in northern Scotland, with four samples targeted for detailed petrologic analysis. Location for the samples are (Fig. 9.2; Table 9.1): the base of the Moine thrust sheet 3 km south of Loch More (MT-07-05); the top of the Moine thrust sheet in immediate footwall to the Ben Hope thrust at the southern tip of Kyle of Tongue (MT-09-09); middle of the Ben Hope thrust sheet along the north coast east of Kyle of Tongue (MT-09-12); and the hanging

wall to the Naver thrust on the summit of Ben Klibreck (MT-09-96). The analytical and computational approaches taken for these samples are as follows.

Table 9.1. Provenance, mineralogical and textural characteristics of rocks discussed in this study

Sample	Locality	BNGRS[a] Coordinates	Barrow's Zone	Quartz Texture[b]	Mineralogy[c]
MT-07-05	S. Loch More	NC 33351 33943	biotite	SGR	grt*-ep-chl-bt-wm-qz-fsp-zrn
MT-09-09	S. Kyle of Tongue	NC 55375 53025	staurolite	GBM	st-grt-bt-chl-wm-qz-fsp-zrn (ilm-gr-ap-tur)
MT-09-12	Tongue bay – Skullomie	NC 61698 61551	staurolite	GBM	Grt-wm-bt-chl-qz-fsp-zrn (ilm)
MT-09-96	Ben Klibreck summit	NC 58546 29921	staurolite	GBM	Grt-bt-wm-qz-fsp-mnz-zrn (ilm)

[a]British National Grid Reference System
[b]Quartz recrystallization mechanism; SGR – subgrain rotation, GBM – grain boundary migration
[c]Mineral abbreviations from Whitney & Evans (2010); wm – white mica (unspecified); starred (*) minerals are interpreted as detrital and bracketed minerals are accessory

Energy-dispersive X-ray spectroscopy (EDS) element mapping and quantitative spot analyses were performed for garnet, feldspar, biotite, muscovite, chlorite, ilmenite and epidote in each sample, using the Cameca SX-50 electron microprobe at Virginia Tech. Element maps were collected using a 15 kV accelerating potential and a 50 nA beam current for a period of >8 h to improve resolution for element spatial distribution analysis. Spot analyses were collected for Si, Ti, Al, Mg, Ca, Mn, Fe, Zn, Na, K, F and Cl using a 20 nA beam current (15 nA for feldspar and mica) with a measurement time of 20 s on the peak and 10 s on the background of the X-ray lines. Analytical traverses were made across metamorphic phases to assess chemical heterogeneity (zoning). Ti analyses were conducted on quartz inclusions in garnet using the Cameca SX-100 electron microprobe in the Department of Earth and Environmental Sciences, Rensselaer Polytechnic Institute (RPI). This microprobe contains five wavelength dispersive spectrometers equipped with oversized diffraction crystals for trace element analysis. Analyses were conducted at 200 nA and 15 kV beam conditions, with 400 s peak and 200 s background times, allowing for detection limits of ~8 ppm.

X-ray fluorescence (XRF) bulk rock analyses of metapelitic samples were made for isochemical forward stability modeling (Table 9.2). Representative samples (>5 g) of whole rock were prepared, with weathered edges removed. In instances where samples had large garnet porphyroblasts or were

lithologically heterogeneous, larger sample quantities were prepared to provide a more meaningful representation of bulk rock composition. Samples were powdered in an aluminum ball mill until particles passed through a 200-mesh sieve. Major element chemistry was measured at Franklin and Marshall College using a PANalytical 2404 X-ray fluorescence vacuum spectrometer, with ferric iron estimation (through titration) and loss on ignition (for volatile and combustible amounts).

Table 9.2. X-ray fluorescence bulk rock data (wt. %)

Sample	SiO_2	TiO_2	Al_2O_3	FeO_{tot}	MnO	MgO	CaO	Na_2O	K_2O	P_2O_5	LOI	Total
MT-07-05	66.76	0.69	16.28	4.44	0.08	1.34	1.32	1.21	5.81	0.15	2.22	100.43
MT-09-09	55.46	0.88	20.35	9.00	0.23	3.61	1.23	1.36	4.40	0.17	3.06	99.90
MT-09-12	70.58	0.55	12.71	6.10	0.15	2.71	0.90	1.46	3.01	0.15	1.93	100.44
MT-09-96	59.38	0.91	19.59	6.87	0.18	1.96	1.49	2.14	4.42	0.19	2.44	99.70

FeO_{tot}: total Fe represented in the divalent state ($Fe^{2+} = Fe^{3+}$ x 0.8996); LOI: lost on ignition

CL imaging was performed on the Cameca SX-100 electron microprobe at RPI, which is equipped with a Gatan Mono-CL detector with red, green and blue filtration capabilities. Images were collected using a 15 kV accelerating voltage and variable 5-50 nA beam currents. During collection, electrical artifacts resulting in raster steps of variable brightness occasionally occurred. To alleviate this noise, shorter scan times were applied (~30 s scans) through 10 or more iterative collections; resultant images were summed and resulted in more consistent backgrounds.

Pseudosections were computed for the system MnO-Na_2O-CaO-K_2O-FeO-MgO-Al_2O_3-SiO_2-H_2O-TiO_2 (MnNCKFMASHT), with the 2004 update of the Holland and Powell (1998) dataset in the program Perple_X (Connolly, 2009), through a *P*-*T* space projection. Solution models utilized in these calculations include: ideal solution model for ilmenite-geikielite-pyrophanite; omphacitic-pyroxene (Diener & Powell, 2010), a modification of the Green *et al.* (2007) omphacite model; feldspar (Fuhrman & Lindsley, 1988); chloritoid, hydrous cordierite, staurolite, garnet and chlorite (Holland & Powell, 2011); white mica (Coggon & Holland, 2002; Auzanneau *et al.*, 2010), not allowing for tschermaks or Ti substitutions in the Ca- and Na-subsystems; and Ti-Fe^{3+}-biotite (Tajčmanová *et al.*, 2009), extended to Mn solution after Tinkham *et al.* (2001). Quartz, rutile and sphene were considered as pure phases and water was

considered to be in excess. In order to reduce computation time, melt was not considered. Melt production is largely outside of the modeled *P-T* window, and excluding this component should not significantly impact the resultant pseudosection. These models are used to constrain peak and prograde metamorphic conditions related to observed metamorphic paragenesis and phase compositions.

9.4 Petrography and Thermodynamic Phase Stability Calculations

For garnets analyzed in this study that are chemically internally zoned, it is possible the cores contain a record of crystallization that pre-dates Silurian age Scandian metamorphic events that produced the penetrative S_2 foliation the Moine Supergroup metasedimentary rocks (Vance *et al.*, 1998; Bird *et al.*, 2013). Taking the approach of Thigpen *et al.* (2013), we limit application of core chemistries in quantitative thermobarometry for Scandian thrust-related penetrative deformation to garnet grains with spiral inclusion trails that are continuous with the surrounding pervasive S_2 foliation. A summary of mineral chemistries used for quantitative thermobarometry and samples containing garnets with spiral inclusion trails that are continuous with the pervasive S_2 matrix foliation is shown in Table 9.3.

Table 9.3. Summary of mineral chemistries used for thermobarometry constraints in S_2-parallel matrix grains and in cores and rims of garnets

	Garnet		
Sample	**core**	**rim**	**Matrix minerals used†**
MT-07-05	No*	No	wm (+ksp, +ep)
MT-09-09‡	Yes	Yes	bt + wm + plag + st + ilm
MT-09-12‡	Yes	Yes	bt + wm + ilm
MT-09-96	No*	Yes	bt + wm + plag

** chemistry not used for quantitative thermobarometry, but to infer growth origins*
† bracketed phases used for pseudosection assemblage constraints only
‡ garnets contain spiral inclusion trails that are continuous from core to rim with pervasive S_2 fabric in the matrix

At the base of the Scandian orogenic wedge, mylonitic psammite from the hanging wall of the Moine thrust (sample MT-07-05; Fig. 9.2) contains the assemblage quartz, feldspar, white mica, epidote,

garnet, biotite and Fe-oxide accessories (Table 9.1). Rare, anhedral garnets are rounded with asymmetric (sigma-clast) strain shadows comprised of white mica and quartz oriented parallel to the enveloping S_2 foliation (Fig. 9.3a); epidote clasts exhibit tails of quartz and biotite (Fig. 9.3c). Mica fish are locally present and arranged between C-type shear bands (Fig. 9.3b). All shear sense indicators suggest top-to-the-WNW shearing. Pressure solution seams are common, and includes selvages of Fe-oxides and biotite. At the base of the Moine thrust sheet, quartz recrystallizes dominantly by subgrain rotation (Stipp *et al.*, 2002), with recrystallization dominated by grain boundary migration becoming increasingly prevalent toward structurally higher levels traced towards the east (Thigpen *et al.*, 2010b, their Fig. 15; see also Law, 2014, Figs. 23 and 24). The existence of metamorphic plagioclase feldspar provides a lower-limit on peak metamorphic conditions, as below ~420 °C, albite and K-feldspar are expected to be pure due to a solvus existing between the endmembers, with anorthite-rich plagioclase not being stable below the peristerite gap. The presence of ubiquitous epidote (Fig. 9.4), which is unstable and reacts out at ~500 °C, provides a maximum temperature constraint for these structurally lower samples.

Sample MT-09-09, which was collected from the top of the Moine thrust sheet (Fig. 9.2, Table 9.1) is a pelite that contains the assemblage garnet, biotite, white mica, quartz, feldspar, staurolite, ilmenite, tourmaline, zircon, apatite, and chlorite. Garnets from this sample are large (>5 mm), euhedral, and contain spiral inclusion trails of quartz, ilmenite and tourmaline in the core, with linear inclusion trail overgrowths at the rim (Fig. 9.3e). Staurolite forms as strain caps on the garnet porphyroblasts (Fig. 9.3d), with quartz, white mica, biotite and chlorite comprising the paragenesis in the asymmetric strain shadows. The presence of staurolite and absence of kyanite/sillimanite in the peak metamorphic paragenesis restricts maximum temperatures to ~600 °C (~6 kbar; Fig. 9.4). Although projection of staurolite stability is sensitive to the solution model chosen, it is not expected to substantially impact our thermodynamic modeling. The presence of chlorite is largely restricted to altered zones of matrix

biotite and as mats preferentially developed in the strain shadows. Like MT-07-05, shear sense indicators for this sample are all top-to-the-WNW.

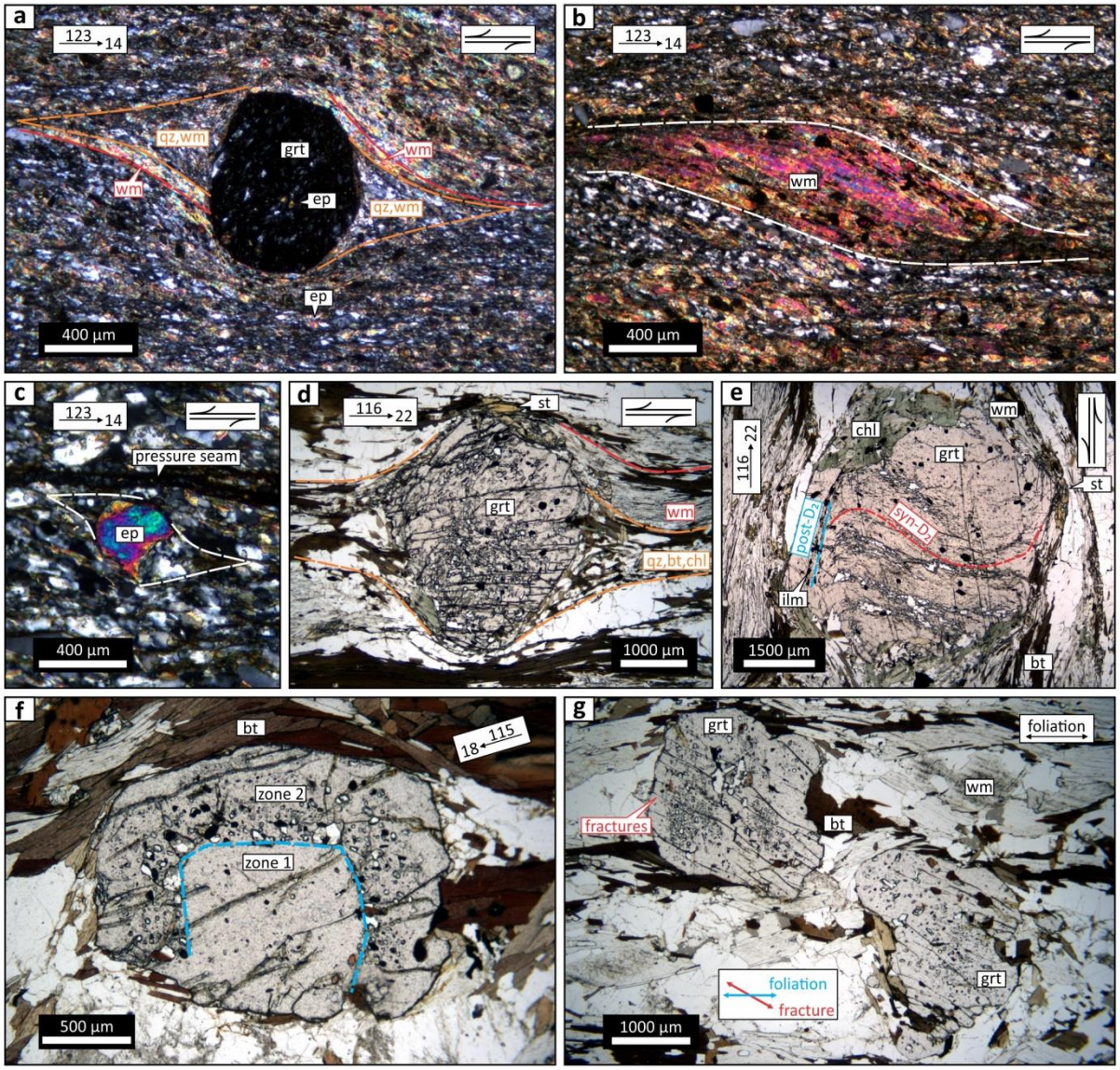

Figure 9.3. Cross polarized (a-c) and plane-polarized (d,e) transmitted light photomicrographs of samples from the base and top of Moine thrust sheet (MT-07-05 and MT-09-09, respectively) and base of Naver thrust sheet (MT-09-96 and -94). Plunge and trend of mineral stretching lineations indicated in a-f. Shear sense indicated in a-e. (a) Anhedral garnet porphyroclast with strain shadows of quartz and white mica (MT-07-05). (b) Mica fish arranged between C-type shear bands (MT-07-05). (c) Epidote with strain shadows of quartz and fine-grained biotite (MT-07-05). All suggest sinistral (top-to-the-WNW) shear sense. (d) Euhedral garnet with staurolite strain caps and shear sense indicating top to the WNW (MT-09-09). (e) Large, euhedral garnet containing syn-D_2 spiral inclusion trails with linear post-kinematic overgrowths (MT-09-09). (f) Sample MT-09-94 (<0.5 km from MT-09-96; Fig. 9.2) contains two generations of garnet growth: an earlier event indicated by nearly inclusion free garnet ("zone 1") and a later event indicated by poikiloblastic rims ("zone 2"). (g) Euhedral garnet porphyroclasts with linear fractures oriented oblique to the dominant matrix foliation (sample MT-09-96).

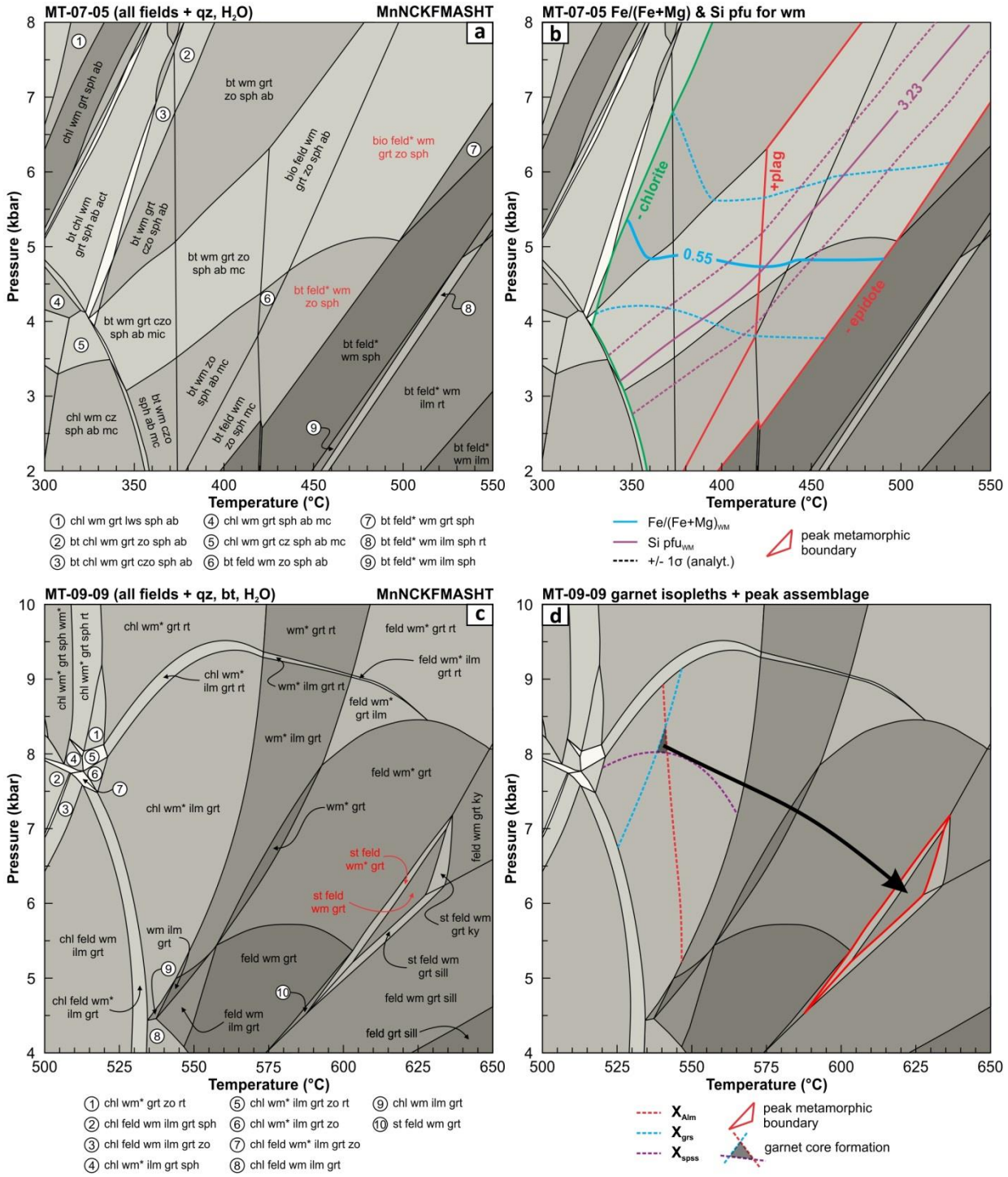

Figure 9.4. Isochemical phase stability models for samples (a,b) MT-07-05 and (c,d) MT-09-09, in the system MnO-Na_2O-CaO-FeO-MgO-Al_2O_3-SiO_2-H_2O-TiO_2 (MnNCKFMASHT). Peak metamorphic paragenesis are highlighted in red (a,c). Assemblage and phase-chemical restrictions to prograde and peak conditions reached are denoted in (b) and (d).

Sample MT-09-12, which was collected from the middle of the Ben Hope thrust sheet on the north coast (Fig. 9.2, Table 9.1), contains the assemblage garnet, white mica, biotite (extensively chloritized), quartz, feldspar, ilmenite (as inclusions in garnet), rutile (as inclusions in garnet) and accessories. Chlorite forms thin retrogressive rims around garnet; however, biotite inclusions in garnet are unaltered. Rutile stability is expected for pressures >8–9 kbar (at T>525 °C; Fig. 9.5); however, its presence may result from increased rutile stability when ferrous iron is present (see discussion for details).

In the immediate hanging wall to the Naver thrust, sample MT-09-96 contains garnet, biotite, white mica, quartz, feldspar, monazite, ilmenite, and zircon (Figs. 9.2 and 9.5; Table 9.1). Euhedral garnets frequently contain parallel fractures at an oblique angle to the dominant foliation (Fig. 9.3g). Although growth zones are not clearly defined in sample MT-09-96, garnets from a nearby sample (<0.5 km away; MT-09-94) contain two growth zones: a nearly inclusion-free core ("zone 1") and a poikiloblastic overgrowth rim ("zone 2"; Fig. 9.3f). The chlorite-out, biotite-in reaction for these samples requires balancing through the removal of K from muscovite. This drives the white mica chemistry to the muscovite-paragonite-margarite miscibility gap, stabilizing two white micas for the majority of the modeled *P-T* space. Quartz proliferation in these samples is a consequence of plagioclase formation in reaction balancing and increased Al budgeting with increased margarite compositions.

9.5 Phase Chemistry and P-T Path Reconstruction

9.5.1 Chemical Zonation

Garnets in the Moine samples all yield bell-shaped compositional profiles, indicative of prograde growth zoning (Tracy *et al.*, 1976; Spear, 1993). Very thin, µm-scale rims of increased Mn (decreased Ca; Fig. 9.6 and 9.7) suggest very minor resorption of garnet through either intracrystalline volume diffusion

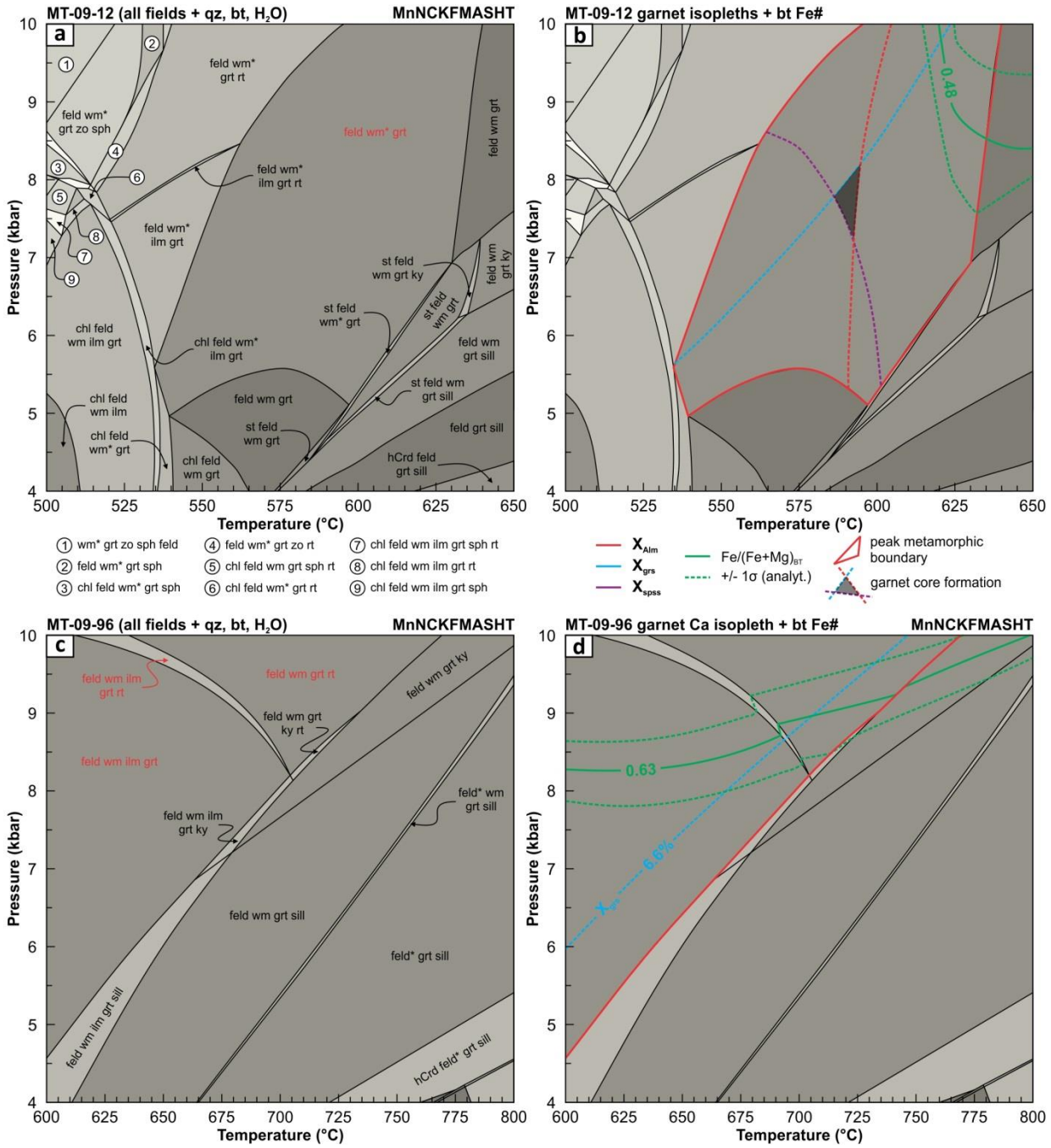

Figure 9.5. Isochemical phase stability models for samples (a,b) MT-09-12 and (c,d) MT-09-96, in the system MnO-Na_2O-CaO-FeO-MgO-Al_2O_3-SiO_2-H_2O-TiO_2 (MnNCKFMASHT). Peak metamorphic paragenesis are highlighted in red (a,c). Assemblage and phase-chemical restrictions to prograde and peak conditions reached are denoted in (b) and (d).

or microscale infiltration metasomatism (Hames & Menard, 1993). These rims increase in width at higher structural levels, where cation diffusion is expected to be higher (e.g. MT-09-96 at the base of the Naver thrust sheet; Fig. 9.7d). Volume diffusion modification would occur only if the equilibrium

condition changed (e.g. change in rim formation temperature or bulk composition change due to cation-charged fluid infiltration). At lower structural positions, the limited depth of diffusion penetration suggests that compositional evolution through peak conditions occurred quickly, preventing diffusion further into the crystal. Higher diffusivities result from higher temperatures up structural section (e.g. within the Naver thrust sheet), which can result in significant modification even under short time scales.

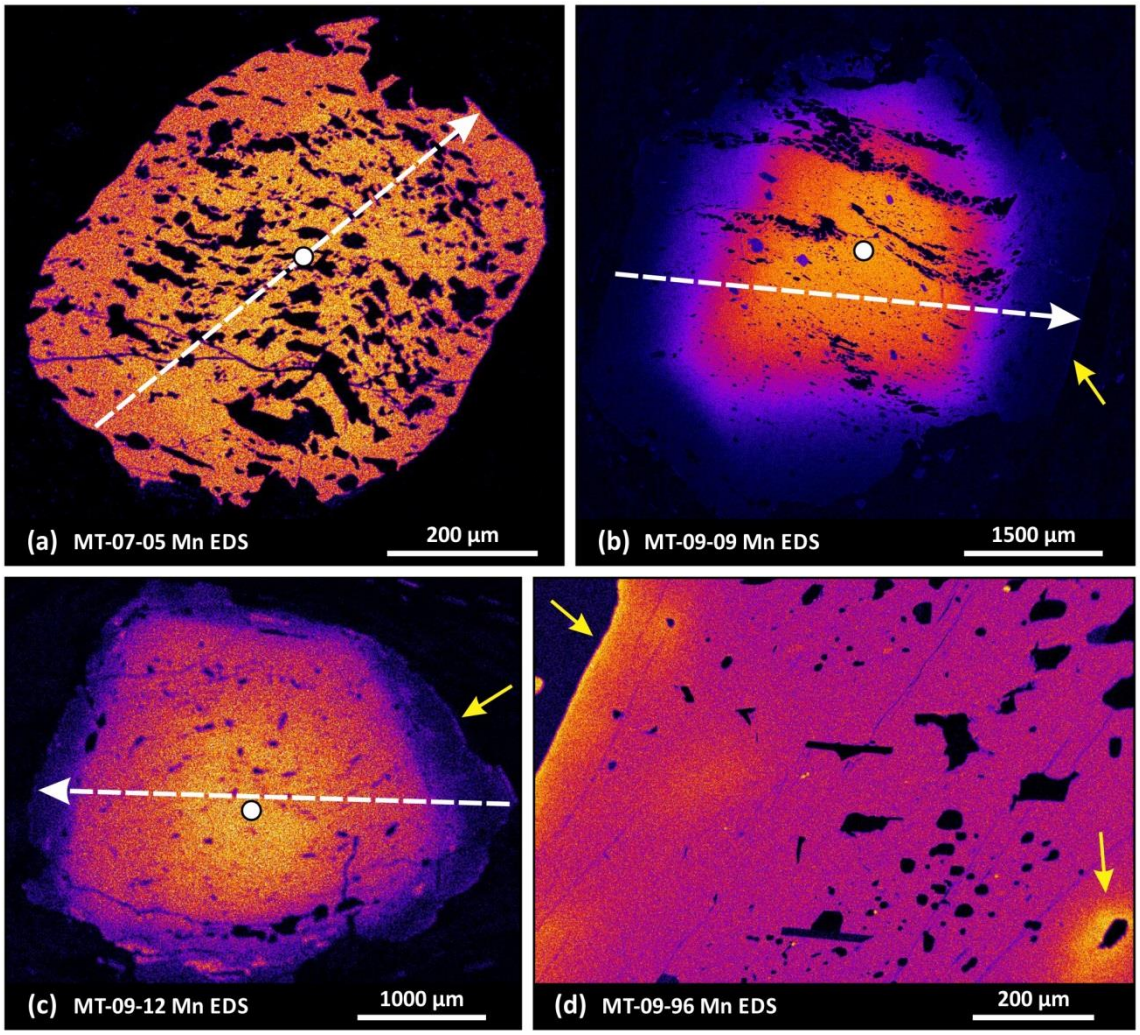

Figure 9.6. Mn electron dispersive spectrometry element maps for samples: (a) MT-07-05, (b) MT-09-09, (c) MT-09-12, and (d) MT-09-96. Dashed arrows show analytical transects shown in Fig. 9.7. White circles show location of core compositions used for early garnet growth modeling. Yellow arrows highlight areas where Mn resorption on the rims is pronounced. Extent of Mn diffusion is greater in samples from higher structural positions (e.g. MT-09-96). Yellow arrow in the bottom right of (d) points to zone of Mn diffusion away from a mineral inclusion.

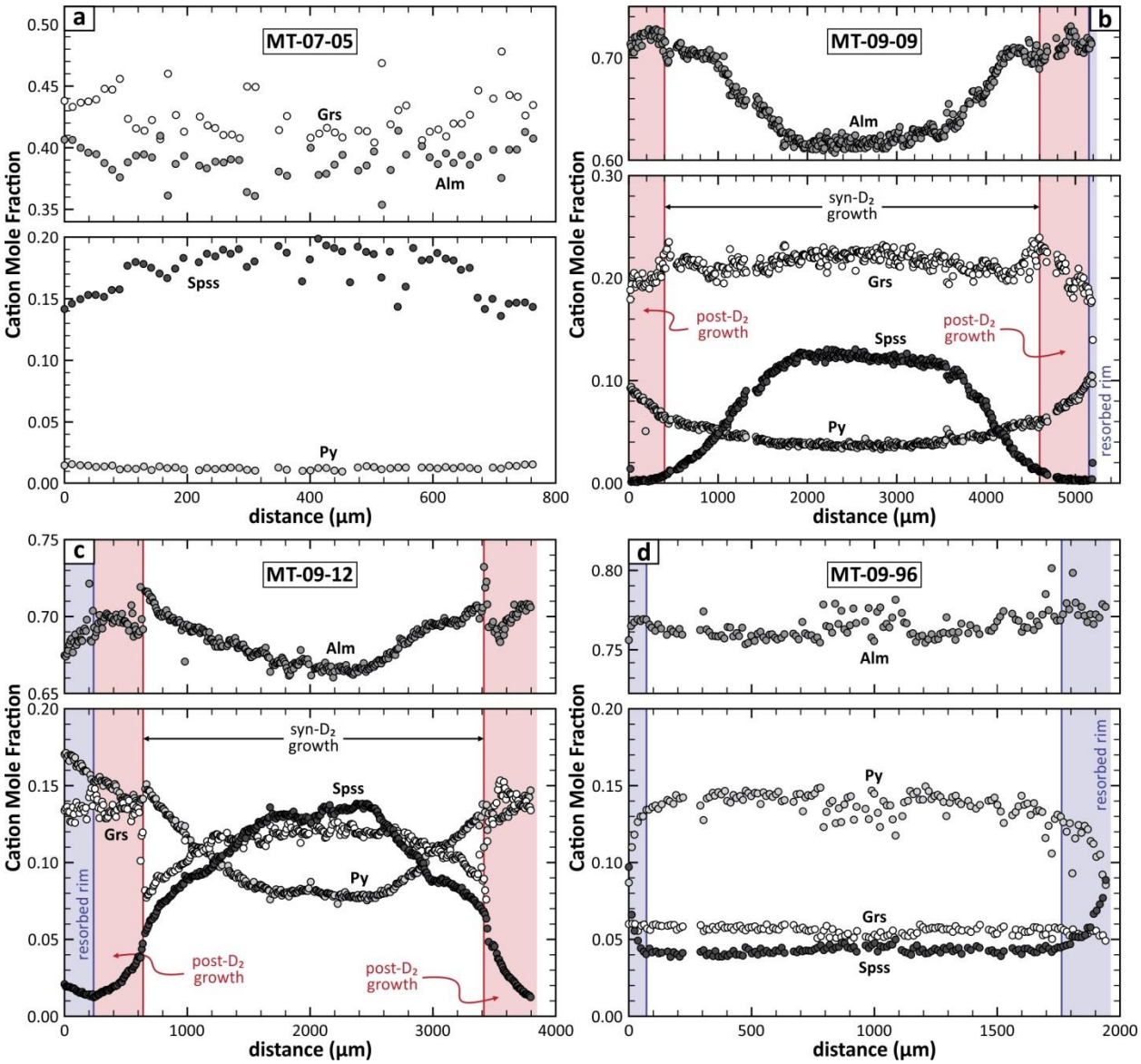

Figure 9.7. Chemical transects across garnet porphyroblasts for samples (a) MT-07-05, (b) MT-09-09, (c) MT-09-12, and (d) MT-09-96. "Syn-D_2 growth" indicates portions of garnets in (b) and (c) where spiral syn-kinematic inclusion trails are preserved, and "post-D_2 growth" where linear inclusion trails indicate continued growth post-deformation. Resorbed rims of increased Mn are present and more pronounced at higher structural positions within the orogenic wedge (i.e. diffusion depth within garnet grains increases from (b) to (d)).

Fluid-aided chemical modification may also be indicated in samples MT-09-09 and MT-09-12 (top of the Moine thrust sheet and middle of overlying Ben Hope thrust sheet, respectively), based on the abundance of chlorite overgrowths. Modification of the core compositions also becomes more pronounced in the structurally higher samples, where compositional profiles flatten (Fig. 9.7d).

From the hanging wall of the Moine thrust (MT-07-05) to the hanging wall of the Naver thrust (MT-09-96), a decrease in garnet grossular and spessartine components is accompanied by an increase in pyrope and almandine (Fig. 9.7). This reflects a garnet composition trend with increasing metamorphic grade, where low-*T* compositions are Mn and Ca-rich and high-*T* compositions are Mg-rich (c.f. Caddick *et al.*, 2010).

9.5.2 Garnet Core Isopleth Thermobarometry

Garnet core composition isopleths for almandine, grossular and spessartine were modeled and projected in *P-T* space to constrain conditions experienced during the initiation of garnet growth (determined by the isopleth intersection; Figs. 9.4 and 9.5; Table 9.4). Pyrope is not considered because it is typically in very low abundance (~1–5 mol %), and small uncertainties in this component lead to large extrapolated uncertainties in the models. The largest garnets observed in thin sections were analyzed in an attempt to measure core compositions nearest the geometric center (with largest cross sectional areas assumed to be correlated with core intersections). These models assume that metamorphic duration is sufficiently short to prevent significant modification of the core composition, especially for the spessartine component. Quality of isopleth intersection was used as a proxy for degree of chemical modification. Both samples from the Moine thrust sheet (MT-07-05 and MT-09-09) have tight intersections; however, structurally higher samples that reached elevated temperatures (>600 °C; MT-09-12 and MT-09-96) have more widely spaced isopleths (i.e. intersection of the isopleths span a large *P-T* window; Fig. 9.5).

Isopleths for cores of anhedral garnets in sample MT-07-05, collected from the immediate hanging wall of the Moine thrust, intersect at a single point at 430 °C and 15.2 kbar. Although Scandian garnet growth is considered unlikely for this sample from the base of the Moine thrust sheet due to the

Table 9.4. Microprobe analysis of garnet

Sample	MT-07-05		MT-09-09		MT-09-12		MT-09-96	
Loc.	core	rim	core	rim	core	rim	core	rim
SiO_2	38.86	39.21	38.54	39.20	37.42	38.63	38.87	38.44
TiO_2	0.26	0.14	0.15	0.03	n.a.	n.a.	0.00	0.01
Al_2O_3	21.24	21.49	21.82	22.06	21.21	21.55	21.84	21.73
FeO	17.45	18.83	27.28	32.70	30.68	32.63	33.59	34.44
MnO	9.05	6.44	6.08	0.06	5.99	0.56	2.01	1.89
MgO	0.31	0.38	0.97	2.43	2.08	3.82	3.68	3.61
CaO	14.81	15.83	8.00	6.95	4.41	4.83	1.88	2.16
Total	101.98	102.32	102.84	103.43	101.79	102.03	101.86	102.27
Si	3.023	3.029	3.006	3.017	2.976	3.010	3.036	3.007
Ti	0.015	0.008	0.009	0.002	n.d.	n.d.	0.000	0.001
Al	1.948	1.957	2.006	2.001	1.988	1.980	2.010	2.003
Fe	1.135	1.216	1.779	2.105	2.041	2.126	2.194	2.253
Mn	0.596	0.422	0.402	0.004	0.404	0.037	0.133	0.125
Mg	0.036	0.044	0.113	0.278	0.247	0.444	0.428	0.421
Ca	1.235	1.310	0.668	0.573	0.376	0.403	0.157	0.181
Alm%	37.81	40.65	60.06	71.11	66.54	70.63	75.33	75.60
Pyr%	1.20	1.46	3.81	9.40	8.05	14.74	14.70	14.12
Sps%	19.86	14.09	13.56	0.12	13.16	1.23	4.57	4.21
Grs%	41.13	43.80	22.56	19.37	12.25	13.40	5.41	6.07
Fe#	96.93	96.54	94.03	88.32	89.21	82.74	83.67	84.26

Notes: Rim compositions are just inside the zone interpreted as resulting from resorption. n.a. – not analyzed; n.d. – not determined.
*Fe# = 100*Fe/(Fe+Mg)*

low temperatures reached (<500 °C) and the psammitic bulk rock composition, the anomalously high grossular content (~41 molar %; other Moine rocks analyzed <20 molar %; Fig. 9.7) could indicate a high-*P* (low-*T*) origin for these detrital garnets (e.g. Willner *et al.*, 2000). This was confirmed by measuring the Raman spectroscopic peak positions of quartz inclusions completely encapsulated in garnet to determine residual inclusion pressures that result from exhumation volume relaxation, following the protocol analytical procedure of Ashley *et al.* (2014) and Kohn (2014). Retained inclusion pressures above 2.5 kbar (see *Appendix C*) in these garnets suggest formation conditions must have exceeded 9 kbar if growth temperature was >450 °C. These pressure estimates are far greater than for any of the other garnets analyzed from the Moine metasedimentary rocks at higher structural positions within the Scandian thrust sheets (see following text). As a working hypothesis, we suggest that these anhedral garnets were deposited as detrital clasts in the Neoproterozoic age Moine Supergroup (Morar Group) sediments. Because of the low temperatures of metamorphism at the base of the Moine thrust sheet (~420–500 °C), it is unlikely that rim compositions of these anhedral garnets were re-equilibrated with the matrix assemblage during S_2 foliation development. Microprobe analyses of these anhedral garnets

were therefore not used as thermobarometric constraints for Scandian S_2 foliation development associated with penetrative thrust-related shearing.

The remaining garnets (samples MT-09-09, MT-09-12, and MT-09-96) from structurally higher positions in the Scandian thrust sheets yield chemical compositions typical for Barrovian prograde metamorphism of semi-pelitic and pelitic rock compositions. In MT-09-09 (top of Moine thrust sheet) garnet growth was initiated at 540 °C and 8.1 kbar, with isopleth intersection occurring within a 5 °C window (Fig. 9.4d). The isopleth intersection is more dispersed for MT-09-12 (Fig. 9.7c; middle of Ben Hope thrust sheet), with an intersection polygon spanning 1 kbar and a centroid at 590 °C and 7.8 kbar (Fig. 9.5b). The lack of intersecting isopleths for garnet from MT-09-96 (Fig. 9.7d; base of the Naver thrust sheet) is inferred to be related to flattening of the bell-shaped chemical profile, and makes determination of formation *P-T* for this sample more difficult. Despite this, contouring of the least mobile cation in garnet (Ca) suggests growth would have occurred along a line from 600 °C and 6 kbar to 700 °C and 8 kbar (Fig. 9.5d). This is consistent with the trend of garnet core growth initiating at higher temperatures and lower pressures at structurally higher positions (Fig. 9.8).

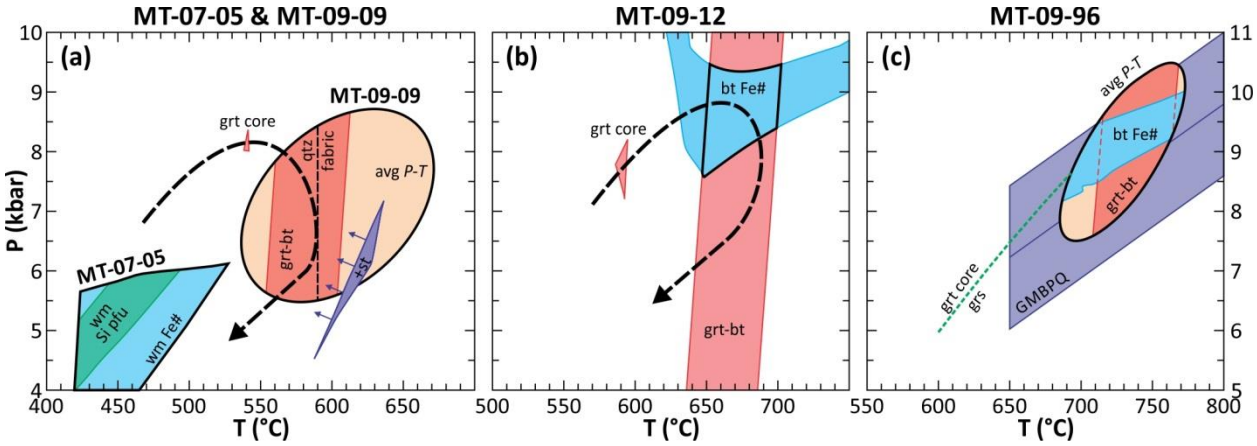

Figure 9.8. Prograde and peak thermobarometric constraints for samples (a) MT-07-05 and MT-09-09 from the Moine thrust sheet, (b) MT-09-12 from the Ben Hope thrust sheet, and (c) MT-09-96 from the Naver thrust sheet. Core isopleth intersection, peak paragenesis and mineral chemistry results presented in Figs. 9.4 and 9.5 are shown, with conventional thermobarometric calculations (garnet-biotite and garnet-muscovite-biotite-plagioclase-quartz) included for further peak metamorphic constraints. Quartz c-axis fabric opening angle thermometry results for sample MT-09-09 (Thigpen *et al.*, 2013; their sample MT-09-07 from same location) are included for reference in (a).

9.5.3 Chemical Thermodynamic Calculations and Thermobarometry

To calculate peak *P-T* conditions for our samples, we used a combination of conventional thermobarometry and chemical thermodynamic modeling. Peak conditions were difficult to constrain for MT-07-05 at the base of the Moine thrust sheet due to the relatively low temperatures of metamorphism (<450 °C), inferred from earlier studies of deformation temperatures (e.g. Thigpen *et al.*, 2013). At greenschist facies conditions, relatively low cation diffusivities limit equilibrium mineral and matrix exchange. In addition, biotite in sample MT-07-05 is present as very small, platy grains, typically observed in association with pressure solution seams (making analyses difficult due to beam drift during analyses). As previously mentioned, the presence of plagioclase feldspar and epidote restricts the peak temperature to 420–500 °C; however, other methods for further constraining peak *P-T* are considered here. For the window of peak paragenesis, we considered the average composition of white mica (Table 9.5), with the standard deviation of this data used to represent analytical uncertainty and chemical heterogeneities in the mica analyses. The Fe/(Fe+Mg) (Fe#) was projected in pseudosection model *P-T* space (Fig. 9.4b), which constrains peak pressures (5.0 ± 1.0 kbar). Likewise, the Si per formula unit (Si pfu) of white mica further refined the field of peak metamorphism (450 ± 30 °C; Fig. 9.8a). These results are in good agreement with deformation temperatures (450 °C) indicated by quartz c-axis fabric opening angles for nearby samples (Thigpen *et al.*, 2013).

The abundance of metamorphic mineral phases present in sample MT-09-09 (top of Moine thrust sheet) made thermobarometric calculations more straightforward. The chemistry of garnet (rim), biotite, white mica, plagioclase, staurolite, and ilmenite (Tables 9.4-7) were used for average *P-T* calculations in the program THERMOCALC (Powell & Holland, 1994). The activity of quartz and a pure H_2O fluid phase is assumed to be 1.0. The program calculates an independent set of reactions between the end members of the mineral assemblage, which is assumed to be in equilibrium. Uncertainties are calculated through a least-squares approach. Chlorite was excluded from the calculation because it

Table 9.5. Microprobe analysis of the phyllosilicates

Sample	MT-07-05	MT-09-09		MT-09-12		MT-09-96	
Min. (n)	Wm (15)	Bt (14)	Wm (11)	Bt (40)	Wm (14)	Bt (16)	Wm (14)
SiO_2	48.21	36.88	48.38	36.86	46.10	35.23	46.80
TiO_2	0.32	1.66	0.54	1.61	0.40	2.79	1.03
Al_2O_3	30.10	19.23	34.13	18.64	34.82	19.16	35.28
FeO	3.94	17.47	1.47	18.58	2.94	21.14	1.22
MnO	0.05	0.01	0.00	0.16	0.01	0.11	0.01
MgO	1.80	11.09	1.10	11.10	0.69	7.43	0.64
CaO	0.01	0.00	0.00	0.02	0.00	0.01	0.00
Na_2O	0.16	0.24	0.89	0.20	0.69	0.26	0.80
K_2O	11.19	9.34	8.58	8.34	8.51	9.17	10.32
Total	95.79	95.95	95.10	95.52	94.17	95.34	96.10
Si	3.245	2.748	3.185	2.776	3.098	2.701	3.085
Al^{IV}	0.755	1.252	0.815	1.224	0.902	1.299	0.915
Tet. tot.	4.000	4.000	4.000	4.000	4.000	4.000	4.000
Al^{VI}	1.632	0.437	1.832	0.430	1.855	0.432	1.826
Ti	0.016	0.093	0.027	0.091	0.020	0.161	0.051
Fe^{2+}	0.222	1.089	0.081	1.170	0.165	1.356	0.067
Mn	0.003	0.001	0.000	0.010	0.001	0.007	0.001
Mg	0.181	1.233	0.108	1.246	0.069	0.849	0.063
Oct. tot.	2.054	2.853	2.048	2.947	2.110	2.805	2.008
Ca	0.001	0.000	0.000	0.002	0.000	0.001	0.000
Na	0.021	0.034	0.113	0.030	0.089	0.038	0.102
K	0.961	0.888	0.720	0.801	0.729	0.897	0.868
A tot.	0.982	0.922	0.833	0.833	0.819	0.935	0.970
Fe#	55.05	46.90	42.91	48.43	70.57	61.47	51.51
Mg#	44.95	53.10	57.09	51.57	29.43	38.53	48.49

Notes: Formulas on the basis of 11 oxygens. Biotite (bt) and white mica (wm) ferric calculated by a tetrahedral and octahedral cation sum of 6.9 and 6.05, respectively.
*Fe# = 100*Fe/(Fe+Mg); Mg# = 100*Mg/(Fe+Mg).*

Table 9.6. Microprobe analysis of feldspar

Sample	MT-07-05	MT-09-09		MT-09-96
Loc. (n)	core (1)	core (3)	rim (12)	all (13)
SiO_2	64.20	62.72	61.93	60.90
Al_2O_3	17.63	23.48	23.78	24.20
FeO	0.17	0.19	0.12	0.02
MgO	0.00	0.00	0.00	0.01
CaO	0.00	4.33	4.98	5.49
Na_2O	0.43	9.06	8.78	8.41
K_2O	16.03	0.18	0.08	0.16
Total	98.46	99.96	99.68	99.19
Si	3.015	2.778	2.754	2.726
Al	4.985	5.222	5.246	5.274
Fe^{3+}	0.007	0.007	0.004	0.001
Mg	0.000	0.000	0.000	0.000
Ca	0.000	0.206	0.237	0.263
Na	0.039	0.778	0.756	0.730
K	0.960	0.010	0.005	0.009
% Or	96.06	1.01	0.48	0.93
% Ab	3.94	78.31	75.74	72.79
% An	0.00	20.69	23.78	26.28

Note: All iron is considered ferric. Formulas on the basis of 8 oxygens.

appears to have formed during retrogression and should not have been stable at the temperatures reached by this sample. The results of these calculations suggest peak metamorphism occurred at 600 ± 65 °C and 7.0 ± 1.8 kbar (Fig. 9.8a). Garnet-biotite (Holdaway, 2000) and garnet-muscovite (Wu & Zhao,

2006) exchange thermometry yields peak temperatures of 590 ± 25 °C. These results for sample MT-09-09 are consistent with previously published temperature estimates for the same sample by Thigpen *et al.* (2013) using garnet-biotite thermometry (601 °C) and quartz c-axis fabric opening angles (590 °C).

Table 9.7. Microprobe analyses of staurolite, ilmenite and epidote

Staurolite		Ilmenite			Epidote		
Sample	MT-09-09	Sample	MT-09-09	MT-09-12	Sample	MT-07-05	
(n)	(16)	(n)	(4)	(10)	(n)	Grain 1 (6)	Grain 2 (4)
SiO_2	28.96	SiO_2	0.05	0.17	SiO_2	38.55	38.13
TiO_2	0.61	TiO_2	51.42	16.67	TiO_2	0.10	0.09
Al_2O_3	54.62	Al_2O_3	0.02	0.17	Al_2O_3	26.60	23.44
FeO	13.03	FeO	45.82	14.42	FeO	8.10	11.77
MnO	0.08	MnO	0.31	0.45	MnO	0.18	0.20
MgO	1.65	MgO	0.06	0.07	CaO	23.10	23.19
ZnO	0.84	$Fe_2O_3^{\dagger}$	1.37	67.84	K_2O	0.03	0.03
Total	99.78	Total	99.04	99.77	Total	96.67	96.86
Si	8.203	Ti	0.987	0.362	Si	3.024	3.023
Al^{IV}	0.000	Al	0.000	0.003	Ti	0.006	0.006
Total	8.203	Fe^{2+}	0.978	0.349	Al	2.459	2.190
Al^{VI}	18.237	Fe^{3+}	0.026	1.272	Fe^{3+}	0.531	0.780
Ti	0.131	Mn	0.007	0.011	Mn	0.012	0.014
Fe	3.087	Mg	0.002	0.003	Ca	1.942	1.971
Mn	0.019	% Ilm	97.77	34.88	K	0.003	0.003
Mg	0.695	% Prn	0.67	1.07	Total	8.976	8.987
Zn	0.176	% Geik	0.22	0.26	% Ep	54.78	80.37
Fe#	81.62	% Hem	1.32	63.62	% Zo	45.22	19.63
Mg#	18.38	Fe#	99.10	96.15			

Notes: Staurolite formula on the basis of 48 oxygens, with all iron considered ferrous. Ferrous iron for ilmenite calculated on the bases of 2 formula cations per 3 oxygens.
*Fe# = 100*Fe/(Fe+Mg); Mg# = 100*Mg/(Fe+Mg).Ferric iron for epidote calculated on the basis of Si + Al + Fe^{3+} = 6 for 12.5 oxygens.*

Because of the semi-pelitic composition of MT-09-12 (center of Ben Hope thrust sheet), metamorphic phases were limited, which led to the projection of large assemblage fields in the pseudosection models (Fig. 9.5b) and made constraining peak conditions difficult. Average *P-T* calculations in THERMOCALC also yielded very large resultant uncertainties (T = 662 ± 119 °C; P = 7.6 ± 2.6 kbar). Peak temperatures were calculated using the garnet-biotite thermometer of Holdaway (2000), with pressure estimated by modeling Fe# composition of biotite in *P-T* space (taking the same approach as used for MT-07-05; Tables 9.4 and 9.5), yielding results of 675 ± 25 °C and 8.5 ± 0.9 kbar (Fig. 9.8b).

For sample MT-09-96 (base of Naver thrust sheet), average *P-T* was calculated in THERMOCALC using compositions from the assemblage garnet (rim), biotite, white mica, plagioclase and ilmenite, with resultant conditions of 729 ± 35 °C and 9.0 ± 1.2 kbar (Fig. 9.8c; Tables 9.4-7). For these calculations, a

garnet rim composition must be considered; however significant resorption has modified the original rim chemistry (Fig. 9.7d). Mn (the fastest cation to diffuse in garnet; Chakraborty & Ganguly, 1992; Carlson, 2006) was used as a proxy for the extent of resorption, and the composition immediately inside this profile was used as the "rim" composition, and thus our results may deviate slightly from actual peak metamorphic conditions attained due to the inability to assess the original (unmodified) rim composition. This field was further refined by using garnet-biotite thermometry (733 ± 25 °C) and the modeled Fe# projection for biotite (9.2 ± 0.7 kbar). These pressures are consistent with garnet–muscovite–biotite–plagioclase–quartz (GMBPQ) results of 8.6 ± 1.2 kbar (Hoisch, 1990) and the upper-limit results from garnet-biotite-plagioclase-quartz (GBPQ) barometry of 7.8 ± 1.2 kbar (Wu *et al.*, 2004).

9.6 Determining Duration of Metamorphism Through Trace Element Diffusion Geospeedometry

9.6.1 Modeling Assumptions and Approach

The slow diffusivity of Ti in quartz can be used to constrain the duration of heating in metamorphic rocks with a higher level of sensitivity than is possible with conventional geochronological techniques (Spear *et al.*, 2012). For this method, it is assumed that quartz is included in garnet and has an original homogeneous distribution of [Ti]. Upon heating, garnet which has a much higher concentration of Ti than quartz, supplies Ti to the inclusion via diffusion for the duration of heating, with a reversed diffusion vector during cooling. A linear proportionality between [Ti] and cathodoluminescence (CL) intensity through blue filtration has been previously recognized (Wark & Spear, 2005; Spear & Wark, 2009; Leeman *et al.*, 2012) and can be used to describe Ti distribution in the inclusions. Spear *et al.* (2012) measured CL intensity profiles across imaged inclusions and evaluated these profiles against profiles derived using a finite difference method, implementing the Ti-in-quartz

diffusivity measurements of Cherniak *et al.* (2007). With selected temperature steps, heating and cooling rates can be adjusted to optimize fit to the measured CL profiles. The minimum temperature used in the five-sequence *T-t* path is 450 °C, the temperature at which diffusion would be too sluggish to result in appreciable chemical modification (Cherniak *et al.*, 2007; Spear *et al.*, 2012). Pressure effects on diffusivity are ignored because: (i) metamorphic pressures from this study only deviate slightly (a few kbar) from pressures experiments were conducted at, and (ii) hydrogen diffusion and Si self-diffusion in quartz is not strongly impacted by pressure (Kronenberg *et al.*, 1986; Cherniak, 2010). If there is a significant pressure-dependence on Ti diffusion in quartz, diffusivities would be expected to be higher for rocks reaching peak pressure <10 kbar (such as in this study), which would cause heating duration estimates to decrease. Ti diffusivities parallel and perpendicular to the *c*-axis in quartz are nearly identical (Cherniak *et al.*, 2007), therefore Ti diffusion is treated as being isotropic.

9.6.2 Heating Duration

Quartz inclusions in garnet from sample MT-09-09 (top of Moine thrust sheet) are homogeneous grains with thin (<5 μm), high-Ti rims interpreted to be the result of post-entrapment diffusion (Fig. 9.9a). Regions of higher [Ti] are observed in the inclusion cores; however, these are interpreted to be undeformed porphyroclast cores that pre-date garnet growth and thus they are not considered in our models (Fig. 9.9b,d; Jessell *et al.*, 2003; Ashley *et al.*, 2013). For numerical modeling, we used 540 °C for the temperature of entrapment (associated with calculated garnet core growth conditions) and a peak *T* at 590 °C. Cooling steps at 530 °C, 480 °C and 450 °C were established to constrain the duration of early retrogression and to constrain the timing of the thermal pulse. Modeled profiles from sample MT-09-09 match sample 79-149d of Spear *et al.* (2012; modeled for 600 °C);

however, our profiles do not extend as far into the quartz grain (<5 µm, relative to ~6 µm for 79-149d) and thus they have a more diffuse CL pattern where they approach the inclusion interface.

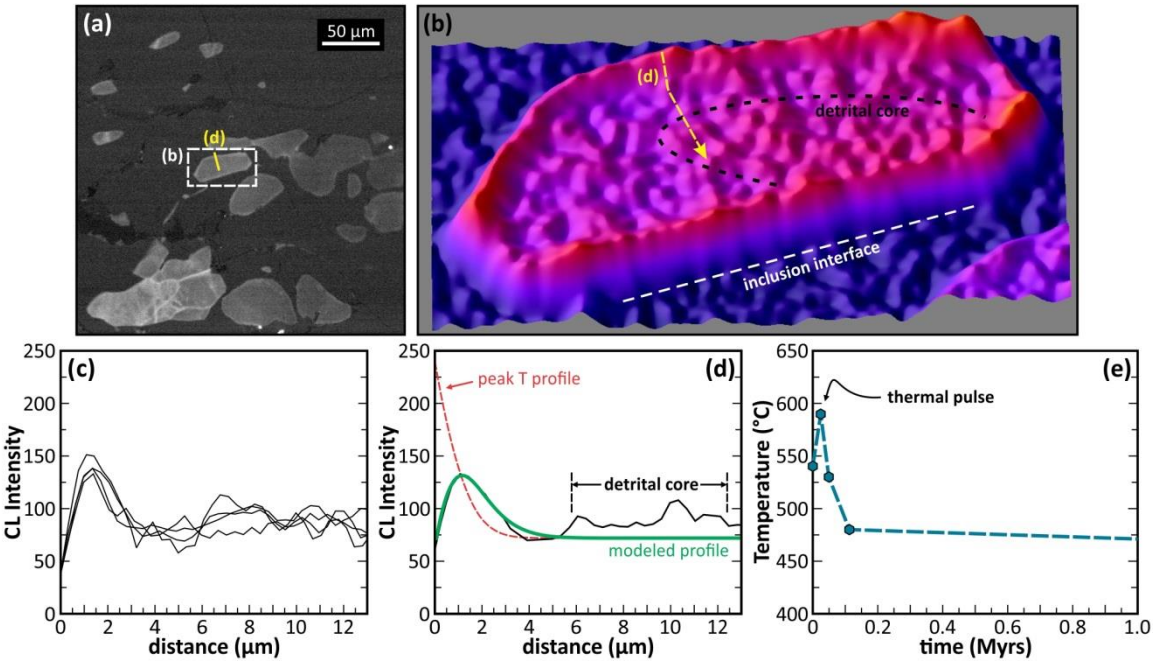

Figure 9.9. Modeled heating/cooling duration for sample MT-09-09 using Ti diffusion profiles across quartz inclusions in garnet. (a) Cathodoluminescence (CL) image under blue filtration showing quartz inclusions (lighter) in garnet (darker). Ti concentration is proportional to CL intensity, showing higher [Ti] present in thin bands around the rims of the inclusions. (b) 3D surface plot of CL intensity for inclusion shown by box outline in (a). A slight increase in Ti near the inclusion core is interpreted to be a preserved undeformed porphyroclast core. (c) Suite of CL profiles across inclusions showing very similar trends in peak position and width. (d) Modeling results for profile shown in (a) and (b). The final modeled profile is a good fit to the measured profile. The detrital core outlined in (b) is shown and correlates with higher CL intensities. (e) Temperature-time (*T-t*) path for the modeling results shown in (d). The near-peak thermal pulse lasted <200,000 years, with a sharp decrease in cooling rate below 480 °C.

The prograde heating path must have occurred in <100,000 years, because diffusion would have extended deeper into the quartz inclusions if heating occurred under longer timescales. Likewise, the early cooling history must be sufficiently short to prevent further diffusion. Once the rock is cooled below 500 °C, sluggish diffusion kinetics in which very little further redistribution of Ti would occur suggests the rate of cooling slowed and extend over significantly longer time scales. In our model, the duration of the cooling between 500 and 450 °C is on the order of 2 Myrs. The resultant *T-t* history modeled for sample MT-09-09 is summarized in Fig. 9.9e.

9.7 Discussion

9.7.1 Thermodynamic Considerations

A primary assumption of our thermodynamic models is that water is in excess, and this isochemical treatment does not allow for the fractionation of water during dehydration reactions. We consider this treatment to be valid, based on the abundance of hydrous double chain and sheet silicates present in the prograde and peak parageneses. If free water was produced and subsequently removed during the prograde evolution of these rocks, it is likely that there was still abundant water present to stabilize these phases. We did consider a pure H_2O fluid phase; however the presence of graphite and calcite in some of the samples indicates that the actual fluid composition was likely a mixed C-O-H fluid phase (Connolly & Cesare, 1993). These carbonaceous phases were restricted to only a couple of samples, and the low abundance suggests that assuming a pure H_2O fluid is a safe approximation.

Another primary assumption of our models is that we considered all iron to be in a ferric state while trying to model Ti-phase (i.e. rutile, ilmenite, and titanite) stability. The presence of ferrous iron drives the production of phases with iron in an increased oxidation state (e.g. hematite, magnetite). This, in turn, would sequester iron and reduce the stability of ilmenite. The obvious consequence of this is the increased abundance of free Ti in the system, which would extend the stability of rutile to lower pressures (Lo Pò and Braga, 2014). In Al-undersaturated systems (in the absence of Al-silicate phases), biotite is capable of budgeting larger quantities of Ti and in doing so becomes a potential reservoir for Ti with increasing temperature. For most of our samples, ilmenite is very abundant, especially as inclusion phases in garnet. This indicates that the majority of Fe in the system is in a reduced state, and thus considering all iron as ferric is a good assumption. In samples that contain rutile as inclusions in garnet cores (MT-09-12), and where isopleth intersection is outside the rutile stability field, this is the probable mechanism to account for the presence of the titania phase. XRF measurements of bulk rock chemistry include titration results that estimate the amount of ferric and ferrous iron present; however, this is

generally an overestimation because a significant amount of oxidation occurred post-exhumation due to surficial chemical weathering processes. Most of the samples collected have thick weathering rinds. Although care was taken to take representative XRF measurements from the un-weathered portion of the samples, it was not always possible to avoid them during sample preparation and processing; particularly in samples where large garnets required large sample volumes for the bulk composition to be adequately represented.

9.7.2 Two-Stage Garnet Growth in the Naver Thrust Sheet

Garnets from supplementary sample MT-09-94 (located near MT-09-96 at the base of the Naver thrust sheet; Fig. 9.2) contain two growth zones (Fig. 9.3f). The inclusion-free cores may be the result of growth during high heat flow when temperatures were sufficiently high to allow for the complete diffusive removal of minerals present in proximity to the growing garnet (but not participating in the reaction), resulting in "gemmy" inclusion-poor crystals (Passchier & Trouw, 2005). Garnet rim overgrowth, which occurred in a convergent, overthickened crust setting, experienced peak temperatures that were insufficient to allow complete diffusive removal of surrounding quartz during garnet growth and resulted in passive inclusion of quartz.

9.7.3 Time Scales of Scandian Nappe Stacking

The accuracy of our estimate from geospeedometry for duration of near-peak temperatures for sample MT-09-09 (top of the Moine thrust sheet) is dependent upon our ability to constrain peak metamorphic temperature. For this sample, the Fe and Mg exchange between garnet and biotite was used. However, Spear (1991) has discussed the effects of diffusion during cooling on calculated peak metamorphic temperature, which is largely controlled by garnet size, relative volume proportions of

garnet to biotite in the sample, and the rate of cooling. The effects of diffusional modification of garnet and biotite chemistries during retrogression could result in underestimating metamorphic temperature by ~100 °C (Spear, 1991). A peak temperature uncertainty of 25 °C will impact the calculated duration of the thermal pulse by a factor of ~2 (Spear, 2014). Thus, it is clear that using temperatures well removed from conditions actually reached could have a large impact on thermal time scale estimates. Although some chemical modification exists in MT-09-09, because of the relatively low temperatures reached (<600 °C) and short time spent at temperatures >500 °C (<200,000 years; Fig. 9.9e), such modification is only expected to have a nominal effect on calculated peak metamorphic temperatures and assuming a peak temperature of 590 ± 25 °C is reasonable for our models. Uncertainty in the experimental diffusion data also contributes to the overall uncertainty of our calculated time scales. However, with minor extrapolation beyond the experimental conditions (down to 648 °C) and small uncertainties in the activation energy reported by Cherniak *et al.* (2007; ±12 kJ mol^{-1}), it is expected that uncertainties in the diffusion parameters will attribute little error to the modeled heating duration (Spear, 2014). The uncertainty in this activation energy may result in a decrease in diffusivity by an order of magnitude at 590 °C. The modeled peak T diffusion profile would require increasing the heating duration by nearly half an order of magnitude. This is a relatively significant increase, but for MT-09-09 would still suggest rapid near-peak thermal evolution, with the prograde portion occurring over a maximum of <250,000 years.

The heating path from garnet growth to peak *P-T* for sample MT-09-09 at the top of the Moine thrust sheet occurred during decompression and, as previously discussed, must have occurred under short geologic time scales (<100,000 years). We interpret this decompressive heating to be the result of high heat flow following advection of isotherms across the overlying Ben Hope thrust while exhumation accompanied reverse sense of motion along the underlying Moine thrust. A conservative estimate for the amount of decompression is 1 kbar (Fig. 9.8). Considering an average overburden density of

psammitic composition (2.8 g cm^{-3}), this would suggest vertical displacement at a rate of >3.5 cm yr^{-1}. These rapid rates (several cm per year) are similar to: (i) exhumation rates along the Main Central Thrust in the central Himalaya (Harrison *et al.*, 1997; Catlos *et al.*, 2001), (ii) heating and cooling rates for amphibolite-facies metamorphism of pelites from eastern Vermont (Spear *et al.*, 2012; Spear, 2014) and, (iii) eclogite exhumation rates in the Alps (Rubatto & Hermann, 2001; Smye *et al.*, 2011) and Papua New Guinea (Baldwin *et al.*, 2004). However, it should be noted that our calculated rates are general; the uncertainties in pressure estimates present in this study would result in large uncertainties in the exhumation rate.

While these estimates are at variance with the conventional view of Barrovian metamorphic evolution, where tens of millions of years are required for development of metamorphic heating and cooling cycles driven principally by conductive heat flow (e.g. England and Thompson, 1984), recent studies have reached similar conclusions using various analytical and numerical modeling techniques. Dachs and Proyer (2002) and Spear (2014) determined modification of Mn profiles in garnet to occur in <1 million years, requiring exhumation rates of 4.6–7.4 cm yr^{-1} for the Grossgockner region of the Austrian Alps (Dachs and Proyer, 2002). In addition, short metamorphic timescales (200–300 kyr near the thermal peak) are required for the Dalradian of Scotland based on diffusional modification of Sr in apatite (Ague & Baxter, 2007) and Mn zoning in garnet (Viete *et al.*, 2011), which may be attributed to high heat flow fluxes through extension and perhaps contact metamorphism (Viete *et al.*, 2013). Geologic processes inferred to be associated with rapid exhumation and heating rates include short thermal pulses resulting from advective heat transfer and fluid flow (Ague & Baxter, 2007), advective heat transport in shear zones (Viete *et al.*, 2011), and tectonic controls on short thermal pulses in thrust nappe complexes (Spear, 2011, 2014). The entire duration of the thermal pulse (to ~500 °C) must have occurred in <200,000 years, and may be explained by the proximity to the Ben Hope thrust where advection of isotherms would be most pronounced. Cooling rates at temperatures below 500 °C may

slow considerably, taking >2 Myrs to reach 450 °C in our model. This change in cooling rate would correlate with a change from the impact advection of isotherms (by local thrusting) has on heating of individual samples, to crustal-scale thickening and erosional cooling controls that operate over much longer geologic timescales.

9.7.4 Thermo-Mechanical Models of Orogenic Evolution

Most collisional systems are assumed to evolve as asymmetric bivergent wedges resulting from collision and subduction of pro-wedge continental lithosphere beneath the retro-wedge side of the orogen (Fig. 9.10; Willett *et al.*, 1993; Jamieson *et al.*, 1998; Willett, 1999; Jamieson & Beaumont, 2013). In thermomechanical models of these systems (see Jamieson *et al.*, 1998, and references therein), the earliest deformational response is marked by the development of conjugate thrust-sense shear zones forming an uplifted plug (Fig. 9.10; often with the retroward shear zone accommodating the majority of shortening) above the locus of pro-wedge lithosphere subduction. Following this, the orogenic wedge evolves either by basal accretion of progressively lower grade thrust sheets to the wedge base (generally dominant in the hinterland; Fig. 9.10), or by accretion of material at the leading toe of the wedge (generally dominant in the foreland fold-thrust belts), with both mechanisms following a broadly foreland-propagating kinematic sequence (e.g. Willett *et al.*, 1993; McClay and Whitehouse, 2004; Naylor and Sinclair, 2007; Graveleau *et al.*, 2012). In these systems, thrust faulting acts as the dominant mechanism for both wedge thickening and taper adjustment. If the orogenic hinterland evolves by basal accretion of progressively lower grade thrust sheets to the wedge base, the *P-T* evolution of each thrust sheet should record punctuated segments of whole-wedge growth (and possibly the early stages of thermal decay).

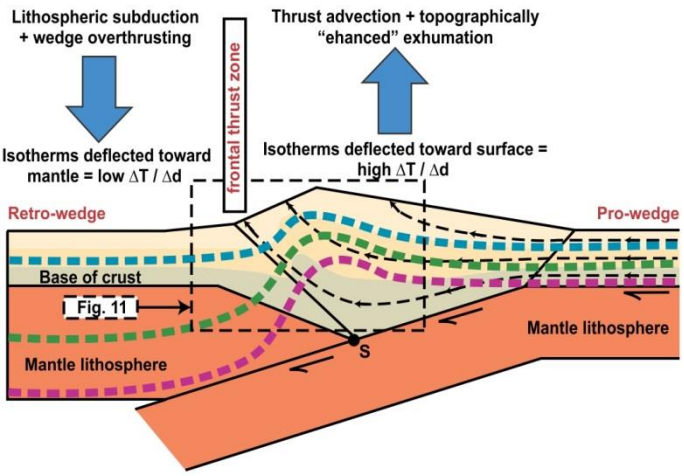

Figure 9.10. Schematic thermal-mechanical model showing wedge thickening and approximate collisional particle trajectories (dashed black lines) following exhumation. Based on models of this type, exhumed peak metamorphic grade rocks are localized in the vicinity of the major retroshear zone. Isotherms on the retro-side of the wedge show mantle-directed deflection in the thrust wedge due to thrust-aided advection. Mechanical model from the isostatic model of Willet *et al.* (1993). Orogen-scale isotherm geometry loosely based on collisional steady-state phase models CE and CF of Jamieson *et al.* (1998). Colored dashed lines are schematic isotherms. Dashed box contains retroshear zone included in Fig. 9.11. S – singularity.

In summary, these models yield testable predictions of the deformational-kinematic response, including: (i) the shear zones bounding the initially uplifted plug (retrowedge and prowedge directed) should be the earliest, and possibly longest-lived, structural zones in the orogen, (ii) these shear zones, when coupled with erosion, should drive exhumation of rocks experiencing the highest metamorphic grade conditions in the core of the orogenic wedge, and (iii) the relatively low metamorphic grade uplifted plug should rest structurally above these shear zones, if it is not been removed by erosion during prolonged orogenesis (as appears to be the case in NW Scotland). The latter implies that each side of the orogen should have a relatively high-grade core thrust sheet(s) juxtaposed between relatively low-grade thrust sheets, with the leading edge of the wedge represented by a foreland-fold thrust belt.

In addition to the mechanical response, synorogenic thermal response can also be characterized by thermo-mechanical numerical models. Jamieson *et al.* (1998) used bivergent wedge models similar to those discussed above (and similar to the tectonic evolution inferred for northwest Scotland), to show that the thermal state of the orogen reflected in isotherm geometry is controlled by evolving competition between cooling due to lithospheric subduction and radioactive heat production occurring

in the structurally higher crustal rocks that are progressively thickened by ongoing collision (Fig. 9.10). This interplay is manifested at the orogen scale as two distinct thermal zones: (i) a region coincident with the major deformation zone in the retro-wedge (designated as the retroshear zone by Jamieson *et al.*, 1998) that exhibits a relatively high thermal gradient due to the surface-directed deflection of isotherms driven by thrusting, and, (ii) a zone on the retro-wedge side of the retroshear that exhibits a relatively low thermal gradient resulting from lithospheric subduction-related cooling. In the next section of this paper, we propose new thermal-kinematic models for Scandian orogenesis in northern Scotland based on our new *P-T* data placed within the context of the models described in these previous studies.

9.7.5 Coupled Kinematic (Burial-Exhumation) and Thermal Evolution of the Scandian Orogen

In the Scandian orogenic wedge of northern Scotland the Naver and Skinsdale thrusts (Fig. 9.1) are responsible for aiding exhumation of rocks and migmatites recording the highest temperature conditions (>700 °C) observed in the retro-wedge hinterland. Additionally, both thrusts are interpreted as the earliest formed structures in the Scandian wedge, based on syn- to late-kinematic U-Pb monazite ages of 431 ± 10 Ma in the Kirtomy migmatite (Naver thrust sheet; Friend *et al.*, 2000) and 426 ± 2 Ma in the Strath Halladale granite (Kocks *et al.*, 2006). In our easternmost sample, which lies in the immediate hanging wall of the Naver thrust, multi-system *P-T* estimates record a metamorphic evolution from garnet growth that initiated at as low as 6.0 kbar and 600 °C and progressed to peak conditions at 9.0 kbar and 730 °C (Fig. 9.11a-b). The progressive pressure increase in the Naver thrust sheet is assumed to reflect burial by the overriding Skinsdale thrust, which is interpreted as accommodating the majority of shortening during early Scandian orogenesis. However, because motion on the Naver thrust leads to exhumation of rocks with a slightly higher metamorphic grade than those in the Skinsdale thrust sheet

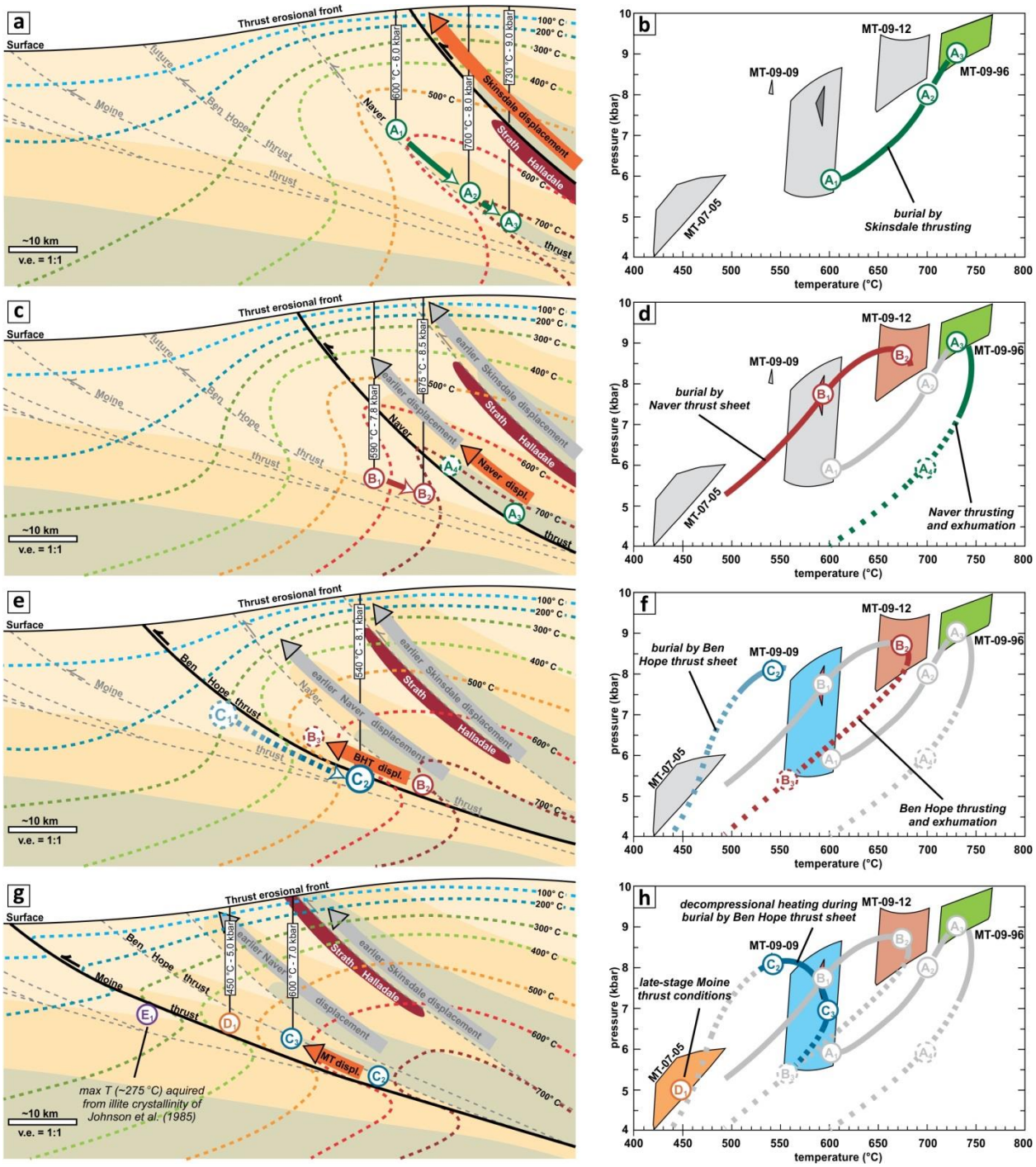

Figure 9.11. Conceptual thermal-kinematic models of Scandian orogenesis. (a) Motion along the Skinsdale thrust results in burial of sample MT-09-96, (b) inferred from P-T data from the onset of garnet growth (A_1) to peak conditions (A_3). The Skinsdale thrust sheet was likely accommodating the majority of collision-related shortening during early Scandian orogenesis and led to surface-directed perturbation of the crustal-scale isotherm sequence. (c) Motion along the Naver thrust results in burial of sample MT-09-12, (d) along a burial path from the onset of garnet growth (B_1) to peak conditions (B_2). (e) Subsequent motion along the Ben Hope thrust coincides with (f) the onset of garnet growth in MT-09-09 in the immediate footwall (C_2). Hornblende and muscovite $^{40}Ar/^{39}Ar$ ages indicate rapid exhumation and cooling, which we attributed to surface-directed motion due to thrusting (B_3; ~423–416 Ma). (g) Rapid motion along the Moine thrust results in (h) decompression of MT-09-09 (C_3) with continued heating due to isotherm advection along the Ben Hope thrust. Sample MT-07-05 records late-stage deformation conditions (D_1), coincident with final motion on the Moine thrust. The juxtaposition of rocks deformed at ~450 °C

(Figure 9.11 continued) with footwall rocks (E_1) deformed at <275 °C indicates that the Moine thrust represents a major thermal kinematic boundary. Orogen-scale isotherm geometries are loosely based on coupled thermal-mechanical models CE and CF of Jamieson *et al.* (1998), which simulates accretion of heat-producing sedimentary material into the wedge prior to the main collision phase, similar to the tectonic history inferred for northern Scotland during Scandian orogenesis. Isotherms on the retro-side of the wedge show mantle-directed deflection due to the cooling effect of continental lithosphere subduction.

(Fig. 9.11c-d), we interpret both the Naver and Skinsdale thrusts as primary components of the Scandian core retroshear zone, following Thigpen *et al.* (2013).

Following initiation of motion along the Naver and Skinsdale thrusts, shortening begins to migrate toward the foreland, where it is accommodated by motion on the structurally lower Ben Hope thrust and subsequently the Moine thrust. In the footwall to the Naver thrust, our sample from the Ben Hope thrust sheet (MT-09-12) yields initial *P-T* conditions of 590 °C and 7.8 kbar (the onset of garnet growth), followed by prograde burial and heating to 675 °C and 8.5 kbar (Fig. 9.11c-d). This prograde path is interpreted to reflect emplacement of the structurally higher Naver thrust sheet and heating driven by surface-directed migration of isotherms via thrusting-related advection. An interpretation of motion along the Ben Hope thrust following emplacement of the Naver thrust sheet (Fig. 9.11e-f) is supported by U-Pb zircon crystallization ages of deformed metagranites that are younger in the Ben Hope thrust sheet (415 ± 6 Ma; Alsop *et al.*, 2010) than those in the Naver thrust zone (431 ± 10 Ma; Kinny *et al.*, 1999). Further, indistinguishable muscovite and hornblende cooling ages (Dallmeyer *et al.*, 2001) indicate rapid exhumation and cooling through closure temperatures of 550 °C and 350 °C, respectively, from 421–416 Ma, and titanite cooling (T <650 °C) data in the Vagastie Bridge granite (Fig. 9.2; upper part of Ben Hope thrust sheet) yield a similar age of 413 ± 3 Ma (Kinny *et al.*, 2003).

Beneath the Ben Hope thrust sheet, samples MT-09-09 and MT-07-05 record the thermal and kinematic evolution of the structural top and bottom of the Moine thrust sheet, respectively (Fig. 9.11g-h). Garnet core conditions of 540 °C and 8.1 kbar for MT-09-09 are interpreted to reflect peak burial by the overriding Ben Hope thrust sheet, prior to substantial motion along the Moine thrust (Fig. 9.11e-f).

Later peak temperature conditions of 600 °C occurred at shallower depth (~7.0 kbar), suggesting that garnet growth occurred during decompression. This decompression-associated garnet growth was rapid, as suggested by the <200 kyr duration of near-peak thermal conditions obtained from the Ti-in-quartz geospeedometry. A decompressional heating path is supported by the observation of rutile and ilmenite inclusions in the core and rim of these garnets, respectively. To produce a decompressional heating *P-T* path, surface-directed motion along the Moine thrust would have to precede foreland-directed migration of the compressed isotherm sequence across the entire Moine thrust sheet. This is likely to be the case either with high rates of thrusting within the orogenic wedge or more likely as a consequence of very short lag times between the onset of Moine and Ben Hope thrusting. In the latter scenario, the incipient Moine thrust sheet would "feel" the pressure of the overriding Ben Hope thrust sheet, but the Moine thrust would then quickly become active before the thermal wave of the hotter overriding wedge could heat the entire Moine thrust sheet.

At the base of the Moine thrust sheet, sample MT-07-05 (Fig. 9.11g-h) records late stage deformation conditions of 450 °C and 5.0 kbar, reflecting final emplacement of the Moine thrust sheet over the structurally lower MTZ. These conditions are consistent with quartz c-axis fabric opening angle-derived deformation conditions reported along the Moine thrust from Eriboll to Assynt (Thigpen *et al.*, 2010a, 2010b, 2013; Law, 2014). Below the Moine and upper MTZ thrusts, peak deformation and/or burial temperatures are substantially lower (<275 °C; Johnson *et al.*, 1985) than those in the overlying thrust sheets (>450 °C). This thermal break is most pronounced in southern Assynt (including exposure of the Moine thrust at Knockan Crag; Fig. 9.1), where anchizone-grade rocks of the fold-thrust belt lie structurally beneath Moine rocks deformed at temperatures >550 °C. The magnitude of this thermal break indicates that the Moine thrust sheet must have been rapidly cooled following final emplacement in order to preserve the thermal juxtaposition of these vastly different footwall and hanging wall deformation temperatures. Rapid exhumation of the entire thrust wedge is also indicated by nearly

indistinguishable thermochronologic ages of multiple mineral systems (Dallmeyer *et al.*, 2001) in the frontal parts of the wedge (Moine and Ben Hope thrust sheets) and by deposition of Devonian rocks on the eroded top of the Skinsdale thrust sheet during Emsian (407–397.5 Ma) times (British Geological Survey, 2003). Gradual eastward younging of thermochronological ages in the Naver and Skinsdale thrust sheets may reflect the deeper and more prolonged exhumation due to longer wavelength post-orogenic rebound (Dallmeyer *et al.*, 2001).

9.8 Conclusions

Petrologic data collected from foreland to hinterland in northern Scotland establishes a prograde, syn-orogenic evolution for the Scandian orogenic wedge. Results are used to constrain coupled thermal-kinematic models of Scandian nappe stacking. The models can account for high heat flow during Scandian metamorphism as the result of surface-directed isotherm deflection driven by thrusting. Near-peak heating for samples located at the top of the Moine thrust sheet was "pulsed" in nature, occurring over very short geologic time scales (<200 kyr). This rapid thermal event can account for an observed decompressional heating profile for sample MT-09-09 from the top of the Moine thrust sheet. Emplacement of the Ben Hope thrust sheet must have been rapid and immediately followed by motion on the underlying Moine thrust, resulting in heating of the footwall to the Ben Hope thrust, which mainly occurred during decompression.

Acknowledgements

Reviews by Rob Strachan and Daniel Viete greatly improved the quality of this manuscript. We thank Frank Spear, Mark Caddick and Donald Stahr for thoughtful discussions pertaining to this study. Frank Spear also graciously shared his program to model Ti diffusion profiles for geospeedometry

purposes. Luca Fedele and Bob Tracy are thanked for assistance with microprobe analysis. This paper is based on work supported by the National Science Foundation under grant No. EAR-1220345 (awarded to R.D. Law) and by a graduate research grant by the Department of Geosciences, Virginia Tech (awarded to K.T. Ashley).

References

Ague, J. J. & Baxter, E. F. (2007). Brief thermal pulses duing mountain building recorded by Sr diffusion in apatite and multicomponent diffusion in garnet. *Earth and Planetary Science Letters* **261**, 500-516.

Alsop, G. I., Cheer, D. C., Strachan, R. A., Krabbendam, M., Kinny, P. D. & Holdsworth, R. (2010). Progressive fold and fabric evolution associated with regional strain gradients across a Scandian ductile thrust nappe, Scottish Caledonides. In: Law, R. D., Butler, R. W. H., Holdsworth, R., Krabbendam, M. & Strachan, R. A. (eds.) *Continental Tectonics and Mountain Building - The Legacy of Peach and Horne*. London: Geological Society, Special Publications 335, 255-274.

Ashley, K. T., Caddick, M. J., Steele-MacInnis, M., Bodnar, R. J. & Dragovic, B. (2014). Geothermobarometric history of subduction recorded by quartz inclusions in garnet. *Geochemistry Geophysics Geosystems* **15**, 350-360.

Ashley, K. T., Webb, L. E., Spear, F. S. & Thomas, J. B. (2013). *P-T-D* histories from quartz: A case study of the application of the TitaniQ thermobarometer to progressive fabric development in metapelites. *Geochemistry Geophysics Geosystems* **14**, 3821-3843.

Auzanneau, E., Schmidt, M. W., Vielzeuf, D. & Connolly, J. A. D. (2010). Titanium in phengite: A geobarometer for high temperature eclogites. *Contributions to Mineralogy and Petrology* **159**, 1-24.

Baldwin, S., Monteleone, B. D., Webb, L. E., Fitzgerald, P. G., Grove, M. & Hill, E. J. (2004). Pliocene eclogite exhumation at plate tectonic rates in eastern Papua New Guinea. *Nature* **431**, 263-267.

Barr, D., Holdsworth, R. & Roberts, A. M. (1986). Caledonian ductile thrusting in a Precambrian metamorphic complex: The Moine of northwestern Scotland. *Geological Society of America Bulletin* **97**, 754-764.

Beaumont, C., Jamieson, R. A., Nguyen, M. H. & Medvedev, S. (2004). Crustal channel flows: 1. Numerical models with applications to the tectonics of the Himalayan-Tibetan orogen. *Journal of Geophysical Research* **109**, B06406.

British Geological Survey (1996). Strathy Point, Scotland Sheet 115W, Solid and Drift Geology, 1:50 000, Provisional Series. Keyworth, Nottingham: British Geological Survey.

British Geological Survey (1997). Tongue, Scotland Sheet 114E, Solid geology, 1:50 000, Geology Series. Keyworth, Nottingham: British Geological Survey.

British Geological Survey (2003). Reay, Scotland Sheet 115E, Bedrock and Superficial Deposits, 1:50 000, Geology Series. Keyworth, Nottingham: British Geological Survey.

British Geological Survey (2004). Loch Naver, Scotland Sheet 108E, Bedrock, 1:50 000, Geology Series. Keyworth, Nottingham: British Geological Survey.

British Geological Survey (2012). Oykel Bridge, Scotland Sheet 102W, Bedrock, 1:50 000, Geology Series. Keyworth, Nottingham: British Geological Survey.

Bird, A. F., Thirlwall, M. F., Strachan, R. A. & Manning, C. J. (2013). Lu-Hf and Sm-Nd dating of metamorphic garnet: Evidence for multiple accretion events during the Caledonian orogeny in Scotland. *Journal of the Geological Society* **170**, 301-317.

Burns, I. M. (1994). Tectonothermal Evoluion and Petrogenesis of the Naver and Kirtomy nappes, Northern Sutherland, Scotland. England: PhD thesis, Oxford Brookes University.

Butler, R. W. H. (2010). The role of thrust tectonic models in understanding structural evolution in NW Scotland. In: Law, R. D., Butler, R. W. H., Holdsworth, R., Krabbendam, M. & Strachan, R. A. (eds.) *Continental Tectonics and Mountain Building - The Legacy of Peach and Horne*. London: Geological Society, Special Publications 335, 293-320.

Caddick, M. J., Konopásek, J. & Thompson, A. B. (2010). Preservation of garnet growth zoning and the duration of prograde metamorphism. *Journal of Petrology* **51**, 2,327-322,347.

Carlson, W. D. (2006). Rates of Fe, Mg, Mn and Ca diffusion in garnet. *American Mineralogist* **91**, 1-11.

Catlos, E. J., Harrison, T. M., Kohn, M. J., Grove, M., Ryerson, F. J., Manning, C. E. & Upreti, B. N. (2001). Geochronologic and thermobarometric constraints on the evolution of the Main Central Thrust, central Nepal Himalaya. *Journal of Geophysical Research* **106**, 177-204.

Chakraborty, S. & Ganguly, J. (1992). Cation diffusion in aluminosilicate garnets: Experimental determination in spessartine-almandine diffusion couples, evaluation of effective binary diffusion coefficients, and applications. *Contributions to Mineralogy and Petrology* **111**, 74-86.

Cherniak, D. J. (1993). Lead diffusion in titanite and preliminary results on the effects of radiation damage on Pb transport. *Chemical Geology* **110**, 177-194.

Cherniak, D. J. (2010). Diffusion in quartz, melilite, silicate perovskite, and mullite. *Reviews in Mineralogy and Geochemistry* **72**, 735-756.

Cherniak, D. J., Watson, E. B. & Wark, D. A. (2007). Ti diffusion in quartz. *Chemical Geology* **236**, 65-74.

Coggon, R. & Holland, T. (2002). Mixing properties of phengitic micas and revised garnet-phengite thermobarometers. *Journal of Metamorphic Geology* **20**, 683-696.

Connolly, J. A. D. (2009). The geodynamic equation of state: What and how. *Geochemistry Geophysics Geosystems* **10**, 1-19.

Connolly, J. A. D. & Cesare, B. (1993). C-O-H-S fluid composition and oxygen fugacity in graphitic metapelites. *Journal of Metamorphic Geology* **11**, 379-388.

Coward, M. P. (1990). Shear zones at the Laxford Front, NW Scotland and their significance in the interpretation of lower crustal structure. *Journal of the Geological Society of London* **147**, 279-286.

Dachs, E. & Proyer, A. (2002). Constraints on the duration of diffusion modelling of discontinuous growth zones in eclogite garnet. *Journal of Metamorphic Geology* **20**, 769-780.

Dallmeyer, D., Strachan, R. A., Rogers, G., Watt, G. R. & Friend, C. R. L. (2001). Dating deformation and cooling in the Caledonian thrust nappes of north Sutherland, Scotland: Insights from $^{40}Ar/^{39}Ar$ and Rb-Sr chronology. *Journal of the Geological Society of London* **158**, 501-512.

Dewey, J. F. & Shackleton, R. J. (1984). A model for the evolution of the Grampian tract in the early Caledonides and Appalachians. *Nature* **312**, 115-120.

Dewey, J. F. & Strachan, R. A. (2003). Changing Silurian-Devonian relative plate motion in the Caledonides: Sinistral transpression to sinistral transtension. *Journal of the Geological Society of London* **151**, 615-628.

Diener, J. F. A. & Powell, R. (2010). Influence of ferric iron on the stability of mineral assemblages. *Journal of Metamorphic Geology* **28**, 599-613.

England, P. & Thompson, A. B. (1984). Pressure-temperature-time paths of regional metamorphism, Part I: Heat transfer during the evolution of regions of thickened continental crust. *Journal of Petrology* **25**, 894-928.

Freeman, S. R., Butler, R. W. H., Cliff, R. A. & Rex, D. C. (1998). Direct dating of mylonite evolution: A multidisciplinary geochronological study from the Moine thrust zone, NW Scotland. *Journal of the Geological Society of London* **155**, 745-758.

Friend, C. R. L., Jones, K. A. & Burns, I. M. (2000). New high-pressure event in the Moine Supergroup, northern Scotland: Implications for Taconic (early Caledonian) crustal evolution. *Geology* **28**, 543-546.

Fuhrman, M. L. & Lindsley, D. H. (1988). Ternary-feldspar modeling and thermometry. *American Mineralogist* **73**, 201-215.

Graveleau, F., Malavielle, J. & Dominguez, S. (2012). Experimental modelling of orogenic wedges: A review. *Tectonophysics* **538-540**, 1-66.

Green, E., Holland, T. & Powell, R. (2007). An order-disorder model for omphacitic pyroxenes in the system jadeite-diopside-henenbergite-acmite, with applications to eclogitic rocks. *American Mineralogist* **92**, 1181-1189.

Hames, W. E. & Bowring, S. A. (1994). An empirical evaluation of the argon diffusion geometry in muscovite. *Earth and Planetary Science Letters* **124**, 161-167.

Hames, W. E. & Menard, T. (1993). Fluid-assisted modificaiton of garnet composition along rims, cracks, and mineral inclusion boundaries in samples of amphibolite facies schists. *American Mineralogist* **78**, 338-344.

Harris, A. L. (1995). The nature and timing of orogenesis in the Scottish Highlands and the role of the Great Glen Fault. In: Hibbard, J. P., van Stall, C. R. & Cawood, P. A. (eds.) *Current Perspectives in the Appalachian-Caledonian Orogen*. Canada: Geological Association of Canada.

Harrison, T. M. (1981). Diffusion of ^{40}Ar in hornblende. *Contributions to Mineralogy and Petrology* **78**, 324-332.

Harrison, T. M., Ryerson, F. J., Le Fort, P., Yin, A., Lovera, O. M. & Catlos, E. J. (1997). A late Miocene-Pliocene origin for the central Himalayan inverted metamorphism. *Earth and Planetary Science Letters* **146**, 1-7.

Hoisch, T. D. (1990). Empirical calibration of six geobarometers for the mineral assemblage quartz + muscovite + biotite + plagioclase + garnet. *Contributions to Mineralogy and Petrology* **104**, 225-234.

Holdaway, M. J. (2000). Application of new experimental and garnet Margules data to the garnet-biotite geothermometer. *American Mineralogist* **85**, 881-892.

Holdsworth, R. (1987). Basement/Cover Relationships, Reworking and Caledonian Ductile Thrust Tectonics of the Northern Moine, North-West Scotland. England: PhD thesis, University of Leeds.

Holdsworth, R. & Grant, C. J. (1990). Convergence-related 'dynamic spreading' in a mid-crustal ductile thrust zone: A possible orogenic wedge model. In: Knipe, R. J. & Rutter, E. H. (eds.) *Deformation, Rheology and Tectonics*. London: Geological Society, Special Publications 54, 491-500.

Holdsworth, R., Strachan, R. A. & Alsop, G. I. (2001). *Geology of the Tongue District*: Memoir of the British Geological Survey, HMSO.

Holdsworth, R. E. (1989). The geology and structural evolution of a Caledonian fold and ductile thrust zone, Kyle of Tongue region, Sutherland, northern Scotland. *Journal of the Geological Society of London* **146**, 809-823.

Holland, T. & Powell, R. (2011). An improved and extended internally consistent thermodynamic dataset for phases of petrological interest, involving a new equation of state for solids. *Journal of Metamorphic Geology* **29**, 333-383.

Holland, T. J. B. & Powell, R. (1998). An internally consistent thermodynamic data set for phases of petrological interest. *Journal of Metamorphic Geology* **16**, 309-343.

Huerta, A. D., Royden, L. H. & Hodges, K. V. (1998). The thermal structure of collisional orogens as a response to accretion, erosion, and radiogenic heating. *Journal of Geophysical Research* **103**, 15,287-215,302.

Jamieson, R. A. & Beaumont, C. (2013). On the origin of orogens. *Geological Society of America Bulletin* **125**, 1671-1702.

Jamieson, R. A., Beaumont, C., Fullsack, P. & Lee, B. (1998). Barrovian regional metamorphism: Where's the heat? In: Treloar, P. J. & O'Brien, P. J. (eds.) *What Drives Metamorphism and Metamorphic Reactions*. London: Geological Society, Special Publications 138, 23-51.

Jessell, M. W., Kostenko, O. & Jamtveit, B. (2003). The preservation potential of microstructures during static grain growth. *Journal of Metamorphic Geology* **21**, 481-491.

Johnson, M. R. W., Oliver, G. J. H., Kelley, S. P. & Winter, D. A. (1985). Thermal effects and timing of thrusting in the Moine thrust zone. *Journal of the Geological Society of London* **142**, 863-873.

Johnson, M. R. W. & Strachan, R. A. (2006). A discussion of possible heat sources during nappe stacking: The origin of Barrovian metamorphism within the Caledonian thrust sheets of NW Scotland. *Journal of the Geological Society of London* **163**, 579-582.

Kelley, S. P. & Powell, D. (1985). Relationships between marginal thrusting and movement on major, internal shear zones in the N. Highland Caledonides, Scotland. *Journal of Structural Geology* **7**, 43-56.

Kinny, P. D., Strachan, R. A., Friend, C. R. L., Kocks, H., Rogers, G. & Paterson, B. A. (2003). U-Pb geochronology of deformed metagranites in central Sutherland, Scotland: Evidence for widespread late Silurian metamorphism and ductile deformation of the Moine Supergroup during the Caledonian orogeny. *Journal of the Geological Society of London* **160**, 259-269.

Kocks, H., Strachan, R. A. & Evans, J. A. (2006). Hetrogeneous reworking of Grampian metamorphic complexes during Scandian thrusting in the Scottish Caledonides: Insights from the structural setting and U-Pb geochronology of the Strath Halladale Granite. *Journal of the Geological Society of London* **163**, 525-538.

Kohn, M. J. (2014). "Geoba-Raman-try": Calibration of spectroscopic barometers and thermometers for mineral inclusions. *Earth and Planetary Science Letters* **388**, 187-196.

Kronenberg, A. K., Kirby, S. H., Aines, R. D. & Rossman, G. R. (1986). Solubility and diffusional uptake of hydrogen in quartz at high water pressures: Implications for hydrolytic weakening. *Journal of Geophysical Research* **91**, 12723-12744.

Law, R. D. (2014). Deformation thermometry based on quartz c-axis fabrics and recrystallization microstructures: A review. *Journal of Structural Geology* **66**, 129-161.

Law, R. D. & Johnson, M. R. W. (2010). Microstructures and crystal fabrics of the Moine thrust zone and Moine nappe: History of research and changing tectonic interpretations. In: Law, R. D., Butler, R. W. H., Holdsworth, R., Krabbendam, M. & Strachan, R. A. (eds.) *Continental Tectonics and Mountain Building - The Legacy of Peach and Horne*. London: Geological Society, Special Publications 335, 443-503.

Leeman, W. P., MacRae, C. M., Wilson, N. C., Torpy, A., Lee, C.-T. A., Student, J. J., Thomas, J. B. & Vicenzi, E. P. (2012). A study of cathodoluminescence and trace element compositional zoning in natural quartz from volcanic rocks: Mapping titanium content in quartz. *Microscopy and Microanalysis* **18**, 1322-1341.

Leslie, A. G., Krabbendam, M., Kimbell, G. S. & Strachan, R. A. (2010). The Oykel transverse zone: Linking mullions, regional gravity, and large-scale lateral variations in ductile thrust architecture in the Moine nappe, Northern Highlands, Scotland. In: Law, R. D., Butler, R. W. H., Holdsworth, R.,

Krabbendam, M. & Strachan, R. A. (eds.) *Continental Tectonics and Mountain Building - The Legacy of Peach and Horne*. London: Geological Society, Special Publications 335, 359-381.

McClay, K. R. & Whitehouse, P. (2004). Analogue modelling of doubly vergent thrust wedges. In: McClay, K. R. (ed.) *Thrust Tectonics and Hydrocarbon Systems*: American Association of Petroleum Geologists Memoir, 184-206.

Naylor, M. & Sinclair, H. D. (2007). Punctuated thrust deformation in the context of doubly vergent thrust wedges: Implications for the localization of uplift and exhumation. *Geology* **35**, 559-562.

Passchier, C. W. & Trouw, R. A. J. (2005). *Microtectonics*. Berlin: Springer, Federal Republic of Germany (DEU).

Lo Pò, D. & Braga, R. (2014). Influence of ferric iron on phase equilibria in greenschist facies assemblages: The hematite-rich metasedimentary rocks from the Monti Pisani (Northern Apennines). *Journal of Metamorphic Geology* **32**, 371-387.

Powell, D. & Phillips, W. E. A. (1985). Time of deformation in the Caledonide orogen of Britain and Ireland. In: Harris, A. L. (ed.) *The Nature and Timing of Orogenic Activity in the Caledonian Rocks of the British Isles*. London: Geological Society, Memoir 9, 17-39.

Powell, R. & Holland, T. (1994). Optimal geothermometry and geobarometry. *American Mineralogist* **79**, 120-133.

Rogers, G., Kinny, P. D., Strachan, R. A., Friend, C. R. L. & Paterson, B. A. (2001). U-Pb geochronology of the Fort Augustus granite gneiss: Constraints on the timing of Neoproterozoic and Palaeozoic tectonothermal events in the NW Highlands of Scotland. *Journal of the Geological Society of London* **158**, 7-14.

Royden, L. H. (1993). The steady state thermal structure of eroding orogenic belts and accredtionary prisms. *Journal of Geophysical Research* **98**, 4487-4507.

Rubatto, D. & Hermann, J. (2001). Exhumation as fast as subduction? *Geology* **29**, 3-6.

Smye, A. J., Bickle, M. J., Holland, T. J. B., Parrish, R. R. & Condon, D. J. (2011). Rapid formation and exhumation of the youngest Alpine eclogites: A thermal conundrum to Barrovian metamorphism. *Earth and Planetary Science Letters* **306**, 193-204.

Soper, N. J. & Brown, P. E. (1971). Relationships between metamorphism and migmatization in the northern part of the Moine nappe. *Scottish Journal of Geology* **7**, 305-325.

Spear, F. S. (1991). On the interpretation of peak metamorphic temperatures in light of garnet diffuion during cooling. *Journal of Metamorphic Geology* **9**, 379-388.

Spear, F. S. (1993). *Metamorphic Phase Equilibria and Pressure-Temperature-Time Paths*. Washington D.C.: Mineralogical Society of America.

Spear, F. S. (2011). Prograde *P-T* paths: How steep, how fast, and what they mean. *American Geophysical Union Annual Meeting Abstracts* **2011**, V13G-01.

Spear, F. S. (2014). The duration of near-peak metamorphism from diffusion modelling of garnet zoning. *Journal of Metamorphic Geology* **32**, 903-914.

Spear, F. S., Ashley, K. T., Webb, L. E. & Thomas, J. B. (2012). Ti diffusion in quartz inclusions: Implications for metamorphic time scales. *Contributions to Mineralogy and Petrology* **164**, 977-986.

Spear, F. S. & Wark, D. A. (2009). Cathodoluminescence imaging and titanium thermometry in metamorphic quartz. *Journal of Metamorphic Geology* **27**, 187-205.

Spencer, K. J., Hacker, B. R., Kylander-Clark, A. R. C., Andersen, T. B., Cottle, J. M., Stearns, M. A., Poletti, J. E. & Seward, G. G. E. (2013). Campaign-style titanite U-Pb dating by laser-ablation ICP: Implications for crustal flow, phase transformations and titanite closure. *Chemical Geology* **341**, 84-101.

Stipp, M., Stünitz, H., Heilbronner, R. & Schmid, S. M. (2002). The eastern Tonale fault zone: a 'natural laboratory' for crystal plastic deformation of quartz over a temperature range from 250 to 700 °C. *Journal of Structural Geology* **24**, 1,861-861,884.

Strachan, R. A., Holdsworth, R., Krabbendam, M. & Alsop, G. I. (2010). The Moine Supergroup of NW Scotland: Insights into the analysis of polyorogenic supracrustal sequences. In: Law, R. D., Butler, R. W. H., Holdsworth, R., Krabbendam, M. & Strachan, R. A. (eds.) *Continental Tectonics and Mountain Building - The Legacy of Peach and Horne*. London: Geological Society, Special Publications 335, 233-254.

Strachan, R. A., Smith, M., Harris, A. L. & Fettes, D. J. (2002). The Northern Highland and Grampian Terranes. In: Trewin, N. H. (ed.) *The Geology of Scotland*. London: The Geological Society, 81-147.

Tajčmanová, L., Connolly, J. A. D. & Cesare, B. (2009). A thermodynamic model for titanium and ferric iron solution in biotite. *Journal of Metamorphic Geology* **27**, 153-165.

Thigpen, J. R., Law, R. D., Lloyd, G. E. & Brown, S. J. (2010a). Deformation temperatures, vorticity of flow, and strain at the base of the Moine nappe: Reassessing the tectonic evolution of the Scandian foreland-hinterland transition zone. *Journal of Structural Geology* **21**, 920-940.

Thigpen, J. R., Law, R. D., Lloyd, G. E., Brown, S. J. & Cook, B. (2010b). Deformation temperatures, vorticity of flow and strain symmetry in the Loch Eriboll mylonites, NW Scotland: Implications for kinematic and structural evolution of the northernmost Moine thrust zone. In: Law, R. D., Butler, R. W. H., Holdsworth, R., Krabbendam, M. & Strachan, R. A. (eds.) *Continental Tectonics and Mountain Building - The Legacy of Peach and Horne*. London: Geological Society, Special Publications 335, 623-662.

Thigpen, J. R., Law, R. D., Loehn, C. L., Strachan, R. A., Tracy, R. J., Lloyd, G. E., Roth, B. L. & Brown, S. J. (2013). Thermal structure and tectonic evolution of the Scandian orogenic wedge, Scottish Caledonides: Integrating geothermometry, deformation temperatures, and kinematic-thermal modeling. *Journal of Metamorphic Geology* **31**, 813-842.

Tinkham, D. K., Zuluaga, C. A. & Stowell, H. H. (2001). Metapelite phase equilibria modeling in MnNCKFMASH: The effect of variable Al_2O_3 and MgO/(MgO+FeO) on mineral stability. *Mineralogical Society of America: Geological Materials Research* **3**, 1-43.

Tracy, R. J., Robinson, P. & Thompson, A. B. (1976). Garnet composition and zoning in the determination of temperature and pressure of metamorphism, central Massachusetts. *American Mineralogist* **61**, 762-775.

Vance, D., Strachan, R. A. & Jones, K. A. (1998). Extensional versus compressional settings for metamorphism: Garnet chronometry and pressure-temperature-time histories in the Moine Supergroup, northwest Scotland. *Geology* **26**, 927-930.

Viete, D. R., Hermann, J., Lister, G. S. & Stenhouse, I. R. (2011). The nature and origin of the Barrovian metamorphism, Scotland: Diffusion length scales in garnet and inferred thermal time scales. *Journal of the Geological Society of London* **168**, 115-132.

Viete, D. R., Oliver, G. J. H., Fraser, G. L., Forster, M. A. & Lister, G. S. (2013). Timing and heat sources for the Barrovian metamorphism, Scotland. *Lithos* **177**, 148-163.

Wark, D. A. & Spear, F. S. (2005). Titanium in quartz: Cathodoluminescence and thermometry. *Geochimica et Cosmochimica Acta Supplement* **69**, A592.

Willett, S. (1999). Rheological dependence of extension in wedge models of convergent orogens. *Tectonophysics* **305**, 419-435.

Willett, S., Beaumont, C. & Fullsack, P. (1993). Mechanical model for the tectonics of doubly vergent compressional orogens. *Geology* **21**, 371-374.

Willner, A. P., Hervé, F. & Massonne, H.-J. (2000). Mineral chemistry and pressure-temperature evolution of two contrasting high-pressure-low-temperature belts in the Chonos Archipelago, Southern Chile. *Journal of Petrology* **41**, 309-330.

Wu, C.-M., Zhang, J. & Ren, L.-D. (2004). Empirical garnet-biotite-plagioclase-quartz (GBPQ) geobarometry in medium- to high-grade metapelites. *Journal of Petrology* **45**, 1,907-901,921.

Wu, C.-M. & Zhao, G. (2006). Recalibration of the garnet-muscovite (GM) geothermometer and the garnet-muscovite-plagioclase-quartz (GMPQ) geobarometer for metapelitic assemblages. *Journal of Petrology* **47**, 2357-2368.

Appendix A

This section contains auxiliary material included with the manuscript published in Chapter 1.

Regression and Uncertainty Calculations:

A second order polynomial regression (setting the y-intercept to zero) through the experimental dataset by Schmidt & Ziemann (2000) was used for inclusion pressure calculations retained in the 464-line waveshift from quartz at ambient conditions. This expression is $P(bar) = a\Delta\nu_{464}^2 + b\Delta\nu_{464}$, where a = 4.204 ± 0.81 and b = 1094.5 ± 12 (Fig. A1). Uncertainty in this calculation can be calculated through the square-root of the summed quadratures of all sources of uncertainty (i.e. on fit parameters and peak position):

$$\sigma P = \sqrt{(\Delta\nu_{464}^2\sigma a)^2 + (\Delta\nu_{464}\sigma b)^2 + (2a\Delta\nu_{464} + b)^2(\sigma\Delta\nu_{464})^2} \qquad \text{(eq. A.1)}$$

Reproducibility of measurements on the "Herkimer diamond" and Brazilian quartz standards suggests spectral resolution better than 0.1 cm^{-1} for analyses.

References

Gillet, P., Ingrin, J. & Chopin, C. (1984). Coesite in subducted continental crust: *P-T* history deduced from an elastic model. *Earth and Planetary Science Letters* **70**, 426-436.

Schmidt, C. & Ziemann, M. A. (2000). In-situ Raman spectroscopy of quartz: A pressure sensor for hydrothermal diamond-anvil cell experiments at elevated temperatures. *American Mineralogist* **85**, 1,725-721,734.

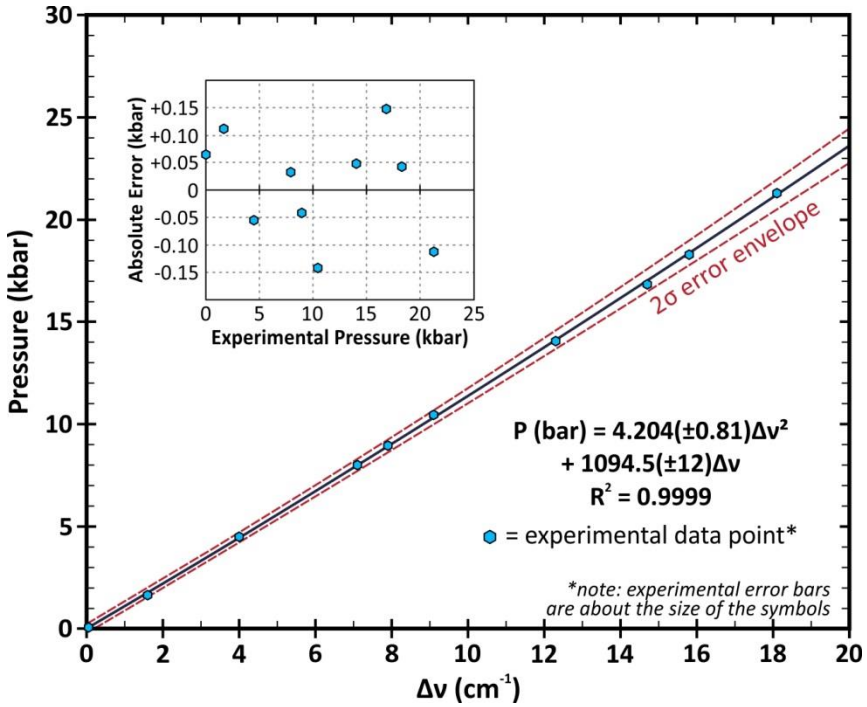

Figure A1. A second-order polynomial regression through the Schmidt & Ziemann (2000) dataset result in a high-quality fit resulting in small uncertainties in calculated inclusion pressures (< ±0.5 kbar uncertainties for pressures <10 kbar, 2σ). Calculated pressures compared to experimental pressures result in absolute error <0.15 kbar (see inset residuals plot). Error bars are smaller than the data points symbols shown.

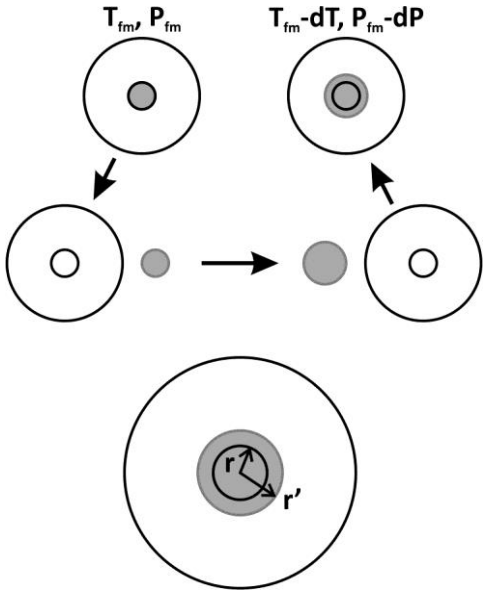

Figure A2. Conceptual diagram illustrating changes in inclusion volume as the result of decompression. At formation, the garnet grows around the volume of the inclusion at that time. During exhumation, the inclusion expands more readily than the host, resulting in overpressuring. At ambient conditions, the inclusion pressure may be measured and elastic modeling may be conducted to determine pressures of formation. From Gillet *et al.* (1984).

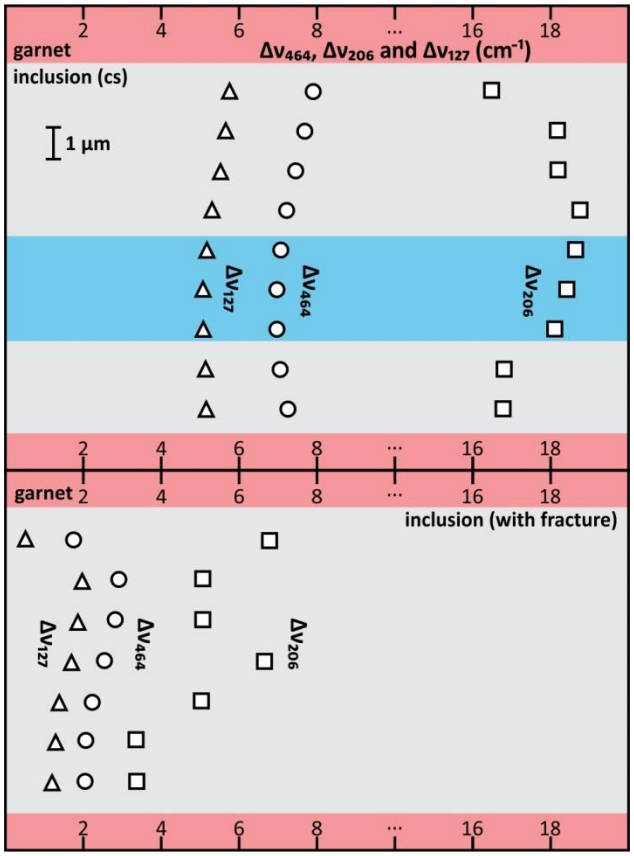

Figure A3. Analytical traverses through depth of quartz inclusions in garnet. Fully encapsulated inclusions (away from the thin section surface and fractures; top) typically have waveshift that increase near the grain boundary due to mechanical stress compaction that occurs. Therefore, the minimum waveshifts near the plateau (around the center of the inclusion) is used in this study to minimize the effects of this stress compaction. If a fracture is present by the inclusion, retained pressure may be lost (bottom).

Appendix B

This section contains auxiliary material included with the manuscript published in Chapter 2, updated with the modeling approach discussed in Chapter 3.

Operating Instructions:

1. Open MATLAB and navigate the current directory to the program file (labeled "QuiB Calc").

2. In the "Command Window", type "run QuiBCalc" and hit return (note: this is case sensitive). The program interface is now open and ready for use. (An alternative approach is to right-click "QuiBCalc.m" and select "run".)

3. Enter in known data in text fields:

-waveshift of the 464 line for quartz (dv464) and uncertainty

-garnet composition in mole fraction (out of 100%)

4. Select temperature and preferred elastic model from the drop-down menus.

5. Click "Calculate!"

Depending on the computer, the calculation may take a few seconds. Additional details can be found by clicking "About the Program". An example is shown below to test the program on your machine:

Example Input/Output:

Input:
dv464 = 6.5 ± 0.1 cm-1
garnet comp = 65% Alm, 10% Pyr, 16% Grs, 5% Sps, 4% And
Temperature = 500 °C
Elastic Model = Zhang (1998)

Output:
Inclusion P (kbar) = 7.2919 ± 0.13899
Formation P (kbar) = 19.64

Program Code (QuIB Calc v. 2.1):

```
%%%%%%%%%%%%%%%%%%%%%%%%%%%%%%%%%%%%%%%%%%%%%%%%%%%%%%%%%%%%%%%%%%%%%%%
%%% Data Input
%%%%%%%%%%%%%%%%%%%%%%%%%%%%%%%%%%%%%%%%%%%%%%%%%%%%%%%%%%%%%%%%%%%%%%%
Alm = str2num(get(handles.Alm_input, 'String'));
Spss = str2num(get(handles.Spss_input, 'String'));
Prp = str2num(get(handles.Py_input, 'String'));
Grs = str2num(get(handles.Grs_input, 'String'));
Tot = Alm+Grs+Prp+Spss;
dv464 = str2num(get(handles.dv464_input, 'String')); %464 cm-1 peak waveshift input
sdv464 = str2num(get(handles.sdv_input, 'String')); %uncertainty in peak position
T_C = str2num(get(handles.T_C, 'String')); %input temperature (deg C)
T = T_C + 273; %input temperature (K)
sT = str2num(get(handles.sT, 'String')); %uncertainty in input temperature
mod = (get(handles.EModel, 'Value')); %elastic model selected
EOSQtz = (get(handles.EOSQtz, 'Value')); %EOS of quartz selected
V298qtz = 2.267958; %kJ kbar^-1, from Angel 1997
Tp = T + sT; %T plus uncertainty in T
Tm = T - sT; %T minus uncertanty in T

%Garnet composition normalization:
Alm2 = (1/Tot)*Alm;
Grs2 = (1/Tot)*Grs;
Prp2 = (1/Tot)*Prp;
Spss2 = (1/Tot)*Spss;

%%%%%%%%%%%%%%%%%%%%%%%%%%%%%%%%%%%%%%%%%%%%%%%%%%%%%%%%%%%%%%%%%%%%%%%
%%% Garnet Properties Loopup Matrix
%%%%%%%%%%%%%%%%%%%%%%%%%%%%%%%%%%%%%%%%%%%%%%%%%%%%%%%%%%%%%%%%%%%%%%%
%%% Matrix Architecture:
%%%
%%% Column: S298 V298 a298 k298 k'298 ao298 u
%%% Row: Alm Grs Pyr Spss
%%%
%%%%%%%%%%%%%%%%%%%%%%%%%%%%%%%%%%%%%%%%%%%%%%%%%%%%%%%%%%%%%%%%%%%%%%%

GrtProp = [342 11.525 2.12 1900 2.98 -0.0016 4.03 921;
    255 12.535 2.2 1720 5.53 -0.0032 3.93 981;
    269.5 11.313 2.37 1743 4.05 -0.0023 4.36 902;
    335.3 11.792 2.27 1740 6.68 -0.0038 4.62 933];

%Linear Garnet Mixing Computation
S298g = (Alm2*GrtProp(1,1)) +
Grs2*(GrtProp(2,1))+Prp2*(GrtProp(3,1))+Spss2*(GrtProp(4,1)); %entropy at room T, J
K^-1
V298g = (Alm2*GrtProp(1,2)) +
Grs2*(GrtProp(2,2))+Prp2*(GrtProp(3,2))+Spss2*(GrtProp(4,2)); %volume, room T, kJ
mol^-1 kbar^-1
a298g = ((Alm2*GrtProp(1,3)) +
Grs2*(GrtProp(2,3))+Prp2*(GrtProp(3,3))+Spss2*(GrtProp(4,3)))*1E-5; %thermal
expansion, room T, K^-1
k298g = (Alm2*GrtProp(1,4)) +
Grs2*(GrtProp(2,4))+Prp2*(GrtProp(3,4))+Spss2*(GrtProp(4,4)); %bulk modulus, kbar
dkg = (Alm2*GrtProp(1,5)) +
Grs2*(GrtProp(2,5))+Prp2*(GrtProp(3,5))+Spss2*(GrtProp(4,5)); %P derivative of bulk
modulus
ddkg = (Alm2*GrtProp(1,6)) +
Grs2*(GrtProp(2,6))+Prp2*(GrtProp(3,6))+Spss2*(GrtProp(4,6)); %2nd derivative bulk
modulus, kbar^-1
```

```
aog = ((Alm2*GrtProp(1,7)) +
Grs2*(GrtProp(2,7))+Prp2*(GrtProp(3,7))+Spss2*(GrtProp(4,7)))*1E-5; %Holland & Powell
(1998) thermal expansion term
ug = (Alm2*GrtProp(1,8)) +
Grs2*(GrtProp(2,8))+Prp2*(GrtProp(3,8))+Spss2*(GrtProp(4,8)); %shear modulus, kbar

ng = 20; %number of atoms in formula unit
EinsteinTg = 10636/((S298g/ng)+6.44); %Einstein T for garnet (for Holland & Powell
(2011) TEOS)
u0g = EinsteinTg/298; %parameter in Einstein function (room T)
EinsteinFun0g = ((u0g^2)*exp(u0g))/((exp(u0g)-1)^2); %Einstein function at room T
Pth = a298g*k298g*(EinsteinTg/EinsteinFun0g)*((1/(exp(EinsteinTg/T)-1))-(1/(exp(u0g)-
1))); %thermal pressure component, kbar
ag = (1+dkg)/(1+dkg+(ddkg*k298g));
bg = (dkg/k298g)-(ddkg/(1+dkg));
cg = (1+dkg+(k298g*ddkg))/((dkg^2)+dkg-(k298g*ddkg));

%%%%%%%%%%%%%%%%%%%%%%%%%%%%%%%%%%%%%%%%%%%%%%%%%%%%%%%%%%%%%%%%%%%%%%%%%%%%
%%% Inclusion Pressure & Volume Calculation
%%%%%%%%%%%%%%%%%%%%%%%%%%%%%%%%%%%%%%%%%%%%%%%%%%%%%%%%%%%%%%%%%%%%%%%%%%%%

Pincl = ((4.204*(dv464^2))+(1094.5*dv464))/10000; %inclusion pressure, GPa
sPincl =
(((((dv464^2)*0.81)^2)+((dv464*12)^2)+((((2*4.204*dv464)+1094.5)*sdv464)^2))^0.5)/1000
0; %1 sigma uncertainty in inclusion pressure, GPa
PinclPLUS = Pincl + sPincl;

a_length = 4.91300-(0.0468*Pincl)+(0.00256*(Pincl^2))-(0.000094*(Pincl^3)); %Angstroms
c_length = 5.40482-(0.03851*Pincl)+(0.00305*(Pincl^2))-(0.000121*(Pincl^3));
%Angstroms
Vincl_ang = (a_length^2)*c_length*sin(pi/3); %Quartz volume at inclusion P, Angstroms
Vincl = (Vincl_ang*6.02214129E23)/(3*1E25); %Quartz volume at inclusion P, kJ mol-1
kbar-1

a_lengthPLUS = 4.91300-(0.0468*PinclPLUS)+(0.00256*(PinclPLUS^2))-
(0.000094*(PinclPLUS^3)); %Angstroms
c_lengthPLUS = 5.40482-(0.03851*PinclPLUS)+(0.00305*(PinclPLUS^2))-
(0.000121*(PinclPLUS^3)); %Angstroms
Vincl_angPLUS = (a_lengthPLUS^2)*c_lengthPLUS*sin(pi/3); %Quartz volume at inclusion
P, Angstroms
VinclPLUS = (Vincl_angPLUS*6.02214129E23)/(3*1E25); %Quartz volume at inclusion P, kJ
mol-1 kbar-1

sa =
((0.00017^2)+((0.0002*Pincl)^2)+((0.00007*(Pincl^2))^2)+((0.000006*(Pincl^3))^2)+(((-
0.0468+(2*.00256*Pincl)-(3*0.000094*(Pincl^2)))*(sPincl))^2))^0.5; %uncertainty in a
length, Angstroms
sc =
((0.00011^2)+((0.00002*Pincl)^2)+((0.00007*(Pincl^2))^2)+((0.000006*(Pincl^3))^2)+(((-
0.03851+(2*.00305*Pincl)-(3*0.000121*(Pincl^2)))*(sPincl))^2))^0.5; %uncertainty in c
length, Angstroms

sVincl_ang =
(((2*a_length*c_length*sin(pi/3)*sa)^2)+(((a_length^2)*sin(pi/3)*sc)^2))^0.5;
%uncertainty in volume calculation, Angstroms
sVincl = (sVincl_ang*6.02214129E23)/(3*1E25); %uncertainty in volume calculation, kJ
kbar^-1


%%%%%%%%%%%%%%%%%%%%%%%%%%%%%%%%%%%%%%%%%%%%%%%%%%%%%%%%%%%%%%%%%%%%%%%%%%%%
%%% Elastic Model Selection
%%%%%%%%%%%%%%%%%%%%%%%%%%%%%%%%%%%%%%%%%%%%%%%%%%%%%%%%%%%%%%%%%%%%%%%%%%%%
```

```
if mod == 1

elseif mod == 2
    %opens dialog box to request inclusion-to-host radius ratio for elastic
    %correction (only when using Zhang, 1998, model)
    prompt = {'Ratio of Inclusion Radius to Host Radius'};
    name = 'Correction for Inclusion Size';
    numlines = 1;
    defaultanswer = {'0.00', 'hsv'};
    answer = inputdlg(prompt,name,numlines,defaultanswer);
end

%%%%%%%%%%%%%%%%%%%%%%%%%%%%%%%%%%%%%%%%%%%%%%%%%%%%%%%%%%%%%%%%%%%%%%%
%%% Formation Pressure Calculation
%%%%%%%%%%%%%%%%%%%%%%%%%%%%%%%%%%%%%%%%%%%%%%%%%%%%%%%%%%%%%%%%%%%%%%%

if EOSQtz == 1 %EOS and parameters from Plymate & Stout (1989)
    m = 0.001;
    p = 0;
    w = 0;
    l = -40;
    for m = 0.001:0.001:30

        Vg = V298g*(1-(ag*(1-((1+(bg*(m-Pth)))^(-cg)))));
        ratioVg = V298g/Vg;

        a0qtz = 3.13E-5; %K^-1
        daqtz = 6.97E-8; %K^-2
        kqtz = 373.1; %kbar
        dkqtz = 6.37;
        dkdTqtz = -0.098; %kbar K^-1

        Vqtz = V298qtz*((1+(((dkqtz*(m-0.001))+((dkdTqtz*(T-298))))/kqtz))^(-
1/dkqtz))*exp(((a0qtz+(dkdTqtz/(kqtz*dkqtz)))+((daqtz-
((dkdTqtz^2)/((kqtz^2)*dkqtz)))*(((T-298)^2)/2))));

        ratioVqtz = Vincl/Vqtz;
        ratioVqtzPLUS = VinclPLUS/Vqtz;

        l = ratioVqtz-((0.75*((10*Pincl)-0.001))/ug)-ratioVg;
        l2 = ratioVqtzPLUS-((0.75*((10*PinclPLUS)-0.001))/ug)-ratioVg;
        if l <= 0
            p = p+1;
        end
        if l2 <= 0
            w = w + 1;
        end

    end
    Po = p*0.001;
    sPo = (w*0.001)-Po; %FROM ANALYTICAL

elseif EOSQtz == 2 %Holland & Powell (1998)a - with Plymate & Stout (1989) elastic
parameters

    aoqtz = 7.44E-5; %ao parameter for Holland and Powell (1998)
    kqtz = 373; %kbar

    m = .001;
    p = 0;
    w = 0;
    l = -40;
    for m = 0.001:0.001:30
```

```
        Vqtz = V298qtz*(1+(aoqtz*(T-298))-(20*aoqtz*((T^0.5)-(298^0.5))))*((1-
((4*m)/((kqtz*(1-((1.5E-4)*(T-298))))+(4*m))))^(0.25)); %volume of quartz at P and T
        Vg = V298g*(1+(aog*(T-298))-(20*aog*((T^0.5)-(298^0.5))))*((1-
((4*m)/((k298g*(1-((1.5E-4)*(T-298))))+(4*m))))^(0.25)); %volume of garnet at P and T
        ratioVg = V298g/Vg;

        ratioVqtz = Vincl/Vqtz;
        ratioVqtzPLUS = VinclPLUS/Vqtz;

        l = ratioVqtz-((0.75*((10*Pincl)-0.001))/ug)-ratioVg;
        l2 = ratioVqtzPLUS-((0.75*((10*PinclPLUS)-0.001))/ug)-ratioVg;
        if l <= 0
            p = p+1;
        end
        if l2 <= 0
            w = w + 1;
        end

    end
    Po = p*0.001;
    sPo = (w*0.001)-Po; %FROM ANALYTICAL

elseif EOSQtz == 3  %Holland & Powell (1998)b - with Dorogokupets (1995) elastic
parameters

    aoqtz = 8.38E-5; %ao parameter for Holland and Powell (1998)
    kqtz = 371; %kbar

    m = .001;
    p = 0;
    w = 0;
    l = -40;
    for m = 0.001:0.001:30
        Vqtz = V298qtz*(1+(aoqtz*(T-298))-(20*aoqtz*((T^0.5)-(298^0.5))))*((1-
((4*m)/((kqtz*(1-((1.5E-4)*(T-298))))+(4*m))))^(0.25)); %volume of quartz at P and T
        Vg = V298g*(1+(aog*(T-298))-(20*aog*((T^0.5)-(298^0.5))))*((1-
((4*m)/((k298g*(1-((1.5E-4)*(T-298))))+(4*m))))^(0.25)); %volume of garnet at P and T
        ratioVg = V298g/Vg;

        ratioVqtz = Vincl/Vqtz;
        ratioVqtzPLUS = VinclPLUS/Vqtz;

        l = ratioVqtz-((0.75*((10*Pincl)-0.001))/ug)-ratioVg;
        l2 = ratioVqtzPLUS-((0.75*((10*PinclPLUS)-0.001))/ug)-ratioVg;
        if l <= 0
            p = p+1;
        end
        if l2 <= 0
            w = w + 1;
        end

    end
    Po = p*0.001;
    sPo = (w*0.001)-Po; %FROM ANALYTICAL

end

set(handles.Pincl_out, 'String', num2str(Pincl*10));
set(handles.sPincl_out, 'String', num2str(sPincl*10));
set(handles.formP_out, 'String', num2str(Po));
set(handles.sPfm, 'String', num2str(sPo));

T_lamb = 847.3+(271.084*(Po/10))-(23.607*((Po/10)^2))+(3.91*((Po/10)^3));
```

```
if T>=T_lamb
    if ispc == 0
        run datafiles/Warn
    else
        run datafiles\Warn
    end
end
```

Appendix C

This section contains auxiliary material included with the manuscript published in Chapter 9.

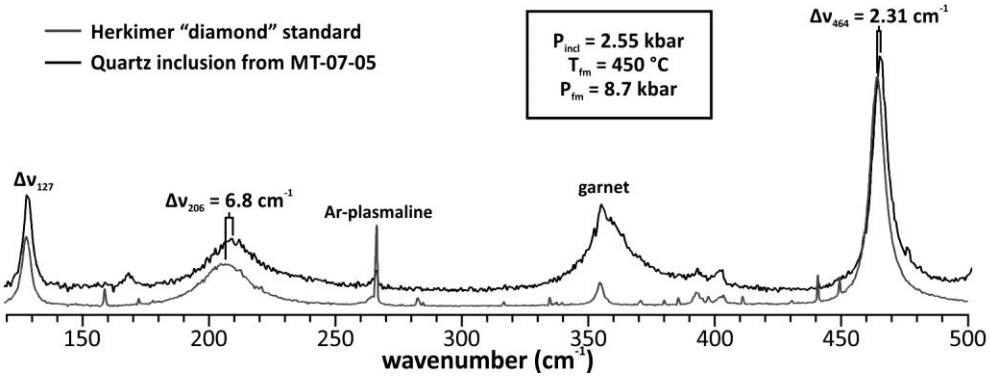

Figure C1. Raman spectra for standard (Herkimer "diamond") quartz and quartz inclusions in garnet from MT-07-05 (following the analytical approach of Ashley *et al.*, 2014). Included quartz has waveshifts of the v464 band of ~2.3 cm-1, suggesting retained inclusion pressures of 2.55 kbar (using P-sensitive waveshift calibration of Schmidt & Ziemann, 2000). Inclusion temperature of 450 °C is assumed, resulting in calculated formation pressures (following the computational approach of Kohn, 2014) of 8.7 kbar.

References

Ashley, K.T., Caddick, M.J., Steele-MacInnis, M., Bodnar, R.J. & Dragovic, B. (2014). Geothermobarometric history of subduction recorded by quartz inclusions in garnet. *Geochemistry Geophysics Geosystems* **15**, 350-360.

Kohn, M.J. (2014). "Geoba-Raman-try": Calibration of spectroscopic barometers and thermometers for mineral inclusions. *Earth and Planetary Science Letters* **388**, 187-196.

Schmidt, C., Ziemann, M.A. (2000). In-situ Raman spectroscopy of quartz: A pressure sensor for hydrothermal diamond-anvil cell experiments at elevated temperatures. *American Mineralogist* **85**, 1725-1734.

Appendix D

This section contains reprinting permissions statements for chapters that are derived from published work and the publisher holds the copyright. Please see the supplementary document that contains full lisence agreements between Kyle T Ashley and the publishers.

Chapter 2

Reprinted from *Geochemistry, Geophysics, Geosystems*, **15**, Ashley, K.T., Caddick, M.J., Steele-MacInnis, M.J., Bodnar, R.J., and Dragovic, B., Geothermobarometric history of subduction recorded by quartz inclusions in garnet, 350-360, Copyright (2014), with permissions from John Wiley and Sons.

Chapter 3

Reprinted from *Computers & Geosciences*, **66**, Ashley, K.T., Steele-MacInnis, and Caddick, M.J., QuIB Calc: A MATLAB® script for geobarometry based on Raman spectroscopy and elastic modeling of quartz inclusions in garnet, 155-157, Copyright (2014), with permissions from Elsevier.

Chapter 6

Reprinted from *American Mineralogist*, **99**, Ashley, K.T., Carlson, W.D., Law, R.D., and Tracy, R.J., Ti resetting in quartz during dynamic recrystallization: Mechanisms and significance, 2025-2030, Copyright (2014), with permissions from the Mineralogical Society of America.

Chapter 7

Reprinted from *Contributions to Mineralogy and Petrology*, **169**, Ashley, K.T., and Law, R.D., Modeling prograde TiO2 activity and its significance for Ti-in-quartz thermobarometry of pelitic metamorphic rocks, 1-7, Copyright (2015), with permissions from Springer.

Chapter 9

Reprinted from *Lithos*, Ashley, K.T., Thigpen, J.R., and Law, R.D., Prograde evolution of the Scottish Caledonides and tectonic implications, http://dx.doi.org/10.1016/j.lithos.2015.03.011, Copyright (2015), with permissions from Elsevier.